Université Lille 1 Sciences et Technologies

Ecole Doctorale Sciences Pour l'Ingénieur
Université Lille Nord-de-France

Doctorat
Micro et Nano Technologies, Acoustique et Télécommunications

Edy WIJAYA

Design and Optimization of Surface Plasmon Resonance (SPR) Biosensors

N° ordre : 40986

Soutenue le 14 décembre 2012 devant la commission d'examen composée de :

Directeur de thèse : Jean-Pierre VILCOT, Directeur de Recherche CNRS, Institut d'Electronique, de Microélectronique et de Nanotechnologie, UMR 8520

Rapporteurs : Michael CANVA, Directeur de Recherche CNRS, Université Paris Sud, Institut d'Optique, Laboratoire Charles Fabry, UMR 8501
Guy LOUARN, Professeur, Université de Nantes, Institut des Matériaux Jean Roussel, UMR 6502

Examinateurs : Olivier DEPARIS, Professeur, Université de Namur, Laboratoire de Physique du Solide
Serge HABRAKEN, Professeur, Université de Liège, Laboratoire Hololab
Yan PENNEC, Maître de Conférences HDR, Université Lille 1, Institut d'Electronique, de Microélectronique et de Nanotechnologie, UMR 8520

Invitée : Catherine FOULON, Maître de Conférences HDR, Université Lille 2, Laboratoire de Chimie Analytique, Faculté des Sciences Pharmaceutiques et Biologiques de Lille

Table of Contents

Abstract

In terms of performance, the ideal biosensor should have high sensitivity, low limits of detection, and extremely short analysis time. Label-free surface plasmon resonance (SPR) biosensors naturally offer the shortest analysis time compared to other types of biosensors. On the other hand, the limits of detection of SPR biosensors are not the most impressive. The inherent sensitivity of SPR biosensors thus needs to be significantly improved to allow lower limits of detection. Several approaches for the enhancement of optical sensitivity of SPR biosensors in the "traditional" attenuated total reflection (ATR) Kretschmann configuration such as the use of bimetallic SPR film, long-range surface plasmons, and near-infrared operating wavelength have been investigated in this work. In addition, some "non traditional" configurations for SPR biosensors including grating-coupled planar optical waveguides and arrays of sub-wavelength structures have been theoretically studied. Novel graphene-based surface functionalization strategy with enhanced biorecognition sensitivity that can be applied to virtually any SPR structure has also been demonstrated.

Résumé

En termes de performance, le biocapteur idéal doit avoir très grande sensibilité, basse limite de détection et temps d'analyse qui est extrêmement court. Les biocapteurs sans marquage à base de résonance de plasmons de surface (biocapteurs SPR) possèdent naturellement le temps d'analyse le plus court parmi différent types de biocapteurs. Leur limite de détection n'est cependant pas la plus impressionnante. Il y a donc un besoin pour augmenter considérablement la sensibilité intrinsèque des biocapteurs SPR afin d'atteindre de plus basses limites de détection. Quelques approches pour exalter la sensibilité optique des biocapteurs SPR dans la configuration « traditionnel » de Krestchmann telles que film SPR bimétallique, plasmons à longues portées et détection dans l'infrarouge proche sont examinées dans ce travail. Des configurations « non traditionnelles » comme guides optiques planaires avec couplage par réseau et structures sub-longueur d'ondes ont été aussi théoriquement étudiées. Nouvelle stratégie de fonctionnalisation de surface à base de graphène qui augmente la sensibilité de reconnaissance biomoléculaire et peut être appliquée à quasiment toute structure SPR a été également démontrée.

Acknowledgements

I would like to thank first and foremost my thesis advisor, Jean-Pierre Vilcot, for his overall guidance over the course of my doctoral research. Thanks in particular for giving me a great deal of freedom and independence to define and pursue my research avenues.

I would like to then thank the Optoelectronics Group in its entirety for offering all their help and warm friendship as well as IEMN clean room (administrative) personnel for their technical (administrative) assistance. In the same vein, my gratitude goes to numerous colleagues within the Plasmobio project for all the fruitful scientific exchanges and collaborations in addition to the friendly work atmosphere.

I am deeply indebted to my family for their invaluable enduring moral support. I am also grateful to my compatriots in Lille area for their fellowship. Last but not least, special thanks to my lovely sweetheart for her patience and encouragement.

Preface

This work is a subset of a larger interdisciplinary French-Belgian research project dubbed Plasmobio whose goal is to develop innovative surface plasmon resonance (SPR) biosensors for biomedical applications. This project is partially funded by the European Regional Development Fund through the INTERREG IVA program for its four-year duration from 2009 to 2013. The cross-border scientific collaboration in the Plasmobio research project involves five partner institutions: the University of Lille 1, the University of Lille 2, the University of Mons, the University of Liège, and Eurasanté.

The University of Lille 1 takes part in the Plasmobio project through three of its associated laboratories:

- the Institute of Electronics, Microelectronics, and Nanotechnology (IEMN). Particularly well equipped for the design and fabrication of devices at the micrometer and nanometer length scales, two independent research groups from this institute actively contribute to the project. The Optoelectronics group provides the required expertise in photonics while the competence in digital microfluidics is supplied by the BioMEMS group.

- the Physics of Lasers, Atoms, and Molecules Laboratory (PhLAM) where the SPR measurement setups at the wavelengths of 760 nm and 1550 nm are developed and housed.

- the Institute of Interdisciplinary Research (IRI). The Nano-Bio-Interfaces group from this institute provides the complementary expertise in surface chemistry.

The University of Lille 2 is involved in the Plasmobio project through its molecular interactions platform housed within the Institute of Predictive Medicine and Therapeutic Research. This platform provides technological assistance in the study of biomolecular interactions by SPR techniques to various research groups of the university and the regional university medical center of Lille as well as other public or private organizations.

The University of Mons participates in the Plasmobio project through its Interfaces and Complex Fluids Laboratory (InFluX) that specializes in the study of surfaces and interfaces as well as polymer chemistry.

The University of Liège contributes to the Plasmobio project through the Laboratory of Optics and Holography (Hololab) that has well-established expertise in holography as well as diffractive optics and the Space Center of Liège

(CSL) which is one of the test centers of the European Space Agency that provides scientific and technical support to industry and research centers in optical instrumentation, solar energy, microsystems, and sensors.

Eurasanté is a non-profit organization whose mission is to promote economic development of the healthcare industry in the Nord-Pas de Calais region. In the framework of the Plasmobio project, Eurasanté is in charge of external communication services to mass media as well as regional players in the life sciences and healthcare sector.

This work is carried out within the Optoelectronics group of IEMN where SPR sensor chips are designed and fabricated. Experimental measurements with these SPR sensor chips are subsequently performed in collaboration with PhLAM and IRI. The collaboration with PhLAM involves SPR sensing measurements at the wavelength of 760 nm (Prof. Bernard Pinchemel) as well as 1550 nm (Dr. Jérôme Hottin). The collaborative work with IRI concerns biosensing experiments on grapene-based SPR interfaces (Nazek Maalouli, Dr. Rabah Boukherroub, and Prof. Sabine Szunerits).

Chapter 1

Introduction

Biosensor research is a vital and rapidly progressing field. It is also a highly interdisciplinary endeavor bringing together physicists and engineers to develop the hardware parts of a sensor, chemists to modify the sensor surfaces and to synthesize sensor labels or specific bioreceptors, and biologists or doctors interested in specific biological systems or biotechnological processes.

Major areas of biosensor applications are basic research in the life sciences [1, 2, 3], health care and medical diagnostics [4, 5, 6, 7], environmental monitoring [8, 9, 10, 11, 12], drug screening and discovery [13, 14, 15, 16, 17], food safety and analysis [18, 19, 20, 21, 22, 23, 24], and the detection of hazardous substances for military applications [25]. With such a myriad of diverse applications, the global market for biosensors is forecast to reach US$ 12 billion by the year 2015 [26].

What exactly is a biosensor? A biosensor can be defined as an analytical device which detects the presence or activity of biomolecules. To do so, a biosensor needs two basic components in very close proximity. The first one is a biorecognition element which is a layer of biomolecules that can bind or interact with specific target molecules in the sample. The second component is a transducer which is able to detect the interaction between the biorecognition element and the target molecules. The transducer then converts this biorecognition event into a measurable signal for further processing. As diagrammatically illustrated in Figure 1.1, the transducers used in biosensors are most commonly based on electrical (e.g., electrochemical impedance, field-effect transistor), mechanical (e.g., cantilever deflection, surface acoustic wave, quartz-crystal microbalance resonance), or optical (surface plasmon resonance, fluorescence, microring resonator) phenomena.

Depending on the detection principle in regard to molecular labeling, biosensors can be divided into two classes. These are labeled biosensors and label-free biosensors. Certain molecules are often easier to detect when first tagged with a molecular label. The presence of the label then acts as an indicator for the presence of the molecule in question. Labels can be fluorophores, magnetic

beads, active enzymes with an easily detectable product, or anything else allowing facile target conjugation and convenient detection. An important example is fluorescence microscopy where molecules are located by signals from their fluorescent labels. The major disadvantage of such labeling method is that the target molecules are chemically modified before they are investigated. Although labeling can potentially improve the detection limits, the label might also interfere with the function of the biomolecules and drastically change its binding properties. The yield of the target-label coupling reaction is also highly variable. Moreover, the labeling process is both time- and cost-consuming. Label-free biosensors on the other hand detect the original unmodified molecules and can be used for online monitoring or fast and direct detection.

Figure 1.1. Diagrammatic illustration of the components of a biosensor.

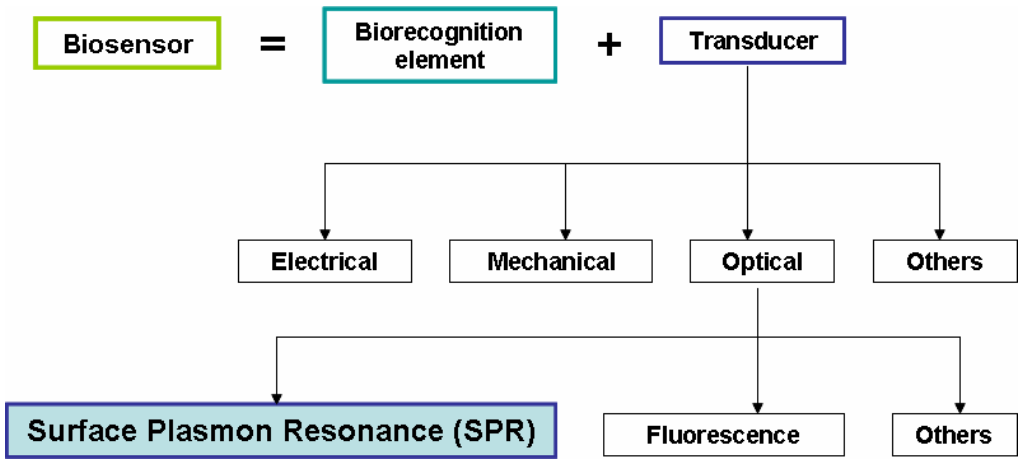

Currently, the most prominent optical biosensors are based on either surface plasmon resonance (SPR) or fluorescence. While fluorescence-based optical biosensors are necessarily labeled, SPR-based biosensors are by and large label-free. Labeled fluorescence techniques can however be combined with SPR in order to achieve very low limits of detection not commonly obtained with label-free SPR.

Figure 1.2 shows the limit of detection versus analysis time on logarithmic scales for different types of biosensors where the black dashed line indicates the present state-of-the-art with longer analysis times leading to lower limits of detection [27]. The solid black sloping lines in Figure 1.2 marks the biosensor

performance needed to detect the secretion of tumor necrosis factor (TNF) protein from a single human cell for both native and stimulated single cell secretion.

Figure 1.2. The limit of detection versus analysis time on logarithmic scales for different types of biosensor: surface plasmon resonance (SPR), suspended microchannel resonator (SMR), nanowire (NW), lateral flow assay (LFA), microring resonator (MRR), quartz crystal microbalance (QCM), biobarcode amplification assay (BBA), immunofluorescent assay (IFA), and microcantilever (MC). The black dashed line shows the present state-of-the-art. Figure is taken from reference [27].

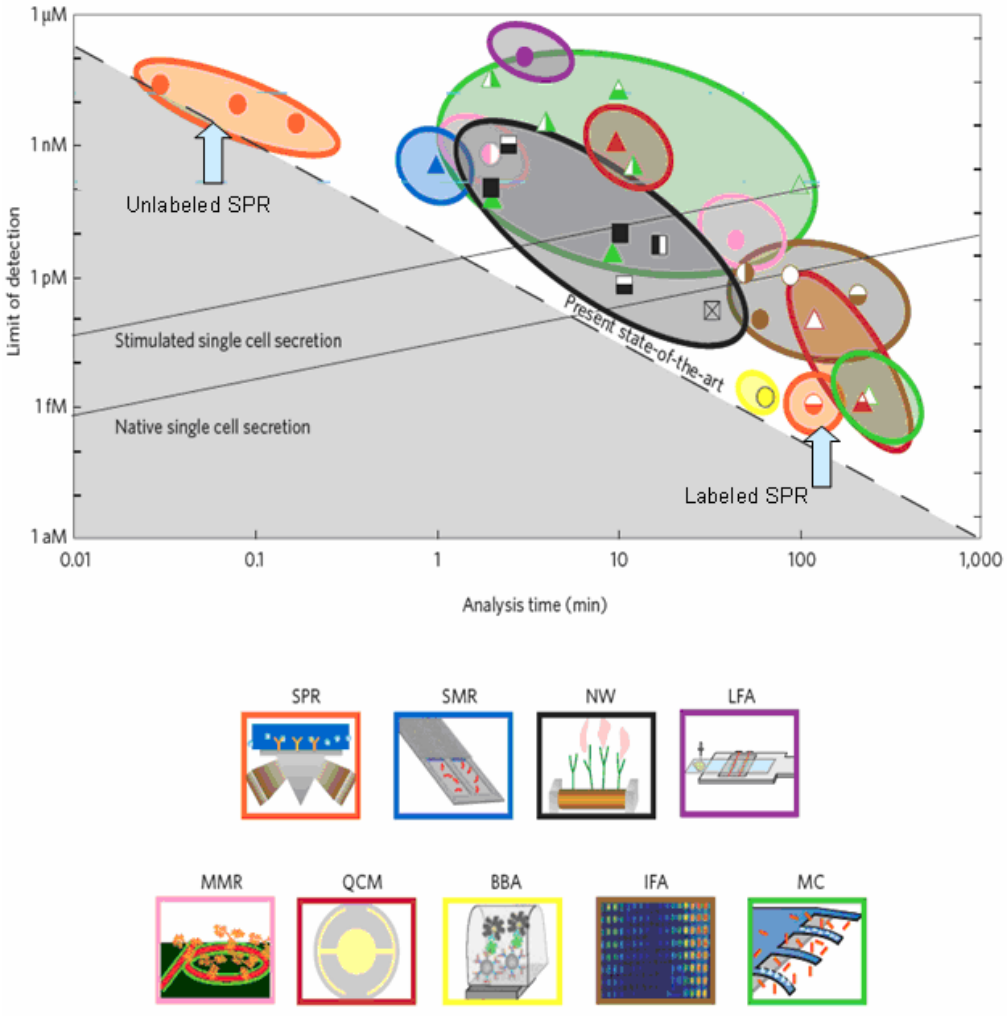

In terms of performance, the ideal biosensor should have exceedingly low limits of detection and simultaneously very short analysis time. In other words, its

performance should be situated in the bottom left region of the graph displayed in Figure 1.2.

It can be immediately seen from Figure 1.2 that among various sorts of biosensors, label-free SPR-based biosensors offer the shortest analysis time on the order of seconds or less thus allowing real-time monitoring of biomolecular interactions [28]. With such an extremely short analysis time, label-free SPR biosensors have the potential to play the dominant role in critical applications of biosensors where time is of the essence such as the detection of hazardous biochemical warfare agents for defense purposes [29]. On the other hand, the limit of detection of unlabeled SPR is only around the nanomolar concentration which is certainly not the most spectacular. Nevertheless, it has been experimentally demonstrated that this limit of detection can be significantly improved by orders of magnitude down to the state-of-the-art femtomolar range by the use of labels at the expense of compromised analysis time which becomes as long as two hours for the resulting labeled SPR biosensor [30].

Figure 1.2 indicates that with a distinctive edge on extremely short analysis time, label-free SPR biosensors are clearly excellent candidates for the ideal biosensor provided their limits of detection are pushed further to be competitive with other types of biosensors. Hence, there is a significant need to boost the inherent sensitivity of label-free SPR biosensors so that lower limits of detection can be achieved. The objective of this work is to contribute to this quest by investigating some novel ideas for the design and optimization of SPR structure to enhance the intrinsic sensitivity of label-free SPR biosensors.

The presentation of this work is subsequently organized as follows. Chapter 2 introduces the necessary theoretical background for solid comprehension of the underlying properties of surface plasmons that are pertinent to biosensing. The basic operating principles of SPR-based biosensors are then covered in Chapter 3. The calculation methods as well as materials modeling for SPR biosensors in the "traditional" configuration used in this work are detailed in Chapter 4. The general influence of some design parameters on the performance of the resulting SPR biosensors are also elaborated in Chapter 4. This is followed by Chapter 5 which discusses the enhancement of the optical sensitivity of SPR biosensors in the "traditional" configuration. Chapter 6 treats the subject of novel graphene-based surface functionalization strategy which can virtually be applied to any SPR structure. In Chapter 7, the focus is shifted from the "traditional" configuration towards some original geometry in the design of SPR biosensors. The "non-traditional" optical designs considered here are integrated optical waveguide

structures and some relatively simple arrays of micro/nanostructures. Chapter 8 finally summarizes the results presented in the preceding chapters as well as outlines some perspectives for future development.

Chapter 2

Electromagnetic Theory of Surface Plasmons

Before discussing the theory of SPR biosensors, a firm understanding of the underlying properties of surface plasmons is essential. The aim of this chapter is to provide the necessary theoretical background for solid comprehension of the properties of surface plasmons that are pertinent to biosensing.

Surface plasmons, also often known in the literature as surface plasmon polaritons (SPPs) or suface plasma waves (SPWs), are electromagnetic excitations in the form of charge density oscillations propagating at the interface between a dielectric and a metal, evanescently confined in the perpendicular direction (Figure 1). It will be shown below that surface plasmons at a metal-dielectric interface are necessarily transverse-magnetic (TM) waves.

Figure 2.1. Schematic illustration of charge density oscillations at a metal-dielectric interface propagating in the x direction.

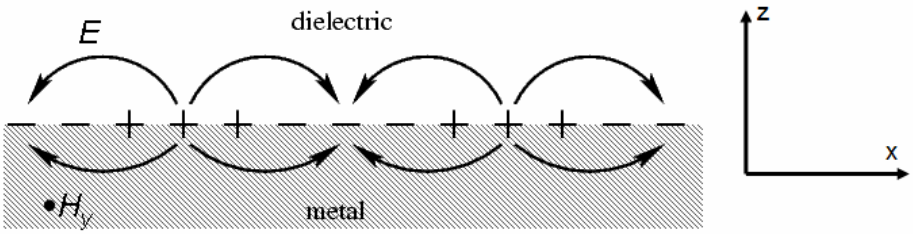

2.1. Surface Plasmons at a Single Interface

Consider first the general case of an interface between two different semi-infinite media described by their respective dielectric functions (relative electric permittivities) and relative magnetic permeabilities as shown in Figure 2.2.

The electric and magnetic fields have to satisfy the following Maxwell's equations:

$$\nabla \times \mathbf{E} = -\frac{\partial \mathbf{B}}{\partial t} = -\mu_r \mu_0 \frac{\partial \mathbf{H}}{\partial t} \tag{2.1}$$

$$\nabla \times \mathbf{H} = \mathbf{j} + \frac{\partial \mathbf{D}}{\partial t} = \sigma \mathbf{E} + \varepsilon_r \varepsilon_0 \frac{\partial \mathbf{E}}{\partial t} \tag{2.2}$$

together with the boundary conditions that the tangential electric and magnetic fields are continuous across the interface.

Figure 2.2. Geometry of surface plasmons propagation at a single interface between two different media.

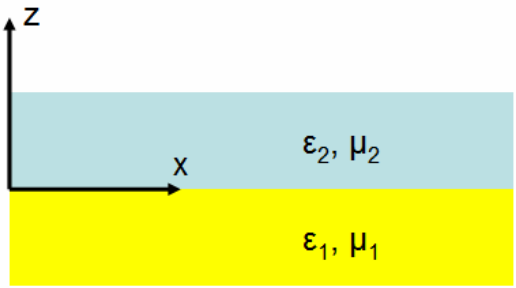

Assuming harmonic time dependence of the form $\mathbf{E} = \mathbf{E}(\mathbf{r})\exp(-j\omega t)$ and $\mathbf{H} = \mathbf{H}(\mathbf{r})\exp(-j\omega t)$ where ω is the angular frequency and $j = \sqrt{-1}$, Equations (2.1) and (2.2) can be written as

$$\nabla \times \mathbf{E} = j\omega\mu\mu_0 \mathbf{H} \tag{2.3}$$

$$\nabla \times \mathbf{H} = -j\omega\varepsilon\varepsilon_0 \mathbf{E} \tag{2.4}$$

Note that in Equation (2.4), the relative electric permittivity has been redefined to include the electrical conductivity as $\varepsilon = \varepsilon_r + j\sigma/(\omega\varepsilon_0)$. This convention has the advantage that the resulting equation applies equally well to both conductive and non-conductive materials, i.e., no separate treatment needs to be considered for conductive and non-conductive materials. Furthermore, the subscript *r* in both the relative electric permittivity and the relative magnetic permeability has been dropped to simplify the notations.

Referring to the geometry in Figure 2.2, a general electromagnetic wave can be decomposed into two linearly independent sets with different polarization properties of the propagating waves, namely the transverse magnetic (TM or p) modes and the transverse electric (TE or s) modes so that the analysis of an

electromagnetic wave can be simplified by investigating these two modes separately.

2.1.1. TM Modes

For the TM modes, only the field components E_x, E_z, and H_y are nonzero. The relationships between these field components are governed by Equations (2.3) and (2.4). From Equation (2.4),

$$-\frac{\partial H_y}{\partial z} = -j\omega\varepsilon\varepsilon_0 E_x \tag{2.5}$$

$$\frac{\partial H_y}{\partial x} = -j\omega\varepsilon\varepsilon_0 E_z \tag{2.6}$$

so that the electric fields E_x and E_z can be derived from the only non-vanishing component of the magnetic field H_y:

$$E_x = \frac{1}{j\omega\varepsilon\varepsilon_0}\frac{\partial H_y}{\partial z} \tag{2.7}$$

$$E_z = -\frac{1}{j\omega\varepsilon\varepsilon_0}\frac{\partial H_y}{\partial x} \tag{2.8}$$

From Equation (2.3),

$$\frac{\partial E_x}{\partial z} - \frac{\partial E_z}{\partial x} = j\omega\mu\mu_0 H_y \tag{2.9}$$

The combination of Equation (2.9) with Equations (2.7) and (2.8) requires that H_y satisfy the following condition:

$$\frac{\partial^2 H_y}{\partial z^2} + \frac{\partial^2 H_y}{\partial x^2} = -\omega^2\mu\varepsilon(\mu_0\varepsilon_0)H_y = -\frac{\omega^2}{c^2}\mu\varepsilon H_y \tag{2.10}$$

Equations (2.7) and (2.8) imply that to characterize a TM mode, it is sufficient to specify H_y. As we are looking for propagating wave solutions confined to the interface, i.e. with evanescent decay in the z direction, the only non-zero magnetic field component H_y can be described by

$$H_{y1} = A_1 \exp\left(j\beta_1 x - jk_1 z\right) \tag{2.11}$$

$$k_1 = j|k_1| \tag{2.12}$$

in medium 1 where z < 0, and by

$$H_{y2} = A_2 \exp\left(j\beta_2 x + jk_2 z\right) \tag{2.13}$$

$$k_2 = j|k_2| \tag{2.14}$$

in medium 2 where z > 0.

Equation (2.7) gives the tangential component of the electric fields as

$$E_{x1} = \frac{1}{j\omega\varepsilon_1\varepsilon_0}\frac{\partial H_{y1}}{\partial z} = -\frac{k_1}{\omega\varepsilon_1\varepsilon_0}H_{y1} \tag{2.15}$$

for medium 1, and

$$E_{x2} = \frac{1}{j\omega\varepsilon_2\varepsilon_0}\frac{\partial H_{y2}}{\partial z} = \frac{k_2}{\omega\varepsilon_2\varepsilon_0}H_{y2} \tag{2.16}$$

for medium 2.

From the continuity of the tangential magnetic fields at the interface z = 0,

$$H_{y1}\big|_{z=0} = H_{y2}\big|_{z=0} \Rightarrow A_1 = A_2 = A;\ \ \beta_1 = \beta_2 = \beta \tag{2.17}$$

The continuity of the tangential electric fields at the interface z = 0 implies

$$E_{x1}\big|_{z=0} = E_{x2}\big|_{z=0} \Rightarrow \frac{k_1}{\varepsilon_1} = -\frac{k_2}{\varepsilon_2} \tag{2.18}$$

Equations (2.12), (2.14), and (2.18) show that for surface plasmons to be supported, the dielectric functions of the two media need to be of opposite signs.

From Equations (2.10), (2.11), and (2.13), the relation

$$k^2 + \beta^2 = \omega^2(\varepsilon_0\mu_0)\varepsilon\mu = \left(\frac{\omega}{c}\right)^2 \varepsilon\mu \tag{2.19}$$

has to be satisfied for both media. Combining this with Equation (2.18) gives

$$\varepsilon_2{}^2 k_1{}^2 = \varepsilon_1{}^2 k_2{}^2 \tag{2.20}$$

$$\varepsilon_2^{\,2}\left[\frac{\omega^2}{c^2}\varepsilon_1\mu_1-\beta^2\right]=\varepsilon_1^{\,2}\left[\frac{\omega^2}{c^2}\varepsilon_2\mu_2-\beta^2\right] \tag{2.21}$$

Solving for the propagation constant β, the dispersion relation is obtained as

$$\beta_{TM}=\frac{\omega}{c}\left\{\frac{\varepsilon_1\varepsilon_2\left(\varepsilon_1\mu_2-\varepsilon_2\mu_1\right)}{\left(\varepsilon_1+\varepsilon_2\right)\left(\varepsilon_1-\varepsilon_2\right)}\right\}^{1/2} \tag{2.22}$$

For the special case of ordinary non-magnetic materials, $\mu_1 = \mu_2 = 1$ so that

$$\beta=\frac{\omega}{c}\left\{\frac{\varepsilon_1\varepsilon_2}{\left(\varepsilon_1+\varepsilon_2\right)}\right\}^{1/2}=k_0\left\{\frac{\varepsilon_1\varepsilon_2}{\left(\varepsilon_1+\varepsilon_2\right)}\right\}^{1/2} \tag{2.23}$$

where k_0 is the wave number in free space.

2.1.2. TE Modes

For the TE modes, the only nonzero field components are H_x, H_z, and E_y. The relationships between these field components are again governed by Equations (2.3) and (2.4). From Equation (2.3),

$$H_x=-\frac{1}{j\mu\mu_0\omega}\frac{\partial E_y}{\partial z} \tag{2.24}$$

$$H_z=\frac{1}{j\mu\mu_0\omega}\frac{\partial E_y}{\partial x} \tag{2.25}$$

Equation (2.4) gives

$$\frac{\partial H_x}{\partial z}-\frac{\partial H_z}{\partial x}=-j\omega\varepsilon\varepsilon_0E_y \tag{2.26}$$

Equation (2.26) together with Equations (2.24) and (2.25) require that

$$\frac{\partial^2E_y}{\partial z^2}+\frac{\partial^2E_y}{\partial x^2}=-\omega^2\mu\varepsilon(\mu_0\varepsilon_0)E_y=-\frac{\omega^2}{c^2}\mu\varepsilon E_y \tag{2.27}$$

As in the case of TM modes, Equations (2.24) and (2.25) imply that to characterize a TE mode, it is sufficient to specify E_y. As we are looking for

propagating wave solutions confined to the interface, i.e. with evanescent decay in the z direction, the only non-zero electric field component E_y can be described by

$$E_{y1} = B_1 \exp\left(j\beta_1 x - jk_1 z \right) \tag{2.28}$$

$$k_1 = j\left|k_1\right| \tag{2.29}$$

in medium 1 where z < 0, and by

$$E_{y2} = B_2 \exp\left(j\beta_2 x + jk_2 z \right) \tag{2.30}$$

$$k_2 = j\left|k_2\right| \tag{2.31}$$

in medium 2 where z > 0.

Equation (2.24) gives the tangential component of the magnetic fields as

$$H_{x1} = -\frac{1}{j\omega\mu_1\mu_0}\frac{\partial E_{y1}}{\partial z} = \frac{k_1}{\omega\mu_1\mu_0}E_{y1} \tag{2.32}$$

$$H_{x2} = -\frac{1}{j\omega\mu_2\mu_0}\frac{\partial E_{y2}}{\partial z} = -\frac{k_2}{\omega\mu_2\mu_0}E_{y2} \tag{2.33}$$

From the continuity of the tangential electric fields at the interface z = 0,

$$E_{y1}\Big|_{z=0} = E_{y2}\Big|_{z=0} \Rightarrow B_1 = B_2 = B;\ \ \beta_1 = \beta_2 = \beta \tag{2.34}$$

The continuity of the tangential magnetic fields at the interface implies that

$$H_{x1}\Big|_{z=0} = H_{x2}\Big|_{z=0} \Rightarrow \frac{k_1}{\mu_1} = -\frac{k_2}{\mu_2} \tag{2.35}$$

For the special case of ordinary non-magnetic materials, $\mu_1 = \mu_2 = 1$ so that

$$k_1 + k_2 = 0 \tag{2.36}$$

Equation (2.36) together with Equations (2.29) and (2.31) require that

$$\left|k_1\right| + \left|k_2\right| = 0 \ \ \Rightarrow \ \ k_1 = k_2 = 0 \tag{2.37}$$

Equation (2.37) is in contradiction with the starting hypothesis that the wave is evanescently confined in the z direction. This implies that for ordinary non-

magnetic materials, surface plasmons cannot be supported by TE modes. As for the general case, Equations (2.27), (2.28), and (2.30) imply that the relation in Equation (2.19) is also satisfied by the TE modes. Combining this relation with Equation (2.35) and solving for β gives the propagation constant of surface plasmons in TE mode:

$$\beta_{TE} = \frac{\omega}{c}\left\{\frac{\mu_1\mu_2(\mu_1\varepsilon_2 - \mu_2\varepsilon_1)}{(\mu_1+\mu_2)(\mu_1-\mu_2)}\right\}^{1/2} \tag{2.38}$$

Equations (2.29), (2.31) and (2.35) show that for surface plasmons to exist in TE modes with the dispersion relation given by Equation (2.38), the magnetic permeabilities of the two media have to be of opposite signs. Naturally occurring materials only have a positive relative magnetic permeability so that this requirement cannot be met by ordinary materials. It is however possible to be satisfied by an emerging class of metamaterials exhibiting a negative relative magnetic permeability.

Comparing the equations for both the TM and TE modes, it is also instructive to note that owing to the symmetry of Maxwell's equations, the equations for the TE modes can be easily obtained from the corresponding equations for the TM modes by the substitutions:

$$\left\{\begin{array}{lcl} \mathbf{E} & \rightarrow & -\mathbf{H} \\ \mathbf{H} & \rightarrow & \mathbf{E} \\ \varepsilon & \rightarrow & \mu \\ \mu & \rightarrow & \varepsilon \end{array}\right\} \tag{2.39}$$

It has just been previously shown that for ordinary non-magnetic materials, surface plasmons can only exist in TM modes at the interface between two media whose dielectric functions have opposite signs. Moreover, Equation (2.23) implies that the absolute value of the dielectric function of the medium with negative dielectric function needs to be larger than that of the other medium with positive dielectric function. At optical frequencies, typical dielectric media such as insulators have a small positive dielectric function while metals naturally possess a large negative dielectric function. Therefore, surface plasmons can be supported at the interface between a dielectric and a metal. In general, the dielectric function of metals is complex. The imaginary part of the dielectric function of metals stems from ohmic losses due to their finite electrical conductivity. Consequently, the propagation constant of surface plasmons as expressed by Equation (2.23) is

generally a complex number. Equations (2.11), (2.13), (2.15), and (2.16) show that if the imaginary part of the surface plasmons propagation constant is nonzero, the amplitude of the electromagnetic fields decays as the surface plasmons propagate. The nonzero imaginary part of the surface plasmons propagation constant is therefore responsible for the propagation loss of surface plasmons.

2.2. Surface Plasmons at Two Interfaces

In the preceding section, it has been shown that for ordinary non-magnetic materials, surface plasmons exist as a TM-polarized mode at the interface between a dielectric and a metal. Both media were however assumed to be semi-infinite. In this section, the case where the metal has a finite thickness is examined. The geometry considered this time is shown in Figure 2.3. A thin metallic film (medium I) of thickness $2a$ is sandwiched between two semi-infinite dielectric layers (II and III). In such a system, the metallic layer (medium I) possesses two metal-dielectric interfaces: one with medium II and another one with medium III where each single interface can support surface plasmons. When the separation distance between these adjacent interfaces is comparable or smaller than the field decay length of the bound interface modes, the surface plasmons from the two interfaces can interact to create coupled modes with interesting properties.

To illustrate these concepts mathematically, consider a general description of TM modes that are non-oscillatory in the z-direction normal to the interfaces. In the cladding regions where $z > a$ and $z < -a$, the fields are therefore exponentially decaying in the z-direction.

Figure 2.3. Geometry of a three-layer system supporting surface plasmons at two interfaces.

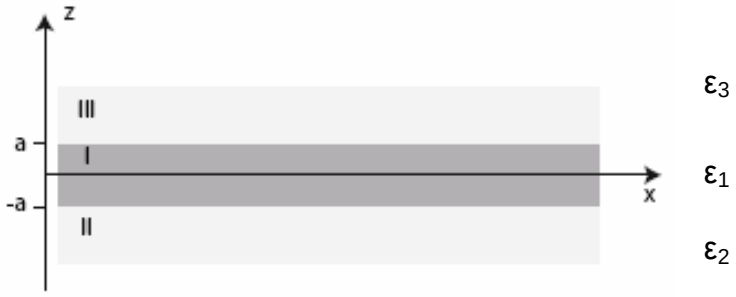

For $z > a$,

$$H_y = Ae^{j\beta x}e^{-k_3 z} \tag{2.40}$$

Using Equations (2.7) and (2.8), the electric field components E_x and E_z can be easily determined to be

$$E_x = \frac{jk_3 A}{\omega\varepsilon_0\varepsilon_3} e^{j\beta x} e^{-k_3 z} \tag{2.41}$$

$$E_z = \frac{-\beta A}{\omega\varepsilon_0\varepsilon_3} e^{j\beta x} e^{-k_3 z} \tag{2.42}$$

The electric and magnetic field components for the region $z < -a$ can be determined in a similar fashion:

$$H_y = Be^{j\beta x} e^{k_2 z} \tag{2.43}$$

$$E_x = \frac{-jk_2 B}{\omega\varepsilon_0\varepsilon_2} e^{j\beta x} e^{k_2 z} \tag{2.44}$$

$$E_z = \frac{-\beta B}{\omega\varepsilon_0\varepsilon_2} e^{j\beta x} e^{k_2 z} \tag{2.45}$$

In the core region $-a < z < a$, the surface plasmons from the lower and upper interface interact yielding a superposition of electromagnetic fields:

$$H_y = Ce^{j\beta x} e^{k_1 z} + De^{j\beta x} e^{-k_1 z} \tag{2.46}$$

$$E_x = \frac{-ik_1 C}{\omega\varepsilon_0\varepsilon_1} e^{j\beta x} e^{k_1 z} + \frac{ik_1 D}{\omega\varepsilon_0\varepsilon_1} e^{j\beta x} e^{-k_1 z} \tag{2.47}$$

$$E_z = \frac{\beta C}{\omega\varepsilon_0\varepsilon_1} e^{j\beta x} e^{k_1 z} + \frac{\beta D}{\omega\varepsilon_0\varepsilon_1} e^{j\beta x} e^{-k_1 z} \tag{2.48}$$

The continuity of the tangential components of the electric and magnetic fields E_x and H_y at the upper interface leads to

$$Ae^{-k_3 a} = Ce^{k_1 a} + De^{-k_1 a} \tag{2.49}$$

$$\frac{A}{\varepsilon_3} k_3 e^{-k_3 a} = -\frac{C}{\varepsilon_1} k_1 e^{k_1 a} + \frac{D}{\varepsilon_1} k_1 e^{-k_1 a} \tag{2.50}$$

The continuity of the tangential components of the electric and magnetic fields E_x and H_y at the lower interface yields similar equations:

$$Be^{-k_2 a} = Ce^{-k_1 a} + De^{k_1 a} \tag{2.51}$$

$$-\frac{B}{\varepsilon_3} k_2 e^{-k_2 a} = -\frac{C}{\varepsilon_1} k_1 e^{-k_1 a} + \frac{D}{\varepsilon_1} k_1 e^{k_1 a} \tag{2.52}$$

Furthermore, H_y has to satisfy Equation (2.10) in the three distinct regions which results in

$$k_i^{\,2} = \beta^2 - k_0^{\,2} \varepsilon_i \tag{2.53}$$

for $i = 1, 2, 3$ where $k_0 = \left(\frac{\omega}{c}\right)$.

Equations (2.49), (2.50), (2.51), and (2.52) constitute a system of four linear equations in four unknowns that when written in matrix form yields

$$\begin{bmatrix} -e^{-k_3 a} & 0 & e^{k_1 a} & e^{-k_1 a} \\ -\frac{k_3}{\varepsilon_3} e^{-k_3 a} & 0 & -\frac{k_1}{\varepsilon_1} e^{k_1 a} & \frac{k_1}{\varepsilon_1} e^{-k_1 a} \\ 0 & -e^{-k_2 a} & e^{-k_1 a} & e^{k_1 a} \\ 0 & \frac{k_2}{\varepsilon_2} e^{-k_2 a} & -\frac{k_1}{\varepsilon_1} e^{-k_1 a} & \frac{k_1}{\varepsilon_1} e^{k_1 a} \end{bmatrix} \begin{bmatrix} A \\ B \\ C \\ D \end{bmatrix} = \begin{bmatrix} 0 \\ 0 \\ 0 \\ 0 \end{bmatrix} \tag{2.54}$$

Equating the determinant in the above matrix equation results in an implicit expression for the dispersion relation:

$$e^{-4k_1 a} = \left(\frac{k_1/\varepsilon_1 + k_2/\varepsilon_2}{k_1/\varepsilon_1 - k_2/\varepsilon_2}\right)\left(\frac{k_1/\varepsilon_1 + k_3/\varepsilon_3}{k_1/\varepsilon_1 - k_3/\varepsilon_3}\right) \tag{2.55}$$

Note that in the limit of an infinitely thick metal ($a \to \infty$), Equation (2.55) reduces to

$$\left(k_1/\varepsilon_1 + k_2/\varepsilon_2\right)\left(k_1/\varepsilon_1 + k_3/\varepsilon_3\right) = 0 \tag{2.56}$$

which when compared to Equation (2.18) shows two uncoupled surface plasmons modes at the I-II and I-III interfaces as expected.

A special case arises when the two adjacent media II and III are identical. In this case, the dispersion relation expressed by Equation (2.55) can be split into a pair of equations, namely

$$\tanh k_1 a = -\frac{k_2 \varepsilon_1}{k_1 \varepsilon_2} \tag{2.57}$$

$$\tanh k_1 a = -\frac{k_1 \varepsilon_2}{k_2 \varepsilon_1} \tag{2.58}$$

As far as the tangential electric field distribution is concerned, it can be shown that Equation (2.57) describes modes of odd vector parity ($E_x(z)$ is an odd function while $H_y(z)$ and $E_z(z)$ are even functions) while Equation (2.58) describes modes of even vector parity ($E_x(z)$ is an even function while $H_y(z)$ and $E_z(z)$ are odd functions) [31]. A different terminology based on the distribution of the magnetic field is also often used to designate these modes. The modes of odd vector parity are referred to as the symmetric mode ($H_y(z)$ is even and therefore symmetric) and the modes of even vector parity are referred to as the antisymmetric mode ($H_y(z)$ is odd). However, the most interesting feature of these distinct modes lies in the dependence of their dispersion relation to the thickness of the metallic layer. Upon decreasing the thickness of the metal film, the modes of odd vector parity become less confined to the metal film and evolve into a plane wave supported by the homogeneous dielectric environment. As a result, the propagation length of the surface plasmons in this case is drastically increased. For this reason, the odd modes are also called the long-range surface plasmons [32]. The even modes on the other hand exhibit the opposite behavior, i.e., their confinement to the metal film increases with decreasing metal thickness resulting in a reduction of propagation length. The even modes are therefore referred to as the short-range surface plasmons.

To further elucidate the long-range and short-range surface plasmons with a physically practical example, consider a three-layer system consisting of water-

gold-water multilayer stack at the wavelength of 1550 nm. The dielectric function of the gold layer is based on a mathematical fit of various measurement results to a Lorentz-Drude model. The dielectric function of water is obtained from an empirical formulation for the refractive index of water and steam as a function of wavelength, temperature, and density. The materials models are discussed in more details in Chapter 4. In this example, the propagation constant of the two surface plasmons modes are calculated as a function of the thickness of the gold layer. As the propagation constant $\beta = \beta' + j\beta''$ of the long-range and short-range surface plasmons is complex, the imaginary part β'' is shown in Figure 2.4 while the real part β' is plotted in Figure 2.5. In both figures, the real and imaginary parts of the propagation constant are normalized by the wave number in free space k_0.

Figure 2.4. Imaginary part of the propagation constant of the long-range and short-range surface plasmons as a function of metal thickness. The layered structure considered here is water-gold-water at λ = 1550 nm.

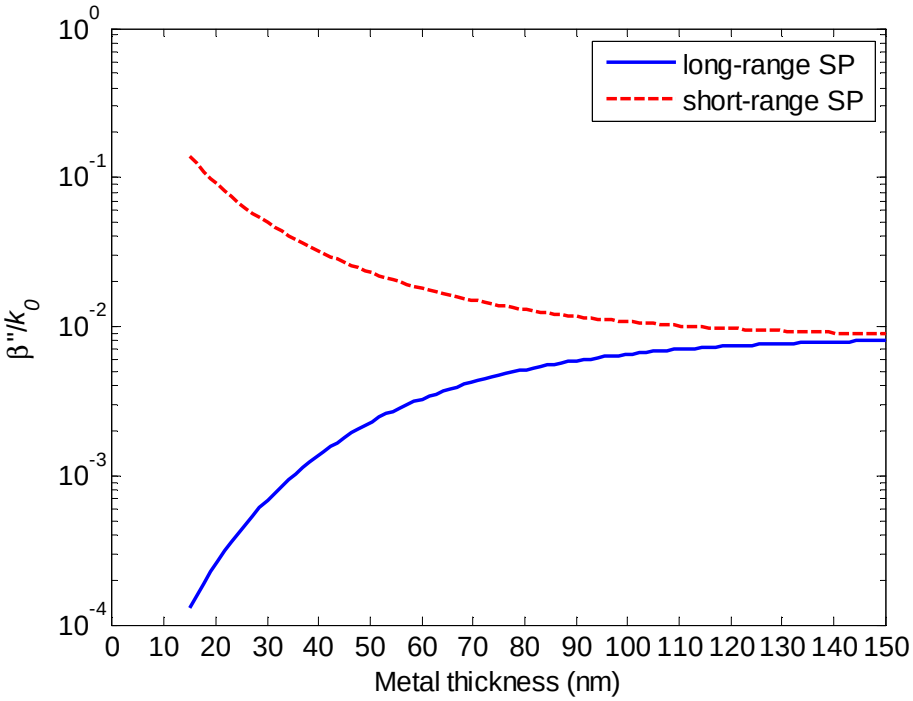

As shown in Figures 2.4 and 2.5, in the limit of very thick metal layer, only a single surface plasmons mode exists. Two independent surface plasmons modes are actually supported, one at each interface. However, when the sandwiched metal layer is sufficiently thick, the electromagnetic fields of the surface plasmons

from one interface cannot reach the other interface due to the strong damping in the metal. As a result, the surface plasmons at the two interfaces do not interact. As the dielectric environment at each interface is identical and there is no interaction between the surface plasmons at one interface with those at the other interface, the long-range and short-range surface plasmons modes can be said to merge into a single mode.

When the thickness of the metal layer is gradually reduced and becomes comparable to the decay length of the electromagnetic fields of the surface plasmons in the metal, the surface plasmons from one interface start to couple with those at the other interface. The reason for this coupling is the spatial overlap of the electromagnetic fields of the surface plasmons from one interface with those at the other interface. The result of this interaction is the splitting of the surface plasmons modes into long-range and short-range surface plasmons.

Figure 2.5. Real part of the propagation constant (effective refractive index) of the long-range and short-range surface plasmons as a function of metal thickness. The layered structure considered here is water-gold-water at λ = 1550 nm.

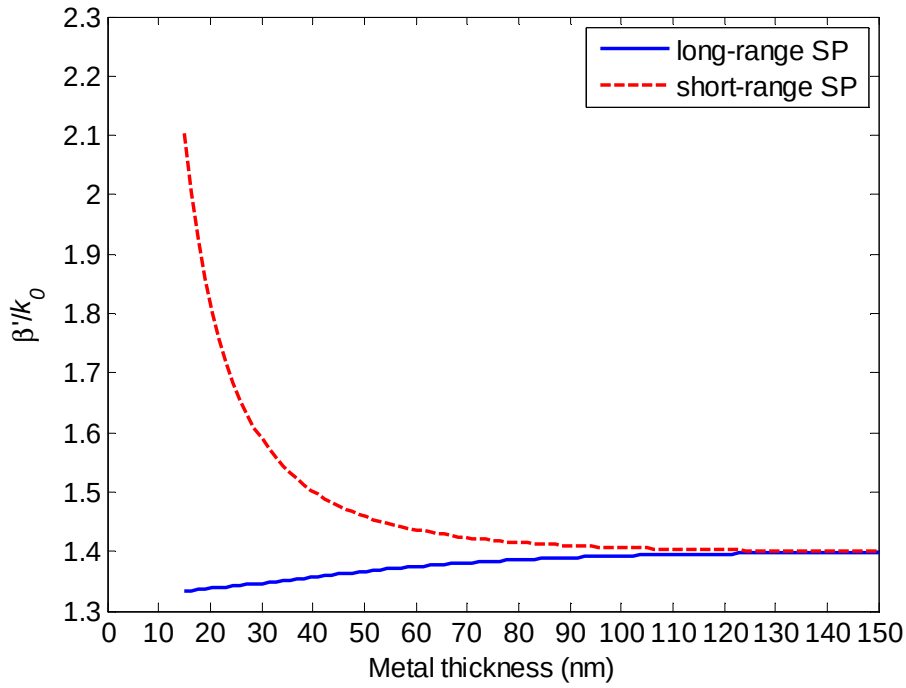

Figure 2.4 shows that the imaginary part of the propagation constant, which is responsible for the propagation loss of the surface plasmons, behaves differently

for the two modes. The imaginary part of the propagation constant of the long-range surface plasmons decreases when the sandwiched metal layer is made thinner. The propagation loss of the long-range surface plasmons is drastically reduced. On the other hand, the imaginary part of the propagation constant of the short-range surface plasmons increases when the thickness of the metal layer is reduced so that the propagation loss of the short-range surface plasmons is drastically increased.

Figure 2.5 shows the real part of the propagation constant of the long-range and short-range surface plasmons normalized by the wave number in free space. Adopting the terminology used in waveguide theory, this quantity is also often called the effective refractive index. Similar to the propagation loss, opposite behavior of the effective refractive index is again observed between the long-range and short-range surface plasmons. As the metal layer is made thinner, the short-range surface plasmons become more confined to the metal-dielectric interface. It is as though the surface plasmons were generated in an optically denser dielectric medium. Therefore, the effective refractive index of the short-range surface plasmons increases when the metal thickness is reduced. On the other hand, the long-range surface plasmons become less confined to the interface as the metal layer is made thinner so that the effective refractive index of the long-range surface plasmons decreases when the metal thickness is reduced.

To some extent, a loose analogy can be drawn between the origin of the long-range and short-range surface plasmons and the splitting of molecular orbitals into bonding and antibonding orbitals in the formation of covalent molecules. Consider for instance the simplest example, namely the hydrogen molecule which is made up of two hydrogen atoms. When the two hydrogen atoms are far apart, the lowest 1s atomic orbitals of the two hydrogen atoms do not overlap. When the two atoms are however brought closer to one another, the atomic orbitals are no longer independent. They start to overlap and form two distinct molecular orbitals. These are designated the σ or bonding and the σ^* or antibonding molecular orbitals. The bonding molecular orbital is the result of a symmetric or in-phase combination of the wave functions ψ_1 and ψ_2 of the two atomic orbitals as in $(\psi_1+\psi_2)/\sqrt{2}$. The antibonding molecular orbital on the other hand results from an antisymmetric or out-of-phase combination of the wave functions ψ_1 and ψ_2 of the two atomic orbitals as in $(\psi_1-\psi_2)/\sqrt{2}$. The energy level of the bonding molecular orbital is lower than that of the antibonding molecular orbital as illustrated in Figure 2.6. The bonding molecular orbital is therefore analogous

to the long-range surface plasmons while the antibonding molecular orbital is the analog of the short-range surface plasmons.

Figure 2.6. The formation of bonding and antibonding molecular orbitals when two hydrogen atoms interact.

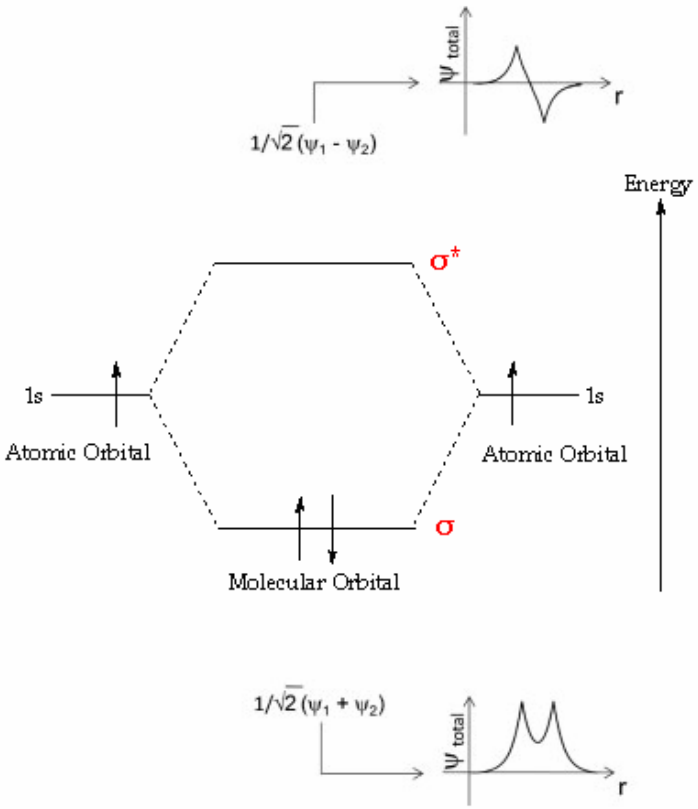

2.3. Spatial Extension of Surface Plasmons

For SPR-based biosensors, the spatial extension of surface plasmons determines the sensing region, namely the 3-D space that can be effectively probed by the surface plasmons. The spatial extension of surface plasmons can be characterized by two parameters, i.e., the propagation length and the field penetration depth.

2.3.1. Propagation Length

Consider first the dispersion relation for surface plasmons at a single metal-dielectric interface, Equation (2.23). The relative electric permittivity ε_d of a dielectric is only weakly dispersive, i.e., the optical propagation loss in a dielectric

is negligible so that it can be simply regarded as a real positive quantity. However, in a metal, the relative electric permittivity $\varepsilon_m = \varepsilon_m' + j\varepsilon_m''$ is generally a complex quantity where ε_m' is the real part and ε_m'' is the imaginary part. This is because the optical propagation loss due to ohmic damping in a metal is non negligible which is reflected in the non zero imaginary part of the relative electric permittivity. At optical frequencies, the real part of the relative electric permittivity of a metal is negative and if it is further assumed that its magnitude is much larger than the imaginary part so that $|\varepsilon_m'| >> \varepsilon_m''$, the complex propagation constant of the surface plasmons at a simple metal-dielectric interface can be analytically approximated by

$$\beta = \beta' + j\beta'' \approx \frac{\omega}{c}\sqrt{\frac{\varepsilon_m'\varepsilon_d}{\varepsilon_m' + \varepsilon_d}} + j\frac{\omega}{c}\frac{\varepsilon_m''}{2(\varepsilon_m')^2}\left(\frac{\varepsilon_m'\varepsilon_d}{\varepsilon_m' + \varepsilon_d}\right)^{3/2} \tag{2.59}$$

As evident from Equation (2.59), the imaginary part of the dielectric function of the metal ε_m'' causes the propagation constant of the surface plasmons to have a non-zero imaginary part which in turn is associated with an attenuation of the surface plasmons intensity as it propagates along the metal-dielectric interface. This attenuation can be characterized by the propagation length L defined as the distance along the propagation direction at which the intensity of the surface plasmons decreases by a factor of $1/e$ from its initial value. The intensity I of the surface plasmons is related to the propagation distance x by

$$I \propto e^{-2\beta'' x} \tag{2.60}$$

so that the propagation length L can be expressed as

$$L = \frac{1}{2\beta''} \approx \frac{(\varepsilon_m')^2}{\varepsilon_m''}\frac{c}{\omega}\left(\frac{\varepsilon_m' + \varepsilon_d}{\varepsilon_m'\varepsilon_d}\right)^{3/2} \tag{2.61}$$

If it is also assumed that $\varepsilon_d << |\varepsilon_m'|$, the propagation length can be approximated by

$$L \approx \frac{\lambda_0}{2\pi(\varepsilon_d)^{3/2}}\frac{(\varepsilon_m')^2}{\varepsilon_m''} \tag{2.62}$$

where λ_0 is the wavelength in free space.

From Equation (2.62), one can draw some physical conclusions. As far as the metal is concerned, the propagation length of surface plasmons is dependent on the both the real and imaginary part of the dielectric function of the metal. For a long surface plasmons propagation length, a large negative real part ε_m' and a small imaginary part ε_m'' are desired, i.e., a low loss metal is required as expected. Interestingly, as the real and imaginary part of the metal determine the propagation length of surface plasmons through the combination $\left(\varepsilon_m'\right)^2/\varepsilon_m''$, the effect of the imaginary part of the dielectric function of the metal can be outweighed by its real part. For example, aluminum has a larger imaginary part of relative electric permittivity compared to silver. However, the surface plasmons of silver and aluminum have the approximately the same propagation length at the wavelength of around 600 nm. This is due to the fact that the magnitude of the real part of the relative electric permittivity of aluminum is much larger than that of silver. As far as the dielectric is concerned, the propagation length of surface plasmons decreases as $\left(\varepsilon_d\right)^{-3/2}$. The propagation length of surface plasmons is therefore shorter in a denser dielectric medium. For some examples, at the wavelength of 760 nm, the typical propagation length of surface plasmons at a gold-water interface is approximately 14 µm while at the gold-air interface it is about 36 µm.

Consider now the surface plasmons at two interfaces. The general dispersion relation in this case is given by Equation (2.55) which is a transcendental equation that is much more complicated compared to that for a single interface. Simple analytical approximation as in the case of the single interface cannot therefore be carried out. It can however be calculated numerically. For some examples, one can take the water-gold-water layered structure at the wavelength of 1550 nm (Figure 2.4). Choosing 20 nm for the thickness of the gold film, the propagation length of the short-range surface plasmons mode is calculated to be about 27 µm while that of the long-range surface plasmons mode is around 1 mm. These values can be contrasted with the propagation length of the surface plasmons at a single water-gold interface at the same wavelength which is approximately 170 µm.

The physical significance of the propagation length of surface plasmons for sensing applications can be illustrated by a multiplexed SPR-based sensing system. In such as system, the propagation length of the surface plasmons dictates a lower limit on the feature size of the individual sensing spot. If the size of this individual sensing spot is made smaller than the surface plasmons propagation

length, there will be an overlap of electromagnetic field of surface plasmons from nearby sensing spots. The electromagnetic field of surface plasmons from the neighboring sensing spots can thus effectively interfere with the electromagnetic signal produced by this particular sensing spot. To avoid crosstalk between different sensing spots, the feature size must therefore be sufficiently larger than the surface plasmons propagation length.

2.3.2. Field Penetration Depth

The propagation length of surface plasmons that has just been discussed determines the spatial extension of the surface plasmons in the lateral dimension along the interface. In the transverse direction, i.e., normal to the interface, the spatial extension of the surface plasmons is characterized by the field penetration depth. It is defined as the distance from the interface at which the amplitude of the electromagnetic field of the surface plasmons decreases by a factor of $1/e$ from its maximum value. As the amplitude of the electromagnetic field of the surface plasmons normal to the interface decreases exponentially as $\exp(-zk_z)$, the field penetration depth δ can be expressed as

$$\delta = \frac{1}{|k_z|} \tag{2.63}$$

The wave vector component of the surface plasmons in the normal direction to the interface k_z is related to the propagation constant of the surface plasmons β by

$$k_z = \sqrt{\left(\frac{2\pi}{\lambda_0}\right)^2 \varepsilon - \beta^2} \tag{2.64}$$

where ε is the relative electric permittivity of the concerned medium (metal or dielectric).

For a single metal-dielectric interface for which $|\varepsilon_m'| >> \varepsilon_m''$, the field penetration depth of the associated surface plasmons can be analytically approximated by

$$\delta_d \approx \left| \frac{\lambda_0}{2\pi} \left(\frac{\varepsilon_m' + \varepsilon_d}{{\varepsilon_d}^2} \right)^{1/2} \right| \tag{2.65}$$

in the dielectric and by

$$\delta_m \approx \left| \frac{\lambda_0}{2\pi} \left(\frac{\varepsilon'_m + \varepsilon_d}{(\varepsilon'_m)^2} \right)^{1/2} \right| \tag{2.66}$$

in the metal. Equations (2.65) and (2.66) clearly show that the exponential decay of the electromagnetic field of surface plasmons into the metal and the dielectric is not the same. If it is further assumed that $\varepsilon_d << |\varepsilon'_m|$ as well, one obtains the limiting approximations

$$\delta_d \approx \frac{\lambda_0}{2\pi} \frac{|\varepsilon'_m|^{1/2}}{\varepsilon_d} \tag{2.67}$$

$$\delta_m \approx \frac{\lambda_0}{2\pi |\varepsilon'_m|^{1/2}} \tag{2.68}$$

From Equations (2.67) and (2.68), one can see the general trend that for a single metal-dielectric interface at a given wavelength, the field penetration depth of the surface plasmons into the metal is approximately constant and independent of the relative electric permittivity of the dielectric. For a gold-water interface at the wavelength of 760 nm, the typical value of the field penetration depth into the gold layer is around 25 nm. The field penetration depth into the dielectric is however strongly dependent on the relative electric permittivity of the dielectric. Equation (2.67) suggests that for a given metal, the field penetration depth of the surface plasmons scales inversely with the relative electric permittivity of the dielectric. For a gold-water interface at the wavelength of 760 nm, the typical value of the field penetration depth into the dielectric layer is around 280 nm. In this particular example, the electromagnetic field of the surface plasmons extends an order of magnitude deeper into the dielectric as compared to the metal. For biosensing applications, if the dielectric is chosen to be liquid, molecules in solution can be made to bind to the surface and interfere with this evanescent field. The field penetration depth into the dielectric is a measure of the length scale over which the surface plasmons are sensitive to refractive index changes, for instance, due to the binding of specific biomolecules in a biosensor. Although the sensitivity of surface plasmons to changes in the dielectric medium falls off exponentially, the distance over which the exponential decay takes place is quite large on a molecular scale. The region where the binding of molecules overlaps

with the evanescent field is referred to as the sensing region. The size of the sensing region is a function of wavelength both directly as in Equation (2.65) and indirectly through the wavelength dependence of the relative electric permittivity of the metal. It also depends on the structure of the sensor in question and will be discussed in more details in subsequent chapters.

Associated with the strong localization of the electromagnetic field of surface plasmons near the metal-dielectric interface, there is also a field enhancement. This enhanced field is the primary reason why surface plasmons are also very interesting for other applications such as second-harmonic generation, surface-enhanced Raman spectroscopy, and fluorescence-based sensing. More details about this electromagnetic field enhancement as well as its mathematical details are discussed in Chapter 4.

2.4. Optical Excitation of Surface Plasmons

As implied by the more rigorous term surface plasmon polaritons (SPP), surface plasmons can be excited by either electrons or photons. Excitation of surface plasmons by electrons is achieved by bombarding a thin metallic film by electrons. As the electron beam penetrates the metal, a transfer of energy and momentum from the incoming electrons to the electrons of the metal occurs enabling the excitation of surface plasmons. However, for sensing applications, excitation of surface plasmons by photons is the more suitable approach. This leads to the development of optical biosensors based on surface plasmon resonance (SPR). The key role in the optical excitation of surface plasmons is played by the propagation constant of the surface plasmons. Surface plasmons can be optically excited if the in-plane wave vector component of the optical wave matches that of the surface plasmons (the real part of the surface plasmons' propagation constant designated here as β_{SP}, see Equation (2.59)). This situation is often referred to as the phase-matching condition. The most common methods of optical excitation of surface plasmons include prism coupling, grating coupling, and waveguide coupling.

2.4.1. Prism Coupling

Consider the dispersion relation of surface plasmons at a metal-dielectric interface, Equation (2.23). Designating the dielectric as material 1 ($\varepsilon_1 = \varepsilon_d$) and the metal as material 2 ($\varepsilon_2 = \varepsilon_m$), Equation (2.23) can be rearranged as follows

$$\beta_{SP} = \frac{\omega}{c}\sqrt{\varepsilon_d}\left\{\frac{\varepsilon_m}{(\varepsilon_d + \varepsilon_m)}\right\}^{1/2} = n_d k_0 \left\{\frac{\varepsilon_m}{(\varepsilon_d + \varepsilon_m)}\right\}^{1/2} \quad (2.69)$$

where $k_0 = \frac{\omega}{c}$ and $n_d = \sqrt{\varepsilon_d}$. The factor outside the brackets in Equation (2.69) is simply the magnitude of the wave vector of light in the dielectric. Since the dielectric function of the metal is negative and $|\varepsilon_m| > \varepsilon_d$, the factor in the brackets in Equation (2.69) is always larger than unity. This means that propagation constant of surface plasmons at a metal-dielectric interface is by nature larger than the magnitude of the wave vector of the light wave in the dielectric. This property is illustrated in Figure 2.7 for surface plasmons at the gold-air interface where the Lorentz-Drude model is used for the gold layer.

Figure 2.7. The dispersion relation of surface plasmons at the gold-air interface (solid blue curve). The linear dispersion relation of light in air (the light line) is shown by the dashed black curve.

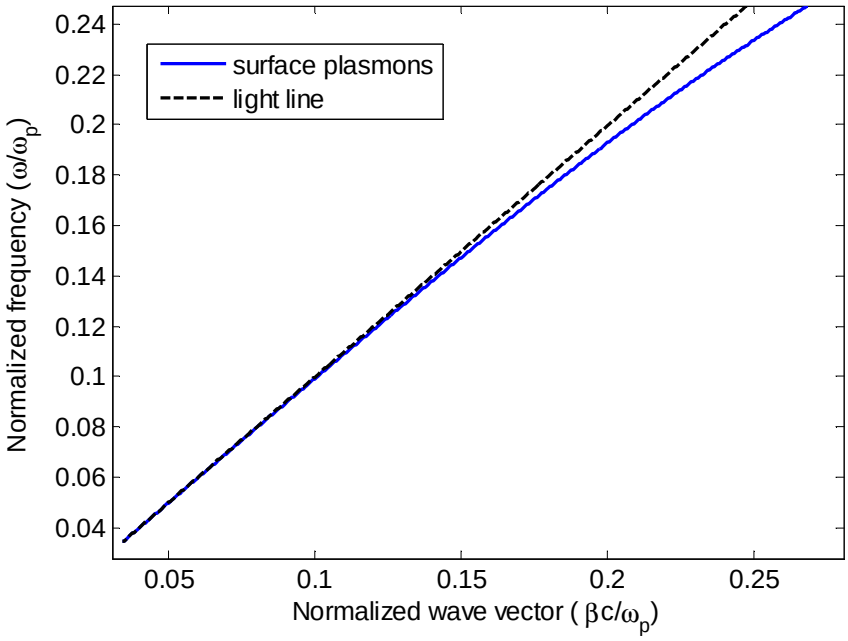

As shown in Figure 2.7, the dispersion curve of the surface plasmons lies to the right-hand side of the light line which means that at any given frequency, the magnitude of the wave vector of the surface plasmons is always larger than that of the light wave in the dielectric. Therefore the surface plasmons cannot be excited directly by a light wave incident on the interface. To allow optical excitation of

surface plasmons, the wave vector of the incident light can however be increased by passing the light wave through an optically denser medium in the attenuated total reflection (ATR) method (Figure 2.8).

Figure 2.8. (a) Excitation of surface plasmons by the attenuated total reflection (ATR) method. **(b)** The light line in the denser medium (green line) is tilted to the right relative to that in the dielectric (red dashed line) resulting in an increase of the incident light's wave vector. Resonance takes place at a specific angle of incidence when this light line intersects the dispersion curve of the surface plasmons (blue line).

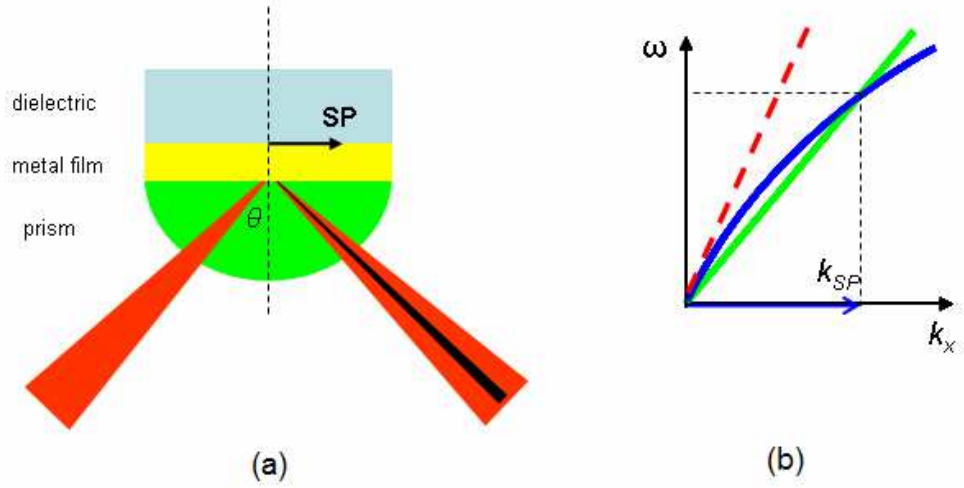

In the ATR configuration, a light wave passing through a high refractive index prism and totally reflected at the prism base generates an evanescent wave penetrating the thin metal film. If the thickness of the metal film is properly chosen, this evanescent wave can then tunnel through the metal film to excite surface plasmons at the other metal-dielectric interface. Surface plasmon resonance occurs when the in-plane wave vector component of the optical wave k_x is equal to the real part of the surface plasmons' propagation constant. This resonance condition can be mathematically expressed as

$$k_x = \frac{2\pi}{\lambda_0} n_p \sin\theta = \mathrm{Re}\{\beta_{SP}\} \tag{2.70}$$

where λ_0 is the wavelength in vacuum, n_p is the prism refractive index, θ is the incident angle, and Re{} signifies the real part of a complex quantity. Physically,

the optical excitation of surface plasmons is accompanied by the transfer of the light wave energy into the surface plasmons and its subsequent dissipation in the metal film. This process results in a drop in the intensity of the totally reflected light at a specific angle of resonance.

There are actually two types of ATR configuration depending on the stacking order of the metal and dielectric media with respect to the prism (Figure 2.9). In the first configuration known as the Kretschmann geometry after E. Kretschmann, the author who first popularized it [33], a metal film is sandwiched between the prism and the dielectric. It has just been discussed in the previous paragraph. The other configuration is known as the Otto geometry after A. Otto, the first author to use it [34]. In this configuration, the dielectric is sandwiched between the prism and the metal. In SPR-based optical biosensors, the dielectric is the role played by the sample to be analyzed which is usually an aqueous solution. For practical reason, it is extremely difficult to place an aqueous sample with a uniform spacing (on the order of several tens of nanometers) between the prism and the metal as in the Otto configuration. Conversely, the uniform deposition of metal thin film required in the Kretschmann configuration can be more easily achieved. For this reason, the Kretschmann configuration is much more commonly employed in SPR-based optical biosensors as the most ubiquitous coupling method thanks to its simplicity.

Figure 2.9. (a) Kretschmann configuration. **(b)** Otto configuration

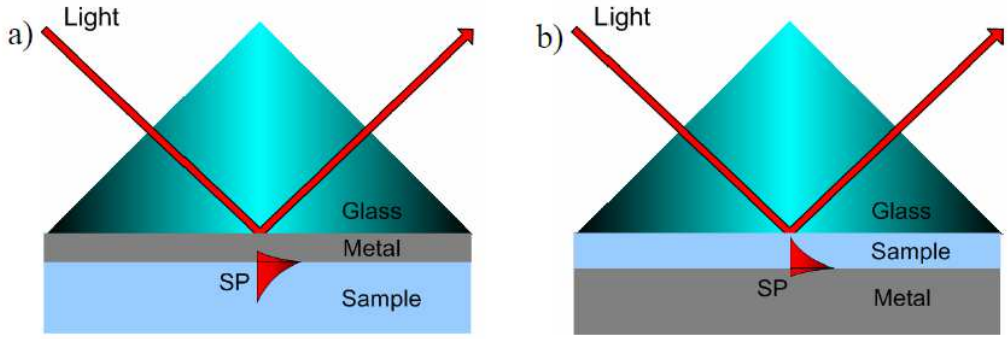

2.4.2. Grating Coupling

The in-plane wave vector of the incident light wave impinging on a dielectric-metal interface can also be increased to match that of the associated surface plasmons by a diffraction grating (Figure 2.10). The diffraction grating scatters the incident light wave and modifies its in-plane wave vector by an integer

multiple of the grating vector G depending on the diffraction order. The coupling condition when the m-th diffraction is coupled to the surface plasmons can then be expressed by

$$k_x = k_{ph} + mG = \frac{2\pi}{\lambda_0} n_d \sin\theta + m\frac{2\pi}{\Lambda} = \mathrm{Re}\{\beta_{SP}\} \qquad (2.71)$$

where k_{ph} is the original in-plane wave vector of the incident photons, G is the grating scattering vector, m = 0, ±1, ±2,… is the diffraction order, Λ is the grating period, and n_d is the refractive index of the dielectric.

Figure 2.10. (a) Excitation of surface plasmons by a diffraction grating. **(b)** Dispersion diagram illustrating the phase-matching condition. The original in-plane wave vector of the incident photons k_{ph} is increased by G through m = +1 diffraction order to match that of the surface plasmons.

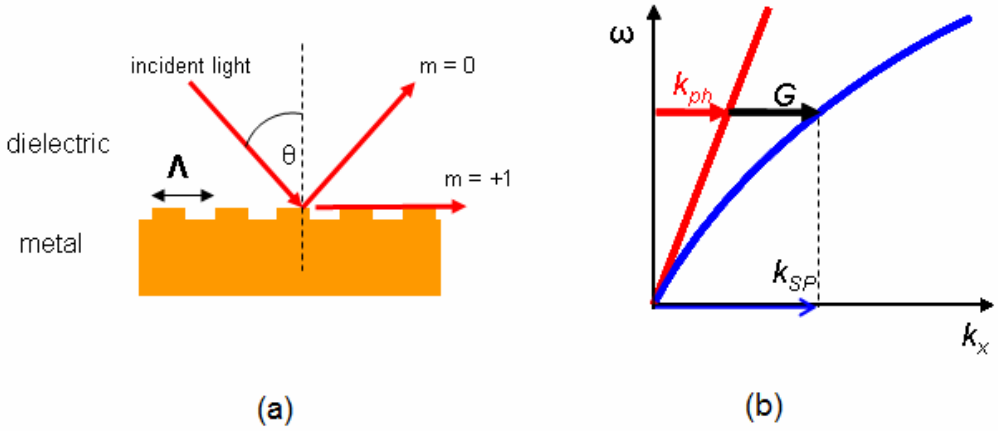

Compared to prism coupling technique, there is more angular flexibility in grating coupling method. This extra flexibility is provided by the last term in Equation (2.61). With the grating coupling method, the resonance angle can take on any value from 0° to 90° depending on the choice of the grating period Λ and the order of diffraction m. Although there is more flexibility in the choice of incident angles in grating coupling, the incident light has to pass through the dielectric sample which limits the method to transparent, non-turbid samples. In sensing applications, this is considered a disadvantage of the direct grating coupling method.

2.4.3. Waveguide Coupling

Surface plasmons can also be excited by guided modes of an optical waveguide (Figure 2.11). When a guided mode propagating along the optical waveguide enters the region covered by a thin metal film, its field can penetrate through the metal film. Resonance can then take place if the wavelength-dependent propagation constant of the guided mode matches that of the surface plasmons at the outer metal-dielectric boundary. As this phase-matching condition is only satisfied for a narrow wavelength range, a dip in the transmitted spectrum can be observed.

Figure 2.11. Excitation of surface plasmons by waveguide coupling.

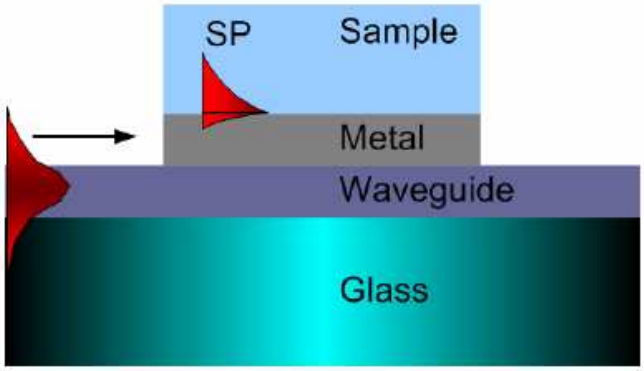

Chapter 3

Basic Concepts of Surface Plasmon Resonance (SPR) Biosensors

After the preliminary discussion of some fundamental physical properties of surface plasmons in the preceding chapter, the basic principles of biosensors based on surface plasmon resonance (SPR) is now elaborated in this chapter.

Historically speaking, the first documented observation of SPR-related phenomenon actually dates back as early as 1902 when R.W. Wood reported unexplained narrow dark bands in the diffracted spectrum of metallic gratings illuminated with polychromatic light [35]. This anomalous phenomenon, referred to as Wood's anomaly, was then explained in 1968 in terms of SPR when the name surface plasmons was first coined [36]. In the same year, optical excitation of surface plasmons by attenuated total reflection was introduced by Otto [34] and Kretschmann [33]. The use of surface plasmon resonance for gas detection and biosensing was later demonstrated in 1983 [37]. Thereafter, the newly discovered potential of SPR for the detection and analysis of chemical and biological substances has been receiving growing interest from the scientific community. In fact, the successful commercialization of Biacore SPR biosensor systems since the early 1990s has been continually leading to innumerable scientific reports on applications of SPR biosensors for the study of biomolecular interactions and biochemical detection in many important fields.

3.1. Sensing Principles

As described in Section 2.3.2, the vast majority of the electromagnetic field of surface plasmons is concentrated in the dielectric which plays the role of the sensed medium in SPR biosensors. The propagation constant of the surface plasmons is therefore extremely sensitive to changes in the relative electric permittivity, or equivalently, the refractive index of the dielectric. This is the underlying physical principle of biosensors based on surface plasmon resonance. In SPR-based biosensors, biomolecular recognition elements in extremely close proximity to the metal surface recognize and capture specific analytes present in a liquid sample such as an aqueous biological solution. This analyte capture induces

a local increase in the refractive index of the dielectric near the metal surface. In turn, this increase in refractive index gives rise to a modification of the propagation constant of the associated surface plasmons propagating along the metal-dielectric interface. This variation of propagation constant of surface plasmons can then be accurately measured by a number of optical means.

3.2. Optical Detection Mechanisms

In SPR biosensors, surface plasmons are excited by a light wave and the effects of the interaction between the excitation light wave and the surface plasmons on the characteristics of the light wave is measured. Through this interaction, variations in the propagation constant of the surface plasmons will alter the light wave's characteristics such as amplitude, phase, and spectral distribution. Based on which characteristic of the light wave is measured, SPR biosensors can be categorized into several classes.

In SPR biosensors with angular interrogation, a p-polarized monochromatic light wave is used to excite surface plasmons. The angle of incidence is varied and the intensity of the reflected light as a function of the angle of incidence is recorded so that an angular spectrum of the reflected light is obtained. The excitation of surface plasmons is characterized by a dip in the angular spectrum of the reflected light at the angle of resonance. When the refractive index of the sensed dielectric medium is altered, e.g., following the binding of specific biomolecules, the angle of resonance changes accordingly (Figure 3.1). This shift of the angle of resonance can be monitored in real time and is an indication of the amount of the captured biomolecules. Angular interrogation is typically employed in SPR biosensors with ATR prism coupling method.

In SPR biosensors with wavelength interrogation, a polychromatic optical wave is used to excite surface plasmons at a fixed angle of incidence. Surface plasmons are only excited at a certain wavelength that meets the requirement of phase matching condition. Changes in the refractive index of the sensed dielectric medium alter the resonance wavelength (Figure 3.1). Similar to the case of angular interrogation, the shift of the resonance wavelength can then be correlated with the amount of captured biomolecules. Wavelength interrogation can be employed in SPR biosensors with prism coupling as well as waveguide coupling method.

In SPR biosensors with intensity interrogation, the wavelength and angle of incidence of the light wave used to excite surface plasmons are kept constant. The intensity of the optical wave after its interaction with the surface plasmons is then monitored. In SPR biosensors with ATR coupling method and intensity interrogation, the variation of the reflectance is recorded as the refractive index of the sensed medium changes (Figure 3.1).

Figure 3.1. Illustration of angular Δθ, wavelength Δλ, and intensity interrogation ΔR in the prism coupling configuration as the refractive index of the sensed dielectric medium changes from n (dashed curve) to n+Δn (solid curve). The point labeled A marks the onset of total internal reflection.

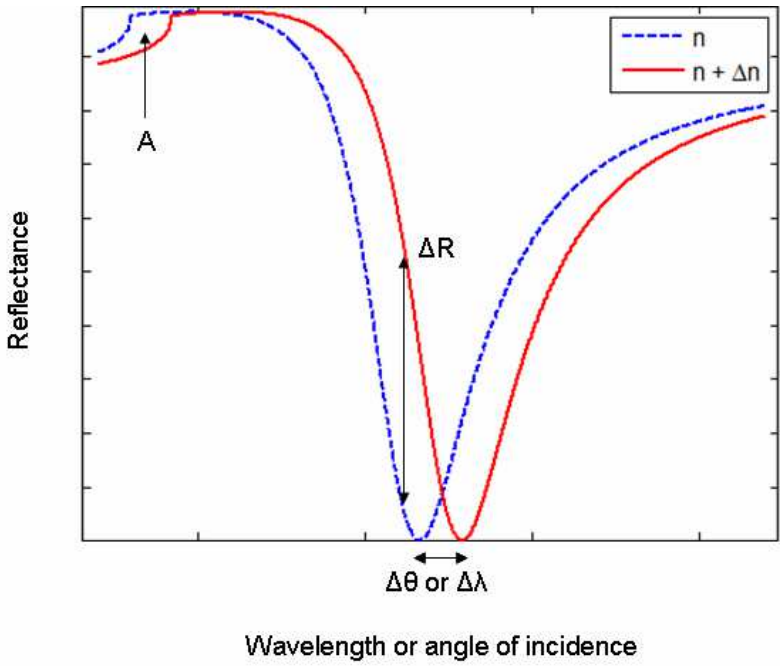

Similar to intensity interrogation, in SPR biosensors with phase interrogation, the wavelength and angle of incidence of the light wave used to excite surface plasmons are kept constant. In this method, the phase of the optical wave after its interaction with the surface plasmons is monitored.

Of these different interrogation schemes, the angular, wavelength, and intensity interrogations are the most commonly employed in SPR biosensors owing to their high resolution and relatively simple instrumentation. The phase interrogation requires much more sophisticated instrumentation but it generally gives the highest resolution.

3.3. Surface Functionalization

Conceptually, an SPR biosensor can be thought of as being made up of an SPR sensor and suitable surface functionalization acting as the biorecognition element (Figure 3.2). When a biomolecular interaction (e.g. specific binding of analytes) takes place, the refractive index near the surface is altered. By itself, the SPR sensor only detects the refractive index change in the sensed medium. The specificity of the refractive index change to the binding of a particular type of analytes is controlled by the surface functionalization. This specific change of refractive index is then simply detected by the SPR sensor.

Figure 3.2. An SPR sensor equipped with some suitable surface functionalization acting as biorecognition element is transformed into an SPR biosensor. Biological analytes (represented as green dots) are shown to interact with the biorecognition element (represented as brown tuning fork-like elements). The large blue arrow indicates a microfluidic system to inject the samples onto the biosensor.

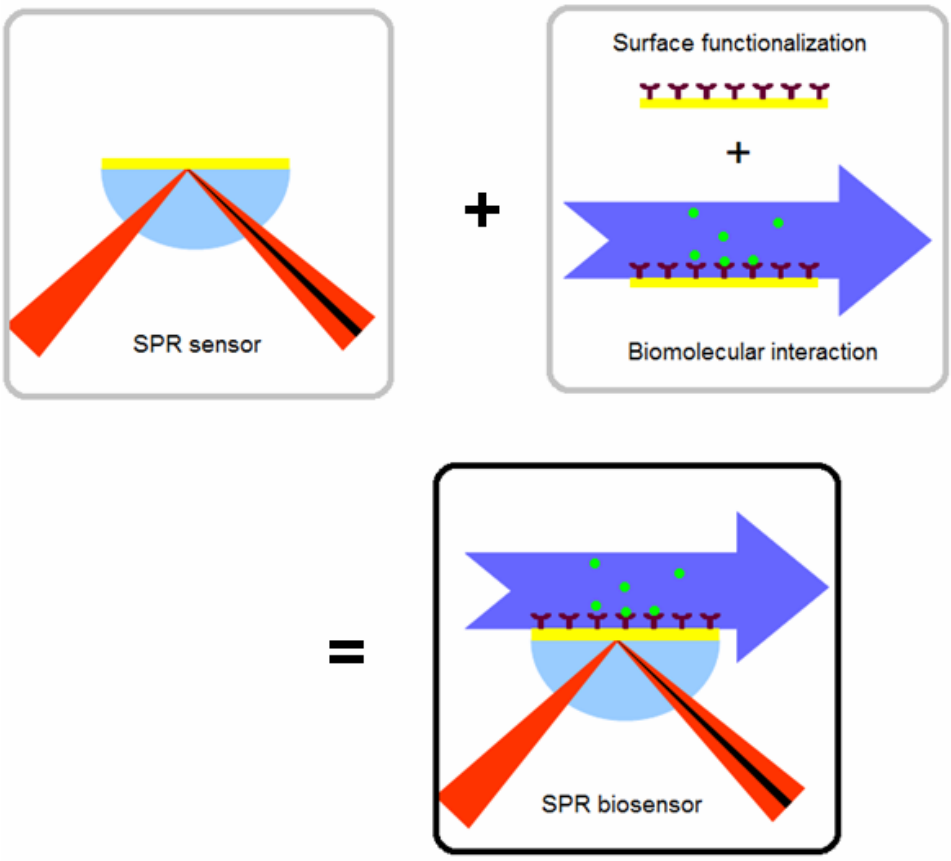

As an SPR sensor and appropriate surface functionalization form the building blocks of an SPR biosensor, it is clear that the overall performance of an SPR biosensor depends on both the intrinsic optical performance of the SPR sensor and the characteristics of the surface functionalization. Both of these factors are separately discussed in later chapters of this manuscript. More specifically, the enhancement of optical sensitivity of SPR biosensors in ATR Kretschmann configuration is discussed in Chapter 5 while the optimization of surface functionalization sensitivity is discussed in Chapter 6.

3.4. Performance Characteristics of SPR Biosensors

The main performance characteristics of SPR biosensors are sensitivity, resolution, limit of detection, and dynamic range.

Consider an SPR biosensor used to detect a specific analyte with concentration *c*. As has just been discussed in the preceding section, the overall performance of an SPR biosensor depends on both the intrinsic optical performance of the SPR sensor and the characteristics of the surface functionalization. The total sensitivity S_{tot} of this SPR biosensor in detecting the aforementioned specific analyte with concentration *c* can thus be decomposed into two components Sopt and Sfunct as expressed in the following equation

$$S_{tot} = \frac{\partial Y}{\partial c} = \frac{\partial Y}{\partial n}\frac{\partial n}{\partial c} = S_{opt} S_{funct} \tag{3.1}$$

where S_{opt} denotes the optical sensitivity of the SPR sensor (i.e. the ratio of the change in sensor output *Y*, e.g., angle of resonance, to the change in refractive index of the sensed medium *n*) and S_{funct} describes the biomolecular performance of the surface functionalization.

The surface functionalization performance factor S_{funct} in Equation (3.1) is sort of a measure of the efficiency of the biorecognition elements in capturing the specific analytes to be detected. It can be defined as the ratio of the local change in refractive index of the sensed medium to the amount of specific binding of the analyte on the sensor surface. The surface functionalization performance factor depends solely on the surface physicochemical properties of the biorecognition element affecting the biomolecular interaction. It is a function of the specific biomolecular systems being investigated. Different biomolecular interactions

generally give rise to different surface functionalization performance factors. On the other hand, for a given surface functionalization scheme, the optical sensitivity factor S_{opt} is independent of the details of the involved biomolecular interactions. It is therefore convenient to decouple S_{funct} and S_{opt} in analyzing the performance of SPR biosensors.

The optical performance of SPR biosensors is most frequently assessed by their optical sensitivity and resolution. As expressed in Equation (3.1), the optical sensitivity S_{opt} is defined as the ratio of the change of the sensor output ΔY (e.g. angle or wavelength of resonance) to the change of the refractive index of the sensed medium Δn. For this reason, it is often simply referred to as the refractive index sensitivity. It is usually expressed in degrees/RIU (refractive index unit) or nm/RIU for SPR biosensors using angular or wavelength interrogation, respectively. For SPR biosensors with intensity interrogation, it is usually quoted as %/RIU, i.e., as a percentage change in intensity per unit change in refractive index.

To take into account the linewidth of the resonance, the optical sensitivity of SPR biosensors is also often evaluated in terms of figure-of-merit *FOM* defined by the ratio of the refractive index sensitivity to the linewidth of the resonance:

$$FOM = \frac{S_{opt}}{FWHM} \tag{3.2}$$

where *FWHM* is the full-width-at-half-maximum of the resonance. Ideally, SPR biosensors with very high refractive index sensitivity and very narrow resonance linewidth, i.e., with very high figure-of-merit are desired. The figure-of-merit is therefore a measure of the overall optical performance of SPR biosensors.

Sensor resolution refers to the smallest change in refractive index of the sensed medium that produces a detectable change in the sensor output. The lower limit of sensor output change that can be detected is set by the level of uncertainty in the sensor output, i.e., the output noise in the sensor instrumentation. In SPR biosensors, the term resolution usually refers to a bulk refractive index resolution (Section 3.5).

The limit of detection (LOD) of SPR biosensors is usually defined as the concentration of analyte that produces a sensor output corresponding typically to 2 or 3 standard deviations of sensor output measured for a blank sample. It is therefore closely related to the sensor resolution. In fact, it is also often used interchangeably with the sensor resolution.

The dynamic range of SPR biosensors describes the span of values of the measurand that can be measured by the sensor. In terms of refractive index, the dynamic range of SPR biosensors usually indicates the range of values of the refractive index of the sample that can be measured with specified accuracy. In terms of analyte concentration, the dynamic range of SPR biosensors defines the range of concentrations of an analyte which can be measured with specified accuracy which extends from the lowest concentration at which a reliable quantitative measurement can be done, i.e., the limit of detection.

3.5. Bulk and Surface Sensitivities

For SPR biosensors, one may generally distinguish two types of refractive index sensitivities, i.e., bulk and surface sensitivities.

As implied by its name, the bulk refractive index sensitivity refers to the case where the refractive index change in the sensed dielectric medium is uniform and extends into the whole region effectively probed by the surface plasmons.

On the other hand, the surface refractive index sensitivity describes the case where the refractive index change in the sensed dielectric medium is limited to the immediate proximity of the metal-dielectric interface. In this case, the refractive index change is often assumed to occur within a thin layer of thickness t much shorter than the surface plasmons field penetration depth into the sensed dielectric medium δ (Figure 3.3). The thickness t within which the refractive index change occurs is determined by the spatial extent of the biomolecular interaction taking place near the surface. Hence it depends on the specific biomolecular interaction being measured by the SPR biosensor. Conversely, the bulk refractive index sensitivity is independent of the particular biomolecular interaction being considered.

Although one might in principle make a distinction between the bulk and surface sensitivities, it will actually suffice to quote only the bulk refractive index sensitivity when comparing the optical performance of different designs of SPR biosensors. The reason being that the surface refractive index sensitivity S_{surf} is in fact proportional to the bulk refractive index sensitivity S_{bulk}:

$$S_{surf} = \alpha S_{bulk} \tag{3.3}$$

where the proportionality constant α is given by

$$\alpha = \frac{\int_0^t e^{-z/\delta} dz}{\int_0^\infty e^{-z/\delta} dz} \tag{3.4}$$

Figure 3.3. Surface refractive index change. The change in refractive index from n to n+Δn occurs only within a layer of thickness *t* much shorter than the field penetration depth *δ*.

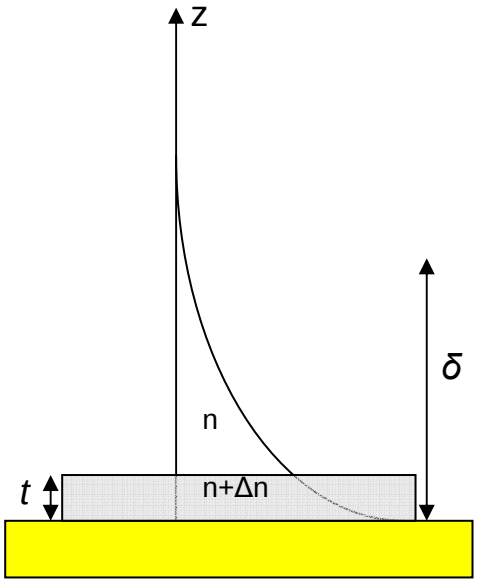

Equation (3.4) stems from the fact that the refractive index sensitivity of SPR biosensors falls off exponentially as a function of distance from the metal-dielectric interface. The integrals in Equation (3.4) can easily be evaluated to yield

$$\alpha = 1 - e^{-t/\delta} \tag{3.5}$$

Under typical experimental conditions for common biomolecules, *t* is on the order of 10-20 nm [38, 39] while δ is generally on the order of 280-1250 nm

depending on the particular design of the SPR biosensors. Under these circumstances, $t << \delta$ so that α can be approximated by

$$\alpha = 1 - \left[1 - t/\delta + O\left(\left(t/\delta \right)^2 \right) \right] \approx t/\delta \tag{3.6}$$

In other words, the surface refractive index sensitivity is proportional to the thickness t within which the refractive index variation occurs near the metal-dielectric interface as expressed by

$$S_{surf} = \frac{t}{\delta} S_{bulk} \tag{3.7}$$

3.6. Instrumentation of SPR Biosensors

This section briefly discusses the instrumentation of the various SPR biosensor systems used for the experimental parts of this work. Laboratory SPR setups developed in-house as well as commercial SPR instruments were used in different experiments.

3.6.1. Commercial Instruments: Biacore and Autolab SPR

The optical setup of a typical Biacore instrument using ATR prism coupling method in Kretschmann configuration is illustrated in Figure 3.4. A convergent wedge-shaped p-polarized light beam at the wavelength of 760 nm is focused onto the sensor surface of the sensor chip in contact with the prism and the microfluidic flow channel. Light reflected from the sensor chip is monitored by a linear array of light-sensitive photodiodes covering the range of the angles of incidence fixed by the wedge-shaped incident beam. Surface plasmon resonance shows up on the detecting photodiode as a dark spot. Computer interpolation algorithms then determine the angle of minimum reflection (the SPR angle) to very high accuracy. The advantage of using a wedge of incident light and a fixed array of detectors in this setup is that the SPR angle is monitored accurately in real time, with no physical movement of the light source, the sensor chip or the detector. However, the dynamical range is consequently fixed and cannot be adjusted.

Real time monitoring of SPR signal, in this case the angular shift, results in a sensorgram, i.e., a plot of SPR response as a function of time. The unit of SPR response in Biacore systems, called RU for resonance unit, is an arbitrary unit,

chosen so that 1 RU corresponds to a change in refractive index of 10^{-6}, which in turn correlates with a shift in angle of about 10^{-4} degrees. For proteins on Biacore CM5 Sensor Chip, 1 RU corresponds to a change in surface concentration of approximately 1 pg/mm^2. This correlation may however vary significantly for non-protein molecules and should be taken as a very approximate guideline.

Figure 3.4. Schematic illustration of the SPR setup used in Biacore instruments. The initial SPR curve before analyte binding is shown by the curve marked I. The SPR curve following analyte binding is shown by the curve marked II. The angular shift is monitored in real time resulting in a sensorgram.

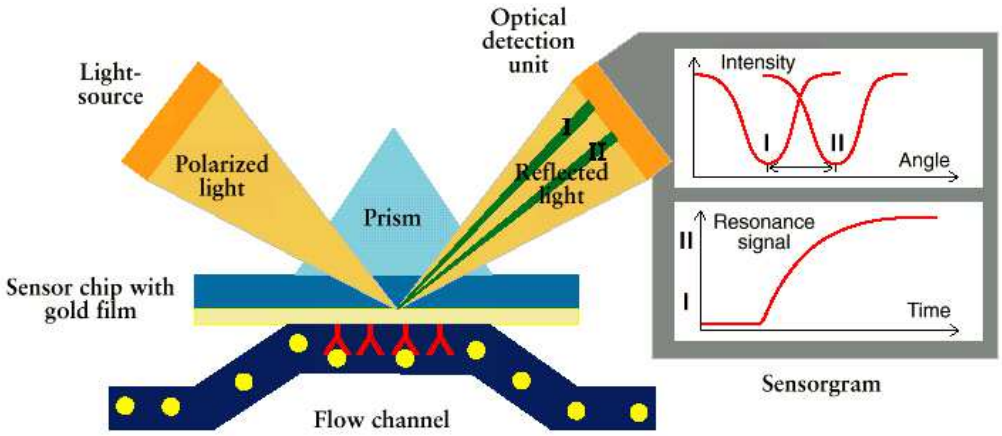

The Autolab SPR instrument also makes use of the ATR prism coupling method in Kretschmann configuration at the wavelength of 680 nm. However, in contrast to Biacore instruments with no moving optical parts, the reflection in the Autolab SPR instrument is measured as a function of the incident angle of the light beam where the incident angle is varied by using a vibrating mirror. The advantage of this system is that within a short time a broad range of incident angles can be measured. The unit of SPR response in Autolab SPR systems is also called RU for response unit. It is defined as an SPR angular shift of 10^{-3} degrees which corresponds to a change in refractive index of about 10^{-5}.

It is extremely important to keep in mind that despite the same abbreviation, the physical significance of RU (resonance or response unit) as an arbitrary unit of SPR response in commercial SPR systems is instrument-specific and can be quite different from one commercial instrument to the other. For instance, in Biacore systems, 1 RU corresponds to an angular shift of 0.1 millidegree while in Autolab

SPR systems, 1 RU is defined differently so as to correspond to an angular shift of 1 millidegree.

3.6.2. In-house SPR Setup

Commercial SPR systems such as Biacore and Autolab SPR instruments provide standard reference in the study of biomolecular interactions. However, these commercial instruments have a fixed dynamical range. For some novel sensor chips developed in this work, it is necessary to modify the optical setup to accommodate a different range of measurement variables. In-house laboratory SPR setups, one at the wavelength of 760 nm and another one at 1550 nm, are used for these purposes. In the framework of the Plasmobio project that encompasses this work, these setups are developed by the Phlam laboratory.

The in-house laboratory SPR setup with an operating wavelength of 760 nm is schematically illustrated in Figure 3.5. Light beam from the laser source is polarized and focused onto the sensor surface of the sensor chip sitting on a semi cylindrical prism. Light beam reflected from the sensor chip is monitored by a CCD linear detector covering the range of the angles of incidence and surface plasmon resonance shows up as a dark pixel. The angle of minimum reflection (the SPR angle) is then determined by computer fitting algorithms to the measured reflection spectra.

Figure 3.5. Schematic illustration of the in-house laboratory SPR setup at the wavelength of 760 nm.

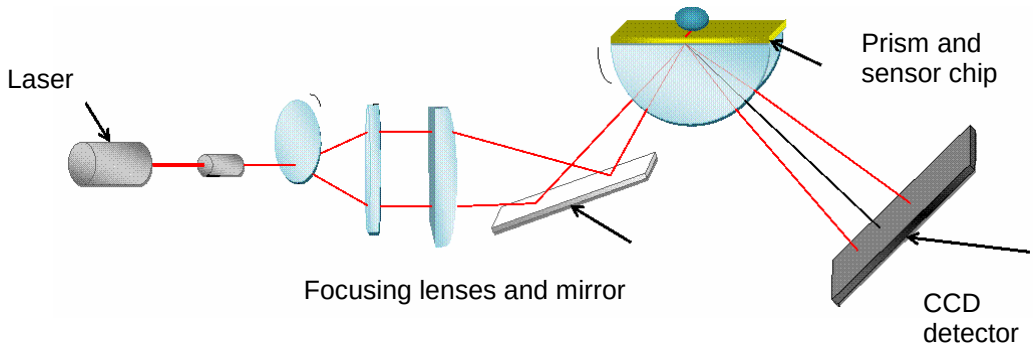

Similar to the optical setup in Biacore instruments, the incident light is also focused in a wedge-shaped beam. However, unlike the fixed optical parts in Biacore instruments, the semi cylindrical prism here is mounted on a rotation

platform. This allows the range of incident angles to be varied if necessary by a simple rotation of the platform. Such an added versatility is the key advantage of this system.

Another difference of this in-house laboratory SPR setup compared to Biacore instruments lies in the system used for introducing the sample. Whereas a microfluidic flow channel is employed in Biacore, this in-house laboratory SPR setup is droplet-based. This gives an additional advantage as it requires a smaller sample volume. The main disadvantage is that well-established (Biacore) standard protocols for interaction monitoring cannot be directly applied in this case.

The in-house laboratory SPR setup with an operating wavelength of 1550 nm is schematically illustrated in Figure 3.6. Light beam from the laser source is polarized and focused onto the sensor surface of the sensor chip in contact with the prism and the flow channel. Light beam reflected from the sensor chip is monitored by an InGaAs CCD camera covering the range of the angles of incidence and surface plasmon resonance shows up as a dark line in the two-dimensional image captured by the camera. The angle of minimum reflection (the SPR angle) is then determined by computer fitting algorithms to the measured reflection spectra. The system can be used in intensity interrogation mode as well as angular interrogation.

Figure 3.6. Schematic illustration of the in-house laboratory SPR setup at the wavelength of 1550 nm.

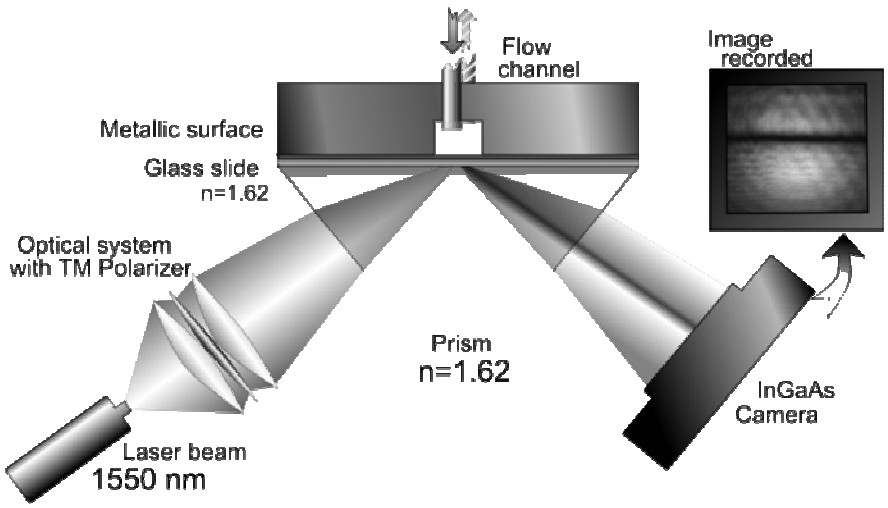

Similar to Biacore instruments, the in-house system constructed for the wavelength of 1550 nm is also equipped with a flow channel through which liquid

samples can be introduced. In addition, the optical parts can be moved to adjust the range of desired incident angles. This is the primary advantage offered by this system. Moreover, the use of a camera instead of a linear array of detectors enables a two-dimensional view allowing multiple parallel channels to be measured simultaneously.

3.7. Comparison with Biosensors Based on Localized Surface Plasmons

Based on the confinement nature of surface plasmons, SPR biosensors can generally be divided into two categories: those that make use of propagating surface plasmons and those that rely on localized surface plasmons. Propagating surface plasmons are supported on continuous metal film whose lateral dimension is large compared to the propagation length of the surface plasmons. If the lateral dimension of the metallic material is shrunk down to nanometers as in nanoparticles, the surface plasmons can no longer propagate. As a result, the surface plasmons of metallic nanoparticles are localized. There are several important differences between propagating and localized surface plasmons that affect their applications in SPR biosensors.

The typical field penetration depth into the dielectric of localized surface plasmons is on the order of 30-40 nm [40]. This restricts the sensing capability of SPR biosensors based on localized surface plasmons to molecules whose dimension is no larger than 30-40 nm. As a consequence, large biomolecules such as single-stranded DNA with feature size on the order of 100 nm cannot be effectively sensed by SPR biosensors based on localized surface plasmons [41]. On the other hand, the field penetration depth into the dielectric of propagating surface plasmons is on the order of 280 nm. With proper designs discussed in the next chapters, this value can be pushed further to around 1250 nm or more depending on the particular design of the SPR biosensors. This enables SPR biosensors based on propagating surface plasmons to probe much larger biological objects such as viruses and bacteria.

The refractive index sensitivity of SPR biosensors based on localized surface plasmons for various sorts of metallic nanoparticles is on the order of 100-300 nm/RIU with typical figure-of-merit on the order of 3 [42, 43]. By comparison, the refractive index sensitivity of the simplest SPR biosensor based on propagating surface plasmons is already over 4000 nm/RIU with typical figure-of-merit of around 23. However, for analyte thickness $\leq$ 10 nm, the sensitivity of

SPR biosensors based on localized surface plasmons is actually on par with that of simple SPR biosensors based on propagating surface plasmons [44, 38]. Beyond this limit, the sensitivity of simple SPR biosensors based on propagating surface plasmons is superior to that of SPR biosensors based on localized surface plasmons. Moreover, for biomolecular interactions most relevant to biosensing, the bioanalytical performance of SPR biosensors based on localized surface plasmons which detect a single binding event has been recently demonstrated to be inferior to that of SPR biosensors based on propagating surface plasmons which integrate a large number of simultaneously occurring binding events [45].

For reasons of superior biosensing performance as discussed above, this work mostly focuses on SPR biosensors based on propagating surface plasmons to fulfill the need for more sensitive biosensors. It is in order however to note that despite the aforementioned limitations on the biosensing performance, SPR biosensors based on localized surface plasmons are not at all without merit. Compared to SPR biosensors based on propagating surface plasmons, the instrumentation of SPR biosensors based on localized surface plasmons is in fact generally much simpler, less expensive, and easier to miniaturize. Some micro/nanostructures supporting quasi-localized surface plasmons are also investigated in this work.

Chapter 4

Calculation Methods, Materials Modeling, and Consideration of Design Parameters

This chapter details the calculation methods used in this work for SPR biosensors in Kretschmann ATR configuration. The modeling of various materials involved will also be discussed. Finally, the influence of several design parameters such as the choice of metals, the prism material, and the operating wavelength on the performance of the resulting SPR biosensors will also be elaborated.

4.1. Calculation Methods

The interaction between an optical wave and the surface plasmons in the ATR configuration can be conveniently analyzed by using Fresnel multilayer reflection method. Details of the method starting from the simplest case of a single interface to the more complex structure with multiple interfaces will be elucidated in this section.

4.1.1. Fresnel Reflection and Transmission: Single Interface

Consider first the simplest case of optical reflection and transmission occurring at the interface of two media where the optical wave is incident from medium 1 to medium 2 (Figure 4.1). The propagation direction of the incident light and the normal to the interface define a plane referred to as the plane of incidence. In general, there exist two types of polarizations, namely perpendicular and parallel polarizations. In the perpendicular polarization, also referred to as the s-polarization or TE (transverse-electric) polarization, the electric field of the optical wave is perpendicular to the plane of incidence while its magnetic field is in the plane of incidence. In the parallel polarization, also referred to as the p-polarization or TM (transverse-magnetic) polarization, the magnetic field of the optical wave is perpendicular to the plane of incidence while its electric field is in the plane of incidence. As shown in Chapter 2, surface plasmons are necessarily p-polarized electromagnetic modes. Therefore in what follows, only the p-

polarized wave will be discussed. Furthermore, the media concerned are all assumed to be non-magnetic so that the only material parameters that enter the ensuing equations are the refractive indices.

Figure 4.1. Fresnel reflection and transmission of a p-polarized light wave at a single interface. The light wave is incident from medium 1 to medium 2.

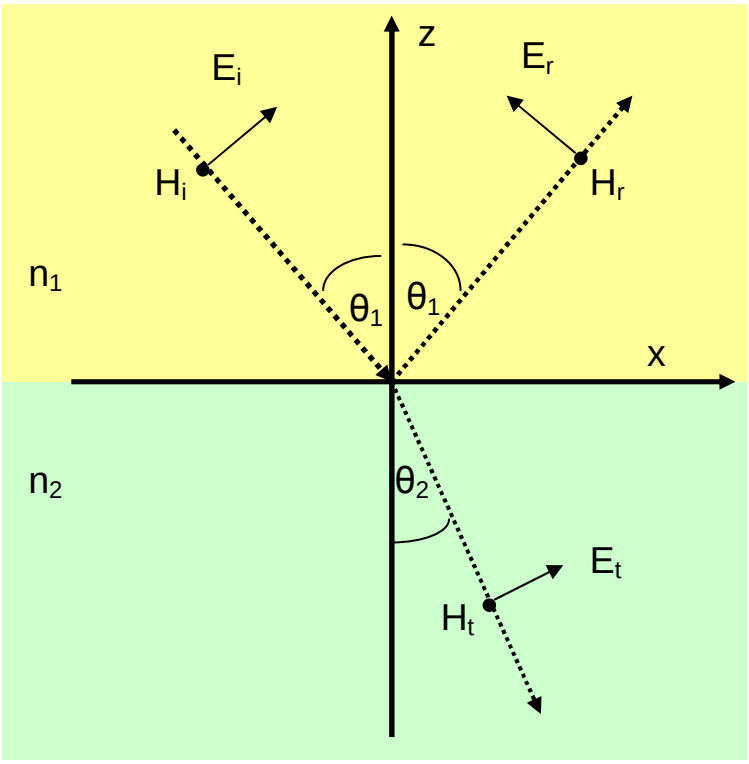

Based on some boundary conditions for the electromagnetic field, namely the continuity of the tangential components of both the electric and magnetic fields, the reflection and transmission coefficients at a single interface can be derived. The results can easily be shown to be

$$r_{12}^{E} = \frac{E_r}{E_i} = \frac{n_2 \cos\theta_1 - n_1 \cos\theta_2}{n_2 \cos\theta_1 + n_1 \cos\theta_2} \tag{4.1}$$

$$t_{12}^{E} = \frac{E_t}{E_i} = \frac{2n_1 \cos\theta_1}{n_2 \cos\theta_1 + n_1 \cos\theta_2} \tag{4.2}$$

where r_{12}^{E} and t_{12}^{E} are respectively the reflection and transmission coefficients for the electric field. The subscripts 12 indicate that the optical wave is incident from medium 1 to medium 2 while the superscript E indicates that the coefficients apply to electric fields. Alternatively, if the magnetic field is concerned, the results are

$$r_{12}^{H} = \frac{H_r}{H_i} = \frac{n_2 \cos\theta_1 - n_1 \cos\theta_2}{n_2 \cos\theta_1 + n_1 \cos\theta_2} \tag{4.3}$$

$$t_{12}^{H} = \frac{H_t}{H_i} = \frac{2n_2 \cos\theta_1}{n_2 \cos\theta_1 + n_1 \cos\theta_2} \tag{4.4}$$

where r_{12}^{H} and t_{12}^{H} are respectively the reflection and transmission coefficients for the electric field. The subscripts 12 indicate that the optical wave is incident from medium 1 to medium 2 while the superscript H indicates that the coefficients apply to magnetic fields.

It is interesting to note from Equations (4.1) and (4.3) that

$$r_{12}^{E} = r_{12}^{H} \tag{4.5}$$

i.e., the reflection coefficient for the electric field is identical to that for the magnetic field. Moreover, from Equations (4.3) and (4.4), the following relation is easily verified

$$1 + r_{12}^{H} = t_{12}^{H} \tag{4.6}$$

This is a direct consequence of Maxwell's continuity condition, as can be seen by multiplying both sides of Equation (4.6) by the incident magnetic field H_i. On the other hand, Equations (4.1) and (4.2) show that for the electric field

$$1 + r_{12}^{E} = \frac{n_2}{n_1} t_{12}^{E} \tag{4.7}$$

This looks slightly different from Equation (4.6) for the magnetic field but Maxwell's continuity condition for the electric field is in fact satisfied. This is so because the electric fields are not all collinear, which is the case for the magnetic

fields. Furthermore, from Equations (4.1)-(4.4), the following useful relations can be easily verified

$$r_{12} = -r_{21} \tag{4.8}$$

$$t_{12}t_{21} - r_{12}r_{21} = 1 \tag{4.9}$$

Equations (4.8) and (4.9) apply to both the electric field and the magnetic field. The superscripts are therefore dropped in these equations. It is also instructive, by noting that $\varepsilon_i = n_i^2$ and defining $k_{zi} = (2\pi n_i/\lambda_0)\cos\theta_i$ for $i = 1, 2$, to rewrite Equations (4.1) or (4.3) into the following compact form

$$r_{12} = \frac{\varepsilon_2 k_{z1} - \varepsilon_1 k_{z2}}{\varepsilon_2 k_{z1} + \varepsilon_1 k_{z2}} \tag{4.10}$$

where k_{zi} is the wave vector component in medium i normal to the interface. Equation (4.10) can be slightly rearranged to yield

$$r_{12} = \frac{k_{z1}/\varepsilon_1 - k_{z2}/\varepsilon_2}{k_{z1}/\varepsilon_1 + k_{z2}/\varepsilon_2} \tag{4.11}$$

It is interesting to see that the dispersion relation of surface plasmons at a single interface in the form of Equation (2.18) can be obtained by equating the denominator of Equation (4.11) to zero. Hence the poles of the reflection coefficient are related to the dispersion relation of surface plasmons.

Analogous to Equation (4.10), Equation (4.4) can also be rewritten in the following useful form

$$t_{12}^H = \frac{2\varepsilon_2 k_{z1}}{\varepsilon_2 k_{z1} + \varepsilon_1 k_{z2}} = 1 + r_{12} \tag{4.12}$$

which shows that the transmission coefficient for the magnetic field can be easily obtained from the reflection coefficient. Computationally, this means that only the reflection coefficient needs to be calculated and the rest can be simply computed from it.

4.1.2. Fresnel Reflection and Transmission: Two Interfaces

Consider now a more sophisticated case of optical reflection and transmission from a three-layer stack of materials (Figure 4.2). This time, one needs to take the multiple reflections in the middle layer (medium 2) of thickness d into account. The total reflected amplitude is obtained from an infinite summation of waves due to the multiple reflections in the middle layer. Each time a wave impinges on an interface, the Fresnel equations are used and the phases of the waves are taken into account. The phase 2Δ is the phase difference for two successive waves such as depicted by ray A and B (also by ray B and C, and so on). The first wave is one that is reflected at the first interface (ray A). The second wave (ray B) is one that is first transmitted through the first interface (1-2 interface), passing through layer 2, is reflected at the second interface (2-3 interface), passing through layer 2 again and is finally transmitted through the first interface (2-1 interface).

Figure 4.2. Fresnel reflection and transmission of a p-polarized light wave from a three-layer stack.

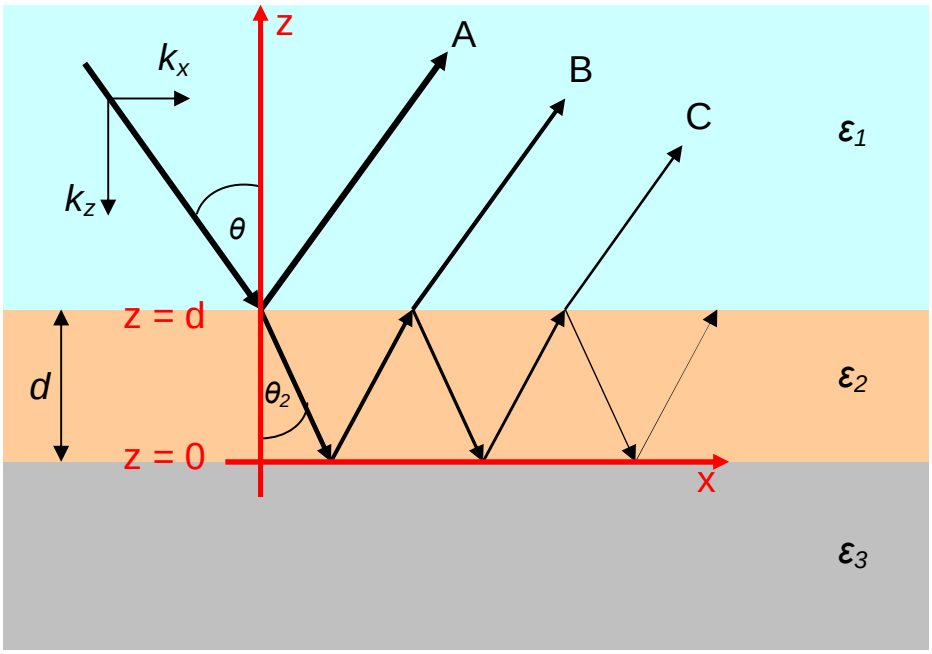

Mathematically, Δ is given by the following

$$\Delta = \left(\frac{2\pi n_2}{\lambda_0} \cos\theta_2 \right) d = k_{z2} d \qquad (4.13)$$

which physically means that Δ is the phase acquired by the wave as it traverses medium 2 once in its path.

The total reflected amplitude E_r can be obtained from the infinite summation of the contributions of rays A, B, C, and so on:

1) The contribution from ray A is simply $r_{12}E_i$,

2) The contribution from ray B that traverses the middle layer once is given by $t_{12}(e^{j\Delta}r_{23})(e^{j\Delta}t_{21})E_i = t_{12}e^{2j\Delta}r_{23}t_{21}E_i$,

3) The contribution from ray C that traverses the middle layer twice is given by $t_{12}(e^{j\Delta}r_{23})(e^{j\Delta}r_{21})(e^{j\Delta}r_{23})(e^{j\Delta}t_{21})E_i = t_{12}e^{2j\Delta}r_{23}(r_{21}e^{2j\Delta}r_{23})t_{21}E_i$,

4) The contribution from the next ray that traverses the middle layer three times is given by $t_{12}e^{2j\Delta}r_{23}(r_{21}e^{2j\Delta}r_{23})^2t_{21}E_i$, and so on so that

$$\begin{aligned} E_r = {} & r_{12}E_i + t_{12}e^{2j\Delta}r_{23}t_{21}E_i + t_{12}e^{2j\Delta}r_{23}(r_{21}e^{2j\Delta}r_{23})t_{21}E_i \\ & + t_{12}e^{2j\Delta}r_{23}(r_{21}e^{2j\Delta}r_{23})^2t_{21}E_i + \ldots \end{aligned} \tag{4.14}$$

The reflection coefficient $r_{13} = E_r/E_i$ is then obtained as

$$r_{13} = r_{12} + t_{12}\left\{e^{2j\Delta}r_{23}\left[1 + r_{21}e^{2j\Delta}r_{23} + \left(r_{21}e^{2j\Delta}r_{23}\right)^2 + \ldots\right]\right\}t_{21} \tag{4.15}$$

By recognizing that the factor enclosed by the square brackets in Equation (4.15) is a convergent geometric series, the reflection coefficient can be simplified as

$$r_{13} = r_{12} + t_{12}t_{21}\frac{r_{23}e^{2j\Delta}}{1 - r_{21}r_{23}e^{2j\Delta}} \tag{4.16}$$

Furthermore, by using the useful relations expressed by Equations (4.8) and (4.9), Equation (4.16) can be rewritten in a more compact form as

$$r_{13} = \frac{r_{12} + r_{23}e^{2j\Delta}}{1 + r_{12}r_{23}e^{2j\Delta}} \tag{4.17}$$

It is instructive to note that by substituting Equation (4.11) for r_{12} and r_{23} in Equation (4.17) and equating the denominator in Equation (4.17) to zero, one obtains

$$1+\left(\frac{k_{z1}/\varepsilon_1-k_{z2}/\varepsilon_2}{k_{z1}/\varepsilon_1+k_{z2}/\varepsilon_2}\right)\left(\frac{k_{z2}/\varepsilon_2-k_{z3}/\varepsilon_3}{k_{z2}/\varepsilon_2+k_{z3}/\varepsilon_3}\right)e^{2j\Delta}=0 \qquad (4.18)$$

which, after some simple rearrangements, is the dispersion relation of surface plasmons at two interfaces as expressed by Equation (2.55) with $d=2a$.

Furthermore, by following the same reasoning in the derivation of the reflection coefficient, the transmission coefficient can be similarly derived

$$t_{13}=\frac{t_{12}t_{23}e^{j\Delta}}{1+r_{12}r_{23}e^{2j\Delta}} \qquad (4.19)$$

The transmission coefficient is especially useful for the evaluation of field enhancement [46]. The field enhancement factor, which is the ratio of the field intensity of the "transmitted wave" to that of the incident wave, can in fact be simply obtained from the square of the absolute value of the transmission coefficient, i.e., the transmittance [46] (see Appendix A.1 for more explanation).

4.1.3. Fresnel Reflection and Transmission: Multiple Interfaces

Building on the preceding results, the case of optical reflection and transmission from an N-layer stack of materials (Figure 4.2), which is of the most interest, can now be tackled. The strategy is simply evaluating the reflection and transmission successively [47]. At each step, nested three-layer stacks are treated recursively. This is illustrated for the reflection coefficient as follows:

$$r_{1N}=\frac{r_{12}+r_{2N}e^{2jd_2k_{z2}}}{1+r_{12}r_{2N}e^{2jd_2k_{z2}}} \qquad (4.20)$$

$$r_{2N}=\frac{r_{23}+r_{3N}e^{2jd_3k_{z3}}}{1+r_{23}r_{3N}e^{2jd_3k_{z3}}} \qquad (4.21)$$

$$r_{3N}=\frac{r_{34}+r_{4N}e^{2jd_4k_{z4}}}{1+r_{34}r_{4N}e^{2jd_4k_{z4}}} \qquad (4.22)$$

and so on until the last three-layer stack is reached.

Figure 4.3. Fresnel reflection and transmission of a p-polarized light wave from an N-layer stack.

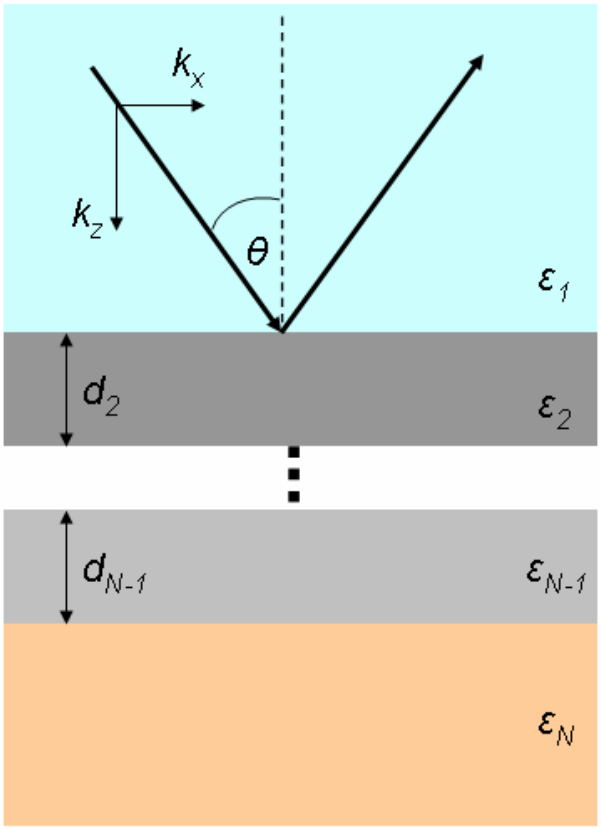

The reflectivity R of p-polarized light incident at an angle θ on a multilayer structure consisting of N layers can therefore be expressed concisely by

$$R = \left| r_{1,N} \right|^2 \tag{4.23}$$

where the recursive reflection coefficients are given by

$$r_{n,N} = \frac{r_{n,n+1} + r_{n+1,N} e^{2\,jd_{n+1}k_{z,n+1}}}{1 + r_{n,n+1} r_{n+1,N} e^{2\,jd_{n+1}k_{z,n+1}}} \tag{4.24}$$

where $n = 1, 2, \ldots, N-2$.

The required reflection coefficients $r_{n,n+1}$ between any two adjacent media indexed by the subscripts n and $n+1$ are given by

$$r_{n,n+1} = \frac{\varepsilon_{n+1} k_{z,n} - \varepsilon_n k_{z,n+1}}{\varepsilon_{n+1} k_{z,n} + \varepsilon_n k_{z,n+1}} \tag{4.25}$$

where $n = 1, 2, \ldots, N-1$.

The wave vector component normal to the interface $k_{z,n}$ in the medium indexed by the subscript n is given by

$$k_{z,n} = \left[\left(\frac{2\pi}{\lambda_0} \right)^2 \varepsilon_n - k_x{}^2 \right]^{1/2} \tag{4.26}$$

for $n = 1, 2, \ldots, N$ where k_x which is the wave vector component along the interface is given by

$$k_x = \frac{2\pi}{\lambda_0} \sqrt{\varepsilon_1} \sin\theta \tag{4.27}$$

Note that as a consequence of phase matching condition, the wave vector component along the interface k_x is identical for all N layers.

Following the same reasoning for the reflectivity described above, the transmittance $T_{1,N}^H$ for the magnetic field intensity of p-polarized light incident at an angle θ on a multilayer structure consisting of *N* layers can similarly be expressed concisely by

$$T_{1,N}^H = \left| \frac{H_N}{H_1} \right|^2 = \left| t_{1,N}^H \right|^2 \tag{4.28}$$

where the recursive reflection coefficients are given by

$$t_{n,N}^H = \frac{t_{n,n+1}^H t_{n+1,N}^H e^{jd_{n+1} k_{z,n+1}}}{1 + r_{n,n+1} r_{n+1,N} e^{2\, jd_{n+1} k_{z,n+1}}} \tag{4.29}$$

where $n = 1, 2, \ldots, N-2$.

The required transmission coefficients $t_{n,n+1}$ between any two adjacent media indexed by the subscripts n and $n+1$ are given by

$$t_{n,n+1}^{H} = \frac{2\varepsilon_{n+1}k_{z,n}}{\varepsilon_{n+1}k_{z,n} + \varepsilon_{n}k_{z,n+1}} = 1 + r_{n,n+1} \tag{4.30}$$

where $n = 1, 2, \ldots, N-1$.

In general, one is mostly interested in the enhancement of the electric field intensity instead of the magnetic field intensity. By the generalization of the results expressed by Equations (4.6) and (4.7), the transmission coefficient for the electric field $t_{n,N}^{E}$ is related to the transmission coefficient for the magnetic field $t_{n,N}^{H}$ by

$$t_{n,N}^{E} = \frac{\sqrt{\varepsilon_{n}}}{\sqrt{\varepsilon_{N}}} t_{n,N}^{H} \tag{4.31}$$

so that the enhancement factor of the electric field intensity is given by

$$T_{1,N}^{E} = \frac{\varepsilon_{1}}{\varepsilon_{N}} T_{1,N}^{H} = \frac{\varepsilon_{1}}{\varepsilon_{N}} \left| t_{1,N}^{H} \right|^{2} \tag{4.32}$$

4.2. Materials Modeling

The most pertinent materials parameter in any work concerning surface plasmons is the relative electric permittivity, also often referred to as the dielectric function from which the refractive indices are derived. In general, the relative electric permittivity of any given material is wavelength, or equivalently, frequency dependent. This is called dispersion and the amount of dispersion depends strongly on the type of materials. For strongly dispersive materials such as metals, precise mathematical modeling is necessary for reliable calculation or simulation results. This section elaborates the modeling of the different materials involved in this work.

4.2.1. Metals

In the context of surface plasmons, metals are the most dispersive materials. In fact, the relative electric permittivity of metals changes drastically over the visible to near infrared range, which is the optical range of the most interest for SPR-based biosensors. For analytical purposes, metals are often modeled by the so-called Drude or free-electron model for its simplicity. In this simple model, the frequency dependent relative electric permittivity can be expressed as

$$\varepsilon(\omega) = 1 - \frac{{\omega_p}^2}{\omega(\omega + j\gamma)} \tag{4.33}$$

where ω is the angular frequency, γ is the damping constant, and ω_p is the plasma frequency given by

$$\omega_p = \sqrt{\frac{q^2 n_e}{m\varepsilon_0}} \tag{4.34}$$

where n_e is the electron density in the metal, q is the elementary electronic charge, and m is the mass of an electron.

Equation (4.34) suggests that the plasma frequency is some kind of measure of the density of free electrons in metals. Below the plasma frequency, the relative electric permittivity is negative and the electromagnetic field cannot penetrate the metals. An optical wave with angular frequency below the plasma frequency will therefore be totally reflected. Above the plasma frequency however, the light waves can penetrate the metals.

Despite its simplicity, the free-electron or Drude model is reasonably good in the far infrared range. It is however not adequate for computational purposes in the visible and near-infrared wavelength range. A more rigorous model for the relative electric permittivity of metals is therefore needed. In this work, the Lorentz-Drude model is used to calculate the relative electric permittivity of metals. It is based on a phenomenological model that gives an excellent fit to measured experimental values [48].

In the Lorentz-Drude model, the complex relative electric permittivity of metals $\varepsilon_m(\omega) = \varepsilon_m'(\omega) + j\varepsilon_m''(\omega)$ can be expressed as a combination of the intraband effects (also referred to as the free-electron effects) denoted by $\varepsilon_m^f(\omega)$

and the interband effects (also known as the bound-electron effects) denoted by $\varepsilon_m^b(\omega)$:

$$\varepsilon_m(\omega) = \varepsilon_m^f(\omega) + \varepsilon_m^b(\omega) \tag{4.35}$$

The intraband part of the relative electric permittivity $\varepsilon_m^f(\omega)$ can be described by the well-known free-electron or Drude model:

$$\varepsilon_m^f(\omega) = 1 - \frac{\Omega_p^{\,2}}{\omega(\omega + j\Gamma_0)} \tag{4.36}$$

The interband part of the relative electric permittivity $\varepsilon_m^b(\omega)$ is described by the simple semiquantum model resembling the Lorentz result for insulators:

$$\varepsilon_m^b(\omega) = \sum_{n=1}^{k} \frac{f_n \omega_p^{\,2}}{\left(\omega_n^{\,2} - \omega^2\right) - j\omega\Gamma_n} \tag{4.37}$$

where ω_p is the plasma frequency, k is the number of oscillators with frequency ω_n, strength f_n, and lifetime $1/\Gamma_n$, while $\Omega_p = \omega_p\sqrt{f_0}$ is the plasma frequency associated with intraband transitions with oscillator strength f_0 and damping constant Γ_0.

To gain some practical insights into the Lorentz-Drude model, the plasma frequency of some important metals for optoelectronic devices is tabulated in Table 4.1. Values of the Lorentz-Drude model parameters for the metals most commonly used in SPR-based biosensors, namely gold, silver, aluminum, and titanium are also listed in Table 4.2.

To illustrate the accuracy of the Lorentz-Drude model, some experimental values of the dielectric function of gold thin film obtained by ellipsometric measurement are listed in Table 4.3. These values along with the corresponding fit based on Lorentz-Drude model are plotted in Figure 4.4. It can be seen from Figure 4.4 that the agreement between the experimental values and the Lorentz-Drude model fit is excellent. A comparison with measurement results published in the literature [49, 50, 51] also reveals an excellent agreement with the Lorentz-Drude model.

Table 4.1 The plasma frequency (expressed in units of eV) of some important metals for optoelectronic devices [46].

Metal	$\hbar\omega_p$
Ag	9.01
Au	9.03
Cu	10.83
Al	14.98
Be	18.51
Cr	10.75
Ni	15.92
Pd	9.72
Pt	9.59
Ti	7.29
W	13.22

Table 4.2. The Lorentz-Drude model parameters (expressed in units of eV) for some selected metals: Ag, Au, Al, Ti [46].

Parameters	Ag	Au	Al	Ti
f_0	0.845	0.760	0.523	0.148
Γ_0	0.048	0.053	0.047	0.082
f_1	0.065	0.024	0.227	0.899
$\Gamma_1{}^a$	3.886	0.241	0.333	2.276
$\omega_1{}^a$	0.816	0.415	0.162	0.777
f_2	0.124	0.010	0.050	0.393
Γ_2	0.452	0.345	0.312	2.518
ω_2	4.481	0.830	1.544	1.545
f_3	0.011	0.071	0.166	0.187
Γ_3	0.065	0.870	1.351	1.663
ω_3	8.185	2.969	1.808	2.509
f_4	0.840	0.601	0.030	0.001
Γ_4	0.916	2.494	3.382	1.762
ω_4	9.083	4.304	3.473	19.43
f_5	5.646	4.384	—	—
Γ_5	2.419	2.214	—	—
ω_5	20.29	13.32	—	—

[a] In electron volts.

Table 4.3. Relative electric permittivity of gold thin film obtained by ellipsometric measurement.

Wavelength (nm)	n	k	ε_{re}	ε_{im}
500	0.84	1.8400001	-2.68	3.09119884
550	0.331	2.32399989	-5.29141	1.53848793
600	0.2	2.8970001	-8.35261	1.15879992
650	0.142	3.37400002	-11.3637	0.95821594
700	0.131	3.84199996	-14.7438	1.00660391
750	0.14	4.26599993	-18.1792	1.19447998
800	0.149	4.65399988	-21.6375	1.38689196
850	0.157	4.99299984	-24.9054	1.56780205
900	0.166	5.33499992	-28.4347	1.77121987
950	0.174	5.69100016	-32.3572	1.98046794
1000	0.179	6.04400049	-36.4979	2.1637523

Figure 4.4. Comparison of the experimental dielectric function of gold thin film measured by ellipsometry (Table 4.3) to theoretical fit using Lorentz-Drude model. The squares and circles correspond respectively to the experimental values of the real part and the imaginary part of the relative electric permittivity. The solid and dotted curves are respectively the Lorentz-Drude fit for the real part and the imaginary part of the relative electric permittivity.

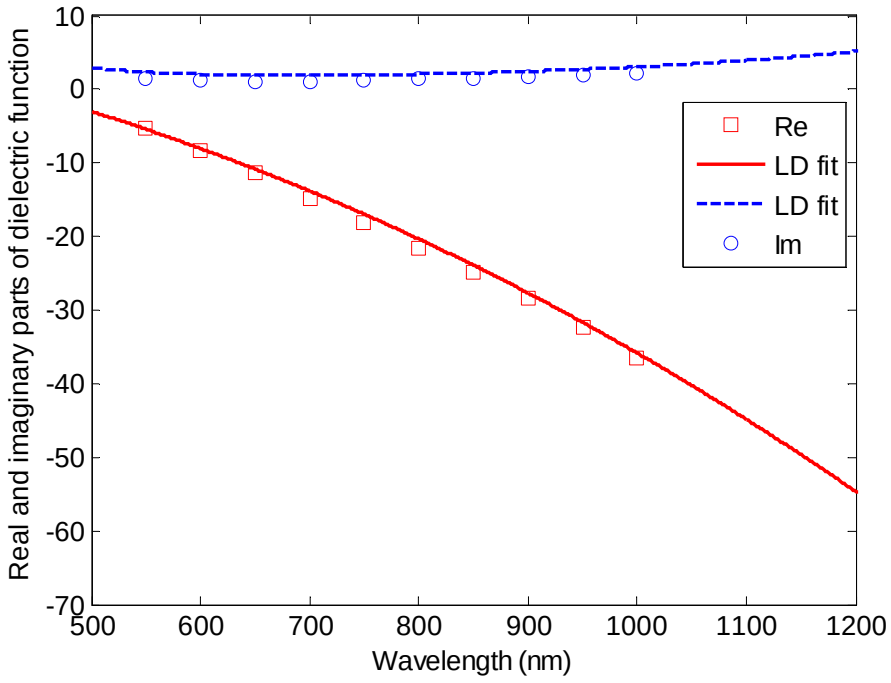

4.2.2. Solid Dielectrics: Glass Prisms and Polymers

Having discussed metals in the preceding subsection, we now turn our attention to solid dielectric media encountered in this work, namely glass prisms and polymers. The refractive index dispersion of glasses and polymers is well described by the Sellmeier model or Cauchy's dispersion equation.

Cauchy's dispersion equation is an empirical relationship between the refractive index and wavelength for a solid transparent dielectric medium. It is usually expressed in the form:

$$n(\lambda) = A + \frac{B}{\lambda^2} + \frac{C}{\lambda^4} \tag{4.38}$$

where $n(\lambda)$ is the wavelength dependent refractive index and λ is the wavelength in free space expressed in µm. *A, B,* and *C* are Cauchy's coefficients that can be determined by fitting the equation to measured refractive indices at some known wavelengths. It is important to note that in general the Cauchy's dispersion equation is only valid for regions of normal dispersion (where the refractive index decreases with increasing wavelength) in the visible wavelength range. In the infrared, the equation becomes inaccurate and it cannot represent regions of anomalous dispersion (where the refractive index increases with increasing wavelength). Despite these drawbacks, the mathematical simplicity of Cauchy's dispersion equation makes it useful in some applications.

Sellmeier equation is also an empirical relationship between the refractive index and wavelength for a solid transparent dielectric medium that can be derived from classical dispersion theory. It was first proposed in 1871 by Wolfgang Sellmeier as a further development of the Cauchy's dispersion equation that handles anomalously dispersive regions. It more accurately models the refractive index dispersion of solid dielectric materials across the ultraviolet, visible, and infrared spectrum.

The Sellmeier dispersion equation is usually written in the form

$$n^2 = 1 + \frac{B_1\lambda^2}{\lambda^2 - C_1} + \frac{B_2\lambda^2}{\lambda^2 - C_2} + \frac{B_3\lambda^2}{\lambda^2 - C_3} \tag{4.39}$$

where *n* is the refractive index and λ is the free-space wavelength expressed in µm. B_1, B_2, B_3, C_1, C_2, and C_3 are experimentally determined Sellmeier

coefficients. To give some examples, the Sellmeier coefficients for BK7 glass and MgF_2 are given in Table 4.4.

Table 4.4. Sellmeier coefficients for BK7 glass and MgF_2 crystal (n_o denotes the ordinary refractive index) [52].

Sellmeier coefficient	BK7 glass	MgF_2 (n_o)
B_1	1.03961212	4.8755108×10^{-1}
B_2	$2.31792344 \times 10^{-1}$	3.9875031×10^{-1}
B_3	1.01046945	2.3120353
C_1	$6.00069867 \times 10^{-3}$	1.882178×10^{-3}
C_2	$2.00179144 \times 10^{-2}$	$8.95188847 \times 10^{-3}$
C_3	1.03560653×10^{2}	5.66135591×10^{2}

Physically, each term in the Sellmeier dispersion equation represents an optical absorption of strength B_i at a wavelength $\sqrt{C_i}$ for i = 1, 2, 3. For common optical glasses, the refractive index calculated with the three-term Sellmeier equation deviates from the actual refractive index by less than 5×10^{-6} over the wavelength range of 365 nm to 2.3 μm.

4.2.3. Water

In the applications of SPR-based biosensors, the samples to be analyzed are mostly aqueous biological solutions. Water usually makes up more than 95 % of the materials present in these samples. It is therefore very important to take into account the refractive index dispersion of water.

Based on a comprehensive collection of data on the experimental refractive index of water and steam, a formulation for the refractive index of water and steam covering the temperature range from -12 °C to 500 °C, the density range from 0 to 1045 kg m^{-3}, and the wavelength range from 0.2 μm to 1.9 μm has been adopted by the International Association for the Properties of Water and Steam (IAPWS) and is available as part of a National Institute of Standards and

Technology (NIST) Standard Reference Database [53, 54, 55]. This formulation is written in the form

$$\left[\frac{n^2-1}{n^2+2}\right]\left(1/\overline{\rho}\right) = a_0 + a_1\overline{\rho} + a_2\overline{T} + a_3\overline{\lambda}^2\overline{T} + \frac{a_4}{\overline{\lambda}^2} + \frac{a_5}{\overline{\lambda}^2 - \overline{\lambda_{UV}}^2} + \frac{a_6}{\overline{\lambda}^2 - \overline{\lambda_{IR}}^2} + a_7\overline{\rho}^2 \tag{4.40}$$

where n is the wavelength, temperature, and density dependent refractive index. $\overline{T}$, $\overline{\rho}$, and $\overline{\lambda}$ are dimensionless variables

$$\overline{T} = T/T^*$$
$$\overline{\rho} = \rho/\rho^*$$
$$\overline{\lambda} = \lambda/\lambda^*$$

in terms of reference temperature T^*, reference density ρ^*, and reference wavelength λ^*

$$T^* = 273.15 \text{ K}$$
$$\rho^* = 1000 \text{ kg m}^{-3}$$
$$\lambda^* = 0.589 \ \mu\text{m}$$

The coefficients a_0 - a_7 and the constants $\overline{\lambda_{IR}}$ and $\overline{\lambda_{UV}}$ are listed in Table 4.5.

Table 4.5. Coefficients and constants of the formulation for the refractive index of water and steam, Equation (4.40) [51, 52, 53].

a_0	0.244257733
a_1	9.74634476 x 10^{-3}
a_2	-3.73234996 x 10^{-3}
a_3	2.68678472 x 10^{-4}
a_4	1.58920570 x 10^{-3}
a_5	2.45934259 x 10^{-3}
a_6	0.900704920

a_7	$-1.66626219 \times 10^{-2}$
$\overline{\lambda_{UV}}$	0.229202
$\overline{\lambda_{IR}}$	5.432937

4.3. Consideration of Design Parameters

Building on the knowledge of calculation methods and materials modeling developed in the preceding sections, the influence of several design parameters such as the choice of metals, the prism material, and the operating wavelength on the performance of the resulting SPR biosensors can now be explored in this section. The discussion that follows pertains to SPR biosensors with standard Kretschmann configuration, which is the coupling method mostly considered in this work. Together with the Fresnel equations elaborated in Section 4.1, the materials models discussed in Section 4.2 are implemented in MATLAB codes to generate the theoretical results presented in the following section as well as the next chapter.

4.3.1. Choice of Metals

In the optical and near infrared range of the electromagnetic spectrum, all metals practically support surface plasmons. This is illustrated in Figure 4.5 that shows the real part of the relative electric permittivity of some important plasmonic metals (silver, gold, titanium, and aluminum). It is based on the Lorentz-Drude model as described in Section 4.2.1 and plotted as a function of wavelength in the 400-1600 nm wavelength range. As can be seen from Figure 4.5, the real part of the relative electric permittivity of these metals is negative which enables surface plasmons. In the wavelength range of 630-1550 nm which is of the most interest for SPR biosensors, metals such as gold, silver, and aluminum have a large negative real part of relative electric permittivity while that of titanium is quite small by comparison. It is to be noted that in these wavelength range, the relative electric permittivity of silver is very close to that of gold.

Based on the real part of the relative electric permittivity alone as has just been discussed, the answer to the question “Which metal is the best choice for SPR biosensors?” is therefore not yet clear-cut. In fact, one also needs to examine the

imaginary part of the relative electric permittivity which, as will be shown in no time, is the determining factor in the choice of metals for SPR biosensors. The imaginary part of the relative electric permittivity of the same selection of metals and wavelength range is plotted in Figure 4.6.

Figure 4.5. The real part of the relative electric permittivity of some important plasmonic metals as a function of wavelength in the 400-1600 nm wavelength range. Note that the vertical axis is on a logarithmic scale.

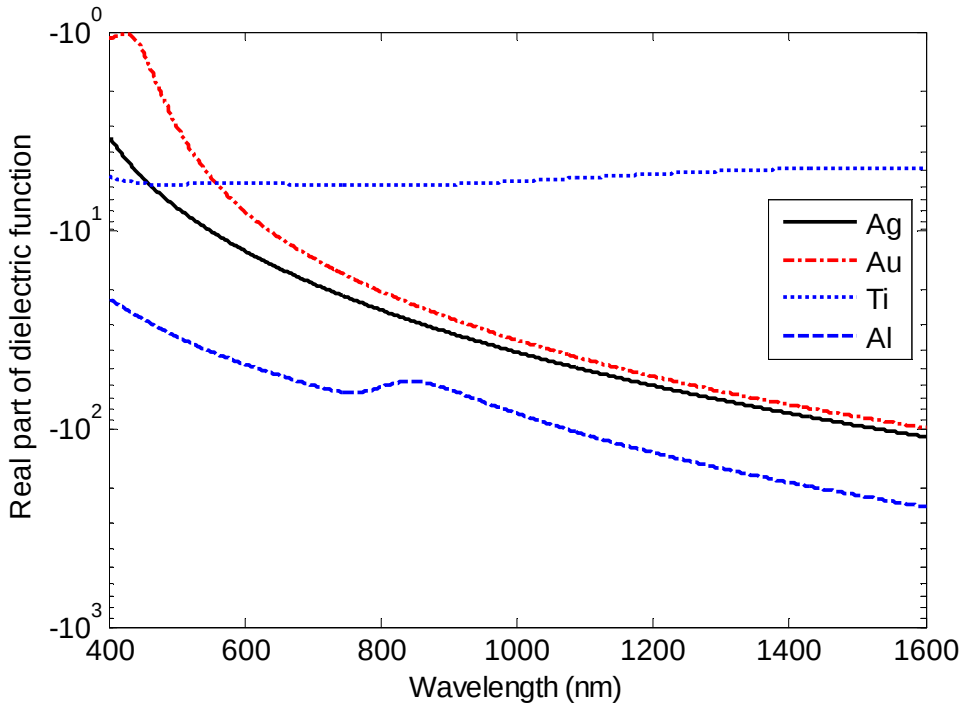

As discussed in Section 2.3, the imaginary part of the relative electric permittivity of metals is related to the propagation loss of the corresponding surface plasmons. The smaller the imaginary part of the relative electric permittivity, the lower the propagation loss of the resulting surface plasmons. Lower propagation loss means that when an optical wave is coupled to surface plasmons resulting in surface plasmon resonance, the resonance linewidth is narrower. For sensing applications, narrow resonance linewidth is a very desirable characteristic. As can be seen from Figure 4.6, gold and silver have the smallest imaginary part of the relative electric permittivity in the 400-1600 nm wavelength range that makes these metals the best candidates for applications in SPR biosensors. It is also to be noted that in the red end of the visible optical spectrum

around 670-780 nm which is of the most interest for SPR biosensors operating in the visible, the imaginary part of the relative electric permittivity of silver is very close to that of gold. Going further into the near infrared region around 1550 nm however, the imaginary part of the relative electric permittivity of gold is noticeably slightly larger than that of silver.

Figure 4.6. The imaginary part of the relative electric permittivity of some important plasmonic metals as a function of wavelength in the 400-1600 nm wavelength range.

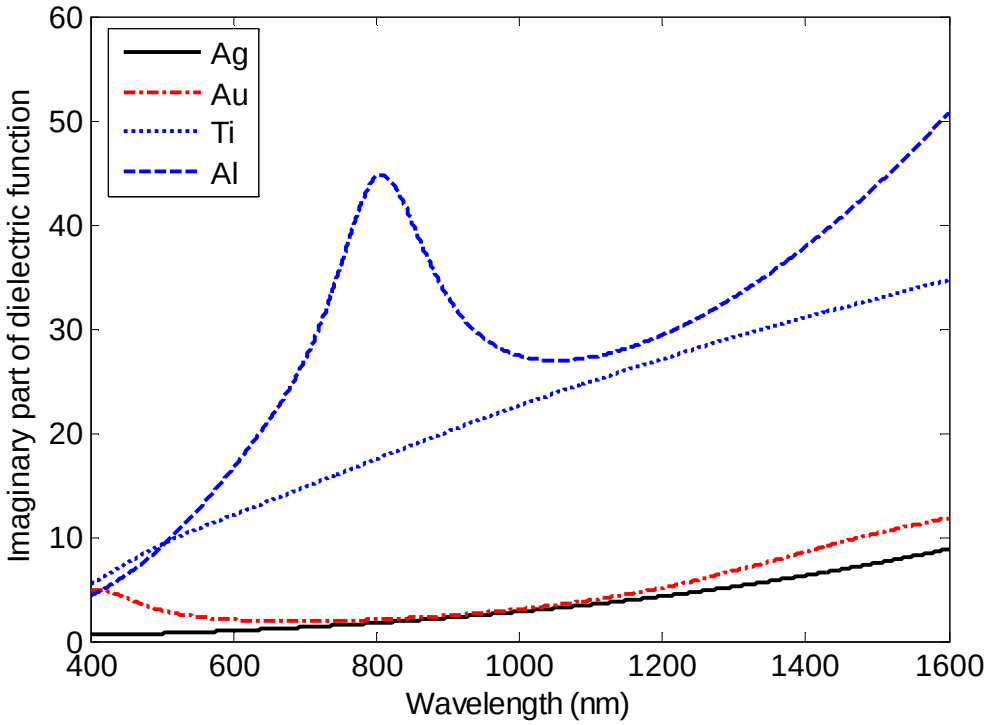

Considering both the real and imaginary parts of the relative electric permittivity, the best metallic candidates for SPR biosensors so far are gold and silver. Although as can be seen from Figure 4.6 that the imaginary part of the relative electric permittivity of silver is consistently lower than that of gold, silver is not the usual choice for metal in SPR biosensors. The reason is the chemical vulnerability of silver, in ambient air as well as aqueous solution. Silver oxidizes easily and the formation of oxides quickly degrades its sensing performance. On the other hand, gold is much more chemically stable compared to silver. In addition, the surface of gold can also be easily functionalized. Gold is therefore the metal of choice for SPR biosensors.

Having established gold as the metal of choice for SPR biosensors, we now turn our attention to the optimum thickness of the gold thin film for SPR biosensors in Kretschmann configuration. That there is an optimum thickness for the metal film in Kretschmann configuration can be physically understood quite easily. If the metal film is too thin approaching zero thickness, the dielectric does not "feel" the presence of the metal. Thus no surface plasmon resonance will be observed in this case. On the other hand, if the metal film is too thick, the evanescent field from the total internal reflection at the prism base is strongly attenuated in the metal. As a result, this evanescent tail cannot effectively reach the metal-dielectric interface on the other side where the sensed dielectric medium lies to excite the associated surface plasmons. Thus no surface plasmon resonance will be observed either in this case.

The influence of the thickness of the gold thin film on the performance of the resulting SPR biosensors can be investigated using the calculation methods and materials models discussed earlier in this chapter. The chosen model system here is a typical SPR biosensor using BK7 glass substrate with water at room temperature (298 K) as the sensed dielectric medium. Figure 4.7 shows the calculated results as a series of SPR curves of water at the wavelength of 760 nm for gold thickness of 40, 45, 50, and 55 nm.

Figure 4.7. Influence of the thickness of the gold film on the SPR curve of water at λ = 760 nm. Prism material considered here is BK7 glass. Optimum gold thickness is in the 45-50 nm range.

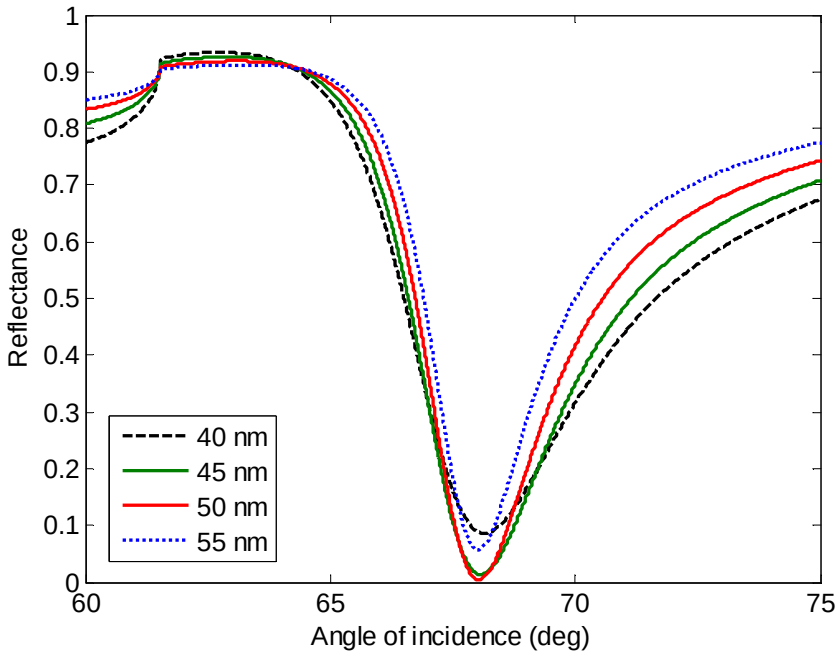

As can be clearly seen from Figure 4.7, the resonance dip in the SPR curve is sharpest with the minimum of reflectance near zero for the gold thickness of around 45nm and 50 nm. For either thinner or thicker film, the minimum of reflectance moves away from zero and the SPR curves start to broaden. The optimum thickness for the gold film is thus somewhere in the 45-50 nm range.

4.3.2. Influence of Prism Materials

The prism materials used for plasmonic devices such as SPR biosensors can be broadly classified into two classes. The first one is common silica-based optical glasses with typical refractive index $n < 2$ such as BK7 and H-ZF1 glass materials. The other one is special prism with very high refractive index ($n > 2$). An example of this second class of prism materials is chalcogenide glass-based optical material such as 2S2G glass. SPR biosensors typically make use of the first class of prism materials. To illustrate the influence of the chosen prism materials on the performance of the resulting SPR biosensors, a comparative theoretical study between BK7 and 2S2G prism materials is elaborated in detail in this section.

Consider first the BK7 prism material. At the wavelength of 760 nm, its refractive index is 1.5116. With water as the sensed dielectric medium, the optimum thickness of the gold film is 50 nm as discussed previously. The resulting SPR curve is shown in Figure 4.8 from which the resonance linewidth (the full-width-at-half-maximum, FWHM) can be seen to be approximately 3.5°. The associated electric field intensity enhancement factor is shown in Figure 4.9. Far from the resonance, the electric field intensity enhancement factor is close to unity. This is expected since there is no excitation of surface plasmons when the angle of incidence is sufficiently far from the angle of resonance which is around 68°. Near the surface plasmon resonance, the electric field intensity enhancement factor increases significantly and reaches its maximum at the angle of resonance. The maximum electric field intensity enhancement factor in this particular example is around 21. This field enhancement at the surface plasmon resonance is the reason why surface plasmons are very useful for diverse applications. As can be inferred from Equation (4.32), the amount of field enhancement depends on the sensed dielectric medium. It is stronger for dielectric medium with lower refractive index.

Figure 4.8. Calculated SPR curve of water with BK7 prism at the wavelength of 760 nm and gold film thickness of 50 nm.

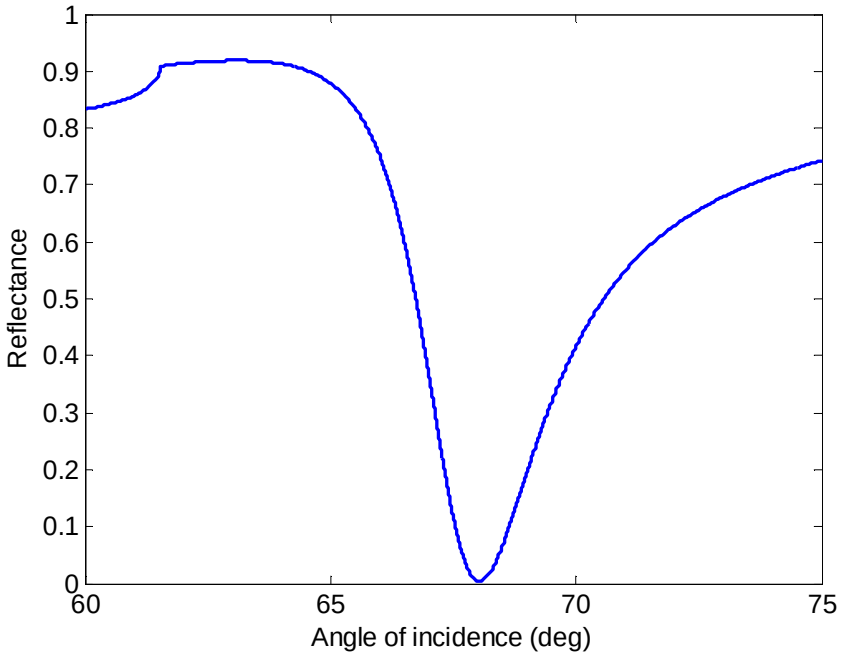

Figure 4.9. Electric field intensity enhancement factor associated with the SPR curve of water with BK7 prism at the wavelength of 760 nm and gold film thickness of 50 nm.

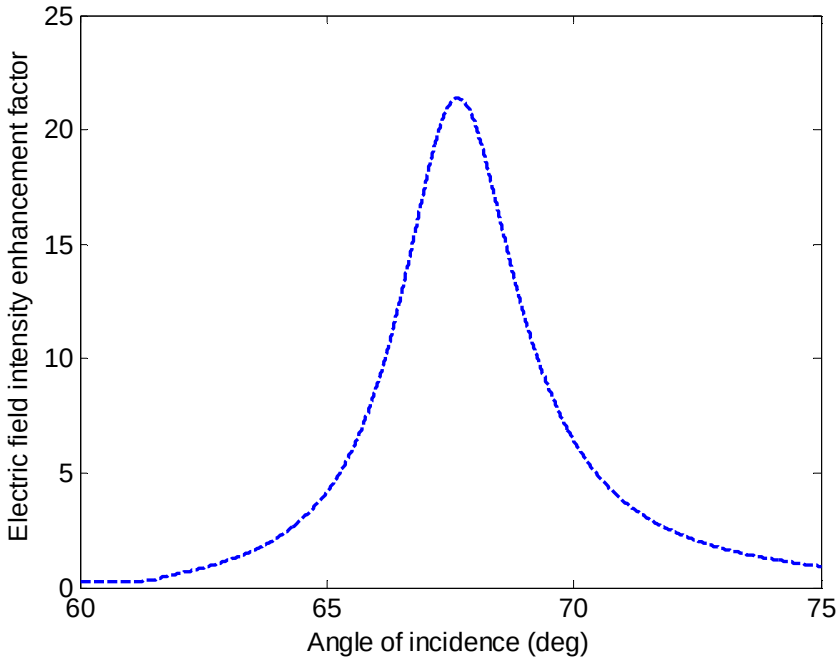

To further theoretically evaluate the performance of this SPR biosensor, we now consider how the surface plasmons react to a change in refractive index of the sensed dielectric medium. Assuming a refractive index change of Δn = 0.005 RIU (refractive index unit), the resulting SPR curve of water is plotted in Figure 4.10.

From the shift of the angle of resonance with the corresponding change in the refractive index of the sensed medium as shown in Figure 4.10, the refractive index sensitivity is calculated to be 116.3 °/RIU. With a resonance linewidth of around 3.5°, the figure-of-merit of this SPR biosensor is easily calculated to be approximately 33. In addition to the refractive index sensitivity and the figure-of-merit, using Equations (4.26) and (4.27) in conjunction with Equation (2.63), the field penetration depth can also be determined to be around 27 nm in the gold film and 280 nm in the sensed dielectric.

Figure 4.10. SPR curves of water showing the resonance shift corresponding to a refractive index change of 0.005 RIU. The system is BK7 prism, 50 nm of gold, and water at the wavelength of 760 nm.

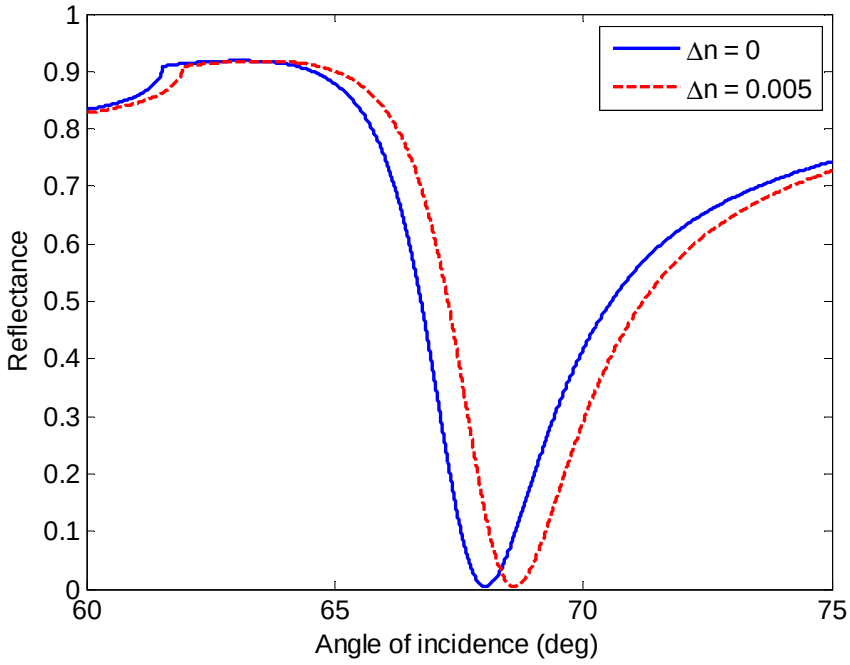

Consider now the other class of prism materials with very high refractive index (n > 2), e.g., chalcogenide glass-based optical materials that have recently

generated significant interest over the past decade owing to their excellent transparency up to the mid-infrared regions. Chalcogenide glasses are formed by adding materials such as As, Ga, Ge, and Sb to the group IV chalcogen elements (S, Se, and Te). The particular chalcogenide glass selected as an example here has the composition $Ge_{20}Ga_5Sb_{10}S_{65}$ which is known as the 2S2G glass [56]. The refractive index dispersion of the 2S2G glass can be conveniently characterized by Cauchy's dispersion equation whose coefficients are listed in Table 4.6.

By using Equation (4.38) and the values given in Table 4.6, the refractive index of the 2S2G glass can easily be calculated to be 2.3113 at the wavelength of 760 nm. With water as the sensed dielectric medium, the optimum thickness of the gold film can also be easily found to be 45 nm. The resulting SPR curve is shown in Figure 4.11. The associated electric field intensity enhancement factor is shown in Figure 4.12. A direct comparison with the previous SPR system using BK7 glass as the prism material can now be performed in order to evaluate the effects of changing the refractive index of the prism.

Table 4.6. Values of Cauchy's coefficients for the 2S2G glass with the wavelength expressed in μm [56].

A	2.24047
B	2.693×10^{-2}
C	8.08×10^{-3}

Figure 4.11 shows that the resonance linewidth (the full-width-at-half-maximum, FWHM) is now approximately 1.4° instead of 3.5° as in the case of BK7 prism. This indicates that for a given operating wavelength and sensed dielectric medium, using a prism material with higher refractive index yields narrower resonance linewidth. This can be mathematically understood by noting that the higher the refractive index of the prism, the faster the wave vector component of the optical excitation impinging on the metal film changes with the variation of the angle of incidence. As a result, surface plasmon resonance in this case occurs over a narrower range of the angle of incidence. It is also readily noticed from Figure 4.11 that the resonance now takes place at around 37.5° instead of 68° as in the case of BK7 prism. The lower angle of resonance for

prism material with higher refractive index is exactly what one expects from Equation (2.70).

Figure 4.11. SPR curve of water with 2S2G prism at the wavelength of 760 nm and gold film thickness of 45 nm.

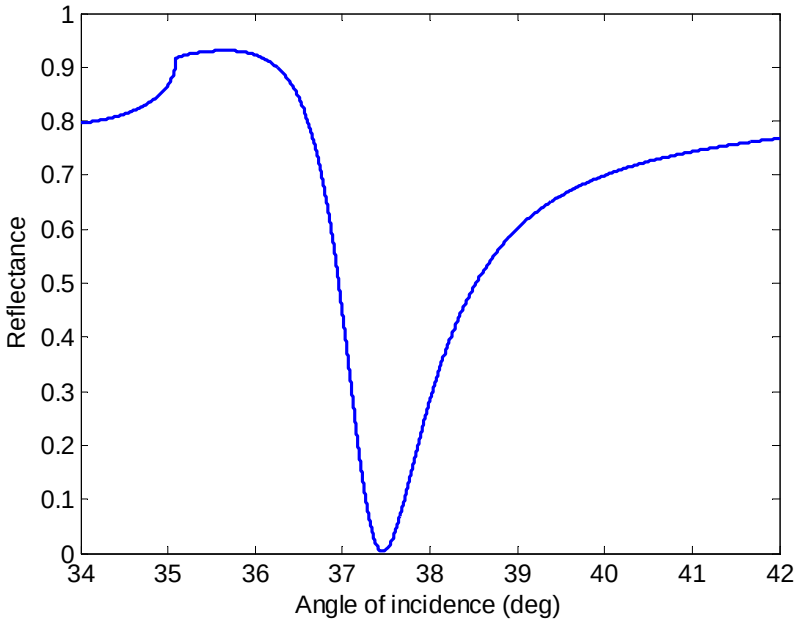

Figure 4.12. Electric field intensity enhancement factor associated with the SPR curve of water with 2S2G prism at the wavelength of 760 nm and gold film thickness of 45 nm.

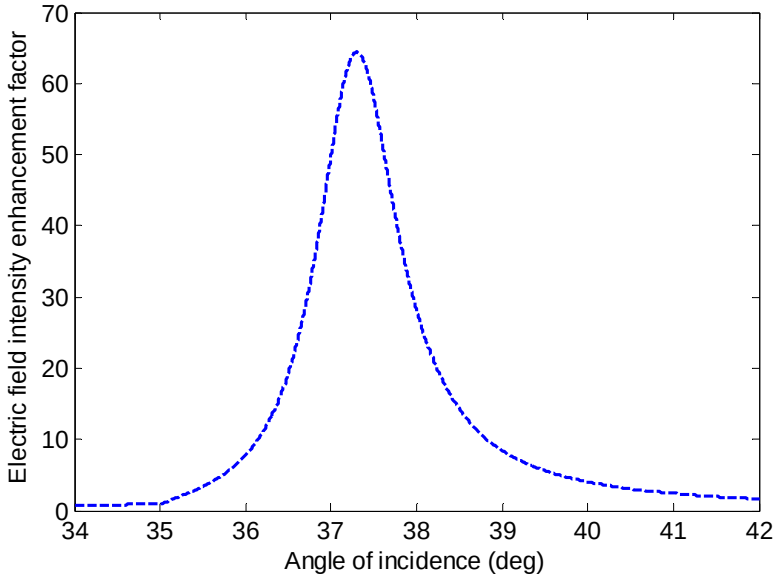

Figure 4.12 shows that the maximum electric field intensity enhancement factor at the angle of resonance is now around 64 instead of 21 as in the case of BK7 prism. The maximum electric field intensity enhancement factor is therefore increased by approximately three-fold. The fact that for a given operating wavelength and sensed dielectric medium, using a prism material with higher refractive index yields stronger field enhancement can be easily understood by referring to Equation (4.32). According to this equation, the electric field intensity enhancement factor scales roughly as the square of the refractive index of the prism.

Finally to complete the characterization of this SPR biosensor and compare its performance to the previous one with BK7 prism, we now consider how the surface plasmons react to a change in refractive index of the sensed dielectric medium. Assuming a refractive index change of Δn = 0.005 RIU (refractive index unit), the resulting SPR curve of water is plotted in Figure 4.13.

Figure 4.13. Resonance shift corresponding to a refractive index change of 0.005 RIU. The system is 2S2G prism, 45 nm of gold, and water at the wavelength of 760 nm.

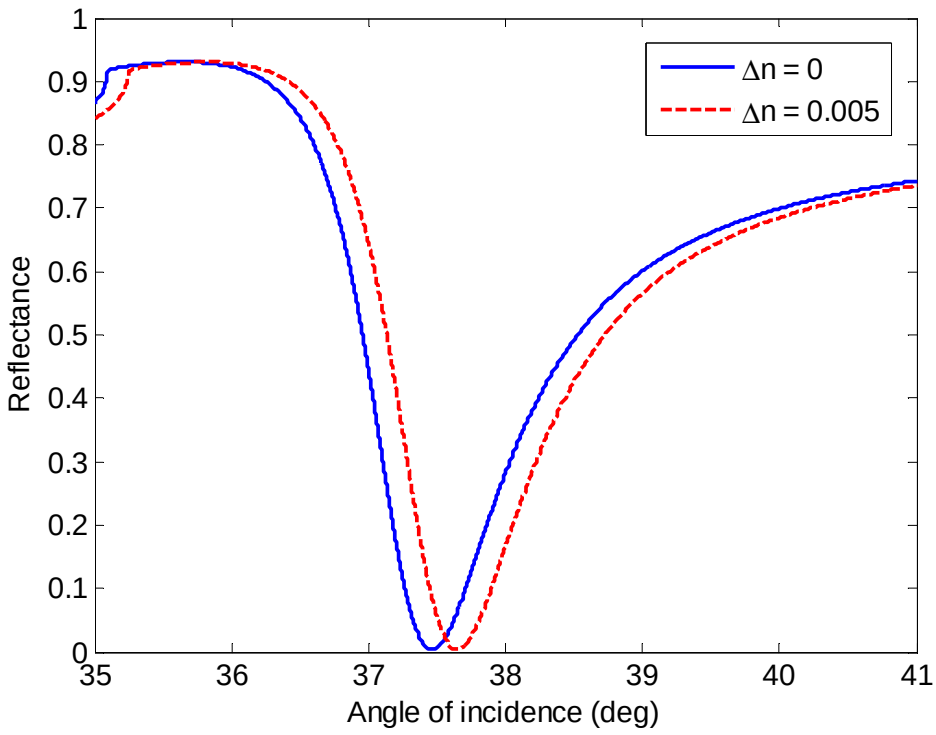

From the shift of the angle of resonance with the corresponding change in the refractive index of the sensed medium as shown in Figure 4.13, the refractive index sensitivity is calculated to be about 37 °/RIU. With a resonance linewidth of around 1.4°, the figure-of-merit of this SPR biosensor is easily calculated to be approximately 26. In addition to the refractive index sensitivity and the figure-of-merit, using Equations (4.26) and (4.27) in conjunction with Equation (2.63), the field penetration depth can also be determined to be around 27 nm in the gold film and 280 nm in the sensed dielectric, similar to the case of BK7 prism. The field penetration depth is therefore independent of the prism material. This is as expected since for a given metal, the field penetration depth depends only on the refractive index of the sensed dielectric medium.

Based on the preceding discussion, the influence of prism materials on the relevant characteristics of SPR biosensors for a given operating wavelength and sensed dielectric medium can now be summed up as follows. Firstly, the higher the refractive index of the prism, the lower the resulting angle of resonance. Secondly, the resonance linewidth is effectively narrowed by using a prism material with higher refractive index. Thirdly, the higher the refractive index of the prism, the stronger the electromagnetic field enhancement at resonance. Finally, as far as angular interrogation is concerned, although the resonance linewidth is narrowed, the figure-of-merit of SPR biosensors is practically unaltered when the refractive index of the prism is increased. This is because by increasing the refractive index of the prism, the angular sensitivity of the resulting SPR biosensors to the refractive index variation of the sensed dielectric is actually decreased to the point that the effect of this decrease annuls that of the narrower resonance linewidth. However, when intensity interrogation is employed, the performance of SPR biosensors is certainly improved by using a prism material with higher refractive index.

4.3.3. Influence of Operating Wavelength

The influence of the operating wavelength on the performance of SPR biosensors is now considered in this section. To evaluate this, a model system is chosen and its performance at two different wavelengths with fixed prism material and sensed dielectric medium is compared. A model system consisting of BK7 prism, gold thin film, and water as the sensed dielectric medium at the wavelength of 760 nm has been discussed in the preceding section. The same model system operating at the wavelength of 1550 nm is now theoretically investigated for comparison.

By using Equation (4.39) and the values given in Table 4.4, the refractive index of the BK7 prism material can easily be calculated to be 1.5007 at the wavelength of 1550 nm. With water as the sensed dielectric medium, the optimum thickness of the gold film can also be easily found to be 35 nm. The resulting SPR curve is shown in Figure 4.14 from which the resonance linewidth (the full-width-at-half-maximum, FWHM) can be seen to be approximately 0.8°. The associated electric field intensity enhancement factor is plotted in Figure 4.15. These results can be compared to those previously obtained at the wavelength of 760 nm shown in Figures 4.8 and 4.9.

Figure 4.14. SPR curve of water with BK7 prism at the wavelength of 1550 nm and gold film thickness of 35 nm.

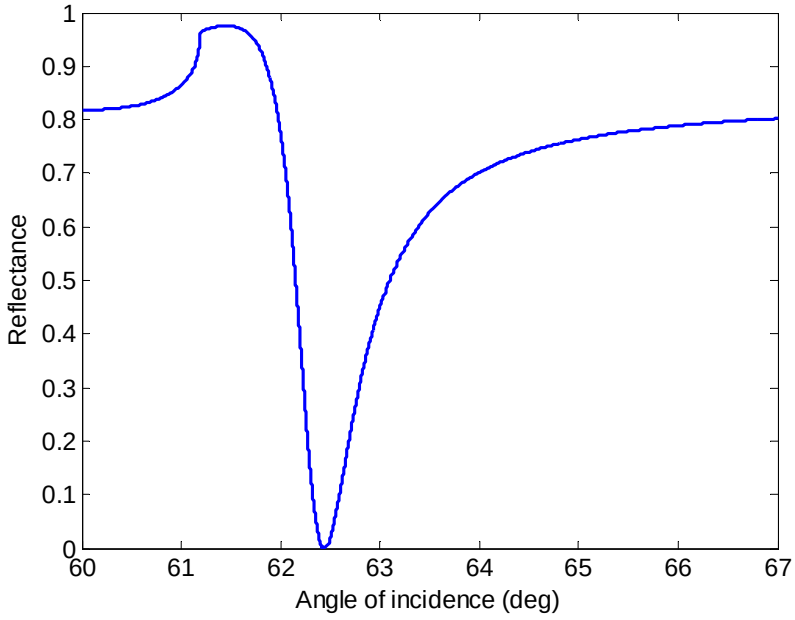

Figure 4.14 shows that the resonance linewidth at the wavelength of 1550 nm is about 0.8° while it is approximately 3.5° at the wavelength of 760 nm. This indicates that by choosing a longer operating wavelength, the linewidth of the surface plasmon resonance can be made narrower. This can be physically understood by recalling that the surface plasmon resonance linewidth is closely related to the propagation loss of the surface plasmons. As mentioned in Chapter 2, the propagation loss of surface plasmons is a result of ohmic damping in the metal which is reflected in its imaginary part of relative electric permittivity being non-zero. Looking at Figure 4.6 showing the imaginary part of relative electric permittivity as a function of wavelength, one readily notice that for gold, the

imaginary part of its relative electric permittivity is larger at the wavelength of 1550 nm compared to that at the wavelength of 760 nm. At first sight, this might seem to indicate that the surface plasmons at the wavelength of 1550 nm would suffer higher propagation loss. However, this is not so because the propagation loss, or equivalently the propagation length of surface plasmons is determined not only by the imaginary part of the metal, but also by its real part. As detailed in Chapter 2, the propagation length of surface plasmons scales roughly as $\left(\varepsilon_m'\right)^2 / \varepsilon_m''$. Looking at Figure 4.5 showing the real part of relative electric permittivity as a function of wavelength, one readily notice that for gold, the negative real part of its relative electric permittivity is much larger at the wavelength of 1550 nm compared to that at the wavelength of 760 nm. This more significant increase in magnitude of the real part of relative electric permittivity of gold effectively compensates for the increase in the imaginary part of its relative electric permittivity. As a result, the propagation length of the surface plasmons at the wavelength of 1550 nm is significantly longer than that at the wavelength of 760 nm. In other words, the propagation loss of the surface plasmons is considerably lower at the wavelength of 1550 nm. As a result, the surface plasmon resonance linewidth is narrower at the wavelength of 1550 nm compared to that at the wavelength of 760 nm.

Figure 4.15. Electric field intensity enhancement factor associated with the SPR curve of water with BK7 prism at the wavelength of 1550 nm and gold film thickness of 35 nm.

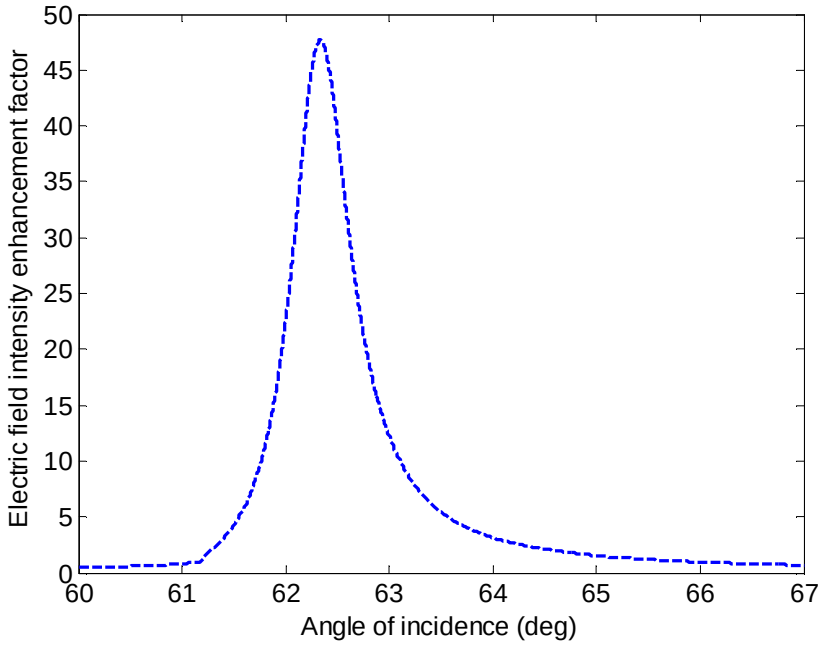

Figure 4.15 shows that the maximum electric field intensity enhancement factor at the angle of resonance is now around 48 while it is approximately 21 at the wavelength of 760 nm. This suggests that the electromagnetic field enhancement of surface plasmons can be increased by choosing a longer operating wavelength. This is the combined effect of the refractive index dispersion of the metal, the dielectric medium, and the prism.

Finally to complete the characterization of this SPR biosensor and compare its performance at the wavelength of 1550 nm to that at the wavelength of 760 nm, we now consider how the surface plasmons react to a change in refractive index of the sensed dielectric medium. Assuming a refractive index change of Δn = 0.005 RIU (refractive index unit), the resulting SPR curve of water is plotted in Figure 4.16.

Figure 4.16. SPR curves of water showing the resonance shift corresponding to a refractive index change of 0.005 RIU. The system is BK7 prism, 35 nm of gold, and water at the wavelength of 1550 nm.

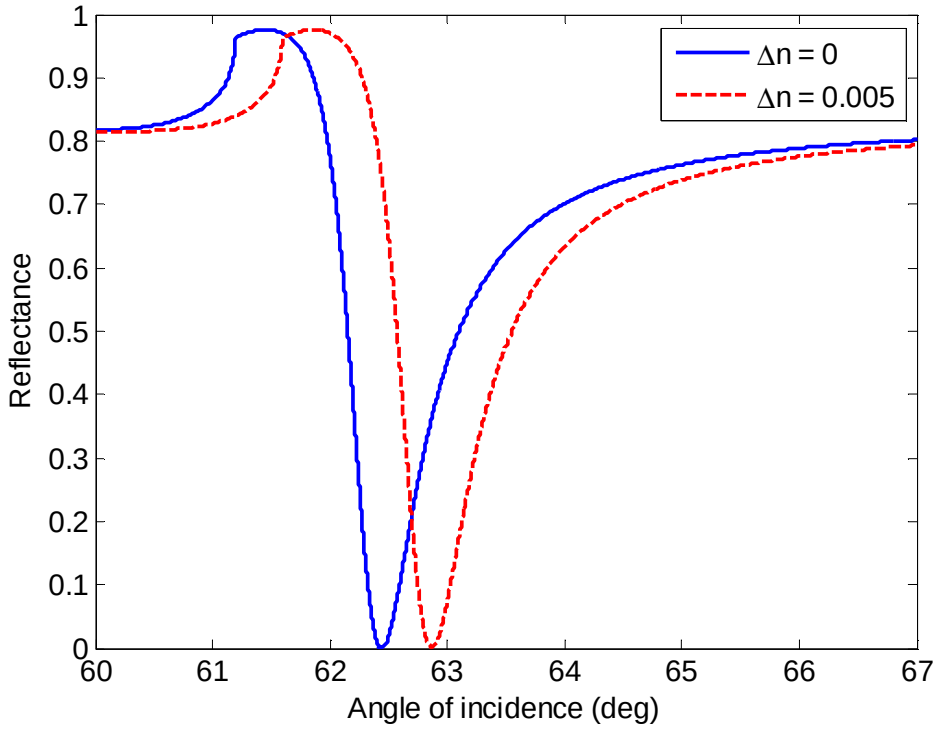

From the shift of the angle of resonance with the corresponding change in the refractive index of the sensed medium as shown in Figure 4.16, the refractive

index sensitivity is calculated to be about 85.8 °/RIU. This is roughly 74 % of the refractive index sensitivity obtained at the wavelength of 760 nm. The figure-of-merit at the wavelength of 1550 nm is however considerably increased to 107 compared to 33 at the wavelength of 760 nm. This is because the surface plasmon resonance linewidth is significantly narrower at the wavelength of 1550 nm. Therefore, the reduction in resonance linewidth effectively outweighs the decrease in angular sensitivity. In addition, the field penetration depth can also be determined to be around 25 nm in the gold film and 1250 nm in the sensed dielectric medium. The field penetration depth in the metal is practically unaltered when the operating wavelength is varied from 760 nm to 1550 nm. The field penetration depth in the dielectric is however multiplied by approximately five-fold. This means that the surface plasmons are able to probe deeper into the sensed dielectric medium.

Based on the preceding discussion, the influence of longer operating wavelength on the relevant characteristics of SPR biosensors for a given prism material, choice of metal, and sensed dielectric medium can now be summed up as follows. Firstly, the longer the operating wavelength, the narrower the surface plasmon resonance linewidth becomes. Secondly, the electromagnetic field enhancement of surface plasmons is stronger for longer operating wavelength. Thirdly, the field penetration depth in the metal is practically unchanged whereas the field penetration depth in the sensed dielectric medium is significantly increased, allowing a much deeper probe depth. Finally, as far as angular interrogation is concerned, although the angular sensitivity to refractive index variation of the sensed dielectric is decreased, the figure-of-merit of SPR biosensors is actually significantly increased by going into longer operating wavelength. Therefore, whether angular interrogation or intensity interrogation method is employed, the performance of SPR biosensors can be greatly improved by using longer operating wavelength [57].

4.3.4. Comparison of Angular and Wavelength Interrogation

As mentioned in Chapter 3, three interrogation methods, i.e., angular, wavelength, and intensity interrogation are the most commonly used detection mechanisms in SPR-based biosensors. The discussion so far has been focused on SPR biosensors using angular interrogation. Wavelength interrogation is investigated in this section along with a comparison to angular interrogation previously discussed.

To evaluate the influence of using wavelength interrogation, a model system consisting of BK7 prism, gold thin film, and water as the sensed dielectric, similar to the one considered in the preceding sections is chosen. The center operating wavelength of this SPR biosensor can be tuned by adjusting the thickness of the gold film as well as the angle of incidence.

Consider first the SPR biosensor whose centered operating wavelength is chosen to be 760 nm. In this system, the optimum thickness of the gold thin film is 50 nm as discussed previously. By evaluating the resonance dip in the spectral reflectivity spectrum for different values of angle of incidence, the optimum angle of incidence is found to be 68°. The resulting SPR curve at the fixed angle of incidence of 68° is plotted in Figure 4.17 from which the resonance linewidth can be seen to be approximately 120 nm.

Figure 4.17. SPR curves of water showing the resonance shift corresponding to a refractive index change of 0.005 RIU. The system is BK7 prism, 50 nm of gold, and water as the sensed dielectric medium. The angle of incidence is fixed at 68° so that the center operating wavelength is around 760 nm.

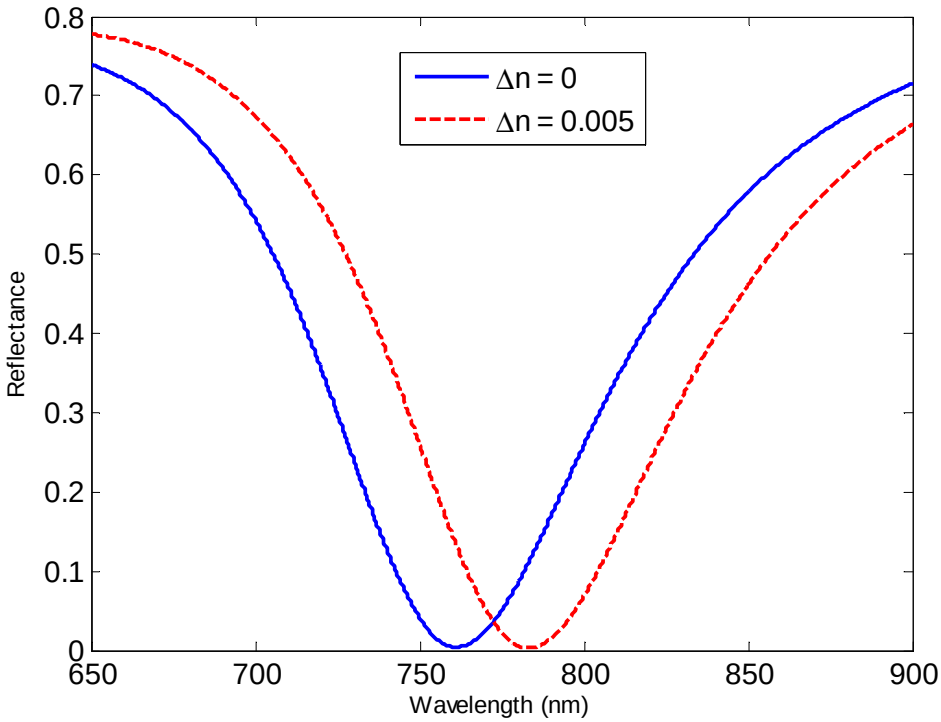

Figure 4.17 also shows the resonance shift corresponding to a refractive index change of Δn = 0.005 RIU. From Figure 4.17, the spectral sensitivity to refractive index variation of the dielectric medium is found to be 4400 nm/RIU. With surface plasmon resonance linewidth of about 120 nm, the figure-of-merit of this SPR biosensor can easily be calculated to be 37. This figure-of-merit is very close to 33, which is the figure-of-merit of the same SPR biosensor obtained using angular interrogation at the wavelength of 760 nm as shown in Figure 4.10.

Consider now the SPR biosensor whose centered operating wavelength is tuned to be 1550 nm. In this system, the optimum thickness of the gold thin film is 35 nm as discussed previously. By evaluating the resonance dip in the spectral reflectivity spectrum for different values of angle of incidence, the optimum angle of incidence is found to be 62.4°. The resulting SPR curve at the fixed angle of incidence of 62.4° is plotted in Figure 4.18 from which the resonance linewidth can be seen to be approximately 260 nm.

Figure 4.18. SPR curves of water showing the resonance shift corresponding to a refractive index change of 0.002 RIU. The system is BK7 prism, 35 nm of gold, and water as the sensed dielectric medium. The angle of incidence is fixed at 62.4° so that the center operating wavelength is around 1550 nm.

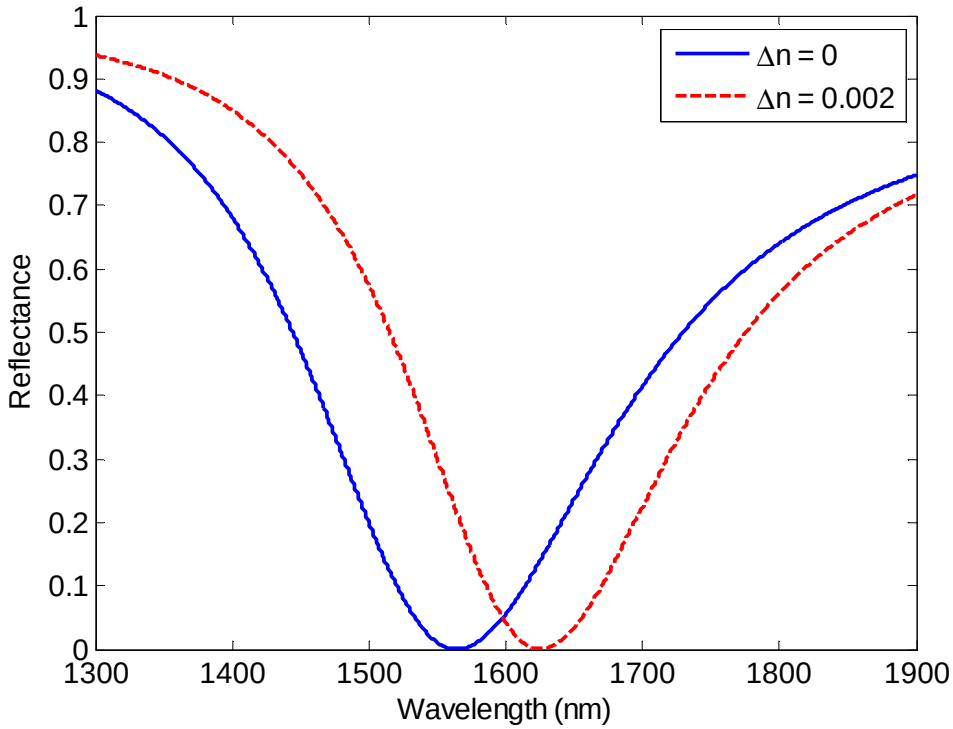

Figure 4.18 also shows the resonance shift corresponding to a refractive index change of Δn = 0.002 RIU. From Figure 4.18, the spectral sensitivity to refractive index variation of the dielectric medium is found to be 30500 nm/RIU. With surface plasmon resonance linewidth of about 260 nm, the figure-of-merit of this SPR biosensor can easily be calculated to be 117. This figure-of-merit is very close to 107, which is the figure-of-merit of the same SPR biosensor obtained using angular interrogation at the wavelength of 1550 nm as shown in Figure 4.16.

Comparing Figures 4.17 and 4.18, it can be noticed that in SPR biosensors using wavelength interrogation, the surface plasmon resonance linewidth is actually broader for the one whose center operating wavelength is 1550 nm. This is so because the dispersion of the optical properties of the metal is significantly increased by going from the visible to the infrared region.

Finally, based on the evaluated figures-of merit, it can be concluded that the performance of SPR biosensors using wavelength interrogation is very similar to those using angular interrogation.

4.3.5. Effects of Adhesion Layer

In practice, the adhesion of thin film of noble metals such as gold or silver to common optical glasses is not sufficiently strong. To overcome this problem, a thin metallic adhesion layer is deposited onto the glass substrate prior to the deposition of the noble metals. This adhesion layer binds strongly to the glass substrate and the subsequently deposited thin film of noble metals also adheres well to the adhesion layer. In this work, titanium thin film (typical thickness of around 2 nm) is chosen as the adhesion layer. Chromium thin film can also be used as an alternative to titanium adhesion layer.

To evaluate the effects of the adhesion layer on the performance of the resulting SPR biosensors, consider a model system consisting of BK7 prism, 2 nm titanium adhesion layer, 50 nm gold thin film, and water as the sensed dielectric medium at the wavelength of 760 nm. The calculated SPR curves of water showing the resonance shift corresponding to a refractive index change of Δn = 0.005 are plotted in Figure 4.19. The associated electromagnetic field enhancement factor of the surface plasmons is plotted in Figure 4.20.

It can be readily seen from Figure 4.19 that the surface plasmon resonance linewidth is approximately 3.5°. This value is identical to the resonance linewidth obtained from the same SPR system without the thin adhesion layer as shown in

Figure 4.10. In addition, the angle of resonance can also be seen to be practically unaltered. The refractive index sensitivity of the SPR system with the thin adhesion layer is found to be 116.6 °/RIU. For the same SPR system without the thin adhesion layer, the refractive index sensitivity has been previously calculated in Section 4.3.2 to be 116.3 °/RIU. The refractive index sensitivity is therefore practically identical with or without the thin adhesion layer. With identical resonance linewidth and refractive index sensitivity, the figure-of-merit is thus unchanged by the inclusion of the thin adhesion layer.

Figure 4.20 shows, by comparison with Figure 4.9, that the electromagnetic field enhancement of surface plasmons is not quite affected either by the inclusion of the thin adhesion layer.

Figure 4.19. SPR curves of water showing the resonance shift corresponding to a refractive index change of 0.005 RIU. The system is BK7 prism, 2 nm titanium adhesion layer, 50 nm of gold thin film, and water at the wavelength of 760 nm.

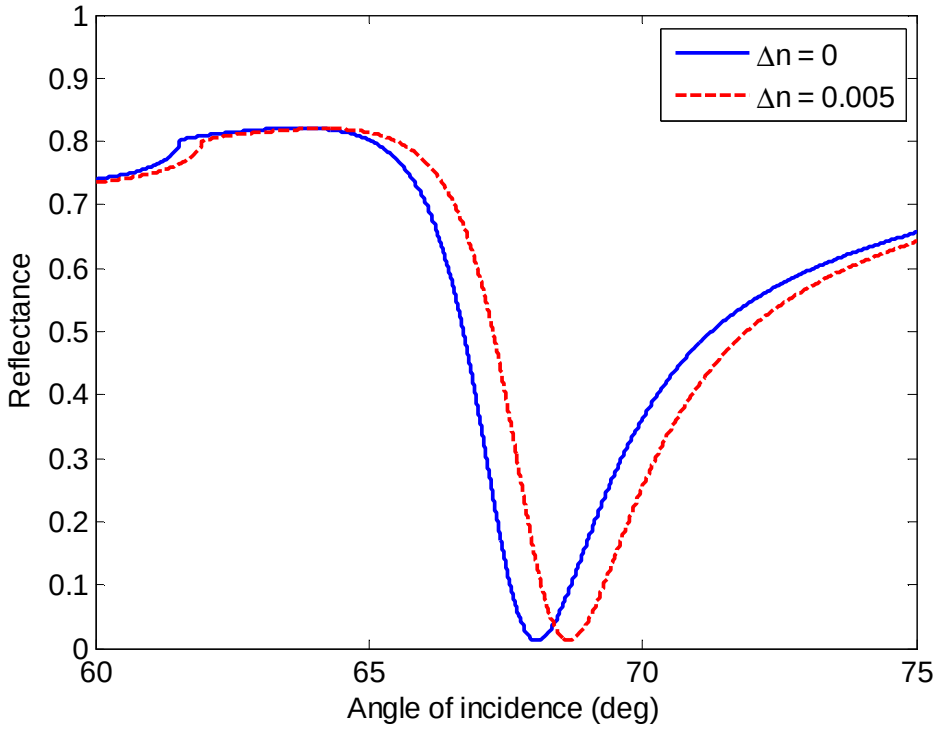

In conclusion, the inclusion of a thin titanium adhesion layer (typical thickness of 2 nm) has quite negligible effects on the performance of the resulting SPR

biosensors. This is so provided the thickness of the thin adhesion layer is kept below 5 nm.

As a note in passing, in contrast to silica-based optical glasses such as BK7 and H-ZF1, no adhesion layer is required on 2S2G substrate. The much better adhesion of gold thin film on 2S2G substrate is likely due to the creation of gold-sulfur bonds between the sulfur atoms present in the 2S2G glass and the gold atoms in the thin film.

Figure 4.20. Electric field intensity enhancement factor associated with the SPR curve of water with BK7 prism, 2 nm titanium adhesion layer, and 50 nm of gold thin film at the wavelength of 760 nm.

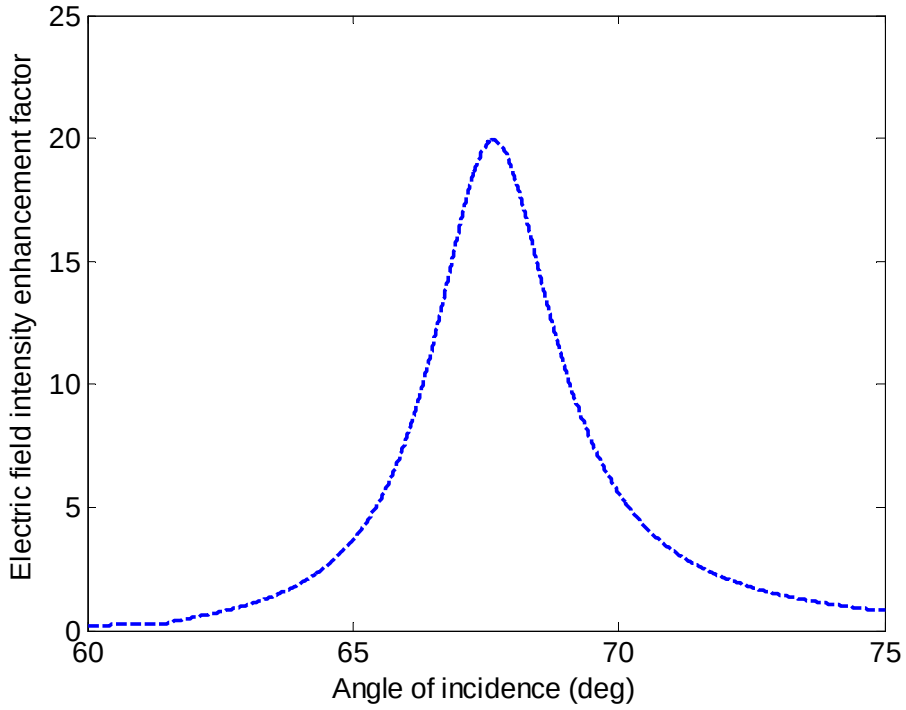

Chapter 5

Enhancement of Optical Sensitivity

This chapter deals with the enhancement of the optical sensitivity components of SPR biosensors using conventional Kretschmann geometry. The key advantage of the methods detailed in this chapter is the fact that the existing SPR sensor instrumentation either only needs minute adjustments or no modification at all.

5.1. Use of Bimetallic Structure

It has been briefly mentioned in Chapter 4 that the best metals for SPR-based biosensing applications are silver and gold. Although the resonance linewidth of silver is narrower than that of gold leading to higher figure-of-merit, silver is not commonly used in SPR biosensors because of its vulnerability to oxidation. Gold, which is much more chemically resistant to oxidation than silver, is therefore the chosen one.

There is in fact a very simple trick to make use of a combination of both silver for its narrow resonance linewidth and gold for its chemical resistance to oxidation. The idea developed here consists in using a thin layer of gold film on top of a thicker silver film. The thin layer of gold film serves mainly as a protection barrier to oxidation for the silver film underneath. It also plays the role of metallic interface to the sensed medium on which well-known surface functionalization can be applied (Chapter 6). The properties of the surface plasmons of this bimetallic structure are determined mostly by the much thicker silver layer [58]. This way, one can simultaneously take advantage of the narrow resonance linewidth of silver and the chemical stability of gold.

Figure 5.1 shows the calculated SPR curves of water on silver (50 nm thick), bimetallic silver/gold (45 nm silver and 5 nm gold on top), and gold (50 nm thick) films. The prism material here is BK7 glass and the wavelength is 680 nm. As can be seen from Figure 5.1, the theoretical surface plasmon resonance linewidth is 2.0° for the simple silver film, 2.5° for the bimetallic silver/gold film, and 6.0° for the simple gold film. The resonance linewidth obtained from the bimetallic silver/gold structure is quite close to that of the simple silver film which is three times narrower than that of the simple gold film.

Figure 5.1. Theoretical comparison of resonance linewidth between silver, bimetallic silver/gold, and gold SPR sensor surfaces at the wavelength of 680 nm.

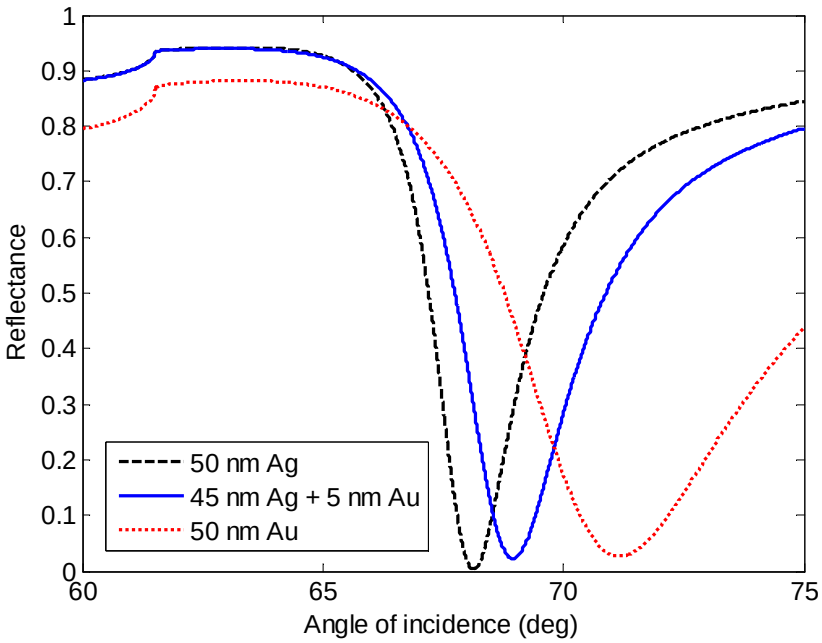

Figure 5.2. Experimental comparison of resonance linewidth between silver, bimetallic silver/gold, and gold SPR sensor surfaces at the wavelength of 680 nm.

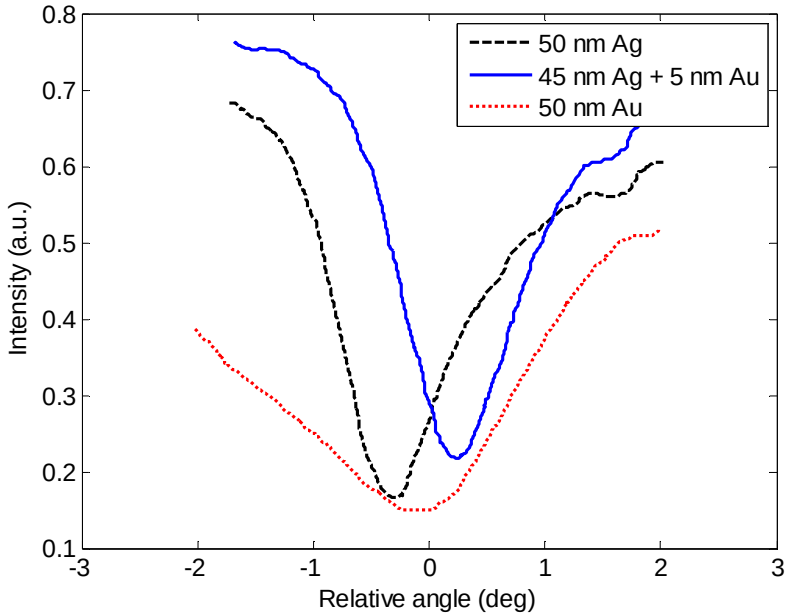

Figure 5.2 shows the experimental SPR curves of water on silver (50 nm thick), bimetallic silver/gold (45 nm silver and 5 nm gold on top), and gold (50 nm thick) films measured with Autolab SPR instrument. The prism material here is BK7 glass and the wavelength is 680 nm. Comparing Figures 5.1 and 5.2, it can be seen that the obtained experimental resonance linewidths are quite consistent with the theoretical calculation.

In Chapter 4, it has been mentioned that shifting the operating wavelength of SPR biosensors towards longer wavelength results in narrower resonance. The case that is made in Chapter 4 is a comparison between 760 nm and 1550 nm as operating wavelengths where it is theoretically shown that by approximately doubling the operating wavelength from 760 nm to 1550 nm, the surface plasmon resonance linewidth can be made about four times narrower. In fact, such an effect depends on the specific wavelength. For example, increasing the operating wavelength by only 80 nm from 680 nm to 760 nm can have quite a significant impact on the resulting resonance linewidth.

Figure 5.3 shows the calculated SPR curves of water on silver (50 nm thick), bimetallic silver/gold (45 nm silver and 5 nm gold on top), and gold (50 nm thick) films. The prism material here is BK7 glass and the wavelength is 760 nm. As can be seen from Figure 5.1, the theoretical surface plasmon resonance linewidth is 1.8° for the simple silver film, 2.0° for the bimetallic silver/gold film, and 3.5° for the simple gold film. Comparing Figures 5.3 and 5.1, it can be seen that increasing the operating wavelength from 680 nm to 760 nm results in narrower resonance linewidths for all three structures. The reduction in resonance linewidth for the simple silver film and consequently, the bimetallic film is not really that remarkable. The decrease in resonance linewidth for the simple gold film is however very significant by a factor of almost two. In addition, the difference in resonance linewidth between silver and gold at the wavelength of 760 nm is not as dramatic as it is at 680 nm.

Figure 5.4 shows the experimental SPR curves of water on bimetallic silver/gold (45 nm silver and 5 nm gold on top), and gold (50 nm thick) films on BK7 glass substrate measured with the in-house SPR setup operating at the wavelength of 760 nm. From Figure 5.4, the experimentally obtained resonance linewidth is 3.27° for the simple gold film. For the bimetallic silver/gold structure, it is 1.87°. Comparing Figures 5.3 and 5.4, it can be seen that the obtained experimental resonance linewidths are quite consistent with the theoretical calculation.

Figure 5.3. Theoretical comparison of resonance linewidth between silver, bimetallic silver/gold, and gold SPR sensor surfaces at the wavelength of 760 nm.

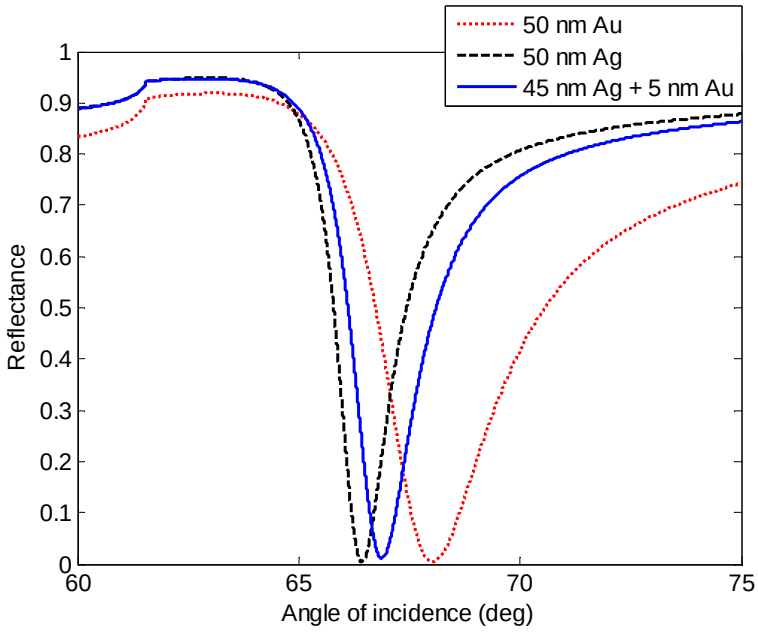

Figure 5.4. Experimental comparison of resonance linewidth between bimetallic silver/gold and gold SPR sensor surfaces at the wavelength of 760 nm.

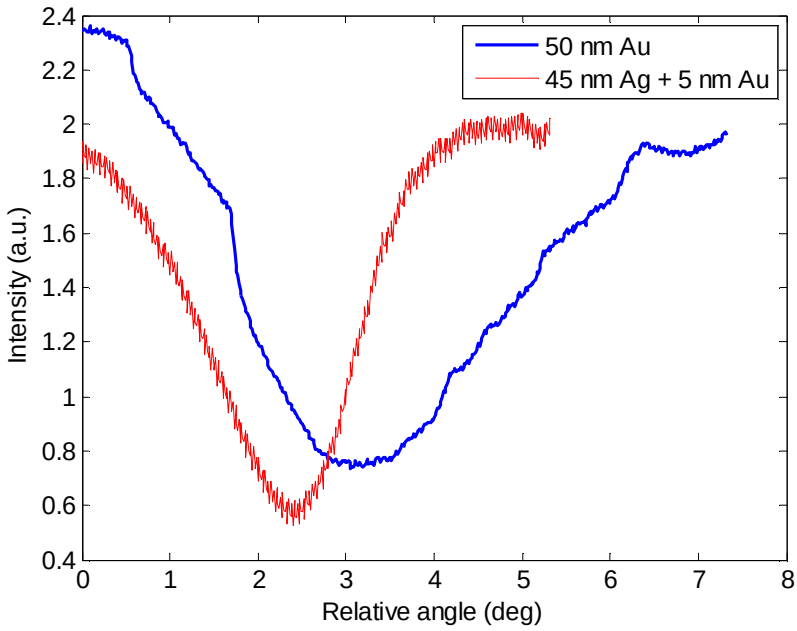

The effects of the narrower resonance linewidth on the optical sensitivity are discussed in more detail in the following section.

5.2. SPR in the Near-Infrared

The concept of bimetallic film introduced in the preceding section for operating wavelengths in the visible is now extended to the near-infrared region at the wavelength of 1550 nm. This choice of the operating wavelength is motivated by two reasons. The first one is the narrower SPR linewidth in the near-infrared region compared to that in the visible. Specific telecommunications wavelength at 1550 nm is particularly attractive as the required optical technology (laser source, camera system, etc) is already well-developed. The second one is the longer field penetration in the near-infrared. As a matter of fact, the field penetration depth is about 1300 nm at the wavelength of 1550 nm while it is only about 250-300 nm in the visible. Longer field penetration is especially desirable for biosensing applications involving large biomolecular objects such as bacteria and viruses.

Figure 5.5. Theoretical SPR curves of water showing a comparison of resonance linewidth between silver, bimetallic silver/gold, and gold SPR surfaces at the wavelength of 1550 nm.

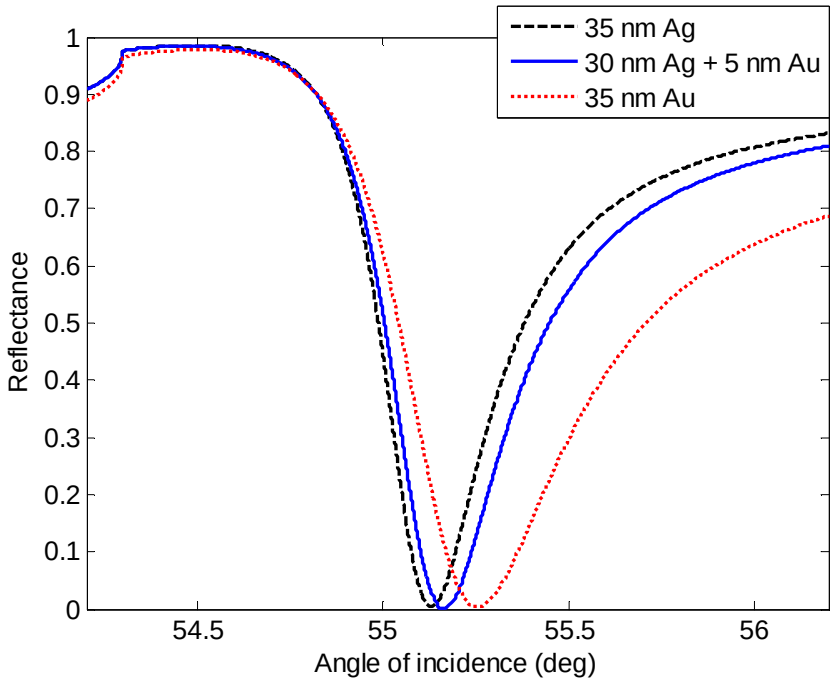

At the wavelength of 1550 nm, the resonance dip of the SPR curve of water is sharpest when the total thickness of the gold or silver film is 35 nm. Based on this optimum thickness, the bimetallic thin film considered this time consists of 30 nm of silver and 5 nm of gold on top. Figure 5.5 shows the calculated SPR curves of water on silver (35 nm thick), bimetallic silver/gold (30 nm silver and 5 nm gold on top), and gold (35 nm thick) films at the wavelength of 1550 nm. The prism material here is H-ZF1 glass whose refractive index is 1.6192 at this chosen wavelength. It can be seen from Figure 5.5 that the resonance linewidth of the bimetallic silver/gold film is very close to that of simple silver film. The SPR linewidth is therefore mainly dominated by the silver film chemically protected by the thin gold overlayer.

To clearly showcase the narrower resonance offered by the bimetallic silver/gold film, the detection of the SPR sensor is this time based on intensity interrogation method. In this technique, the variation of the intensity of the reflected light normalized to that of the incident light, i.e., the reflectance at a fixed angle of incidence is monitored. The reflectivity variation following a change in the refractive index of the sensed dielectric medium can be mathematically expressed as

$$\frac{\partial R}{\partial n} = \frac{\partial R}{\partial \theta}\frac{\partial \theta}{\partial n} \tag{5.1}$$

where R is the reflectance, θ is the angle of incidence at resonance, and n is the refractive index of the sensed dielectric medium.

The second factor on the right-hand side of Equation (5.1), namely $\partial\theta/\partial n$ is simply the angular sensitivity to refractive index variation. It quantifies the shift of the SPR angle when the refractive index of the sensed dielectric medium changes. As will be shown below, the angular sensitivity of the simple gold film is in fact very similar to that of the bimetallic silver/gold structure.

The first factor on the right-hand side of Equation (5.1), namely $\partial R/\partial\theta$ is the slope of the SPR curve near resonance. The steeper the SPR curve near resonance, the higher this $\partial R/\partial\theta$ factor. As can be seen from Figure 5.5, between the simple gold film and the bimetallic silver/gold structure, the slope of the SPR curve is steeper for the bimetallic film. As the angular sensitivity is very similar between the two types of sensor chip, the difference in reflectivity variation following a change in the refractive index of the sensed dielectric medium $\partial R/\partial n$ is mainly determined by the steepness of the SPR in the reflectivity profile.

Figure 5.6. Theoretical SPR curves of water showing the resonance shift corresponding to a refractive index change of 0.001 RIU. The system is H-ZF1 prism, 35 nm of gold, and water at the wavelength of 1550 nm.

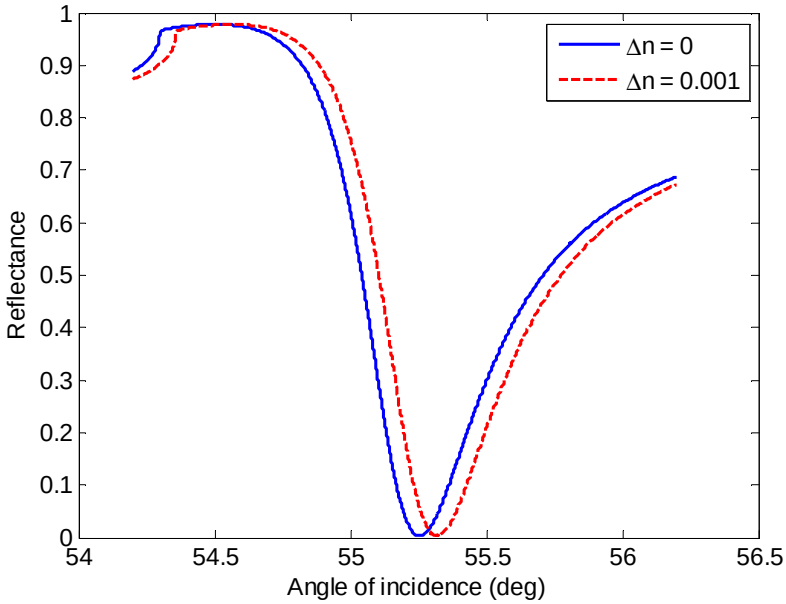

Figure 5.7. Electric field intensity enhancement factor associated with the SPR curve of water with H-ZF1 prism at the wavelength of 1550 nm and gold film thickness of 35 nm.

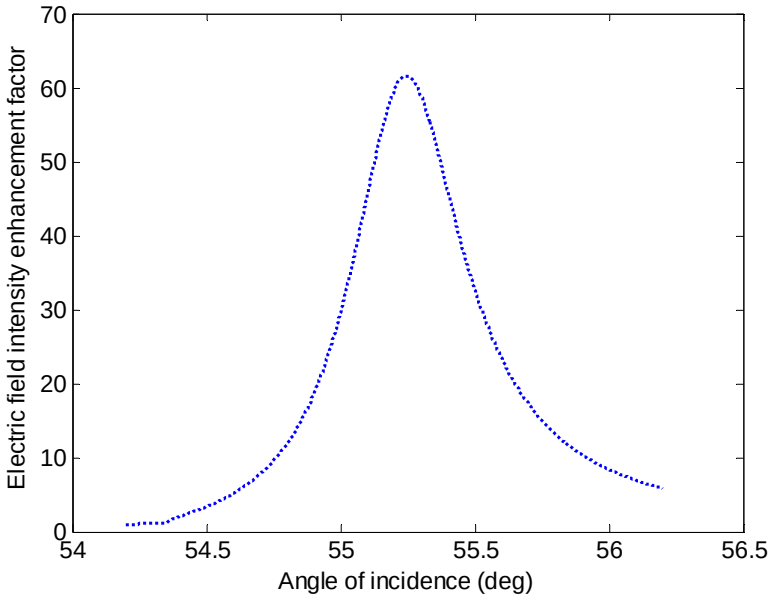

Figure 5.6 shows the calculated resonance shift of the SPR curves of water on the simple gold SPR film following a refractive index variation of 0.001 RIU. Figure 5.7 shows the associated electric field intensity enhancement factor from which the maximum electric field intensity enhancement factor for this simple gold SPR structure can be seen to be about 60. The penetration depth into the dielectric can also be calculated to be around 1250 nm.

From Figure 5.6, the angular sensitivity to refractive index variation can be evaluated to be 64.3 °/RIU. The resonance linewidth is around 0.5° which results in a figure-of-merit of 130. The reflectivity variation monitored at a fixed angle of incidence of 55.15° following a change in the refractive index of the sensed medium is calculated to be 1.7 x 10^4 %/RIU.

Figure 5.8. Theoretical SPR curves of water showing the resonance shift corresponding to a refractive index variation of 0.001 RIU. The system is H-ZF1 prism, 30 nm of silver, 5 nm of gold, and water at the wavelength of 1550 nm.

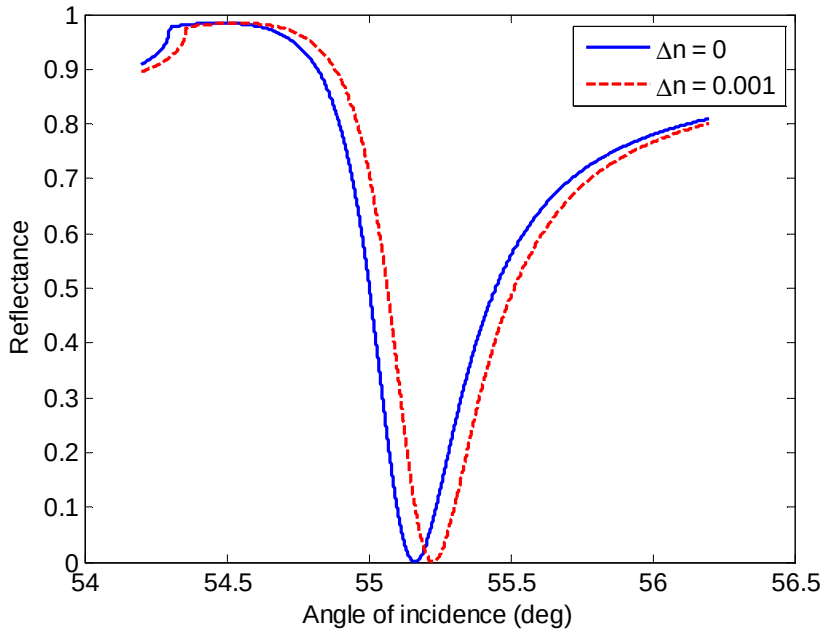

Figure 5.8 shows the calculated resonance shift of the SPR curves of water on the bimetallic silver/gold SPR structure following a refractive index variation of 0.001 RIU. Figure 5.9 shows the associated electric field intensity enhancement factor from which the maximum electric field intensity enhancement factor for

this bimetallic silver/gold SPR chip can be seen to be almost 90. This maximum field enhancement factor is 1.5 times stronger than that of the simple gold SPR film. The penetration depth into the dielectric is now found to be around 1300 nm which is very close to that of the simple gold SPR structure.

Figure 5.9. Electric field intensity enhancement factor associated with the SPR curve of water with H-ZF1 prism and the bimetallic (30 nm of silver and 5 nm of gold) film at the wavelength of 1550 nm.

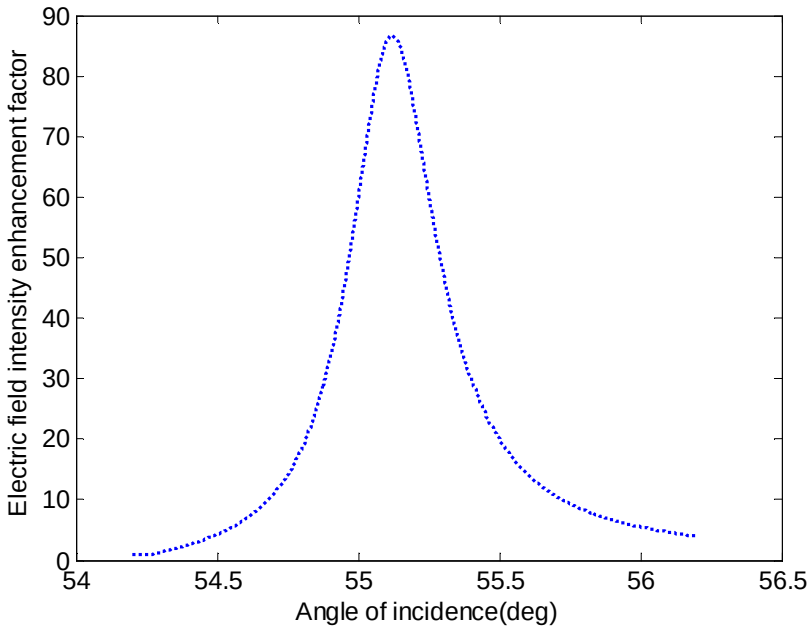

From Figure 5.8, the angular sensitivity to refractive index variation can be evaluated to be 64.0 °/RIU. This is practically the same as that obtained from the simple gold SPR structure. The resonance linewidth around 0.4° is however narrower which results in a slightly higher figure-of-merit of 160. The reflectivity variation monitored at a fixed angle of incidence of 55.15° following a change in the refractive index of the sensed medium is calculated to be 2.5 x 10^4 %/RIU. This is higher by a factor of about 1.5 than the value obtained from the simple gold SPR structure. Therefore, while the sensitivity of the bimetallic silver/gold SPR structure is quite comparable to that of the simple gold film when angular interrogation method is used, it is expected to be higher when intensity interrogation method is employed for the detection of refractive index variation.

Figure 5.10 (a) shows the sensorgram corresponding to experimentally measured reflectivity variation from the bimetallic silver/gold SPR surface following the injection of sucrose solution with different concentrations (0.025 %,

0.05 %, 0.1 %, 0.2 %, 0.4 %, 0.6 %, 0.8 % and 1 %) for three to five minutes each. Demonized water is injected between two successive injections of these sucrose solutions. Based on the standard deviation of each obtained plateau, the average noise level in the reflectivity measurement is evaluated to be 0.047 %. In Figure 5.10 (b), the measured reflectivity variation is normalized to the average noise level showing the signal-to-noise ratio.

Figure 5.10. (a) Measured reflectivity variation from the bimetallic silver/gold SPR surface due to the injection of sucrose solution with different concentrations (0.025 %, 0.05 %, 0.1 %, 0.2 %, 0.4 %, 0.6 %, 0.8 % and 1 %). The inset shows the noise characteristic in the measured reflectivity. Based on the standard deviation, the average noise level is 0.047 %. **(b)** The measured reflectivity normalized to the average noise level showing the signal-to-noise ratio.

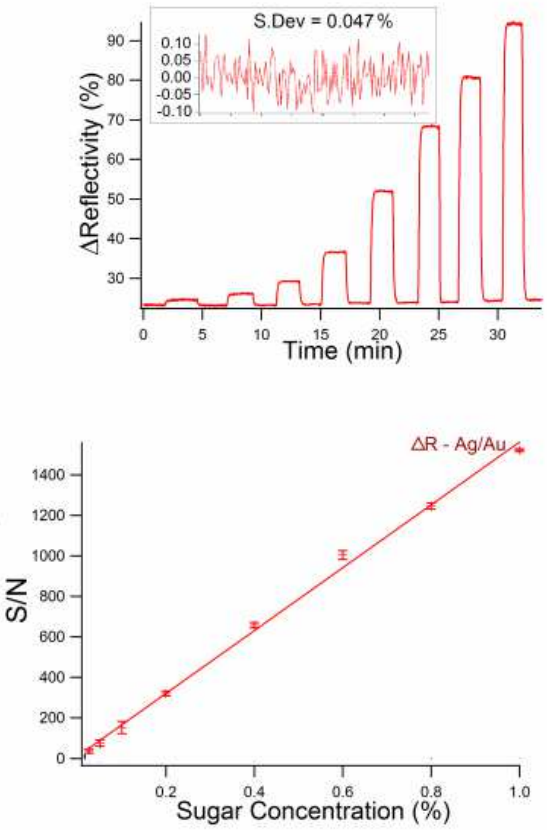

For comparison, the same experiment with various concentrations of sucrose solution is also performed with the simple gold SPR chip. Figure 5.11 shows the measured reflectivity variation from the simple gold SPR surface following the

injection of the same sucrose solutions. The average noise level in this case is 0.048 % and the measured reflectivity variation is also normalized to the average noise level showing the signal-to-noise ratio.

Figure 5.11. The measured reflectivity variation from the simple gold SPR surface due to the injection of sucrose solution with different concentrations normalized to the average noise level showing the signal-to-noise ratio.

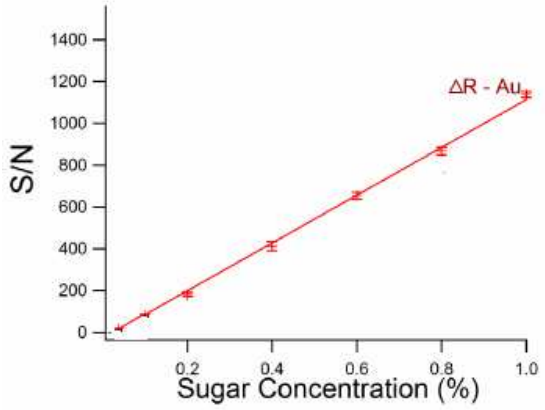

A change of 0.5 % in sucrose concentration modifies the refractive index of the solution by 7×10^{-4} RIU. An increment of 0.025 % in sucrose concentration will thus increase the refractive index by a linear variation of 3.5×10^{-5} RIU. The signal-to-noise ratio corresponding to 1 % sucrose is 1142 for the simple gold SPR chip and 1550 for the bimetallic silver/gold structure. The refractive index sensitivity of the bimetallic silver/gold structure is therefore around 1.36 times higher than that of the simple gold SPR chip. Based on a conservative signal-to-noise ratio of 3, the best limit of detection is estimated to be 3.6×10^{-6} RIU for the simple gold sensor chip. With its higher refractive index sensitivity, the bimetallic silver/gold SPR structure is capable of detecting a slightly lower refractive index variation of 2.7×10^{-6} RIU.

5.3. Long-Range Surface Plasmons

The essential physical concept of long-range surface plasmons has been discussed in Chapter 2. In this section, the theoretical aspects of long-range surface plasmons for biosensing are first explored. The sensor fabrication is subsequently detailed. Finally the obtained experimental results are presented.

5.3.1. Theoretical Analysis

Commonly used SPR structure consists simply of gold thin film on glass substrate as schematically illustrated in Figure 5.12 (a). In this chapter, such simple gold SPR film on glass substrate is referred to as the classical SPR. Figure 5.12 (b) shows a schematic illustration of the long-range surface plasmons sensor chip. As discussed in Chapter 2, long-range surface plasmons require that the gold thin film is sandwiched between two media having similar refractive index. For biosensing applications in aqueous environment, a layer of material whose refractive index is very close to that of water, referred to as the buffer layer which is typically a polymer with low refractive index, must be deposited between the gold thin film and the glass substrate. Together with the sensed aqueous solution as superstrate, this buffer layer creates the necessary symmetric dielectric environment around the sandwiched gold layer in order to support the long-range surface plasmons mode.

Figure 5.12. (a) Schematic illustration of the simple gold SPR sensor chip (classical SPR). **(b)** Schematic illustration of the long-range surface plasmons sensor chip.

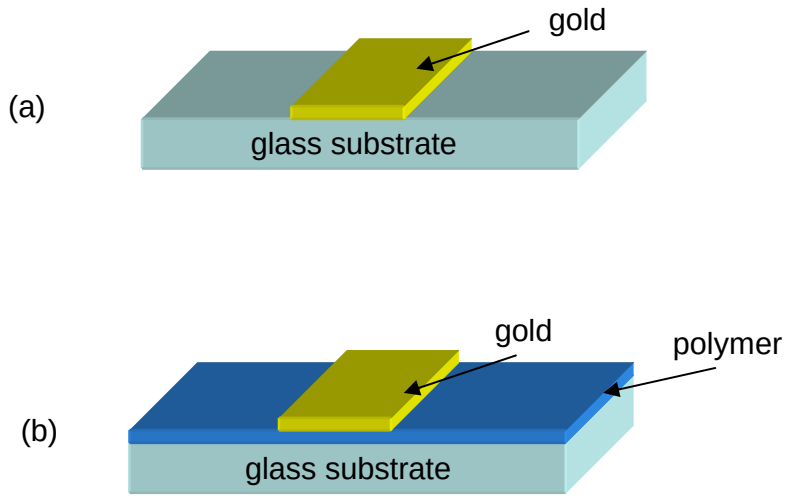

Consider a long-range surface plasmons sensor chip operating at the wavelength of 760 nm in aqueous environment. The refractive index of water at this wavelength is 1.3288 which is to be approximately matched by the buffer layer. This low refractive index requirement in the vicinity of 1.32-1.33 around the red end of the visible electromagnetic spectrum does not leave one with many choices for the buffer layer. In fact, the refractive index of commonly used

dielectric materials in optics is higher than 1.40. However, a certain class of optically transparent amorphous fluoropolymer has this sought-after property. In this work, the chosen material for the buffer layer is an amorphous fluoropolymer known by its commercial name MY-133MC. As detailed in the next section, the refractive index of the buffer layer obtained from this polymer is determined to be 1.320 at the wavelength of 760 nm.

For a given refractive index, there is an optimum thickness of the buffer layer that yields the sharpest plasmonic resonance. In fact, if the buffer layer is too thick, the evanescent field from the total internal refraction at the prism base cannot reach the gold interface to excite surface plasmons. At the other extreme, if the buffer layer is too thin, the surface plasmons do not quite sense the presence of the buffer layer. In the limit of zero thickness, one simply recovers the classical SPR structure.

Figure 5.13. Theoretical SPR curves of water on classical SPR sensor chip (solid red curve) and long-range surface plasmons structure (dotted blue curve) at the wavelength of 760 nm. The refractive index of the buffer layer is taken as 1.320 and its thickness is 1285 nm. The gold layer is 20 nm thick and the substrate is BK7 glass.

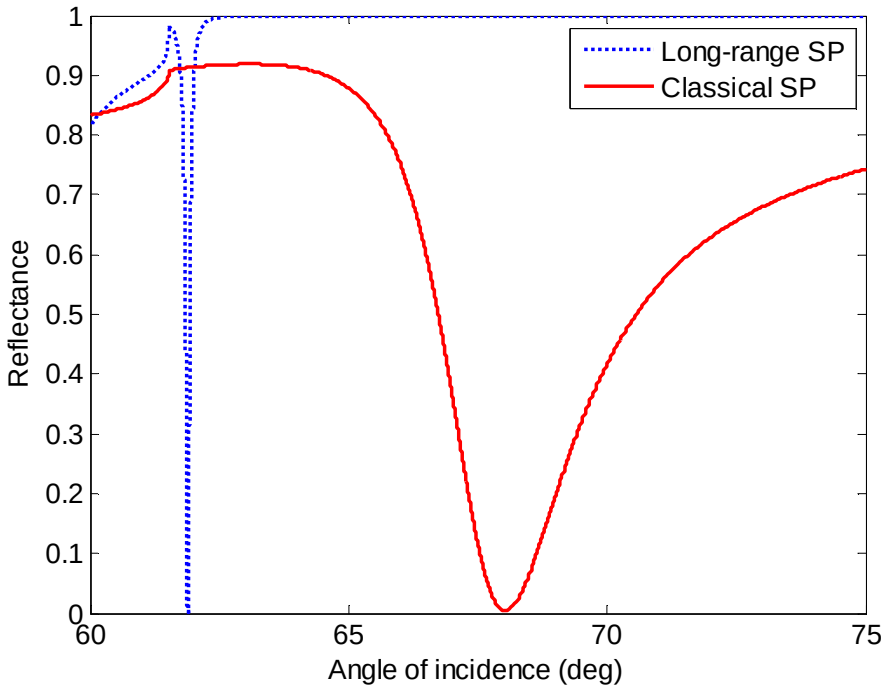

The special interest in long-range surface plasmons for biosensing applications is sparked, among others, by its extremely narrow plasmonic resonance. The dotted blue curve in Figure 5.13 shows the theoretical SPR curve of water on a long-range surface plasmons sensor chip at the wavelength of 760 nm. The thickness of the gold layer is 20 nm and the substrate is BK7 glass. The refractive index of the buffer layer is taken as 1.320 and its optimum thickness can be evaluated to be around 1250-1300 nm. The very narrow plasmonic resonance linewidth obtained from this structure is around 0.08°. For comparison, the solid red curve in Figure 5.13 shows the theoretical SPR curve of water on a classical SPR sensor chip (50 nm gold layer on BK7 glass substrate) at the wavelength of 760 nm. The significantly wider resonance linewidth of this classical SPR structure is about 3.5°. The two curves in Figure 5.13 clearly show the dramatic reduction by a factor of approximately 40 in the plasmonic resonance linewidth by using long-range surface plasmons structure instead of classical SPR.

Figure 5.14. Theoretical SPR curves of water on long-range surface plasmons structure showing the shift of plasmonic resonance at the wavelength of 760 nm when the refractive index is varied by 0.003 RIU. The refractive index of the buffer layer is taken as 1.320 and its thickness is 1285 nm. The gold layer is 20 nm thick and the substrate is BK7 glass.

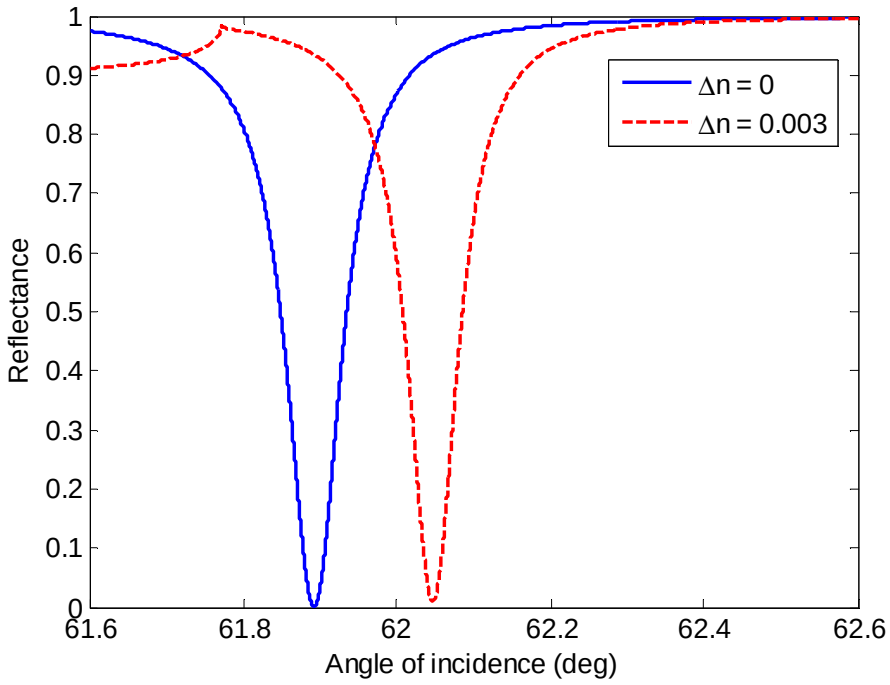

Figure 5.14 shows the theoretical shift of the plasmonic resonance of this particular long-range surface plasmons structure when the refractive index of the sensed dielectric medium is increased by 0.003 RIU. Based on the angular shift of the reflectivity minimum, the refractive index sensitivity of this long-range surface plasmons structure can be evaluated to be 52 °/RIU. With an extremely narrow resonance linewidth of only 0.08°, the theoretical figure-of-merit of this sensor chip is easily calculated to be as high as 650. This figure-of-merit is about 20 times that obtained from the classical SPR structure.

Figure 5.15 shows the electric field intensity enhancement factor associated with the SPR curve of water on the long-range surface plasmons structure at the wavelength of 760 nm. The maximum field enhancement factor in this case is almost 140. This is about seven times stronger than that of the classical SPR structure. Lastly, the field penetration depth into the dielectric of this long-range surface plasmons structure can be calculated to be around 1100 nm. This is about four times that obtained from the classical SPR chip. The long-range surface plasmons structure can therefore probe the sensed dielectric medium four times deeper.

Figure 5.15. Electric field intensity enhancement factor associated with the SPR curve of water on the long-range surface plasmons structure at the wavelength of 760 nm.

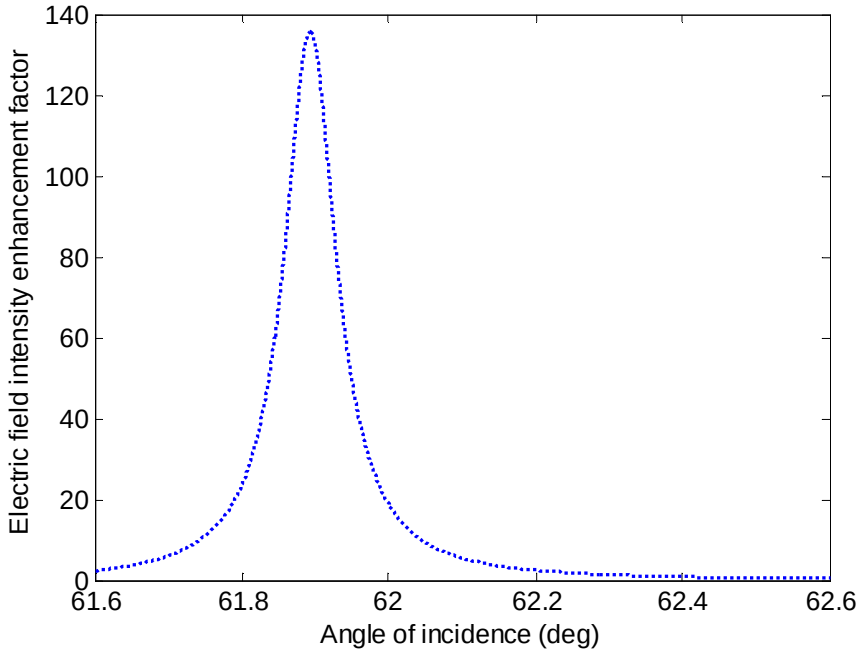

5.3.2. Sensor Fabrication

In this work, microscope glass slides cleaned with piranha solution (2:1 mixture of sulfuric acid and hydrogen peroxide) are used as substrates. Spin coating method is then used to deposit the required polymeric buffer layer on the pre-cleaned BK7 glass substrate. For the spin coating process, the sample is initially spun at 500 rpm for 10 seconds with an acceleration of 300 rpm/s immediately followed by spinning at 1200 rpm for 30 seconds with the same acceleration of 300 rpm/s. The initial spinning at low speed is especially useful to better spread high-viscosity liquid on the substrate before the desired final spinning speed is applied. This is expected to result in a more uniform film. After spin coating, the sample is placed on a hot plate maintained at 90 °C for 30 minutes to evaporate the solvent. The temperature of the hot plate is then raised to 120 °C and the sample is baked at this temperature for an hour. The obtained polymeric film is subsequently characterized by prism coupling measurements. In this work, Metricon prism coupler system is used to simultaneously measure the refractive index and the thickness of the polymer film by prism coupling technique.

Prism coupling measurement, schematically illustrated in Figure 5.16, is a well-adapted method for the determination of refractive index and thickness of a dielectric thin film [59, 60]. In this method, the film to be measured forms the core of a waveguide and the angle of incidence of a laser beam onto the prism base is varied until phase matching condition between the incident laser beam and the guided modes is satisfied so that strong coupling of light into the waveguide occurs. From the measured angles of strongest coupling, the modal indices of the waveguide are experimentally determined from which the refractive index and thickness of the film can then be derived.

Figure 5.16. Illustration of prism coupling measurement [59].

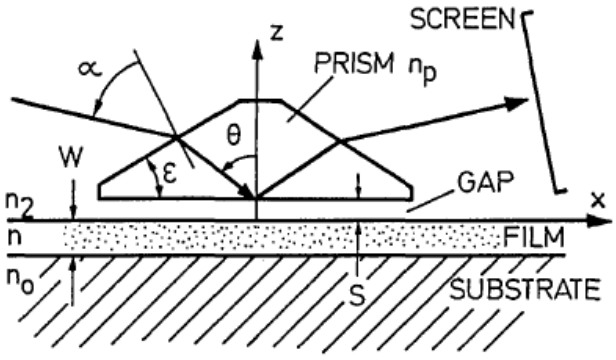

The modal index of the waveguide N is experimentally determined from the angle of strongest coupling θ from

$$N = n_p \sin\theta = n_p \sin\left[\varepsilon + \sin^{-1}\left(\frac{\sin\alpha}{n_p}\right)\right] \tag{5.2}$$

where n_p is the refractive index of the prism, coupling θ is the angle of incidence onto the prism base, ε is the angle of the prism base, and α is the exterior angle of incidence on the entrance face of the prism.

In a typical prism coupling measurement, there are in general several guided modes. The observed modal indices N_m of the film, identified by their mode numbers m = 0, 1, 2, …, are related to the unknown refractive index n and thickness W of the film by the dispersion equation of a planar dielectric waveguide which can be written as

$$k_0 W\left(n^2 - {N_m}^2\right)^{1/2} = \Psi_m\left(n, N_m\right) \tag{5.3}$$

where k_0 is the wave number in free space and

$$\Psi_m\left(n, N_m\right) = m\pi + \phi_0\left(n, N_m\right) + \phi_2\left(n, N_m\right) \tag{5.4}$$

$$\phi_i\left(n, N_m\right) = \tan^{-1}\left[\left(\frac{n}{n_i}\right)^{2\rho}\left(\frac{{N_m}^2 - n_i^2}{n^2 - {N_m}^2}\right)\right]^{1/2} \tag{5.5}$$

with the subscript i taking on the values 0 or 2. The value of ρ in Equation (5.5) depends on the polarization where ρ = 0 for TE polarization and ρ = 1 for TM polarization.

The physical meaning of Equations (5.3)-(5.5) can be easily understood by considering a guided light propagating in a planar film of refractive index n and thickness W on a substrate of refractive index n_0 with a cladding layer of refractive index n_2 as illustrated in Figure 5.17. According to ray optics approach, the guided ray propagates following a zigzag path along the waveguide where it undergoes total internal reflection at each interface. For a guided mode to be supported, the total phase shift experienced by the ray in one complete zigzag cycle (e.g., from point “a” to point “b”) must be an integral multiple of 2π. This total phase shift comes from three sources: the phase shift acquired by the ray as it

traverses the film twice (once in the upward direction and once in the downward direction) given by the quantity $2k_0W\left(n^2 - N_m{}^2\right)^{1/2}$, the phase shift due to total internal reflection at the lower film-substrate interface given by $-2\phi_0$, and the phase shift due to total internal reflection at the upper film-cladding interface given by $-2\phi_2$.

Figure 5.17. Illustration of ray tracing in a planar slab waveguide.

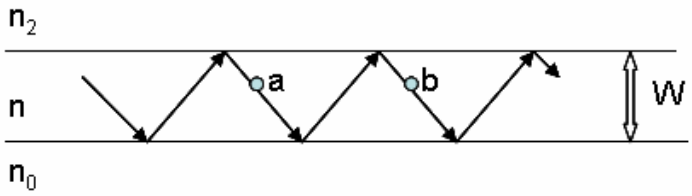

From any two modes of the same polarization indexed by μ and υ, the experimentally obtained modal indices N_μ and N_υ can be inserted into Equations (5.3)-(5.5) to yield two equations from which *W* can be eliminated. The resulting single equation for *n* can be expressed in the form

$$n^2 = F\left(n^2\right) \tag{5.6}$$

where the function $F\left(n^2\right)$ is given by

$$F\left(n^2\right) = \frac{N_\mu{}^2\Psi_\nu{}^2 - N_\nu{}^2\Psi_\mu{}^2}{\Psi_\nu{}^2 - \Psi_\mu{}^2} \tag{5.7}$$

Equation (5.6) can be numerically solved to give the refractive index *n* of the film. Once the refractive index *n* is known, the thickness *W* of the film can then be easily obtained from Equation (5.3).

The key advantage of the prism coupler method for thin film characterization is its ability to simultaneously determine the refractive index and the thickness of the film. It is important that for the thickness and refractive index of the film to be completely determined, at least two guided modes are required. If the film is sufficiently thick to allow the observation of more than two modes, the method is self-consistent because the two unknowns (*n* and *W*) are then determined from more than two independent measurements. This improves the accuracy and greatly increases the confidence in the method. Moreover, the prism coupler measurement is relatively simple and fast. In addition, the precision and accuracy

of the prism coupler technique has been shown to be similar to other common methods for measuring the thickness and refractive index of dielectric films such as reflectance spectroscopy, ellipsometry, and mechanical measurement of step height [61].

The most important limitation of the prism coupling technique is the restriction on the film thickness that can be measured. Films less than about 0.2 μm thick are generally too thin to support guided modes and prism coupling measurements are thus not possible. For film thicknesses between approximately 0.2 μm and 0.5 μm, only one guided mode exists. In this case, the refractive index can be determined only if the thickness is known and vice versa. Therefore, either the refractive index or the film thickness must be known from an independent measurement before the other can be calculated. For films thicker than 0.5 μm, two or more guided modes are usually supported and both the film thickness and the refractive index can be completely determined from prism coupling measurements.

Prism coupling method is also restricted to simple film structure. Hence it is not suitable for complex multilayer films. In addition, prism coupler measurement is usually performed only at several discrete wavelengths of the available laser sources. However, the obtained values of refractive index at these wavelengths can be fitted to known dispersion model such as Cauchy's dispersion equation to allow an interpolation of the results to other wavelengths.

Table 5.1 shows the thickness and refractive index at three different wavelengths (450 nm, 532 nm, and 633 nm) of the polymeric film obtained from 1:6 dilution of MY-133MC polymer in methoxyperfluorobutane (also known by commercial name HFE-7100) solvent measured by prism coupler method.

Table 5.1. Thickness and refractive index at three different wavelengths of MY-133MC polymer film obtained from 1:6 dilution measured by prism coupling method.

Wavelength (nm)	TE mode		TM mode	
	Refractive index	Thickness (μm)	Refractive index	Thickness (μm)
450	1.331	2.61	1.331	2.65
532	1.329	2.58	1.328	2.63
633	1.326	2.47	1.326	2.54

The measured refractive indices in Table 5.1 are very similar for both TE and TM polarizations and therefore are independent of polarization. These values can

then be easily fitted into Cauchy's dispersion equation expressed by Equation (4.38) to obtain the Cauchy's coefficients as A = 1.3017, B = 0.0132 $(\mu m)^2$, and C = -0.0014 $(\mu m)^4$.

From this fitted dispersion model, the refractive index of the polymeric film is estimated to be 1.320 at the wavelength of 760 nm. As it is not too far from the range of wavelengths used for the fitting, the extrapolation in this case is reasonably valid. With a refractive index of 1.320, the optimum thickness of the polymer layer for sharp plasmonic resonance is around 1250-1300 nm. The thickness of the polymeric film obtained from 1:6 dilution of MY-133MC polymer in HFE-7100 solvent as shown in Table 5.1 is approximately twice this optimum value. To get the desired film thickness with the same fabrication procedures, further dilution by a factor of two, i.e., 1:13 dilution is required.

Table 5.2 shows the thickness and refractive index of the polymeric film obtained from 1:13 dilution of MY-133MC polymer in HFE-7100 solvent measured by prism coupler method. The refractive indices are quite consistent with the previous results shown in Table 5.1. The values of the film thickness are more or less half of those obtained from twice more concentrated polymeric solution shown in Table 5.1 as expected. The average film thickness obtained from 1:13 dilution of MY-133MC polymer in HFE-7100 solvent as shown in Table 5.2 is 1285 nm which is well in the range of 1250-1300 nm for optimum thickness.

Table 5.2. Thickness and refractive index at three different wavelengths of MY-133MC polymer film obtained from 1:13 dilution measured by prism coupling method.

Wavelength (nm)	TE mode		TM mode	
	Refractive index	Thickness (μm)	Refractive index	Thickness (μm)
450	1.332	1.30	1.333	1.29
532	1.330	1.25	1.331	1.28
633	1.327	1.26	1.326	1.32

To complete the fabrication of the long-range surface plasmons sensor chip, 20 nm of gold is deposited on top of the polymeric layer obtained from the spin coating of 1:13 dilution of MY-133MC polymer in HFE-7100 solvent as described in the beginning of this section.

5.3.3. Experimental Results

Figure 5.18 shows the experimental SPR curves of water on the classical SPR (50 nm gold on BK7 substrate) and long-range surface plasmons sensor chips measured with the in-house SPR setup operating at the wavelength of 760 nm.

Figure 5.18. Experimental comparison of resonance linewidth between the classical SPR and long-range surface plasmons structures at the wavelength of 760 nm.

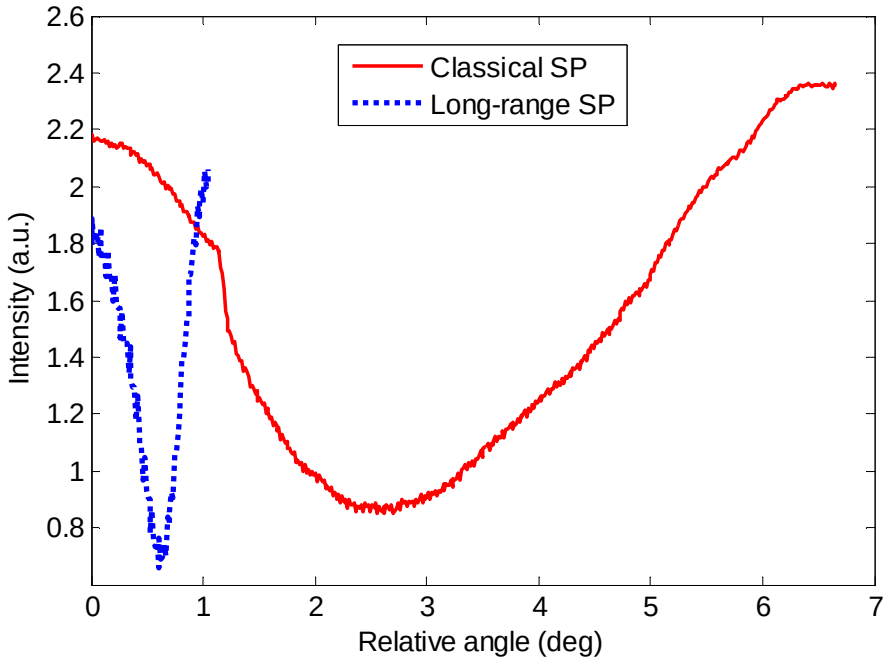

From Figure 5.18, the experimentally obtained resonance linewidth is 3.3° for the classical SPR sensor chip. This is quite consistent with the theoretical prediction of 3.5° as shown in Figure 5.13. However, for the long-range surface plasmons structure, the experimentally obtained resonance linewidth from Figure 5.18 is 0.4° which is five times wider than the 0.08° predicted theoretically as shown in Figure 5.13. However, this resonance linewidth is still significantly narrower by almost an order of magnitude compared to that of classical SPR. The resonance linewidth broadening of the long-range surface plasmons structure here is due to uneven morphology of the interface between the gold film and the polymer layer. In fact, because of the high cohesive energy of metals and relatively weak metal-polymer interaction, metals deposited on a polymer layer tend to aggregate on the surface [62].

Figure 5.19. Experimental sensorgram showing resonance shift at the wavelength of 760 nm when HBS buffer solution with different dilutions are successively put into contact with the surface of the long-range surface plasmons sensor chip.

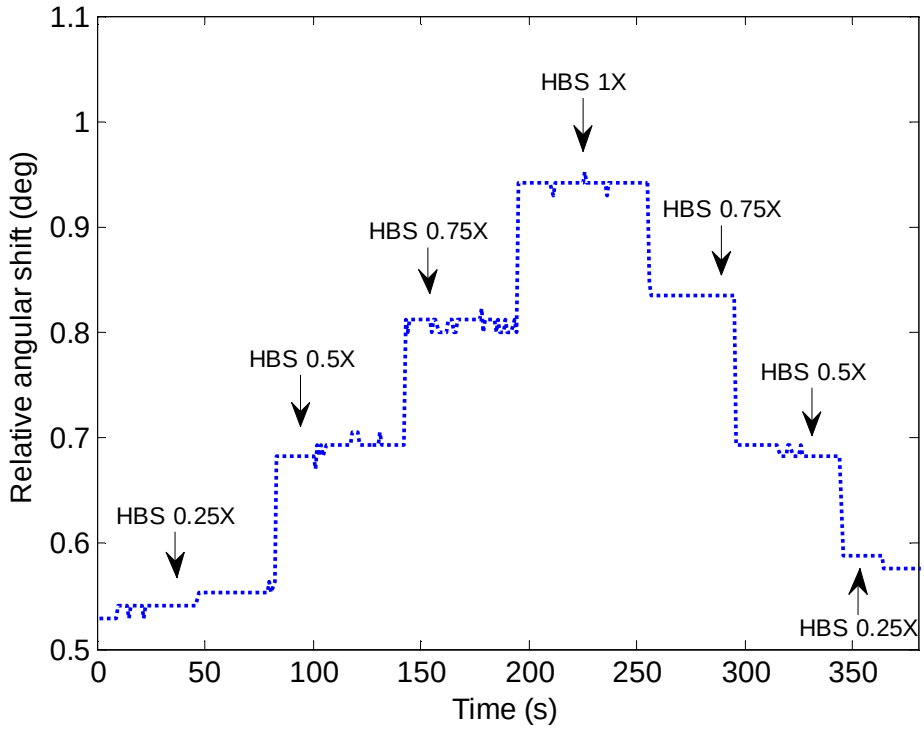

Figure 5.19 shows the obtained experimental sensorgram at the wavelength of 760 nm when HEPES buffer solution (HBS) with different concentrations (25 %, 50 %, 75 %, and 100% of HBS) in water are successively put into contact with the surface of the long-range surface plasmons sensor chip. The refractive index of undiluted HBS buffer solution (HBS 1X) is 0.003 RIU higher than that of water. Further dilution of HBS buffer solution in water (0.25X, 0.5X, and 0.75X) scales this refractive index difference proportionally. The result is a series of linear regular steps in the observed experimental sensorgram when HBS buffer solution with either increasing or decreasing dilution is successively injected.

From Figure 5.19, the refractive index sensitivity of the long-range surface plasmons sensor chip can be evaluated to be 80 °/RIU. With resonance linewidth of 0.4°, the figure-of-merit of this structure is easily calculated to be 200. For comparison, the experimental refractive index sensitivity of classical SPR structure at the same operating wavelength is 67 °/RIU with resonance linewidth

of 3.3° thus yielding a figure-of-merit of 20. The experimental figure-of-merit of the long-range surface plasmons sensor chip is therefore an order of magnitude higher than that of classical SPR structure.

5.3.4. Extension to Near-Infrared

The concept of long-range surface plasmons developed above for operating wavelength in the visible can be extended to the near-infrared region particularly for the wavelength of 1550 nm. At this wavelength, the refractive index of water can be calculated as 1.3149 which is to be closely matched by the buffer layer of the long-range surface plasmons structure. Considering gold thickness of 20 nm, Table 5.3 summarizes the optimum thickness of this buffer layer as a function of its refractive index.

Table 5.3. Optimum thickness of buffer layer as a function of its refractive index for long-range surface plasmons structure operating at the wavelength of 1550 nm.

Refractive index	Optimum thickness (nm)
1.3110	4200
1.3120	4800
1.3130	5400
1.3140	5900
1.3150	6100
1.3160	6300
1.3170	6500
1.3180	6700
1.3190	6900
1.3200	7100

Figure 5.20 shows the theoretical SPR curves of water on long-range surface plasmons structure with 20 nm thick gold layer for some different refractive indices of the buffer layer at the wavelength of 1550 nm. The corresponding optimum thickness of the buffer layer given its refractive index is taken from Table 5.3.

As can be seen from Figure 5.20, the angle of resonance decreases when the refractive index of the buffer layer is reduced. This is due to the fact that for any given superstrate, the effective refractive index of the long-range surface plasmons mode decreases with decreasing refractive index of the buffer layer. Figure 5.20 suggests that the refractive index of the buffer layer should not be

lower than 1.3110. Beyond this limiting value, the plasmonic resonance occurs too close to the critical angle of the total internal reflection which makes its identification difficult.

Figure 5.20. Theoretical SPR curves of water on long-range surface plasmons structure for different refractive indices of the buffer layer at the wavelength of 1550 nm. Table 5.3 is used to determine the optimum thickness of the buffer layer given its refractive index. The gold layer is 20 nm thick.

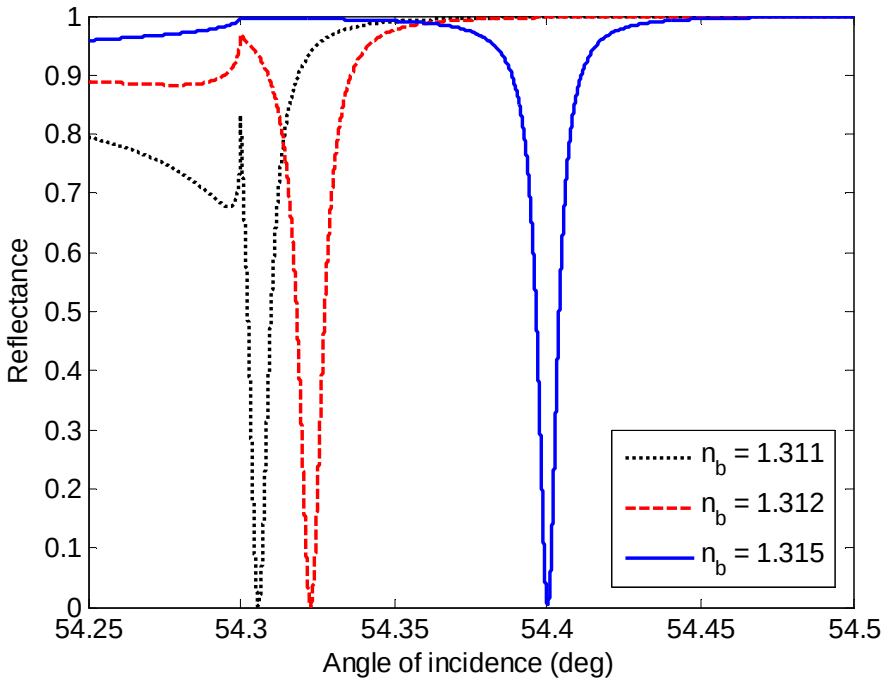

Consider a long-range surface plasmons structure on H-ZF1 glass (refractive index = 1.6192 at the wavelength of 1550 nm). The refractive index of the buffer layer is taken as 1.3120 and its optimum thickness from Table 5.3 is 4800 nm. The gold layer on top is 20 nm thick. This structure is now compared to the bimetallic silver/gold SPR sensor chip discussed in Section 5.2. Figure 5.21 shows the theoretical SPR curves of water on the bimetallic silver/gold and long-range surface plasmons structures at the wavelength of 1550 nm. The extremely narrow plasmonic resonance linewidth of the long-range surface plasmons structure is found to be 0.008°. This is 50 times narrower than that of the bimetallic silver/gold SPR structure.

Figure 5.21. Theoretical comparison of plasmonic resonance linewidth of water on bimetallic silver/gold and long-range surface plasmons structures at the wavelength of 1550 nm.

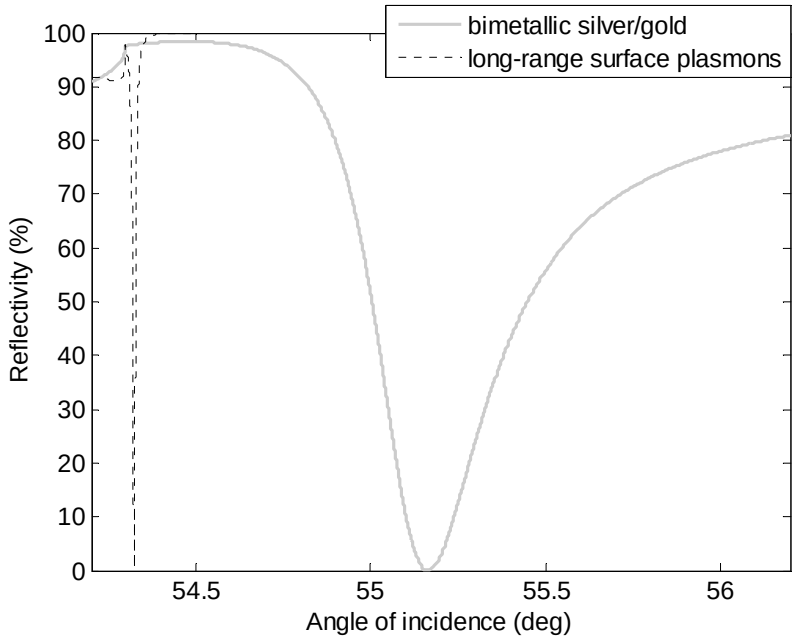

Figure 5.22. Electric field intensity enhancement factor associated with the SPR curve of water on the long-range surface plasmons structure in Figure 5.21.

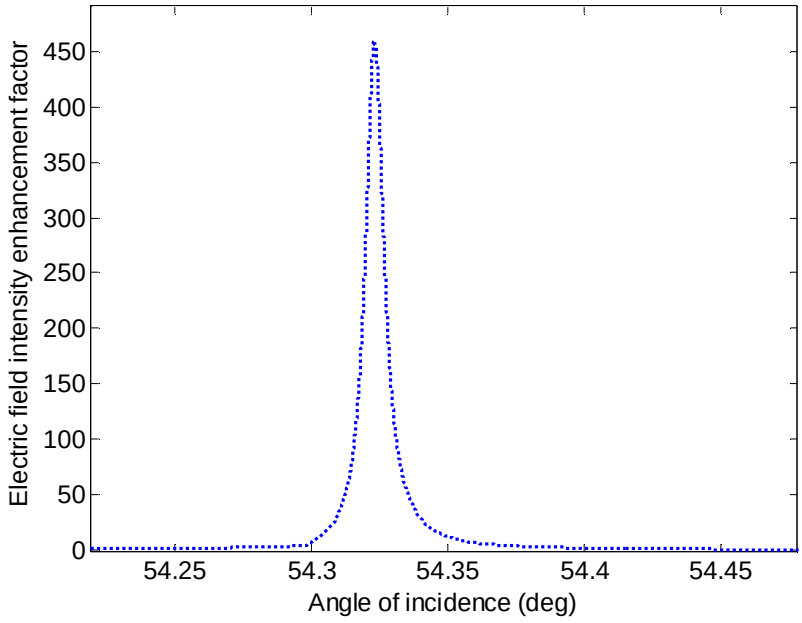

Figure 5.22 shows the electric field intensity enhancement factor associated with the SPR curve of water on the long-range surface plasmons structure in Figure 5.21. The maximum field enhancement factor in this case is as high as 450. This is more than an order of magnitude higher than that obtained from classical SPR operating in the visible.

Figure 5.23. Theoretical SPR curves of water on long-range surface plasmons structure showing the shift of plasmonic resonance at the wavelength of 1550 nm when the refractive index is varied by 0.0005 RIU. The refractive index of the buffer layer is taken as 1.3120 and its thickness is 4800 nm. The gold layer is 20 nm thick and the substrate is H-ZF1 glass.

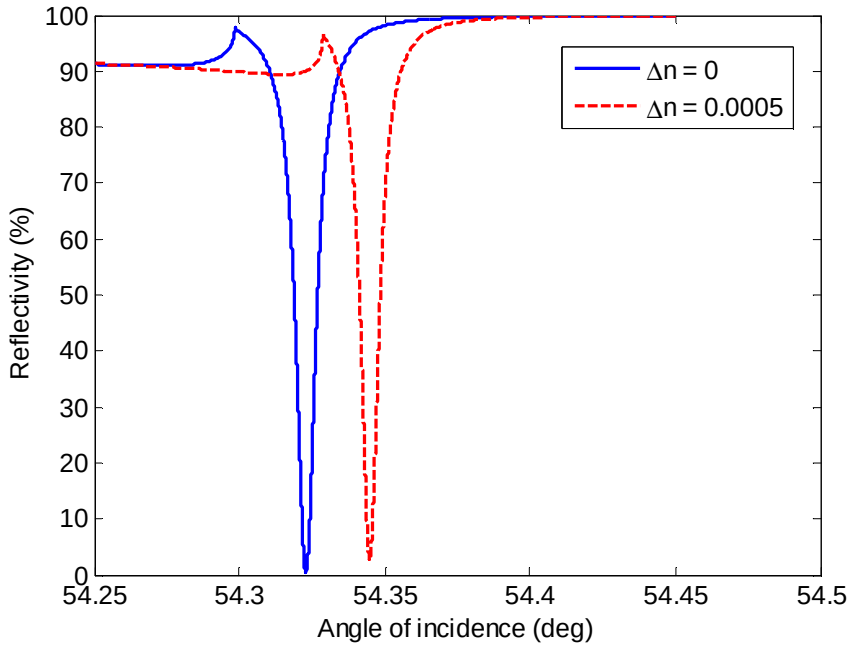

Figure 5.23 shows the theoretical shift of the plasmonic resonance of this particular long-range surface plasmons structure when the refractive index of the sensed dielectric medium is increased by 0.0005 RIU. Based on the angular shift of the reflectivity minimum, the refractive index sensitivity of this long-range surface plasmons structure can be evaluated to be 44 °/RIU. With an extremely narrow resonance linewidth of only 0.008°, the theoretical figure-of-merit of this sensor chip is easily calculated to be as high as 5500. This figure-of-merit is more

than two orders of magnitude higher compared to that of classical SPR operating at the wavelength of 760 nm as used in most commercial SPR instruments.

The field penetration depth into the sensed dielectric medium can also be calculated to be 7500 nm. With such significant probe depth, this long-range surface plasmons structure has promising potential for biosensing applications involving cells whose size is a few microns.

Chapter 6

Novel Graphene-Based Surface Functionalization Strategy

This chapter treats the subject of novel surface functionalization strategy based on graphene proposed and developed in this work. The conventional surface functionalization scheme widely used in SPR biosensors is first briefly introduced followed by an overview of the novel surface functionalization strategy. The fabrication and characterization of sensor chips incorporating the novel surface functionalization strategy are then discussed in details. Finally, some experimental results indicating sensitivity enhancement due to the novel surface functionalization strategy are presented.

6.1. Surface Functionalization in Conventional SPR

In the functionalization of SPR biosensors, the most widely used approach for the introduction of functional groups onto gold SPR surface is based on thiolated organic compounds, typically alkanethiols. These molecules are known to spontaneously form self-assembled monolayers (SAMs) on gold surface [63]. In this chapter, SPR biosensors using this surface functionalization approach will be referred to as conventional SPR biosensors.

A simple alkanethiol molecule is illustrated in Figure 6.1. An alkanethiol can be thought of as containing 3 parts: a sulfur binding group for attachment to a noble metal surface, a spacer chain which is typically made up of methylene groups, $(CH_2)_n$, and a functional head group. The terminal sulfur group links the thiol molecule to the gold surface through gold-sulfur bonds. This sulfur group together with the carbon atoms in the methylene spacer group act as the main driving forces for the self-assembly of the alkanethiols. The spacer group also provides well-defined thickness (typically 1-3 nm) and acts as a physical barrier. The head group then provides a platform where any desired group can be used to produce surfaces of effectively any type of desired chemistry. By simply changing the head group, a surface can be created that is hydrophobic (methyl head group), hydrophilic (hydroxyl or carboxyl head group), protein resistant (ethlylene glycol

head group), or allowing chemical binding (NTA (nitrilotriacetic acid), azide, carboxyl, amine head groups).

Figure 6.1. Schematic diagram of a thiol molecule.

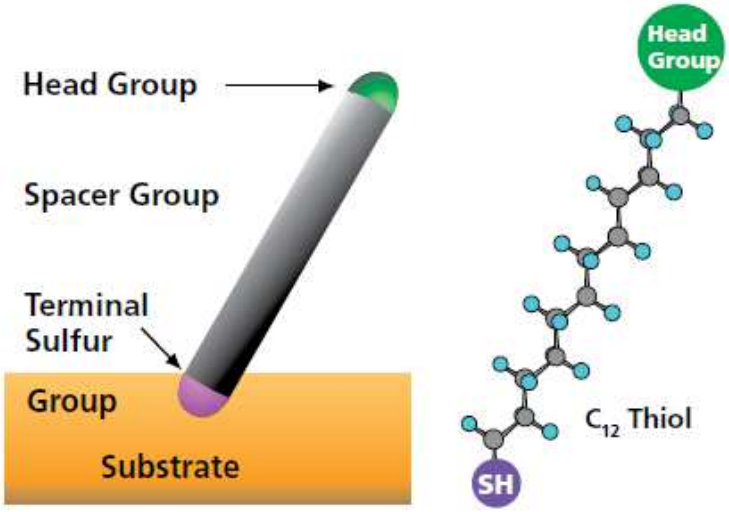

Thiol SAMs on gold, silver, palladium, and other materials are typically made by immersing freshly prepared or clean metal-coated substrate into a dilute solution (around 1 mM) of the desired alkanethiol in ethanol for at least 12-18 hours at room temperature followed by thorough rinsing with ethanol and water. Initial monolayer formation is very fast with monolayer coverage being achieved within seconds to minutes. This initially formed monolayer is however not well ordered and contains many defects within the chains. Over time, a very slow reorganization process takes place so that the layers become more ordered and well packed. Reported assembly times vary throughout the literature, but typically are in the range of 12 hours up to 2 days. Figure 6.2 illustrates these various steps in thiol self-assembly on gold surface.

As an example of common surface functionalization schemes in conventional SPR, consider the 11-mercaptoundecanoic acid (MUA) which is the alkanethiol used in most cases. It is an alkanethiol with 11 carbon atoms in total and a carboxyl head group. Its chemical formula is usually written as $HSCH_2(CH_2)_8CH_2COOH$. Self-assembly of MUA on gold SPR surface is achieved by immersing the gold-coated sensor chip into a 1 mM ethanolic solution of MUA for at least 18 h followed by thorough rinsing with ethanol and water.

Figure 6.2. (a) Various steps in thiol self-assembly on gold surface. Gold-coated glass slide is dipped in an ethanolic solution of thiol. The initial chemical adsorption process is very fast. This is followed by a very slow step of reorganization **(b)** Reorganized monolayer.

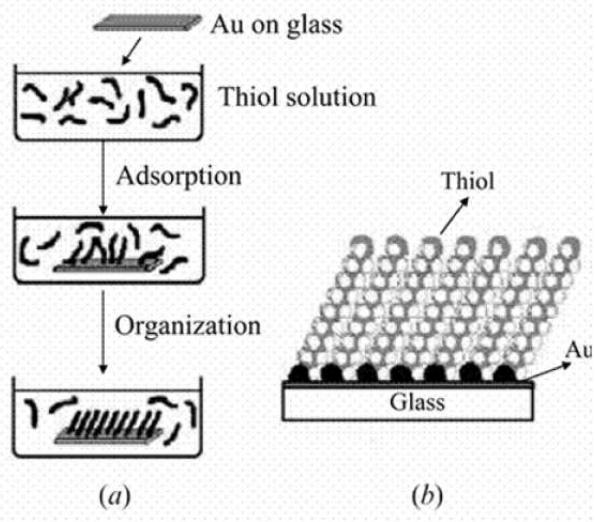

After the self-assembly of the MUA is complete, any desired functional group, biomolecule or bioreceptor referred to simply as ligand can be covalently attached to the sensor surface. Regardless of the chemistry used to attach the ligand to the sensor surface, the first step in almost all covalent immobilization procedures is the activation of the carboxyl head groups of the self-assembled MUA with a mixture of 1-ethyl-3-(3-dimethylaminopropyl)-carbodiimide (EDC, typically 0.2 M) and N-hydroxysuccinimide (NHS, typically 0.05 M) to give reactive succinimide esters (Figure 6.3). The succinimide esters react spontaneously with amine and other nucleophilic groups, allowing direct immobilization of molecules containing such groups, e.g., biotin and amine-terminated DNA. As an example, the covalent attachment of amine-terminated DNA on gold surface mediated by self-assembled MUA is illustrated in Figure 6.4.

Figure 6.3. Activation of head carboxyl group with EDC/NHS.

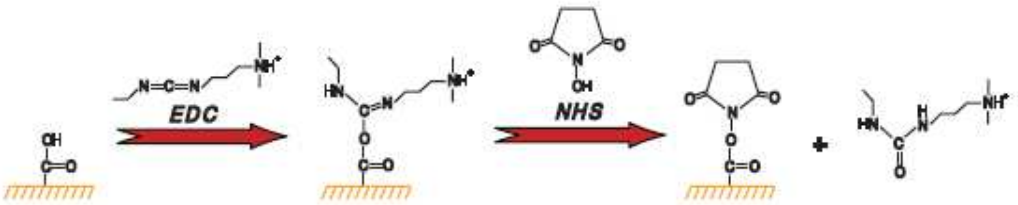

Figure 6.4. Formation of 11-mercaptoundecanoic acid (MUA) SAM on gold surface followed by covalent linking of amine-terminated DNA.

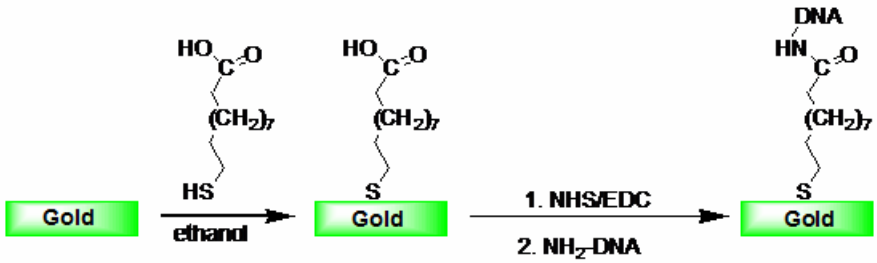

6.2. Novel Approach to Surface Functionalization

Despite its widespread use, there are actually a number of concerns with the use of thiol SAMs on gold surface for SPR-based biosensing. One of the limitations of this approach resides in the kind of functional thiolated molecules which can be synthesized and the follow-up reaction to bind the receptor. Furthermore, the susceptibility of the gold–sulfur bond to oxidation and photodecomposition is a real hurdle to overcome in thiol chemistry. The rapid degradation of alkanethiol-based SAMs on gold surface under ambient laboratory conditions has been systematically investigated [64, 65]. In particular, the thiol bond susceptibility to oxidation in air and water compromises its long-term stability [66]. Upon exposure to ultraviolet light, thiol SAMs on gold are also prone to photooxidation [67].

Currently, the new primary research focus using thiolated SAMs in connection with SPR is also oriented towards decreasing the number of surface reaction steps involved in bioreceptors linking. At the same time, there is a growing interest in the applications of carbon nanomaterials, notably carbon nanotubes and graphene, for biosensing.

6.2.1. Motivations for Graphene-Based SPR Surface

Graphene, a single sheet of carbon atoms arranged in a hexagonal lattice, has attracted great interest in various fields [68, 69]. Recent advances in large-area growth and isolation of graphene established it as a promising candidate for

several potential applications [70, 71, 72]. In particular, graphene is an extremely attractive material for biosensing applications for a number of reasons.

Firstly, the unique surface physicochemical characteristics of graphene enable it to directly interact with biomolecules. Through the pi-stacking interactions between its two-dimensional hexagonal cells and the carbon-based ring structures widely present in biomolecules, graphene can strongly and stably adsorb biomolecules [73]. Hence the incorporation of graphene into SPR biosensors structure can substantially simplify the bioreceptors linking to the sensor surface.

Secondly, the surface of graphene is very stable, robust, and chemically resistant. Therefore, unlike thiol SAMs on gold surface, graphene is not plagued with photodecomposition and photooxidation concerns.

Thirdly, graphene has a large scalability and it can be readily integrated into any existing SPR technology. Gold-graphene SPR combination can be quite easily realized thanks to the similarity of graphene's electronic and surface properties to carbon nanotubes and the strong adhesion between carbon nanotubes and gold [74]. However, well-ordered assembly of carbon nanotubes on gold surface has not yet been reported. On the other hand, the two-dimensional feature of graphene makes it much easier to coat gold SPR surface with graphene.

Finally, it is also expected that the constraint exerted on bioreceptors upon their immobilization on the graphene surface can help prevent non-specific binding of biomolecules. In fact, it has been experimentally shown that functionalized graphene improves the biostability and specificity of single-stranded DNA [75].

6.2.2. Overview of Graphene Synthesis

Any eventual applications of graphene-based devices including biosensors will certainly depend on methods for the reproducible fabrication of high-quality graphene in large volumes and its incorporation into devices on an industrial scale. This "graphene engineering" is still an extremely active and rapidly moving field of research. Currently, there are four main approaches to producing graphene that will be briefly discussed below. The first two are based on a top-down approach while the last two are bottom-up approaches.

The first, also the simplest and the least expensive, technique to produce graphene is micromechanical cleavage or exfoliation of graphite also known as the "Scotch tape" method. In this approach, repeated peeling of fragments from high-quality graphite (e.g., highly-oriented pyrolytic graphite) with pieces of adhesive tape eventually leaves some single layers of graphene. Although this

method tends to produce the best quality, least-modified forms of graphene, it can only produce small area films of the order of a few tens of micrometers and it is not scalable [76]. Moreover, as single layers of graphene are distributed among many other carbonaceous fragments that can have two, three, dozens, or even hundreds of layers, the other challenge in this approach is to identify the fragments of graphene that have the desired number of layers and size. With patience, this method can eventually produce high-quality graphene for laboratory-scale scientific research, but it is hard to see how it will ever form a high throughput, large-volume method for the industrial fabrication of graphene.

The second graphene production method is the chemical reduction of solution-processed graphene oxide. In this approach, graphene is first chemically exfoliated by converting it into graphene oxide under strongly acidic conditions [77]. This oxidation process creates a large number of oxygen-containing functional groups, such as carboxyl, epoxides, and hydroxyl groups, on the graphene surfaces. These polar groups make graphene oxide hydrophilic and thus easily dispersed into single sheets in water or polar organic solvents. The colloidal suspension of graphene oxide produced by this method clearly opens up possibilities for simple deposition methods such as spin or dip coating. However, the physical and chemical properties of graphene oxide are radically different from those of graphene. For instance, graphene is electrically conductive while graphene oxide, due to a large proportion of sp^3 C-C bonds in its distorted layer structure, is an electrical insulator. Therefore, the graphene oxide is typically reduced by chemical agents such as hydrazine or by heating in a reducing atmosphere in an effort to recover the structure and properties of graphene. While this process does return much of the electrical conductivity and flatness to the reduced graphene oxide, the final product is not quite the same as graphene and still contains a significant amount of carbon–oxygen bonds [78, 79, 80, 81]. The main limitation of this method is that the yield is still very low and the graphene films made from such colloidal dispersion of graphene oxide are not continuous [82].

The third approach to fabricating graphene is bottom-up chemical synthesis, a process in which precursor compounds are combined by organic reactions to form molecular fragments of graphene that are subsequently used to grow larger graphene flakes. The main limitation of such chemical synthesis approach is that the “graphene fragments” quickly become insoluble as their size increases. As a result, the final products are currently limited to pieces of graphene smaller than about 5 nm [83].

The fourth method to growing graphene is based on thermal procedures. Although more costly than wet chemical methods, these approaches avoid any chemical modification of graphene. There are in fact several thermal approaches to grow graphene. One approach is the epitaxial growth of graphene layers on the basal faces of single-crystal silicon carbide heated to above 1200 °C in ultrahigh vacuum [84]. In this approach, the graphene layers grow as the silicon atoms evaporate from the heated crystal. However, the resulting graphene layers tend to show various defects such as substrate-induced corrugations, rotational disorder between the layers, and scattering centers [85]. These effects mean that the electronic band structures and properties of epitaxial graphene differ from those of mechanically exfoliated graphene, so that it is effectively a different material [86]. Another thermal approach to graphene growth is the chemical vapor deposition (CVD) technique. Compared to the former approach, CVD is a better thermal method for graphene growth because it offers more similar properties to mechanically exfoliated graphene. The main challenge of this method lies in achieving a monodisperse graphene film with well-controlled number of layers. Recent efforts have focused on growing really large-scale (e.g., centimeter-sized) films of graphene by passing hydrocarbon vapors over metallic substrates such as nickel [87] or copper [88] heated to approximately 1000 °C. Yet another thermal approach is the ion implantation method for graphene synthesis with potential layer-by-layer thickness control [89]. In this method, ion implantation is used to introduce a precise dose of carbon atoms into polycrystalline nickel films. Subsequent graphene growth on the surface of the nickel film occurs upon heat treatment. Gradual increase in average graphene thickness is obtained with increasing implantation dose. However, further optimization of substrate surface homogeneity is still required for the production of large homogeneous films with a precisely controlled number of layers.

6.2.3. Overview of Sensor Chip Fabrication

The structure of the novel graphene-based SPR surface developed in this work is schematically shown in Figure 6.5. The sensor chip consists of a BK7 glass substrate (microscope cover slide is chosen for the production low-cost sensor chips) onto which 2 nm titanium adhesion layer and 50 nm gold thin film are deposited and an additional layer of graphene on top of the gold film. As illustrated in Figure 6.5, the structure of the graphene-based SPR surface is almost identical to that of conventional SPR with the only difference in the use of graphene instead of thiol SAM. The key step in the functionalization of the SPR

surface is therefore shifted from the formation of thiol SAM to the coating of graphene on the gold surface.

The use of graphene for various sensing applications has actually been recently reported in the literature. However, the graphene material in these reports is still limited to graphene made from solution-processed graphene oxide and its subsequent chemical reduction [90, 91, 92, 93]. As mentioned in the preceding section, the yield of this production method is very low and more importantly, graphene films deposited from such colloidal dispersion of graphene oxide are not continuous. This graphene deposition method, despite its attractive low-cost feature, is therefore not suitable for the fabrication of graphene-based SPR surface that requires large-area and continuous graphene coating on the gold film.

Figure 6.5. (a) Schematic illustration of conventional SPR sensor chip. **(b)** Schematic illustration of graphene-based SPR sensor chip.

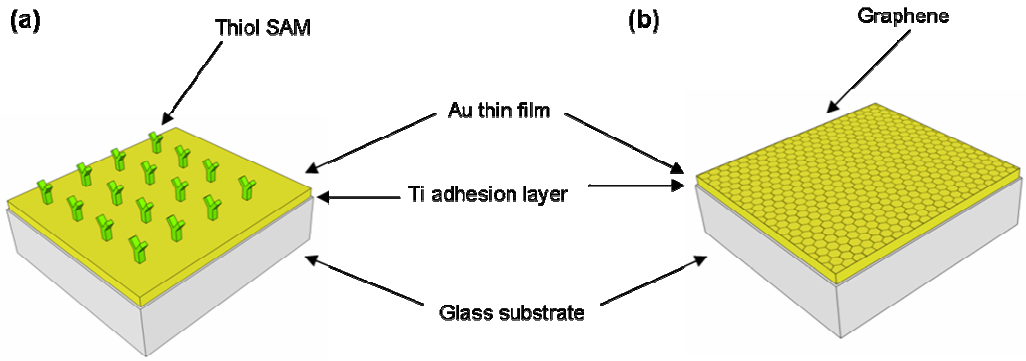

As briefly mentioned in the preceding section, the most appropriate technique for the production of high-quality large-area graphene is CVD growth. The synthesis of graphene on gold foil by a CVD process has recently been reported in the literature [94]. This growth process of graphene on gold surface is however not as well-studied as the CVD growth of graphene on nickel or copper film. Therefore there is a substantial lack of information on the optimum conditions for the direct CVD growth of high-quality, large-area graphene on gold. For this technical reason, it is not directly applied here. There is also a secondary practical cost consideration. In fact, direct CVD growth on gold surface necessitates high temperature of around 800-900 °C while the microscope cover slide used as the glass substrate undergoes glass phase transition at around 500 °C. Special glass substrate such as fused silica would be necessary to directly grow graphene by

CVD on top of the glass/gold stack. This requirement of a special glass substrate would lead to a significant increase in the production cost of the resulting sensor chip, which is clearly not suitable for low-cost sensor chips. A solution to get around this limitation is to transfer CVD graphene grown on other substrates such as nickel or copper onto the glass/gold SPR sensor chip. In this work, the chosen graphene material is commercial CVD-grown graphene on nickel thin film deposited on silicon substrate (Figure 6.6) cut into convenient 1 cm x 1 cm wafers (purchased from Graphene Supermarket, USA).

Figure 6.6. Layer structure of commercial CVD-grown graphene used in this work.

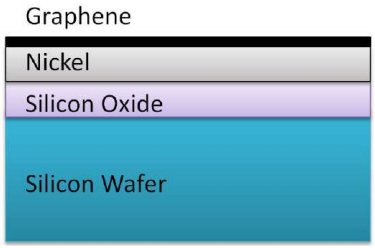

6.2.4. Graphene Transfer

To transfer CVD-grown graphene on metal foils onto other substrates, there are two types of commonly used graphene transfer methods, namely wet transfer and dry transfer.

The principle of wet transfer is basically to etch away the metallic substrate on which the CVD graphene was grown and use a polymer handle as a support material to "catch" the graphene layer. The free-standing polymer/graphene stack is then placed on the desired target substrate (graphene facing the surface). Finally, the polymer support material is removed to yield a graphene film on the desired substrate. As a specific example, Figure 6.7 shows the flowchart of a typical wet transfer process of CVD graphene grown on copper foil [95]. In this process, the as-grown graphene film on copper foil is drop-coated with poly(methyl methacrylate)(PMMA) dissolved in chlorobenzene. Since graphene grows on both sides of the copper foil, after one side of the copper/graphene is coated with PMMA and cured, the opposite side is polished to remove the graphene layer. The copper substrate is then etched away by an aqueous solution of ferric nitrate (0.05 g/mL) over a period of around 12 hours. The PMMA/graphene stack is subsequently washed with deionized water and placed

on the target substrate. After drying, a small amount of liquid PMMA solution is dropped onto the PMMA/graphene. The newly formed PMMA film is then slowly cured at room temperature and finally dissolved by acetone.

Figure 6.7. Flowchart of a typical wet transfer process of CVD graphene grown on copper foil. The top-right and bottom-left insets are optical images of graphene transferred onto SiO_2/Si wafers (285 nm thick SiO_2 layer). The bottom-right inset is a photograph of graphene transferred onto quartz substrate [91].

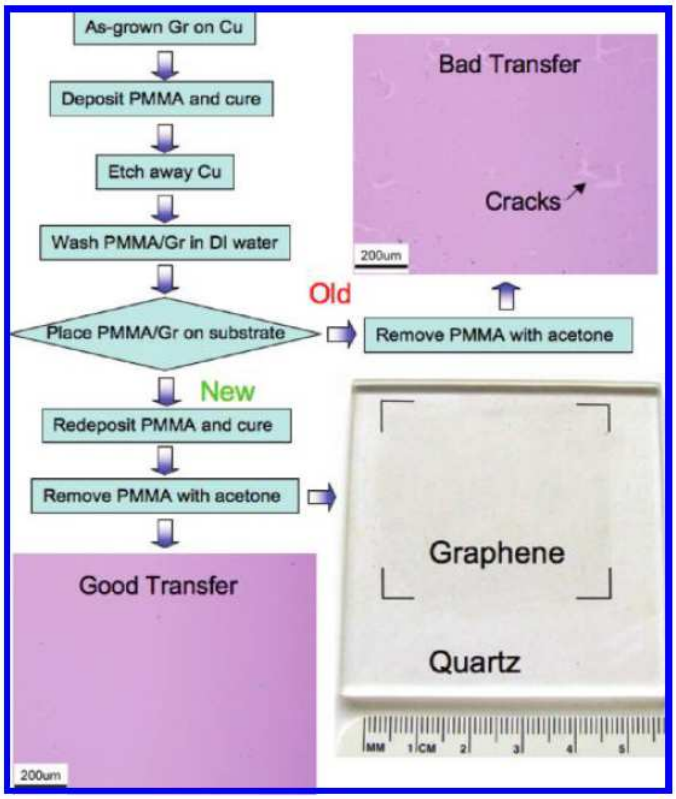

The main problem with such wet transfer method is that the PMMA resist is not completely removed from the graphene surface by acetone [96]. By annealing at 300 °C in ultra-high vacuum for 3 hours, most of the PMMA residues can be removed from the graphene surface but post-anneal X-ray photoelectron spectroscopy (XPS) indicates that some trace of PMMA is still present [97]. To improve the removal of PMMA residue, thermal treatment at higher temperature of around 500 °C to decompose the remaining PMMA has been suggested [98]. The need for such high temperature treatment is a drawback of the wet transfer method as it prevents the transfer technique to be applied to substrates that cannot

withstand excessive heat, e.g., flexible organic polymer. The relatively long processing time also makes the wet transfer method rather inconvenient: the etching of the metal substrate alone takes 12 hours, a few additional hours is required for the high temperature treatment. Moreover, the wet transfer method is clearly not amenable to highly chemically resistant substrates such as silicon carbide.

An alternative to the wet transfer method is the dry transfer technique adopted in this work [99]. Figure 6.8 illustrates the basic steps involved in the dry transfer method. The main idea of this technique is to use thermal release tape to peel the graphene layer off its original substrate and place the tape/graphene stack on the new substrate. The thermal release tape can then be simply removed by heating to moderately low temperature.

Figure 6.8. Illustration of the basic steps in dry transfer technique.

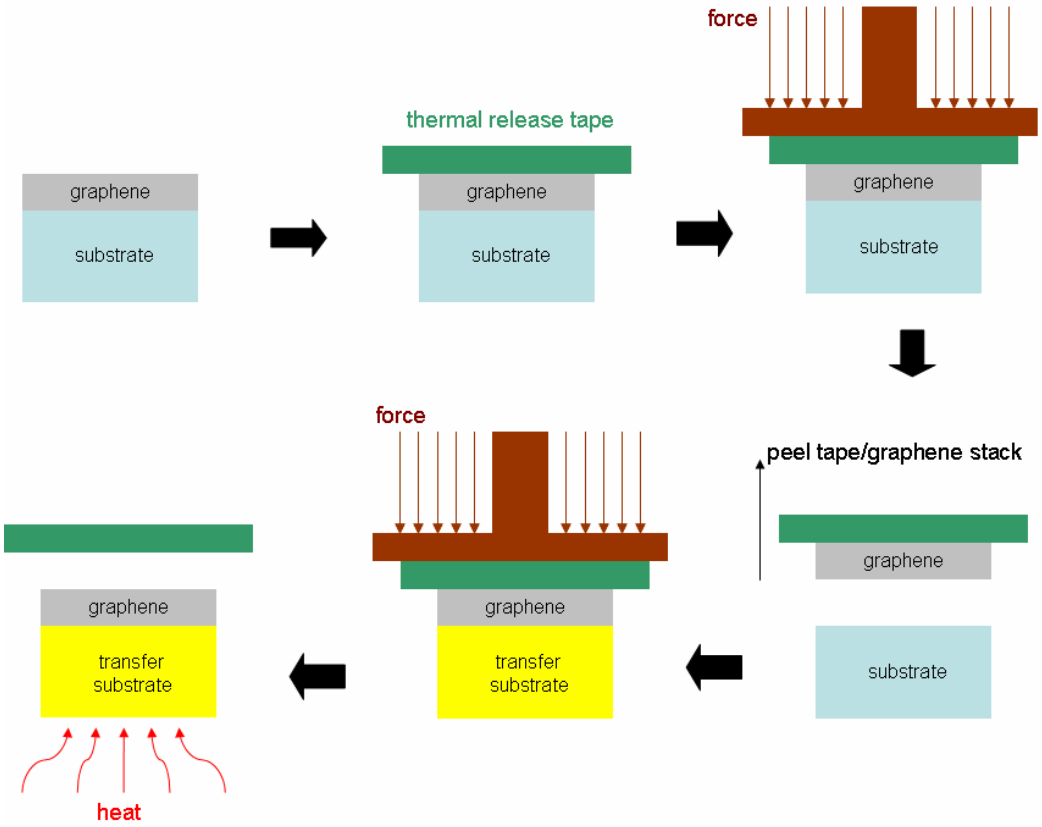

Thermal release tape is a unique adhesive tape that adheres tightly at room temperature and can easily be peeled off just by heating to a certain temperature referred to as the thermal release temperature. When the thermal release

temperature is reached, specific active particles in the thermal release adhesive layer expand. As a result of this expansion, foams are created in the adhesive layer and the adhesion is significantly reduced due to a decrease in contact area between the adhesive layer and the substrate (Figure 6.9). The tape is then released and can be easily removed from the substrate.

The specific thermal release tape used in this work is the Revalpha thermal release tape (Part No.3195MS, 3.7 N/20mm) whose thermal release temperature is 120 °C. It is important to note that there are a number of precautions to be aware of when using the Revalpha thermal release tape. Excessive heating and extended exposure to high temperature may cause rebonding and as such should be avoided. It should also be noted that Revalpha thermal release tape may not separate depending on the material and surface of the substrate to which it is applied. Concerning the particular Revalpha thermal release tape used in this work, such is indeed the case for freshly prepared hydrogenated silicon surface.

Figure 6.9. Decrease in contact area between the thermal release adhesive layer and the substrate when the thermal release temperature is reached.

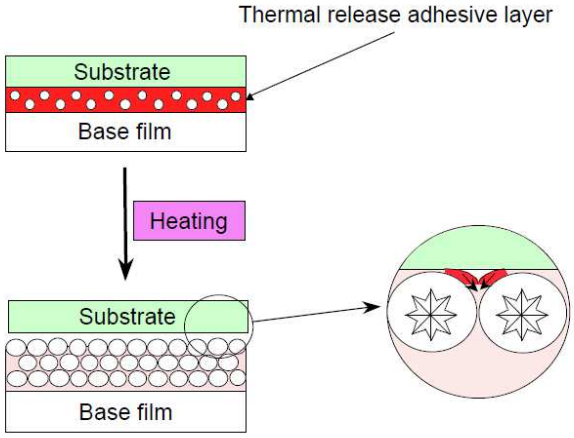

There are several distinctive advantages of dry transfer technique compared to wet transfer method.

Firstly, in dry transfer technique, there is no chemical etching of the substrate as in wet transfer method. Likely chemical contamination to the materials is therefore minimized and it makes dry transfer technique compatible with a wider range of materials, e.g., organic polymer for low-cost substrates, that do not resist etching chemicals. On the other extreme of chemical resistance, highly chemically

resistant substrates that are difficult to treat using wet transfer are also perfectly compatible with dry transfer method.

Secondly, dry transfer technique only requires very short thermal treatment at a moderately low temperature of 120 °C to remove the thermal release tape. There is actually an annealing process at 250 °C to remove any remaining tape residues which will be described later in detail but this temperature is considerably lower than the required annealing temperature of 500 °C in wet transfer method. Compared to wet transfer strategy, a wider range of substrate materials that do not withstand high temperature can therefore be accommodated by dry transfer technique.

Thirdly, dry transfer technique is much faster than wet transfer method. Whereas wet transfer requires 12 hours just for the etching of the substrate, the total time needed including a long final annealing in dry transfer is at most 6 hours.

Finally, dry transfer has the potential to be used for efficient manufacture. With a long thermal release tape, a roll-to-roll continuous manufacturing process can be envisaged. When the release temperature is reached, the thermal release tape separates instantaneously from the substrate with no need of applied force and therefore contributes to better yield and labor saving in a continuous manufacturing process.

For the above reasons, dry transfer technique is the preferred method for the transfer of CVD graphene to the gold-coated glass substrate in this work. The details of the transfer process are now described. A suitably cut piece of the Revalpha thermal release tape is first placed on the surface of the commercial CVD graphene to be transferred. To ensure strong and uniform adhesion of the tape to the graphene layer, the tape/graphene/substrate stack is inserted into a substrate bonding apparatus where a pressure plate is placed on top of the stack. The bonding chamber is then pumped to approximately 5×10^{-4} Torr before a uniform force of 5 bars is applied to the pressure plate for 5 minutes. After this process, the sample stack is removed from the bonder and the tape is peeled from the substrate. Due to very strong adhesion between the graphene layer and the tape, the graphene layer sticks to the tape but it is separated from its original substrate. The tape/graphene stack is now placed on the target substrate, namely the gold-coated glass sensor chip (graphene facing the surface). This new stack is subsequently inserted into the bonding apparatus and the same procedure with the pressure plate is repeated to enhance the adhesion between the graphene layer and the target substrate. After its removal from the bonder, the new stack is placed on

a hot plate stabilized at a temperature of 1-2 °C above the 120 °C release temperature of the tape. This thermal treatment eliminates the adhesion strength of the tape in less than a minute. The tape is then removed, leaving behind the transferred graphene layer on the target substrate which will be called the as-transferred graphene in the discussion that follows. The as-transferred graphene surface on the gold-coated sensor chip is finally rinsed with acetone to dissolve tape residue. To evaluate the effectiveness of acetone rinsing in removing tape residue, X-ray photoelectron spectroscopy (XPS) is performed on the as-transferred graphene after washing by acetone.

XPS is a surface chemical characterization technique that can be used to analyze the surface chemistry of a material, e.g., to identify the chemical species present on the sample surface. XPS spectra are obtained by irradiating a material with an X-ray beam while simultaneously measuring the kinetic energy and number of photoelectrons that escape from the top 1 to 10 nm of the material being analyzed. A typical XPS spectrum is a plot of the intensity of detected photoelectrons versus their binding energy. Each element produces a characteristic set of XPS peaks that correspond to the electron configuration of the electrons within the atoms of that element, e.g., 1s, 2s, 2p, etc and different chemical bonds of a particular element have their own unique binding energy. For example, Table 6.1 lists the characteristic C_{1s} binding energy of several relevant carbon-carbon and carbon-oxygen bonds [100, 101, 78, 102].

Table 6.1. Characteristic C_{1s} core level binding energy of several important carbon-carbon and carbon-oxygen bonds.

Bonds	**Binding energy (eV)**
C-C sp^2	284.5
C-C sp^3	285.1
C-O	285.3
C=O	286.5
O-C=O	289.0

Ideally, only the peak with binding energy at 284.5 eV corresponding to carbon-carbon sp^2 bonds should be present in the C_{1s} core level XPS spectrum of clean, pristine graphene. This is shown in Figure 6.10 by the solid blue curve for the original graphene before transfer. The red dashed curve in Figure 6.10 is the C_{1s} spectrum of as-transferred graphene after simple rinsing with acetone. For this particular graphene surface, in addition to the expected characteristic carbon-carbon sp^2 peak, there are several other peaks that correspond to carbon-carbon sp^3 and various carbon-oxygen bonds listed in Table 6.1. These other bonds are attributed to the presence of foreign organic species from the tape residues.

Figure 6.10. High resolution C_{1s} core level XPS spectrum of original graphene before transfer (solid blue curve) compared to that of as-transferred graphene washed with acetone only (red dashed curve). Signature of carbon-carbon sp^3 as well as various carbon-oxygen bonds is clearly visible in the latter.

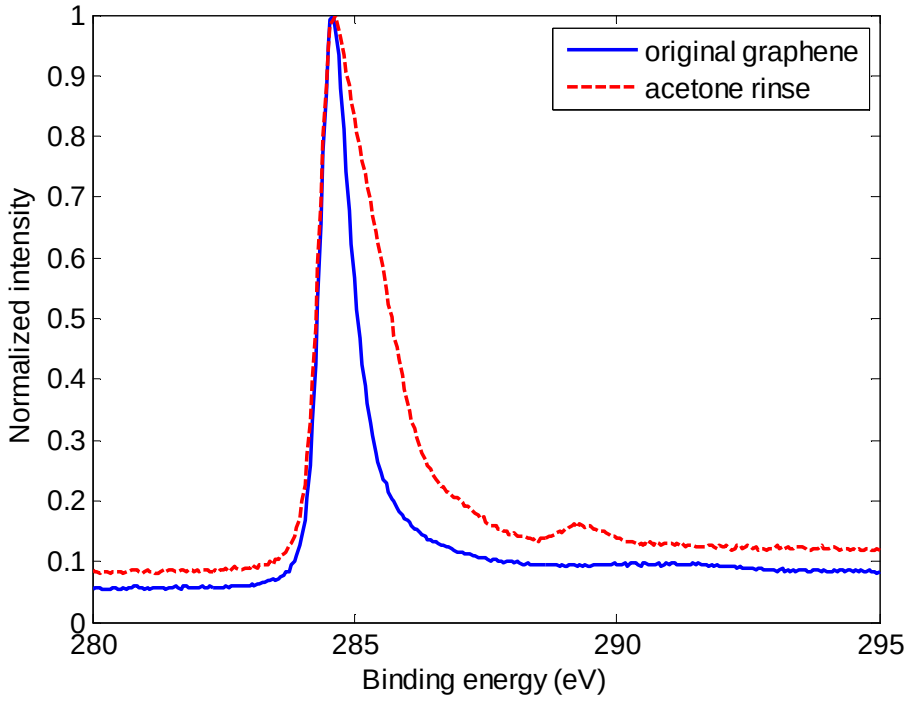

Figure 6.10 clearly shows that a simple rinsing with acetone is not sufficient to clean the surface of the as-transferred graphene. A plausible hypothesis is that some non-polar chemical species from the tape residues are not dissolved by acetone which is a polar solvent. To test this hypothesis, a mixture of polar

(acetone, methanol) and non-polar (toluene) solvents is used to rinse the surface. The mixture of solvents consists of acetone, methanol, and toluene in a 1:1:1 proportion. The red dashed curve in Figure 6.11 shows the resulting XPS spectrum of the surface washed with this mixture of solvents after 3 hours of solvents bath. A comparison with the XPS spectrum of the surface washed with only acetone shown by the solid blue curve in Figure 6.11 reveals that there is no appreciable improvement in the removal of tape residue by using a mixture of solvents (and solvents bath) instead of a simple acetone rinse.

Figure 6.11. High resolution C_{1s} core level XPS spectrum of as-transferred graphene washed with acetone only (solid blue curve) compared to that of as-transferred graphene washed with a mixture of solvents (1:1:1 mixture of acetone: toluene: methanol) after 3 hours of solvents bath (red dashed curve).

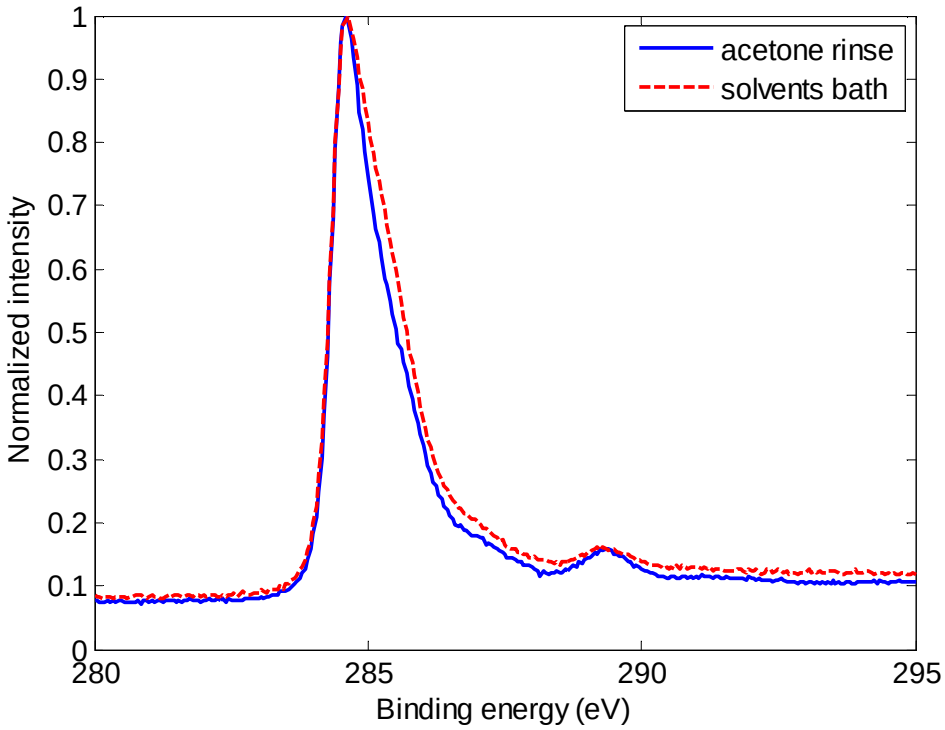

Figure 6.11 indicates that there is actually no need to use a mixture of polar solvents (acetone, methanol) and non-polar solvents (toluene). From the point of view of materials safety and cost, using only acetone is quite advantageous. Acetone is a widely used and very good solvent as it dissolves almost all organic compounds. Acetone is also a relatively safer solvent. It has a much higher flashpoint than alcoholic solvents such as methanol or ethanol, and so it is less

likely to catch fire. Methanol is much more hazardous to use, it is considerably more toxic to the body than acetone, having extremely bad effects on the eyes and the liver. Moreover, acetone is a relatively inexpensive solvent.

Figure 6.11 suggests that in addition to solvent treatment, further processing is required to completely remove tape residue. To confirm this, the as-transferred graphene is annealed after a simple rinse with acetone. The annealing is done at 250 °C under nitrogen flow environment for an hour. After an hour, the nitrogen flow is stopped but the sample is left in the annealing oven maintained at 250 °C for five more hours.

Figure 6.12. High resolution C_{1s} core level XPS spectra of as-transferred graphene washed with acetone only before (solid blue curve) and after annealing (6 hours at 250°C) (dotted red curve). Various carbon-oxygen as well as carbon-carbon sp^3 bonds are effectively removed by annealing.

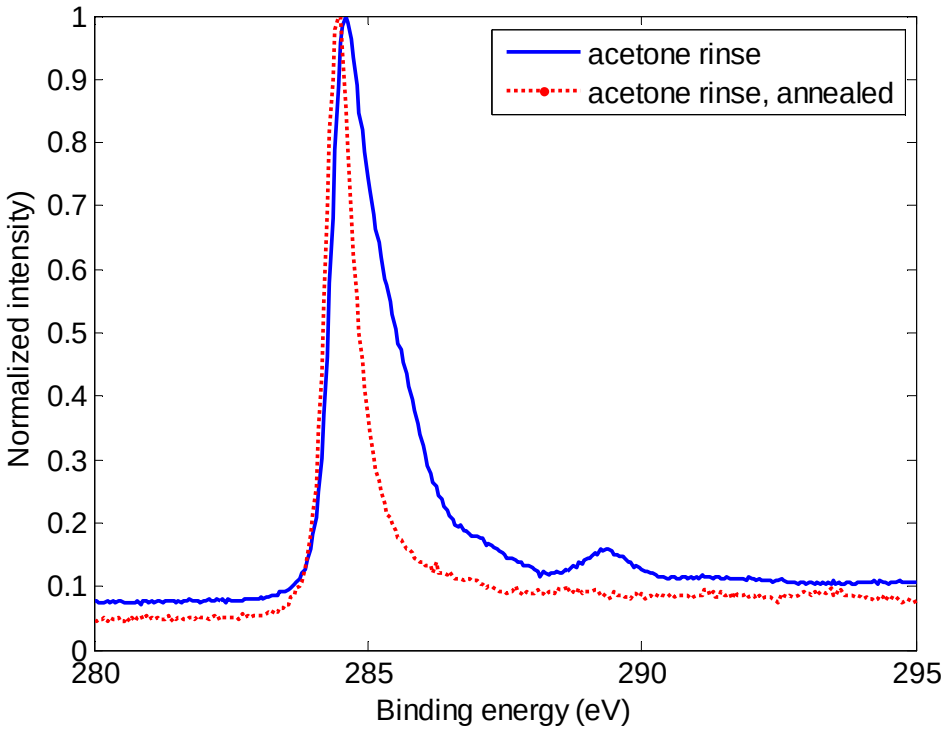

The post-annealing XPS spectrum shown by the red dotted curve in Figure 6.12 indicates that after the thermal treatment at 250 °C, various carbon-oxygen as well as carbon-carbon sp^3 species present before annealing are effectively removed by the annealing process. Further comparison of the XPS spectrum of

the sample after the annealing process to that of original graphene as shown in Figure 6.13 confirms that the original chemical state of the graphene surface is recovered after the complete post-transfer processing, namely a simple rinse with acetone followed by 6 hours of annealing at 250 °C as has just been described. This suggests that some chemical species from the tape residue are so strongly adsorbed, either physically or chemically, on the graphene surface that the attempt to remove these species by solvent treatment alone is not effective. These species are only released from the graphene surface when their kinetic energy is sufficiently increased by the ensuing thermal treatment.

Figure 6.13. High resolution C_{1s} core level XPS spectra of as-transferred graphene before (solid red curve) and after complete post-transfer processing (dashed blue curve).

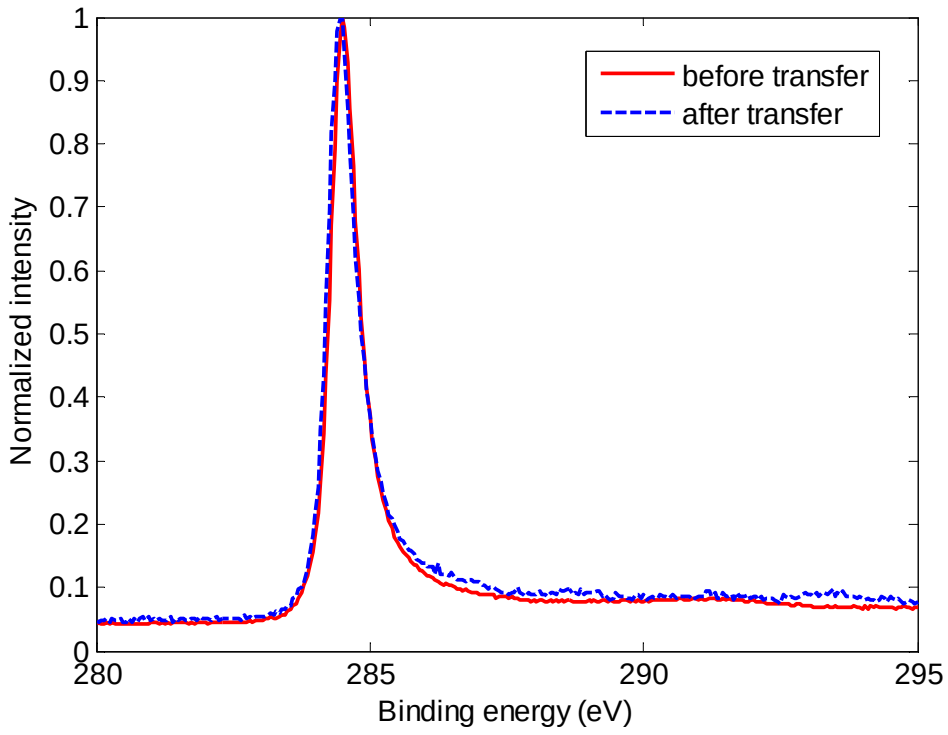

In the microelectronics industry, the UV and ozone (UVO) cleaning is an effective method of removing organic contaminants from silicon, gallium arsenide, quartz, sapphire, glass, mica, ceramics, and metals. It is therefore tempting to see if the UVO cleaning method can also be used to remove tape residue from the surface of the transferred graphene.

The UVO method is a photo-sensitized oxidation process in which the contaminant molecules of photo resists, resins, cleaning solvent residues, and oils are excited and/or dissociated by the absorption of short-wavelength UV radiation. The products of this excitation of contaminant molecules react with atomic oxygen generated when molecular oxygen and ozone are dissociated by short-wavelength UV radiation to form simpler, volatile molecules which desorbs from the surface.

Figure 6.14 shows the XPS spectra of as-transferred graphene rinsed with acetone before and after 10 minutes of UVO treatment. The XPS spectra shown in Figure 6.14 indicate that UVO treatment to remove tape residue from the surface of the transferred graphene should be avoided as it actually increases the oxidation level of the surface and thus adds to the surface contamination. However, if graphene oxide is the desired final product, UVO treatment of the transferred graphene might be a potential alternative to chemical routes for the production of uniform and continuous graphene oxide film [103].

Figure 6.14. (a) XPS spectra of as-transferred graphene rinsed with acetone before UVO treatment and **(b)** after UVO treatment.

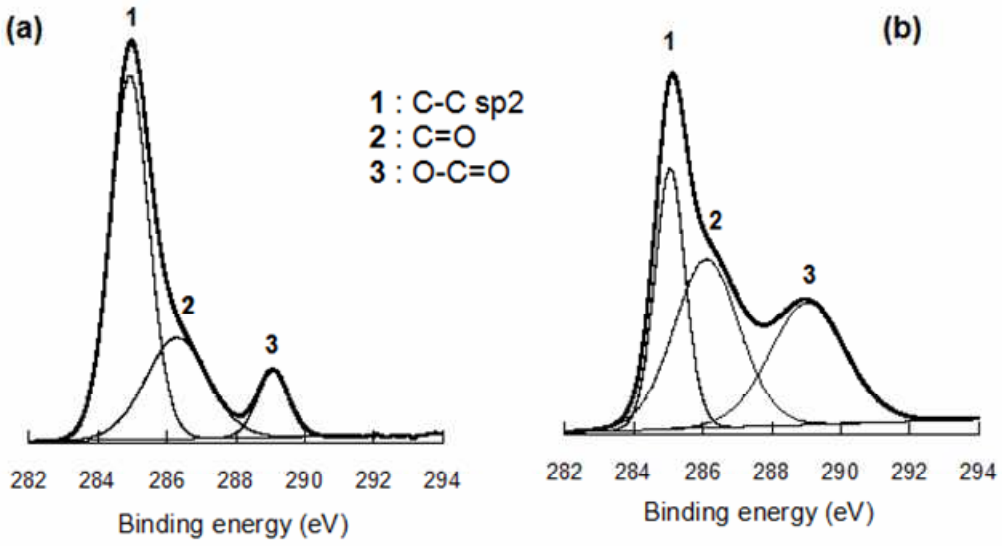

Whereas X-ray photoelectron spectroscopy is used to probe the surface chemical state of the transferred graphene, its physical state can be characterized by Raman spectroscopy. It is based on inelastic scattering, or Raman scattering, of monochromatic light from a laser. The laser light interacts with molecular vibrations, phonons or other excitations in the system, resulting in the energy of

the laser photons being shifted up or down. The shift in energy gives information about the vibrational modes in the system.

Figure 6.15 shows the Raman spectra (532 nm laser excitation) of the original graphene and transferred graphene. There are three prominent characteristic peaks in the Raman spectra of graphene and sp^2 carbons systems. These are the G, D, and 2D peaks [104, 105].

Figure 6.15. Raman spectra of the original graphene (red curve) and transferred graphene (blue curve).

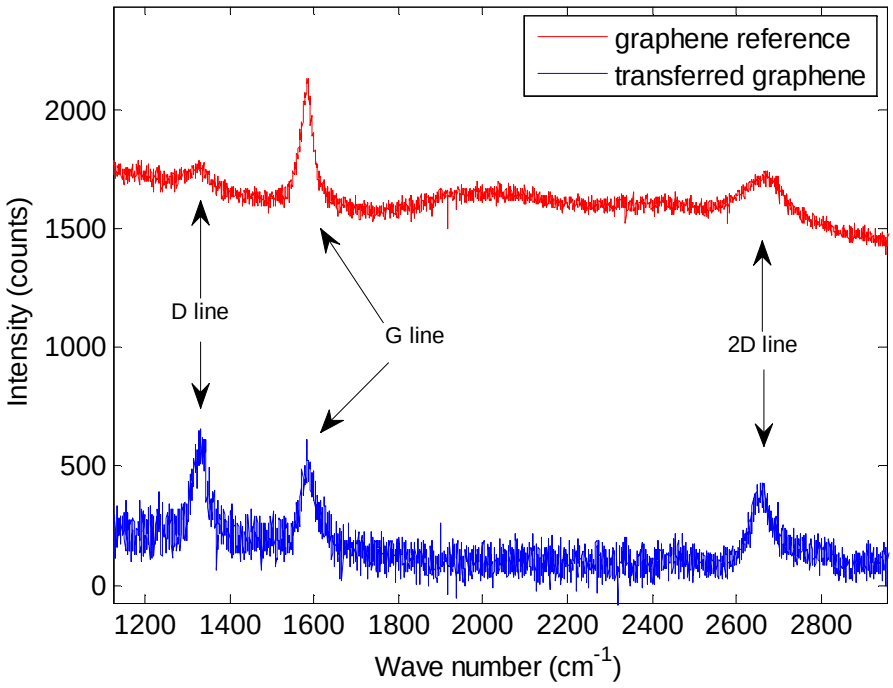

The G peak is the Raman signature of sp^2 carbons, and is observed at around 1585 cm^{-1} for all sp^2 carbons.

The D peak, observed in the range of 1250–1400 cm^{-1}, is the dominant Raman signature of disorder in sp^2 carbons. Its relative signal strength compared to the G peak is an indication of the amount of disorder in the sp^2 material. The scattering process responsible for this peak is only activated or allowed in the presence of disorder.

The 2D peak, also referred to as the G' peak, is the second harmonic of the D peak. It is however independent of the D peak; the 2D peak is always observed in sp^2 material even when there is no material disorder. In single-layer graphene, the

intensity ratio of the 2D to G peaks is related to charge carrier concentration [106].

Table 6.2 summarizes the characteristics (position, width, and integrated intensity) of the D, G, and 2D Raman peaks of the original and transferred graphene.

Table 6.2. Position, width, and integrated intensity (area) of the D, G, and 2D peaks in the Raman spectra of original and transferred graphene.

		original	transferred
D peak	position (cm^{-1})	1319.2	1331.3
	width (cm^{-1})	78.6	29.0
	area (x 1000 cm^{-1})	27.0	41.7
G peak	position (cm^{-1})	1582.3	1588.3
	width (cm^{-1})	29.2	46.3
	area (x 1000 cm^{-1})	54.4	63.3
2D peak	position (cm^{-1})	2666.6	2658.6
	width (cm^{-1})	86.0	61.5
	area (x 1000 cm^{-1})	54.0	66.6
	area(D)/area(G)	0.50	0.66
	area(G)/area(2D)	1.01	0.95

A comparison of the integrated intensity ratio of the D to the G peaks before and after transfer seems to indicate that some mechanical defects are introduced by the transfer process. However, the XPS spectra presented earlier (Figure 6.13) confirm that the transfer process does not alter the chemical state of the graphene surface which is of the most importance for biosensing applications.

The determination of the number of graphene layers from the integrated intensity ratio of the G to 2D peaks has been suggested in the literature [107]. The relation between the number of graphene layers and the integrated intensity ratio of the G to 2D peaks taken from reference [107] is shown in Figure 6.16 (a) (the 2D peak is referred to as the D' peak in the cited reference). This ratio increases systematically with the number of graphene layers from approximately 0.25 for single-layer graphene up to around 0.85 for highly-oriented pyrolytic graphite (HOPG). The integrated intensity ratio of the G to 2D peaks presented in Table 6.2 is however 1.01 for the original graphene which is very close to 0.95 for the transferred graphene. This value is outside the range 0.25-0.85 in Figure 6.16 (a)

so that it cannot be used to determine the number of layers. The reason for this discrepancy is the strong influence of the different underlying substrates. In fact, the substrate used in the study leading to Figure 6.16 (a) taken from reference [107] is silicon dioxide whereas in this work, the substrate for the original graphene is nickel and that for the transferred graphene is gold.

Figure 6.16. (a) Plot of the ratio of the integrated intensities of the G and 2D peaks vs. number of stacked layers. **(b)** G line frequency vs. number of stacked layers. **(c)** G peak for highly-oriented pyrolytic graphite (HOPG) (upper peak), double- (middle peak), and single-layer (lower peak) graphene. The vertical dashed line indicates the value for bulk graphite. The presented graphs are taken from reference [107] in which the 2D peak is referred to as the D' peak.

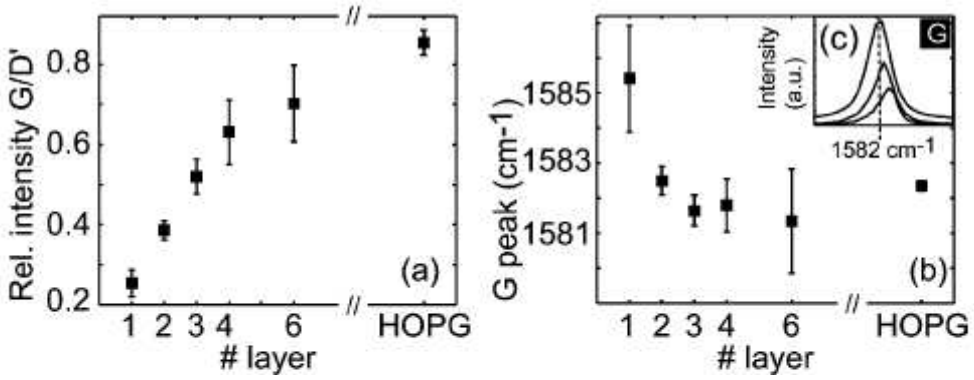

Likewise, the results based on the position of the G peak presented in Figure 6.16 (b), cannot be reliably used to determine the number of layers. In fact, the number of layers determined from Figure 6.16 (b) is even ambiguous when the number of layers is more than 2.

The determination of the number of layers from Raman spectra therefore requires preliminary results from a systematic study of Raman characterization of graphene with different number of layers on various substrates. In addition, Raman spectroscopy measurement is quite time-consuming. For these reasons, Raman spectroscopy is impractical for the determination of the number of graphene layers. On the contrary, as explained in the following section, SPR measurement is a simple, fast, and convenient method to be used to determine the number of layers of the transferred graphene on gold-coated glass substrate.

6.2.5. Optical Influence of Graphene Layers

The influence of the addition of graphene layers on the optical characteristics of the resulting SPR biosensors is easily evaluated using the calculation methods described in Chapter 4. To do this, two parameters need to be known. The first one is the thickness of the layers. As the thickness of a single graphene layer is 0.34 nm, this is easily worked out to be the number of layers times 0.34 nm. The second parameter is the relative electric permittivity, or equivalently its square root, i.e., the refractive index of the graphene layers.

The complex refractive index n_{gr} of graphene as a function of wavelength λ in the visible region can be characterized by

$$n_{gr} = 3.0 + j\lambda\frac{C_{gr}}{3} \tag{6.1}$$

where the constant C_{gr} has the numerical value of 5.446 μm^{-1}. This seemingly simple model can however accurately describe the optical behavior of graphene stacks from the two-dimensional limit which corresponds to single-layer graphene all the way to the bulk limit, i.e., graphite [108].

Equipped with such information, one can now evaluate several optical characteristics of the novel graphene-coated SPR sensor chip. To start with, Figure 6.17 shows the calculated difference in SPR angle of water on graphene-coated and bare gold sensor surface at the wavelength of 680 nm as a function of the number of graphene layers. The addition of graphene layers therefore slightly shifts the initial operating point of the sensor.

The difference in SPR angle of water on graphene-coated and bare gold sensor surface as a function of the number of graphene layers as shown in Figure 6.17 can be conveniently used to determine the number of graphene layers. Compared to Raman spectroscopy, SPR measurement is much simpler and less time-consuming for this purpose. The interpretation of the results is also much more obvious. Moreover, such SPR measurement is not redundant as SPR biosensing experiments require initial SPR curve for reference which is usually obtained from the SPR curve of water or buffer solution whose refractive index is very close to that of water.

Figure 6.18 shows the experimental SPR curves of water on graphene-coated sensor surface and bare gold SPR surface measured with Autolab SPR instrument operating at the wavelength of 680 nm. The angles of minimum reflection, i.e., the

SPR angles here differ by approximately 0.8°. From the correlation shown in Figure 6.17, the graphene in this case can be determined to be a bilayer.

Figure 6.17. Calculated difference in SPR angle of water on graphene-coated and bare gold sensor surface at the wavelength of 680 nm as a function of the number of graphene layers.

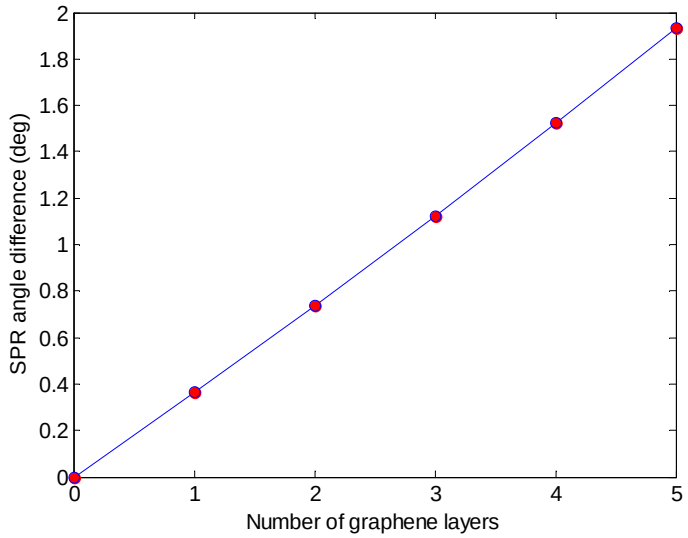

Figure 6.18. Experimental SPR curve of water on graphene-coated sensor surface (solid blue) compared to that on bare gold sensor surface (dotted red).

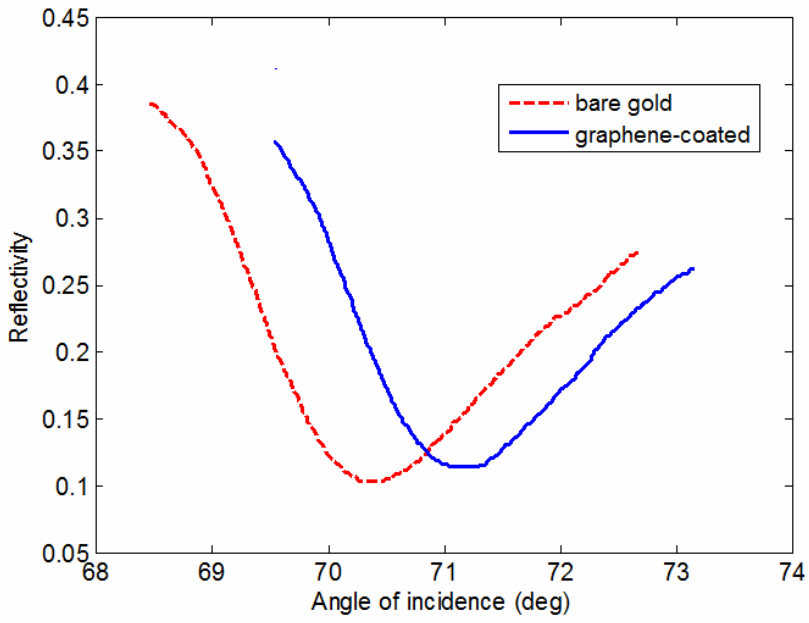

A very important point to note from Figure 6.18 is that although the addition of graphene does shift the initial operating point of the sensor, it does not modify the resonance linewidth. In fact, if the number of layers is less than four, no significant resonance broadening is expected. However, for thicker graphene layers, the resonance linewidth is considerably increased. It can be easily calculated that the resonance linewidth is approximately tripled when the number of layers increases to 10. Such a situation is nevertheless rarely encountered in practice as most graphene has only between 1-3 layers depending on its production method.

Theoretical evaluation of the influence of graphene layers on the optical sensitivity of the graphene-coated gold SPR surface has been proposed in the literature [109]. Figure 6.19 shows the results taken from reference [109] suggesting that the percentage increase in optical sensitivity of graphene-coated sensor surface compared to bare gold SPR surface is an almost linear function of the number of graphene layers. This percentage increase in optical sensitivity is calculated to be 2.5 % per each graphene layer. Thus, with 10 layers of graphene, the optical sensitivity is expected to be increased by 25 %. It is important, however, to keep in mind that adding beyond four layers or so of graphene has a side effect of resonance broadening. As has just been mentioned, the resonance linewidth is about tripled for ten layers of graphene. In this case, the small gain in optical sensitivity is clearly outweighed by the larger loss in resonance linewidth. For optimum performance, the number of graphene layers is therefore to be reasonably kept between 1-3 layers.

Figure 6.19. Percentage increase in optical sensitivity of graphene-coated surface compared to bare gold SPR surface as a function of the number of graphene layers. Graph is taken from reference [109].

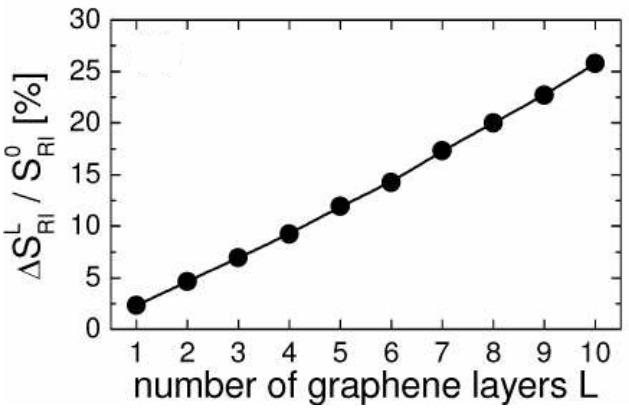

6.2.6. Experimental Results of SPR Biosensing

The model system chosen for SPR biosensing tests in this work is the biotin-streptavidin couple. It is a well-known system commonly used in typical biosensing experiments. The very high binding affinity between biotin and streptavidin makes this system suitable for biosensor testing.

Figure 6.20 shows the obtained sensorgram of biotin-streptavidin binding response on conventional SPR surface, i.e., gold-coated glass substrate functionalized with thiol SAM, measured with Autolab SPR instrument.

Figure 6.20. Sensorgram of the biotin-streptavidin binding response on conventional SPR surface.

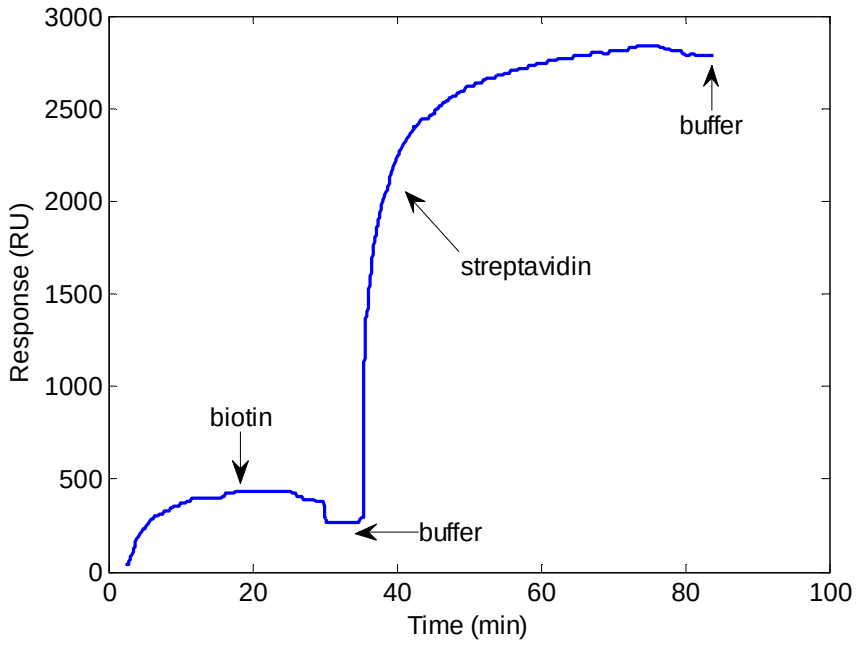

The detailed experimental sequence is as follows. Gold-coated glass substrate used as SPR sensor chip is first functionalized with self-assembled 11-mercaptoundecanoic acid (MUA) on gold surface subsequently activated by EDC/NHS chemistry as described in Section 6.1. The initial SPR reference is then established by the injection of PBS (phosphate-buffered saline) buffer solution. Solution of biotinylated BSA (bovine serum albumin) with a concentration of 0.1 mg/L, which is equivalent to 1.5 μM, is then injected until the saturation of the measured response. This is then followed by rinsing with PBS buffer to wash off

biotin molecules not adsorbed or immobilized on the sensor surface. Solution of streptavidin with a concentration of 0.01 mg/L, which is equivalent to 0.16 μM is subsequently injected until the saturation of the measured response. This is finally followed by another rinsing with PBS buffer to wash off excess streptavidin molecules.

Figure 6.21 shows the SPR curves corresponding to the initial SPR reference, the steady-state immobilization of biotinylated BSA, and the final streptavidin binding on the conventional SPR surface from which the angular shifts can be clearly seen.

Figure 6.21. Experimental SPR curves on conventional SPR surface. Initial SPR reference is shown by the solid black curve. SPR curve following biotin binding is shown by the dashed red curve. Final streptavidin binding is shown by the dotted green curve.

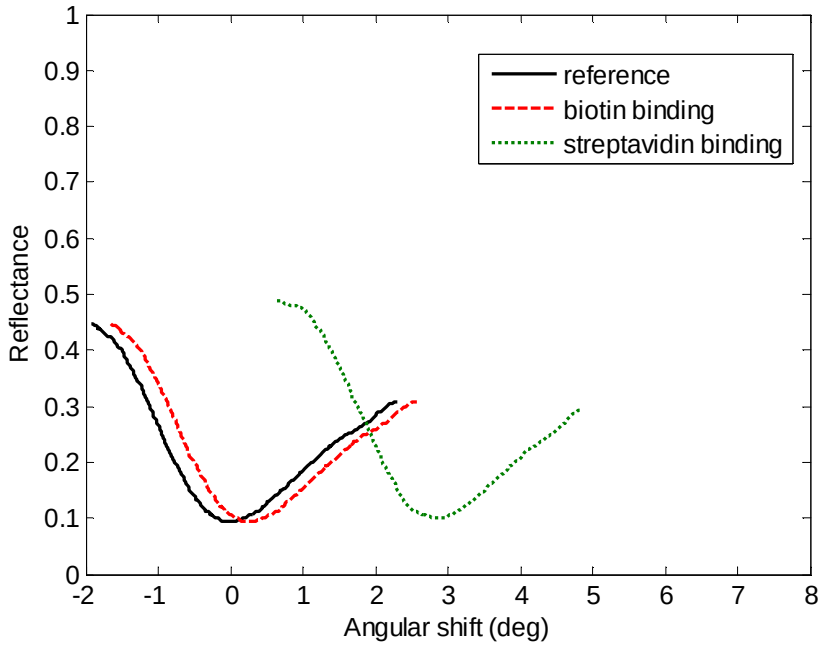

Similar biotin-streptavidin binding experiment is also conducted on the graphene-based SPR surface. It follows the same sequence directly starting from the injection of biotinylated BSA. Figure 6.22 shows the obtained sensorgram of biotin-streptavidin binding response on graphene-based SPR surface measured with Autolab SPR instrument. Figure 6.23 shows the associated SPR curves corresponding to the initial SPR reference, the steady-state immobilization of biotinylated BSA, and the final streptavidin binding.

Figure 6.22. Sensorgram of the biotin-streptavidin binding response on graphene-based SPR surface.

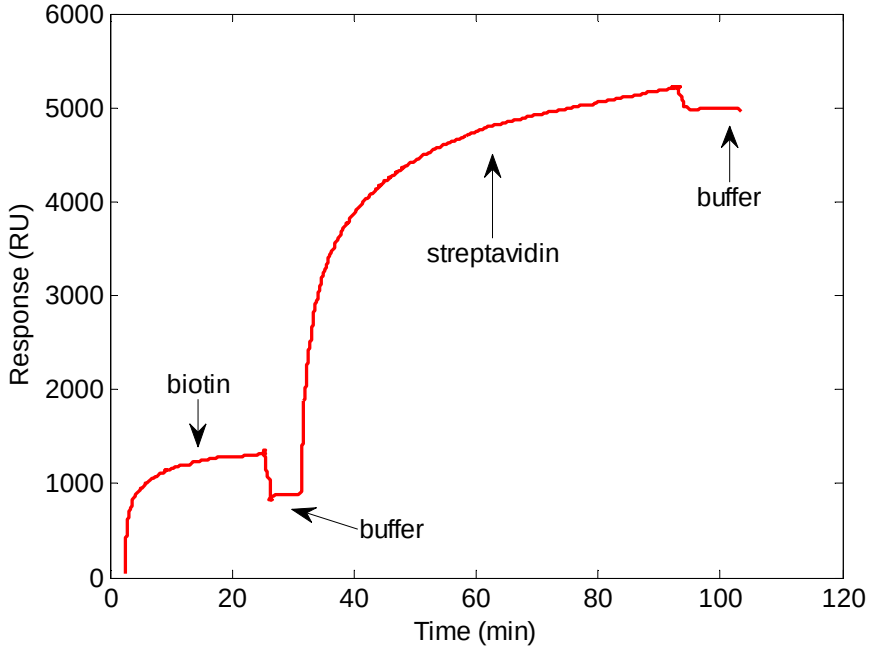

Figure 6.23. Experimental SPR curves on graphene-based SPR surface. Initial SPR reference is shown by the solid black curve. SPR curve following biotin binding is shown by the dashed red curve. Final streptavidin binding is shown by the dotted green curve.

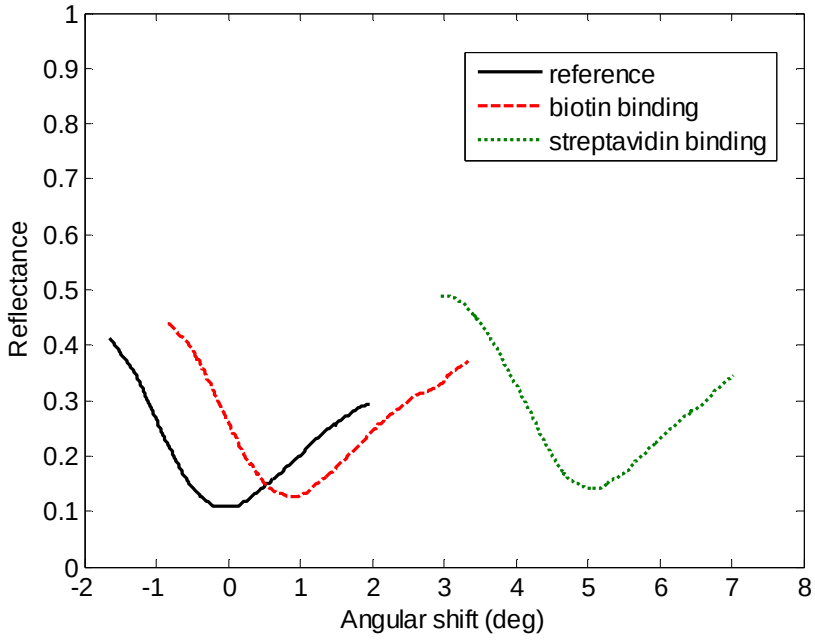

To analyze the obtained sensorgrams to compare graphene-based and conventional SPR surfaces, two cases can be distinguished: primary binding of biotinylated BSA and secondary binding of streptavidin. In the first case, the measured response upon primary steady-state biotinylated BSA immobilization on the graphene-based SPR surface is 896 RU. In contrast, the measured response following steady-state immobilization of biotinylated BSA on the conventional SPR surface is only 264 RU. The measured response on the graphene-based surface in this case is therefore amplified by a factor of 3.40 compared to that on the conventional SPR surface. For the second case, the measured response upon streptavidin binding is 5000-896 = 4104 RU for the graphene-based surface. For the conventional SPR surface, the response following the binding of streptavidin is only measured to be 2780-264 = 2516 RU. This amounts to a sensitivity amplification factor of 1.63, about half the amplification factor for the binding of biotinylated BSA.

To further understand the sensitivity enhancement, one should always keep in mind that the overall sensitivity of an SPR biosensor as expressed by Equation (3.1) is in fact determined by both the intrinsic optical sensitivity of the SPR sensor and the characteristics of the surface functionalization. Considering the optical sensitivity contribution, it has been theoretically predicted that the incorporation of graphene only adds 2.5 % per layer to the optical sensitivity of SPR sensors. For bilayer graphene in this experiment, the expected increase in optical sensitivity is therefore 5 %. The measured percentage increase in sensitivity, 240 % for biotin and 63 % for streptavidin, clearly exceeds by a significant amount this 5% increase theoretically predicted considering the optical contribution alone. Therefore, the extra factor in biosensing sensitivity enhancement of the graphene-based surface can be attributed to the increase of its surface functionalization efficiency. This shows that the sensitivity amplification is mainly dominated by the unique surface physicochemical properties of the graphene layer.

It is also to be noted that apart from an initial reference shift of about 0.8° shown in Figure 6.18, the form of the SPR curves are fairly identical in terms of resonance linewidth for both the graphene-based and the conventional SPR surfaces, i.e., no SPR linewidth broadening is observed due to the graphene overlayer. Together with higher sensitivity as can be easily seen by comparing Figures 6.21 and 6.23, it makes the figure-of-merit of the graphene-based surface more significant compared to that of conventional SPR. In addition, the same experimental setup was used for both surfaces and no instrumental adjustment

was necessary when changing the sensor chips. This shows that the graphene-based SPR surface can easily be used in place of conventional SPR surface without any modification to the measurement system. The graphene-based SPR surface can thus be readily integrated into the existing SPR technology. Moreover, the signal generated upon immobilization and binding is much stronger on the graphene-based surface compared to conventional SPR structure. Since the instrumental setup is identical in the two cases, the signal-to-noise ratio of the graphene-based sensor surface is clearly enhanced. Therefore, this novel structure potentially allows a considerably lower limit of detection to be achieved.

Another distinctive advantage of graphene-based SPR structure is that sophisticated or susceptible surface functionalization is not required as in conventional SPR. Nevertheless, if necessary, chemical modification of graphene to introduce additional functional groups could be easily performed [110, 111]. In particular, the introduction of functional polymer matrices to extend the two-dimensional surface into a three-dimensional sensing volume can potentially boost the already observed sensitivity enhancement even further [112]. This is in fact the kind of strategy used in Biacore CM5 sensor chip that uses dextran matrices attached to thiol SAM to functionalize its SPR gold surface.

Lastly, since the sensitivity enhancement mechanism of the graphene-based SPR surface is mainly dominated by its surface physicochemical rather than optical properties, the biosensing characteristics of the graphene-based SPR surface are likely to depend on the specific biomolecular sytems. For this reason, further study of the interaction between graphene and the biomolecular systems of interest is still needed before mature applications of graphene-based SPR surface can be materialized.

Chapter 7

Novel Optical Geometry in the Design of SPR Biosensors

In this chapter, the focus is shifted from ATR Kretschmann configuration to some more integrated geometry in the design of SPR biosensors. The novel designs considered here are integrated optical waveguide structures and some relatively simple arrays of micro/nanostructures.

7.1. Integrated Optical Waveguides

The first part of this chapter is devoted to the design of SPR biosensors based on integrated optical waveguides. Two types of optical waveguides are considered here. Simple waveguide structure is investigated first to serve as the basis of further elaboration. Building on the results developed for the simple waveguide structure, the long-period waveguide grating structure is subsequently discussed.

7.1.1. Simple Waveguide Structure

Integrated optical waveguide SPR sensors are particularly promising candidates for the development of miniaturized multi-channel sensing devices on a single chip. The excitation of surface plasmons in such devices is accomplished through waveguide coupling method briefly touched upon in Chapter 2. Surface plasmon resonance in an optical waveguide occurs when the wavelength-dependent propagation constant of the guided mode matches that of the surface plasmons. The result of this coupling is the transfer of electromagnetic energy from the guided mode to the surface plasmons. The subsequent dissipation of the electromagnetic energy in the metal causes a dip in the transmitted spectrum of the waveguide.

To illustrate this principle with an example, consider a simple slab waveguide structure schematically illustrated in Figure 7.1. The slab is assumed to have an infinite extension in the x-direction with the guided-wave propagation in the z-direction. An attractive choice for the substrate material is soda-lime silicate glass from which the waveguide core can be easily fabricated by ion-exchange process. Ion-exchanged glass waveguides are particularly inexpensive, compatible with optical fibers, and both mechanically and chemically robust. For the cladding

layer, magnesium fluoride, a commonly used optical material for multilayer interference filters, is a convenient choice. The metal is chosen to be gold and the superstrate in contact with the metal, i.e., the sensed dielectric medium is water.

Figure 7.1. Schematic illustration of simple slab waveguide structure. Guided-wave propagation is in the z-direction. The slab is assumed to have an infinite extension in the x-direction.

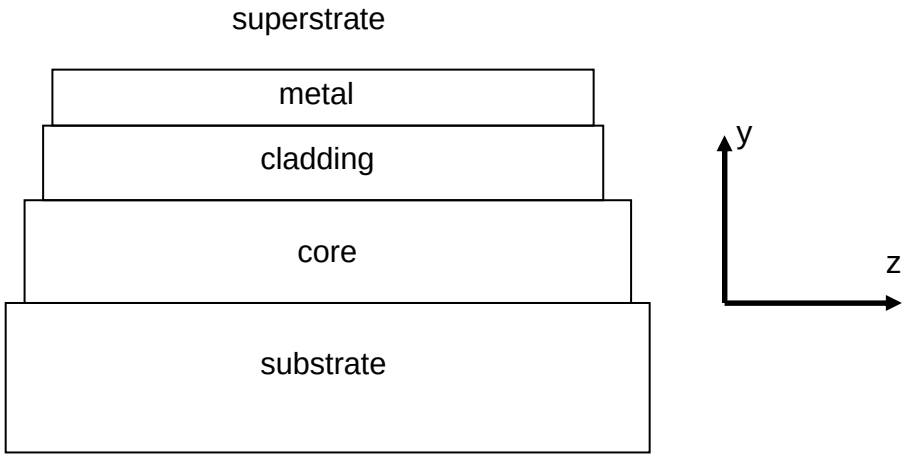

The thickness of the different layers of the waveguide is as follows: 2 µm for the core, 400 nm for the cladding, and 40 nm for the metal. The wavelength range considered here is from 650 nm to 850 nm. The refractive indices are taken as 1.512 for the substrate, 1.521 for the core, and 1.330 for the superstrate. For the cladding, as magnesium fluoride is only weakly birefringent, an average value of 1.378 is taken for its refractive index. To gain substantial computational time for the numerical evaluation presented below, the refractive indices for the substrate, waveguide core, waveguide cladding, and superstrate are assumed to be approximately constant throughout the wavelength range considered here. This assumption is justified by the fact that the dielectric dispersion of insulators is negligible over the relatively narrow wavelength range under consideration. The dielectric dispersion of metals, however, is non-negligible and it must be properly accounted for as discussed in Chapter 4.

Relevant characteristics of the modes supported by the waveguide such as effective refractive index, modal attenuation, and field distribution can be conveniently evaluated using a numerical mode solver. In this work, a commercial mode solver (Lumerical MODE Solutions) was used for these purposes. Figures 7.2 and 7.3 show the calculated magnetic field intensity distributions at the wavelength of 730 nm for the waveguide with the parameters mentioned above.

Figure 7.2. Distribution of magnetic field intensity of the fundamental core mode (TM_0) at the wavelength of 730 nm. The color scale shows refractive index distribution.

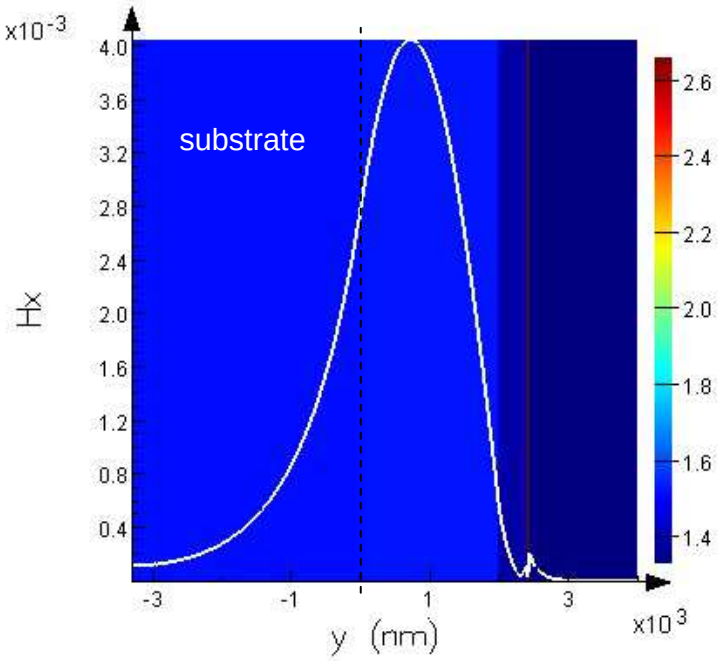

Figure 7.3. Magnetic field intensity distribution of the surface plasmons mode at the wavelength of 730 nm. The color scale shows refractive index distribution.

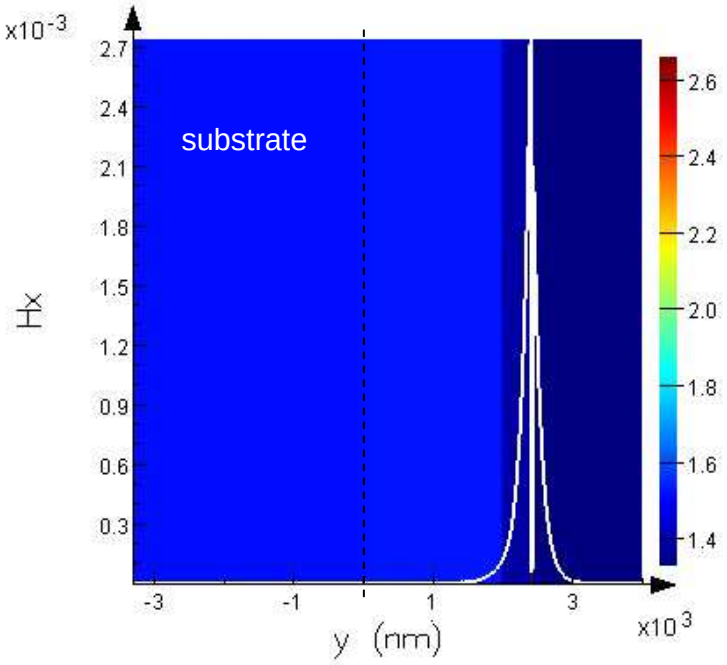

In an optical waveguide, the effective refractive index (modal refractive index) of a guided mode n_{eff} at the wavelength λ is derived from the real part of the propagation constant of the mode β according to

$$\mathrm{Re}\{\beta\} = \frac{2\pi}{\lambda} n_{eff} \tag{7.1}$$

The calculated dispersion of the effective refractive indices of these modes as a function of wavelength is shown in Figure 7.4. Because surface plasmons mode only exists in TM polarization, only the fundamental TM_0 mode is considered for the guided mode.

Figure 7.4. The effective refractive index (modal index) of the fundamental TM mode of the waveguide is shown by the dashed curve. That of the surface plasmons mode is shown by the solid curve.

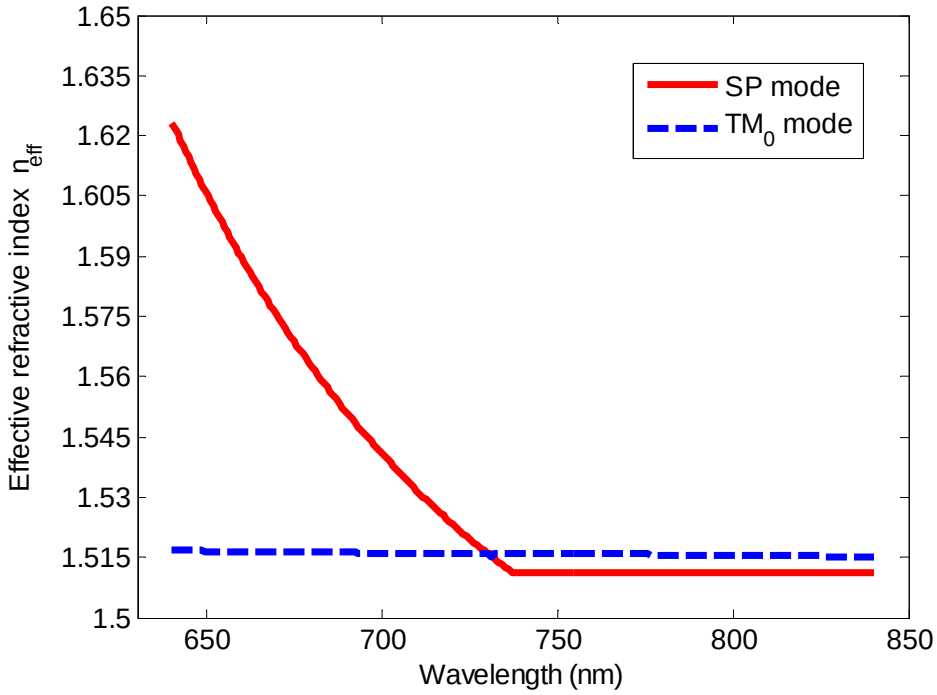

Figure 7.4 shows that the surface plasmons mode is much more dispersive compared to the fundamental guided mode. At approximately 730 nm, the effective index of the surface plasmon mode becomes equal to the effective index of the fundamental TM mode. At this point, the fundamental TM mode will have the highest coupling efficiency to the surface plasmon mode. As a result, the TM waveguide mode suffers from high loss at this wavelength because energy from

the waveguide mode will couple into the high loss surface plasmon mode. It is also interesting to notice the drastic change in the slope of the surface plasmons mode at 736 nm. At this point, its modal refractive index is 1.512 which is the value of the refractive index of the substrate. As a result, the surface plasmons mode is no longer confined to the metal layer and begins radiating power into the substrate.

Figure 7.5 shows the transmission spectrum of the waveguide as a function of wavelength based on the calculated modal attenuation. When the refractive index of the dielectric superstrate is 1.330, there is a resonance dip at the wavelength of 730 nm. This resonance dip shifts to 736 nm when the refractive index of the dielectric superstrate is increased to 1.340.

Figure 7.5. Waveguide transmission spectra when the refractive index of the dielectric superstrate is 1.330 (solid blue curve) and 1.340 (dashed red curve).

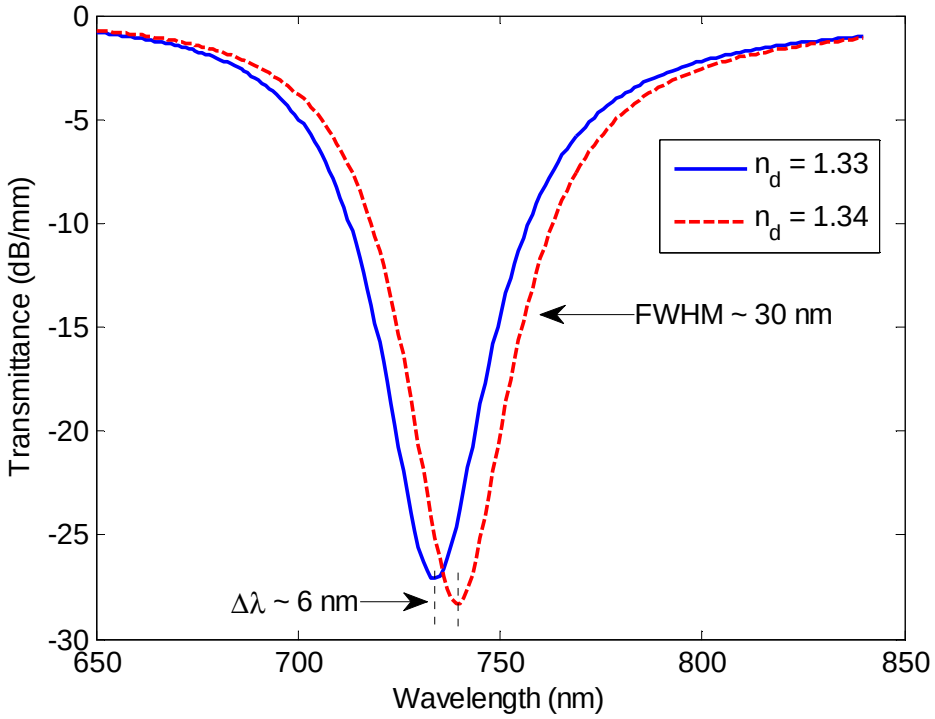

The refractive index sensitivity of this waveguide is therefore easily evaluated to be 600 nm/RIU. It is a few times lower than that of the most basic SPR design in Kretschmann configuration with an operating wavelength of 760 nm which is 4400 nm/RIU as discussed in Chapter 4. However, the resonance linewidth of this slab waveguide structure is only around 30 nm. This results in a figure-of-merit of

approximately 20, roughly half the figure-of-merit of the most basic SPR design in Kretschmann configuration which is 37. Hence as far as the sensitivity is concerned, this simple slab waveguide structure does not offer any significant advantage over the most basic SPR design in Kretschmann configuration. The field penetration depth into the sensed dielectric medium of this simple slab waveguide, as can be seen from Figure 7.3, is however around 500 nm, which is almost twice the field penetration depth of the most basic SPR design in Kretschmann configuration.

7.1.2. Long-Period Waveguide Grating

In this section, the simple slab waveguide considered previously is modified to significantly increase its refractive index sensitivity. The basic idea here is to employ long-range surface plasmons mode. To do this, the refractive index of the cladding layer has to be very similar to that of the superstrate. The refractive index of the core layer should not be too different either. In this case, the modal index of the guided mode will be very close to the effective refractive index of the long-range surface plasmons mode over a large range of wavelength. If direct waveguide coupling method is used to excite the long-range surface plasmons, broadband attenuation instead of a sharp resonance dip will be observed in the resulting transmission spectrum of the waveguide. To circumvent this issue, the excitation of the long-range surface plasmons by a guided mode can be mediated by a corrugated grating at the core-cladding interface along the propagation direction of the guided mode. For a given desired resonance wavelength, the required period of the grating is considerably much larger compared to the wavelength. For this reason, the resulting structure is called long-period waveguide grating (Figure 7.6).

The resonance wavelength λ_{res} of a long-period waveguide grating, i.e., the wavelength at which the coupling between the fundamental core mode and the cladding mode (in this case the long-range surface plasmons mode) is strongest, is obtained from the phase-matching condition

$$\mathrm{Re}\{\beta_{co} - \beta_{cl}\} = \frac{2\pi}{\lambda}\left(N_{co} - N_{cl}\right) = \frac{2\pi}{\Lambda} \tag{7.2}$$

evaluated at $\lambda = \lambda_{res}$ where β_{co} and β_{cl} are the wavelength-dependent propagation constants of the fundamental core and cladding modes, respectively, and Λ is the grating period. Equation (7.1) has also been used to replace the wavelength-dependent propagation constants in Equation (7.2) by the wavelength-

dependent modal indices N_{co} and N_{cl} for the fundamental core and cladding modes, respectively. Hence in terms of modal indices, the phase-matching condition takes the form

$$\frac{\lambda_{res}}{\Lambda} + N_{cl}^{\lambda_{res}} = N_{co}^{\lambda_{res}} \tag{7.3}$$

where $N_{cl}^{\lambda_{res}}$ and $N_{co}^{\lambda_{res}}$ are the modal indices of the cladding and core modes, respectively, evaluated at the wavelength λ_{res}. Once the resonance wavelength is chosen, the required grating period is then determined from

$$\Lambda = \frac{\lambda_{res}}{\left(N_{co}^{\lambda_{res}} - N_{cl}^{\lambda_{res}}\right)} \tag{7.4}$$

It is easy to see from Equation (7.4) that when the modal indices of the core and cladding modes are very similar, the grating period becomes significantly long compared to the resonance wavelength.

Figure 7.6. Structure of an SPR long-period waveguide grating. Propagation direction is in the z-direction. Λ is the grating period and h is the corrugation depth.

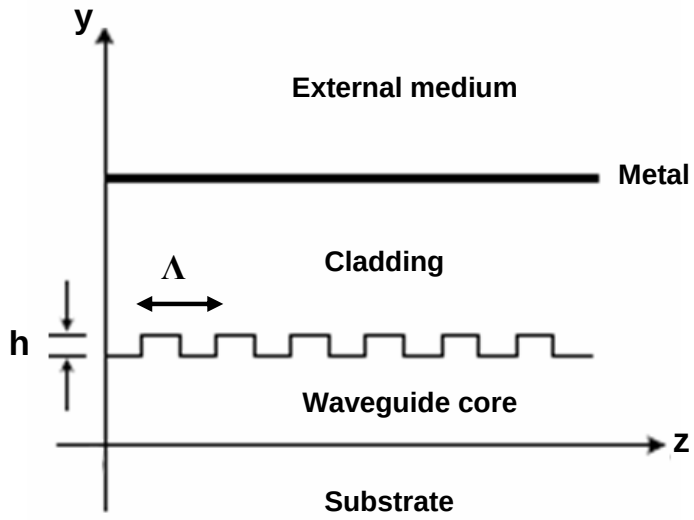

Based on coupled-mode theory [113, 114], the transmission T of a long-period waveguide grating of length L as a function of wavelength is given by the following equation

$$T = 1 - \frac{\kappa^2}{\kappa^2 + \xi^2} \sin^2\left(L\sqrt{\kappa^2 + \xi^2}\right) \tag{7.5}$$

where κ is the grating coupling coefficient and ξ is a detuning or phase mismatch parameter given by

$$\xi = \frac{2\pi}{\lambda}\left(N_{co} - N_{cl}\right) - \frac{2\pi}{\Lambda} \tag{7.6}$$

The grating coupling coefficient κ is determined by the spatial overlap of the electromagnetic fields Ψ_{co} and Ψ_{cl} of the core and cladding modes, respectively in the guiding film region

$$\kappa \propto \left(n_{co}{}^2 - n_{cl}{}^2\right) \int \Psi_{co} \Psi_{cl} \tag{7.7}$$

where n_{co} and n_{cl} are the refractive indices of the core and cladding layers, respectively.

For a given set of waveguide parameters, i.e., thickness and refractive index of the various layers, the grating coupling coefficient depends on the specific geometry of the grating, e.g., the corrugation depth and its form (sinusoidal, square, triangular, etc). For cladding layer thickness between 1-3 μm and corrugation height in the range of 50-100 nm, the typical value of the grating coupling coefficient is around 2 x 10^{-4} to 2 x 10^{-3} μm^{-1} [115]. Equation (7.6) shows that at resonance, $\xi = 0$ so that the waveguide transmission T from Equation (7.5) is minimum when $\kappa L = \pi/2$. This is the condition for maximum contrast. Given the above range of values for the grating coupling coefficient, to satisfy the condition for maximum contrast, the interaction length of the grating L is typically between 1-10 mm.

Consider now a design example of an SPR long-period waveguide grating structure with a center operating wavelength around 820 nm. The thickness of the different layers of the waveguide is as follows: 2 μm for the core, 2 μm for the cladding, and 15 nm for the metal. The wavelength range considered here is from 700 nm to 900 nm. The refractive indices are taken as 1.29 for the substrate, 1.35 for the core, and 1.330 for both the cladding and the superstrate. To gain substantial computational time for the numerical evaluation, the refractive indices

for the substrate, waveguide core, waveguide cladding, and superstrate are again assumed to be approximately constant throughout the wavelength range considered here. The dielectric dispersion of gold is however properly accounted for by the procedure discussed in Chapter 4.

Figure 7.7. Distribution of magnetic field intensity of the fundamental core mode (TM_0) at the wavelength of 820 nm.

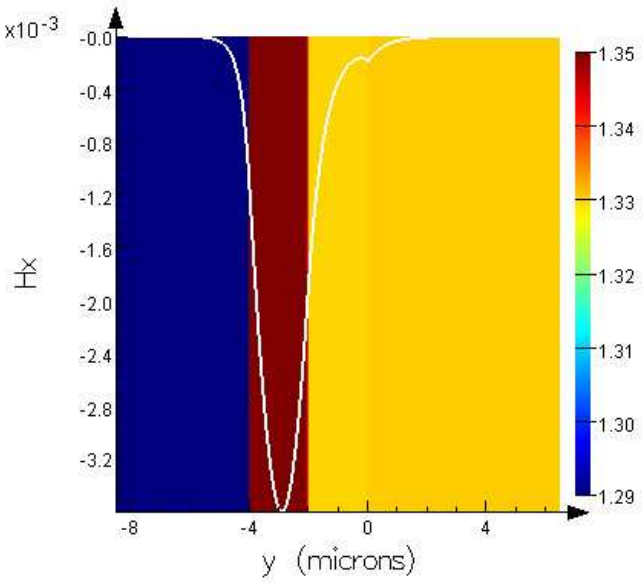

Figure 7.8. Magnetic field intensity distribution of the long-range surface plasmons mode at the wavelength of 820 nm.

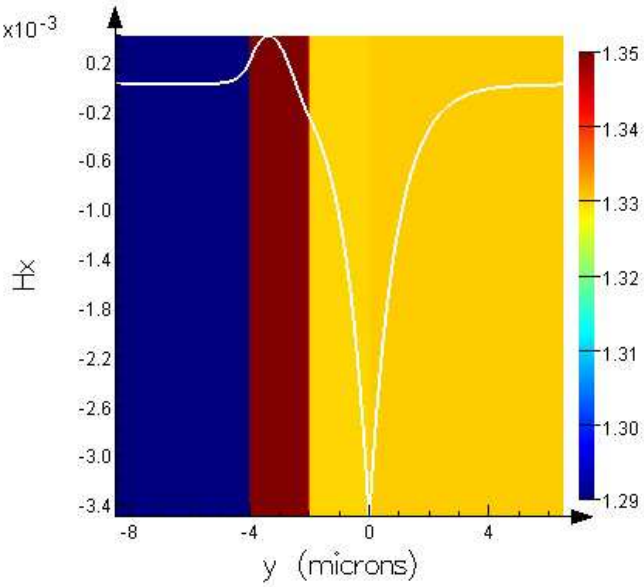

Figures 7.7 and 7.8 show the calculated magnetic field intensity distributions of the fundamental core mode (TM_0) and the long-range surface plasmons mode of this waveguide at the wavelength of 820 nm. These modes are calculated for smooth interfaces ignoring the presence of the grating. The perturbation of the grating on the electromagnetic field distribution of these modes is assumed to be negligible. Considering a maximum corrugation depth of 100 nm, which is only 0.5 % of the dimension of the core and cladding layers, this assumption is readily justified.

Figure 7.9. Modal indices of the fundamental core mode (dashed red curve) and the long-range surface plasmons mode (solid blue curve) as a function of wavelength. Refractive indices are 1.29 for the substrate, 1.35 for the waveguide core, and 1.33 for the waveguide cladding and superstrate. The grating period is 95 µm and the interaction length is 6 mm. The thickness is 2 µm for both the core and cladding regions. The gold layer is 15 nm thick

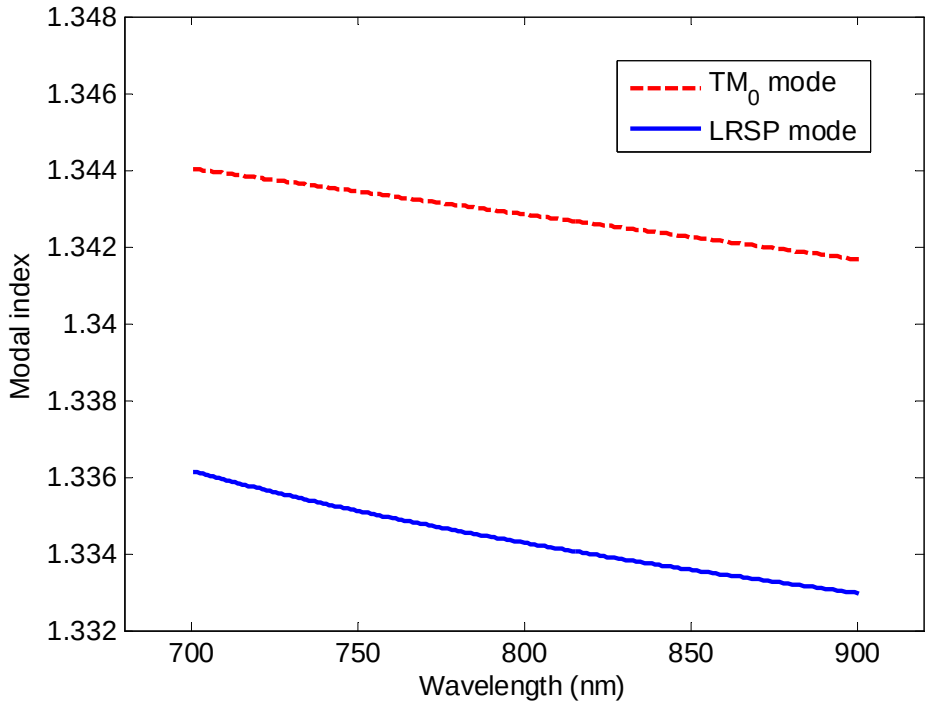

Figure 7.9 shows the calculated wavelength-dependent modal indices of the fundamental guided TM_0 and the long-range surface plasmons modes as a function of wavelength. Using this result and choosing 820 nm as the resonance

wavelength, the required grating period calculated from Equation (7.4) is 95 µm. To complete the design, the grating interaction length L is chosen to be 6 mm. The necessary grating coupling coefficient κ is then obtained from the maximum contrast condition as $\kappa = \pi/(2L)$.

The solid red curve in Figure 7.10 shows the transmission of the long-period waveguide grating calculated using the results presented in Figure 7.9 and Equations (7.5)-(7.6). Similar calculations can be performed for different values of the refractive index of the superstrate. The results are also presented in Figure 7.10 as the dashed blue curve for superstrate refractive index of 1.3305 and the dotted black curve for superstrate refractive index of 1.3295.

Figure 7.10. Long-period waveguide grating transmission as a function of the refractive index of the external dielectric medium n_d. Refractive indices are 1.29, 1.35, and 1.33 for the substrate, waveguide core, and waveguide cladding, respectively. The grating period is 95 µm and the interaction length is 6 mm. The thickness is 2 µm for both the core and cladding regions. The gold layer is 15 nm thick.

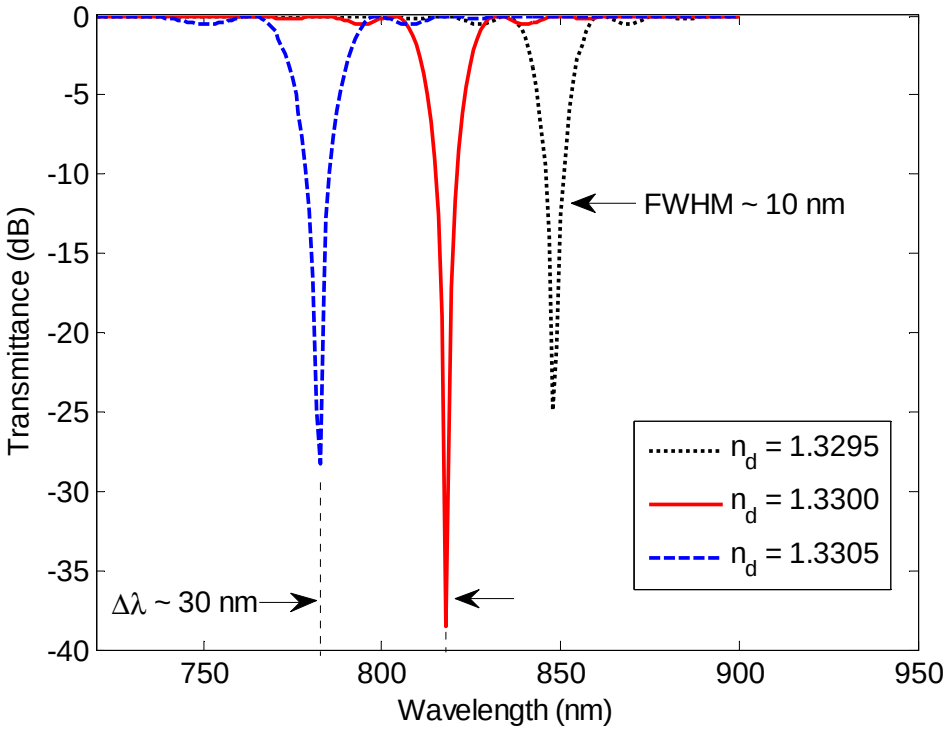

Figure 7.10 shows that increasing the refractive index of the external dielectric medium shifts the resonance towards shorter wavelength. The refractive index sensitivity is 60000 nm/RIU. Together with a very narrow resonance linewidth of 10 nm, this results in a very high figure-of-merit of 6000. Considering typical spectrometers with wavelength noise resolution of 0.15 pm [116, 117], the corresponding refractive index resolution in this best-case scenario can reach 2.5 x 10^{-9} RIU. In addition, as can be seen from Figure 7.8, the field penetration depth into the sensed dielectric medium for this SPR structure is around 3 µm. Despite the very high sensitivity and figure-of-merit, the dynamical measurement range of this particular SPR structure is however quite limited. In fact, the maximum change of refractive index that can be effectively discerned by this SPR construct is estimated to be approximately 0.005 RIU. Beyond this limiting value, interband transitions in metals are bound to get in the way. There is therefore a quite common tradeoff between high sensitivity and narrow dynamical range.

Figure 7.11. Long-period waveguide grating transmission as a function of the refractive index of the external dielectric medium n_d. Refractive indices are 1.29, 1.36, and 1.33 for the substrate, core, and cladding regions, respectively. The grating period is 50 µm and the interaction length is 6 mm. The thickness is 1.5 µm for the core and 3 µm for the cladding regions. The gold layer is 15 nm thick.

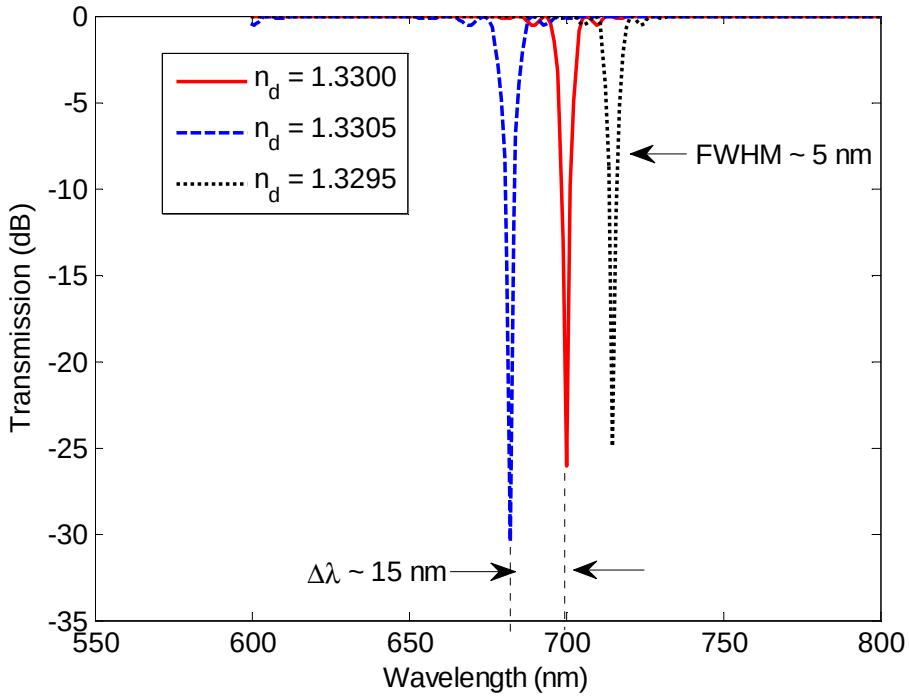

Figure 7.11 shows the transmission of a modified long-period waveguide grating. In this modified version, only the refractive index of the waveguide core is changed from 1.35 to 1.36, the refractive indices of the other layers are left unaltered. The thickness of the waveguide core is now 1.5 µm and that of the cladding region is 3 µm. The gold layer is 15 nm thick and the grating length is 6 mm. Following the same approach presented earlier, based on the calculated wavelength-dependent modal indices of this modified waveguide, the grating period can be determined to be 50 µm for a center resonance wavelength of 700 nm corresponding to superstrate refractive index of 1.3300. With this design, the refractive index sensitivity is now 30000 nm/RIU, which is half the refractive index sensitivity of the previous structure. The resonance linewidth with the new design is however only 5 nm, which is narrower by a factor of 2 compared to the previous structure. As a result, the very high figure-of-merit of 6000 is identical for both design examples.

Despite the very narrow resonance linewidth together with very high refractive index sensitivity and figure-of-merit allowing the detection of extremely small refractive index variation, there are several drawbacks associated with long-period waveguide grating SPR structures. The limited dynamical range has already been previously mentioned. The long interaction length could be a potential handicap for miniaturization. Lastly, broadband optical excitation is necessary and optimum coupling conditions to the waveguide may vary greatly for different wavelengths spanning such a broad excitation spectrum.

7.2. Micro/nanostructures

The second part of this chapter is devoted to the design of SPR biosensors based on some relatively simple arrays of micro/nanostructures. Two types of arrays of micro/nanostructures are considered here. Arrays of sub-wavelength holes on a metallic film are investigated first. The complementary “negative (or positive?) image” structures, namely arrays of sub-wavelength metallic islands, are subsequently discussed.

7.2.1. Arrays of Sub-wavelength Holes

The presence of sub-wavelength holes in an opaque metal film leads to a variety of unexpected optical properties [118]. Of particular interest is the enhanced transmission of light through the holes which is dubbed extraordinary optical transmission. This enhanced transmission is attributed to initial scattering

of the incident light into surface plasmons that penetrate the sub-wavelength holes and are again scattered as transmitted light on the other side of the film. The light transmission through sub-wavelength holes is defined as extraordinary when it is so enhanced that the transmission efficiency of the holes is larger than unity, in other words, when the flux of photons per unit area emerging from the holes is larger than the incident flux per unit area. Note that the transmitted intensity in this definition is normalized to the area of the holes while the incident light covers not only the holes but the whole sample area. This is the reason why the transmission efficiency can be larger than unity.

The extraordinary transmission mediated by surface plasmons as described above depends on the combination of wavelength and holes geometry (shape, orientation, and periodicity) as well as the dielectric constants of the involved media. The latter has motivated the use of sub-wavelength holes arrays for biosensing applications. This has several unique advantages. Firstly, the instrumentation is much simpler compared to other SPR structures. In fact, its transmission mode operation at normal incidence greatly simplifies the optical setup. Secondly, the relatively small footprint of an array of sub-wavelength holes is particularly attractive for sensor miniaturization. Thirdly, arrays of sub-wavelength holes can be easily realized by focused ion beam (FIB) milling or electron beam lithography. Such fabrication process can however be much more time-consuming compared to the metal thin film deposition process for classical SPR sensor chips. Finally, the optical response of sub-wavelength holes arrays can be tuned by simply changing the holes geometry.

Consider as an example an array of sub-wavelength circular holes arranged periodically in a square lattice. These holes are made in gold film supported on glass substrate and the diameter of the holes is 150 nm. For gold thickness of 40 nm and array period of 520 nm, the experimentally obtained refractive index sensitivity is only 20 nm/RIU [119]. Changing the gold thickness to 100 nm and the array period to 450 nm, the experimentally obtained refractive index sensitivity increases to around 300 nm/RIU [120].

The enhanced transmission from an array of sub-wavelength holes is quite influenced by the shape of the holes. In fact, it has been shown in the literature that the extraordinary transmission obtained from rectangular holes is stronger compared to that from circular holes [121]. This is likely due to the strong electromagnetic field concentration around the sharp corners present in rectangular holes. The shape of the sub-wavelength holes analyzed in this work is therefore chosen to be square which is a rectangle with all four sides equal. This

convenient choice makes the response of the sub-wavelength holes array symmetrical with respect to the polarization of the incident light which is directed along either side of the rectangle.

Figure 7.12 illustrates an array of sub-wavelength square holes arranged in a periodical square lattice on gold film. As a specific example, consider square holes whose side is 200 nm arranged in a square lattice whose period is 1000 nm. The thickness of the gold film is 100 nm and the refractive index of the substrate is taken as 1.33 which is identical to that of the superstrate. This deliberate choice of refractive index is made so as to investigate whether there is any significant long-range surface plasmons effects on this structure. Although the gold film here is much thicker than the field penetration depth into the metal, coupling between surface plasmons from the substrate and superstrate may still occur around the edges of the holes where the effective separation distance between the two dielectric media by a metallic material is less than the thickness of the gold film.

Figure 7.12. Array of sub-wavelength square holes arranged in a periodical square lattice on gold film. Here, *a* is the side of the square holes, *p* is the array period, and *t* is the thickness of the gold film. The metallic film is in the x-y plane and the light transmission is along the z-direction.

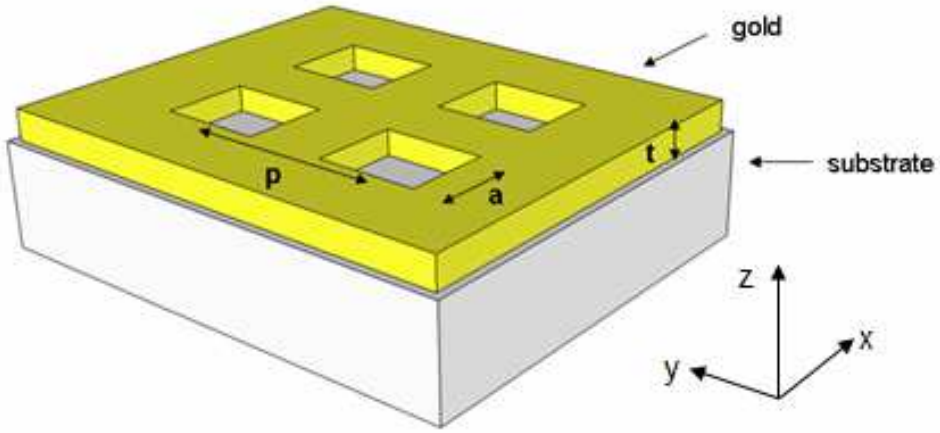

In this work, the transmission of sub-wavelength holes array is simulated by using a commercial finite-difference time-domain (FDTD) software (Optiwave OptiFDTD). The solid red curve in Figure 7.13 shows the calculated transmittance from this specific array of sub-wavelength holes when the refractive index of the superstrate is 1.33. It is essential to note that the transmittance shown in Figure

7.13 is not normalized to the holes area, it is calculated with respect to the whole surface area instead. The transmission normalized to the holes area can be easily calculated by multiplying the values displayed in Figure 7.13 by a factor of $(1000/200)^2 = 25$ which is the ratio of the whole surface area to the holes area. The extraordinary transmission of this array of sub-wavelength holes is therefore 25 times the values shown in Figure 7.13.

The position of the transmission peak of an array of sub-wavelength holes can be estimated by using phase-matching principle. At normal incidence, the required wave vector component to match that of the surface plasmons is obtained from the two-dimensional light wave scattering by the array of sub-wavelength holes. A scattering event of order (u,v) modifies the wave vector of the incident light by $u(2\pi/p)$ in the x-direction and $v(2\pi/p)$ in the y-direction.

Figure 7.13. Calculated transmission for two different values of superstrate refractive index n_d (1.33 for solid red curve and 1.43 for dotted blue curve) from an array of sub-wavelength square holes on gold film arranged in a periodical square lattice. Here, a = 200 nm, p = 1000 nm, and t = 100 nm. The refractive index of the substrate is taken as 1.33.

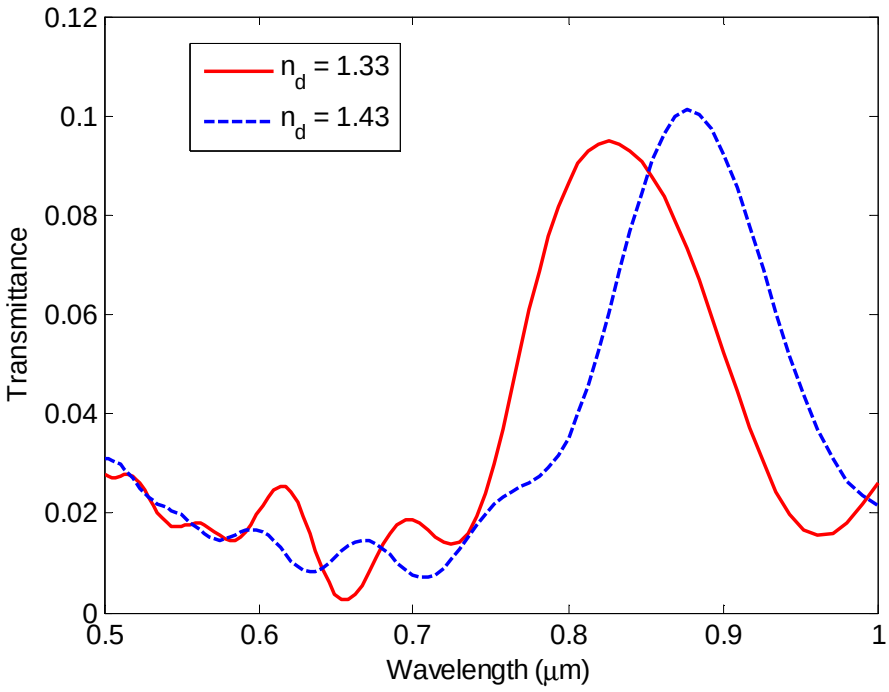

For a square array, the phase-matching condition at normal incidence takes the form

$$\beta_{sp} = \frac{2\pi}{\lambda}\left(\frac{\varepsilon_m \varepsilon_d}{\varepsilon_m + \varepsilon_d}\right)^{1/2} = \left[\left(u\frac{2\pi}{p}\right)^2 + \left(v\frac{2\pi}{p}\right)^2\right]^{1/2} \tag{7.8}$$

where ε_m and ε_d are respectively the dielectric constants of the metal and dielectric superstrate. The wavelength which corresponds to the transmission peak is therefore given by

$$\lambda_{\max} = \frac{p}{\sqrt{u^2 + v^2}}\left(\frac{\varepsilon_m \varepsilon_d}{\varepsilon_m + \varepsilon_d}\right)^{1/2} \tag{7.9}$$

It is important to keep in mind that Equation (7.9) is only a first order approximation because it does not take into account the presence of the holes with the associated scattering losses and it neglects the interference that gives rise to a resonance shift [122]. As a consequence, it often predicts peak positions at wavelengths shorter than those obtained by rigorous numerical simulation. For example, Equation (7.9) suggests that there is a transmission peak of order (1,1) at 700 nm for the array of sub-wavelength holes being discussed. However, the transmission peak shown by the solid red curve in Figure 7.13 obtained by more rigorous FDTD simulation is located at around 800 nm.

The calculated transmittance given by the same FDTD method from this specific array of sub-wavelength holes when the refractive index of the superstrate is increased to 1.43 is shown by the dotted blue curve in Figure 7.13. From the wavelength shift of the transmission peak, the refractive index sensitivity can be evaluated to be 500 nm/RIU. Although it is much higher compared to 20 nm/RIU reported in reference [119], it is only slightly better than the reported value of 300 nm/RIU in reference [120] and 400 nm/RIU in reference [123] using glass substrate.

Consider now a geometric modification of the array of sub-wavelength holes that has just been analyzed. In the modified version, the side of the square holes is 400 nm, the period of the square lattice is 1000 nm, and the thickness of the gold film is 20 nm. The refractive indices are left unaltered. Figure 7.14 shows the calculated transmittance from this modified array of sub-wavelength holes when the refractive index of the superstrate is 1.33 (solid red curve) and 1.43 (dotted blue curve). As in Figure 7.13, the transmittance shown in Figure 7.14 is

normalized to the whole surface area and not the holes area. Equation (7.9) suggests that there is a transmission peak at around 1350 nm which corresponds to the (1,0) or (0,1) scattering order.

Figure 7.14. Calculated transmission for two different values of superstrate refractive index n_d (1.33 for solid red curve and 1.43 for dotted blue curve) from an array of sub-wavelength square holes on gold film arranged in a periodical square lattice. Here, a = 400 nm, and p = 1000 nm, t = 20 nm. The refractive index of the substrate is taken as 1.33.

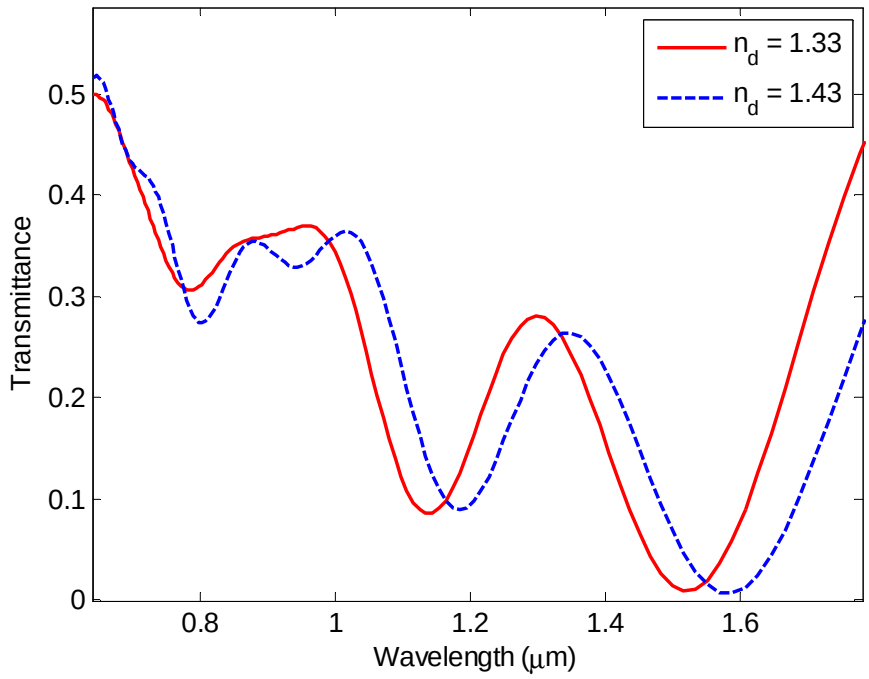

The transmission shown in Figure 7.14 is much higher compared to that presented in Figure 7.13. This is because for the structure evaluated in Figure 7.14, the thickness of the gold film is only 20 nm. The gold film in this case is semitransparent and no longer opaque giving rise to the high transmittance. The transmission peak at 1300 nm in Figure 7.14 is therefore a local one. From the wavelength shift of this transmission peak at 1300 nm, the refractive index sensitivity can be evaluated to be 400 nm/RIU.

Another interesting feature from Figure 7.14 is the near-zero transmittance around 1550 nm. The physical origin of this transmission minimum is not yet clear but it is likely due to destructive interference of surface plasmons modes in

the sub-wavelength holes. The wavelength corresponding to this transmittance minimum also changes when the refractive index of the superstrate is varied. From the wavelength shift of this transmission minimum, the refractive index sensitivity can be evaluated to be around 500 nm/RIU.

Figure 7.15. Electric field intensity distribution around one of the holes from Figure 7.14 at the wavelength of 1300 nm. The incident electric field is linearly polarized in the y-direction. The hole is in the center of the x-y plane delineated by the white dashed lines.

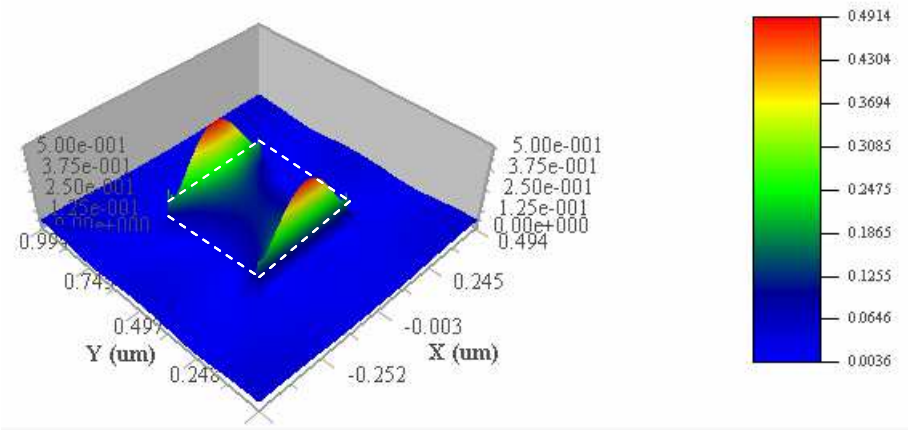

Figure 7.16. Electric field intensity distribution around one of the holes from Figure 7.14 at the wavelength of 1550 nm. The incident electric field is linearly polarized in the y-direction. The hole is in the center of the x-y plane delineated by the white dashed lines.

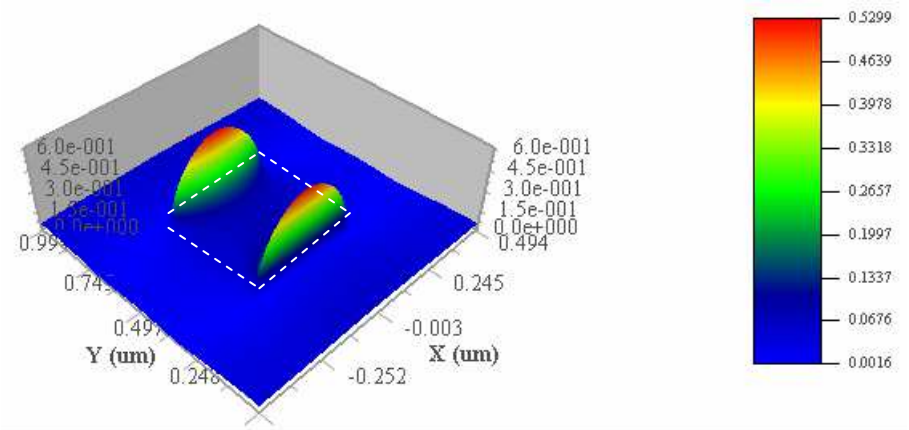

Figures 7.15 and 7.16 depict the electric field intensity distribution around one of the holes from the array whose transmittance is shown in Figure 7.14 at the

wavelengths of 1300 nm and 1550 nm, respectively. The slice here is parallel to the plane of the lattice (x-y plane) and passes through the middle of the gold film. These plots show that the electric field is strongest around the edges of the holes parallel to the electric field polarization direction of the incident light. For best biosensing sensitivity, the regions with the highest electric field intensity, i.e., the hot spots, on the sensor surface should ideally coincide with the locations where biomolecular interactions occur. Biomolecular receptors are usually attached on the functionalized metal SPR surface. The hot spots are therefore preferably located near the metal-dielectric interface which for an array of sub-wavelength holes is around the edges of the holes. Figures 7.15 and 7.16 suggest that this is the case.

7.2.2. Arrays of Sub-wavelength Islands

Whereas there is quite an abundance of published literature on arrays of sub-wavelength holes, the complementary "image" structures, namely arrays of sub-wavelength metallic islands have not been given much attention. Figure 7.17 shows a schematic illustration of an array of sub-wavelength square islands of gold arranged in a periodical square lattice.

Figure 7.17. Array of sub-wavelength square islands of gold arranged in a periodical square lattice. Here, *a* is the side of the square holes, *p* is the array period, and *t* is the thickness of the gold film. The two-dimensional square lattice is in the x-y plane and the light transmission is along the z-direction.

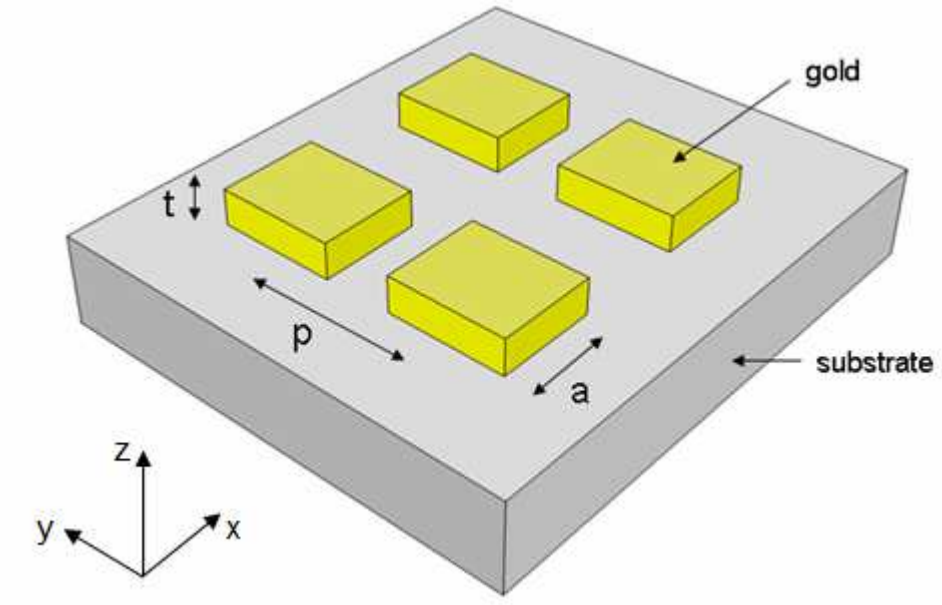

Consider an array of square sub-wavelength gold islands whose side is 400 nm arranged in a periodic square lattice whose period is 1000 nm. The thickness of the gold islands is 100 nm and the refractive index of the substrate is 1.33. In this work, the transmission of sub-wavelength metallic islands arrays is also simulated by using a commercial finite-difference time-domain (FDTD) software (Optiwave OptiFDTD).

The solid blue curve in Figure 7.18 shows the calculated transmittance from this specific array of sub-wavelength holes when the refractive index of the superstrate is 1.31. Equation (7.9) predicts a transmission peak of order (1,0) or (0,1) at around 1300 nm as well as another transmission peak of higher order, namely the (1,1) transmission peak at around 900 nm. These two transmission peaks are indicated in Figure 7.18. The transmittance at all neighboring points is however in general quite high. This is because the light wave can easily pass through the relatively wide space between the gold islands and therefore be transmitted.

Figure 7.18. Calculated transmission for two different values of superstrate refractive index n_d (1.31 for solid blue curve and 1.33 for dashed red curve) from an array of sub-wavelength gold islands arranged in a periodical square lattice. Here, a = 400 nm, and p = 1000 nm, t = 100 nm. The refractive index of the substrate is taken as 1.33.

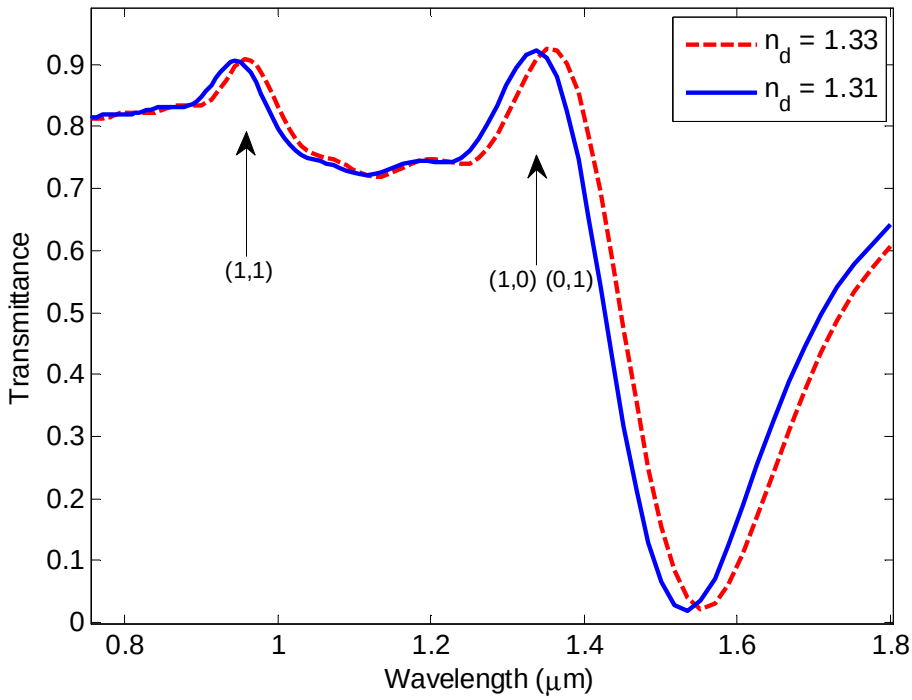

The dashed red curve in Figure 7.18 shows the calculated transmittance when the refractive index of the superstrate is increased to 1.33. From the wavelength shift of the (1,1) transmission peak at 950 nm, the refractive index sensitivity can be evaluated to be 700 nm/RIU. The (1,0) or (0,1) transmission peak at 1300 nm gives rise to a similar refractive index sensitivity of 750 nm/RIU.

At around 1550 nm, there is an interesting feature of near-zero transmittance. The physical origin of this transmission minimum is not yet clear but it is very likely due to the combined absorption by scattered surface plasmons modes of the periodic array of sub-wavelength gold islands. The wavelength corresponding to this transmittance minimum also changes when the refractive index of the superstrate is varied. From the wavelength shift of this transmission minimum, the refractive index sensitivity can be evaluated to be higher at around 900 nm/RIU.

Figure 7.19. Electric field intensity distribution around one of the gold islands from Figure 7.18 at the wavelength of 950 nm. The incident electric field is linearly polarized in the y-direction and the island is in the center of the x-y plane delineated by the white dashed lines.

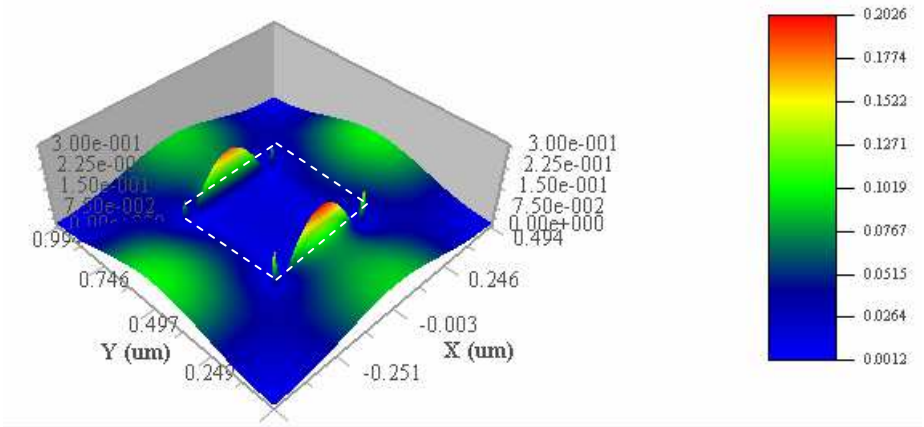

Figures 7.19, 7.20, and 7.21 depict the electric field intensity distribution around one of the islands from the array whose transmittance is shown in Figure 7.18 at the wavelengths of 950 nm, 1320 nm, and 1550 nm, respectively. The slice here is parallel to the plane of the lattice (x-y plane) and passes through the top of the gold islands in contact with the superstrate. These plots show that the electric field is strongest around the corners and edges of the gold islands. In this case,

more hot spots are therefore located near the metal-dielectric interface where biomolecular receptors can be attached once the gold surface is functionalized. This suggests that compared to arrays of sub-wavelength holes on metallic film, arrays of sub-wavelength metallic islands are better structures for SPR-based biosensing applications.

Figure 7.20. Electric field intensity distribution around one of the gold islands from Figure 7.18 at the wavelength of 1320 nm. The incident electric field is linearly polarized in the y-direction and the island is in the center of the x-y plane delineated by the white dashed lines.

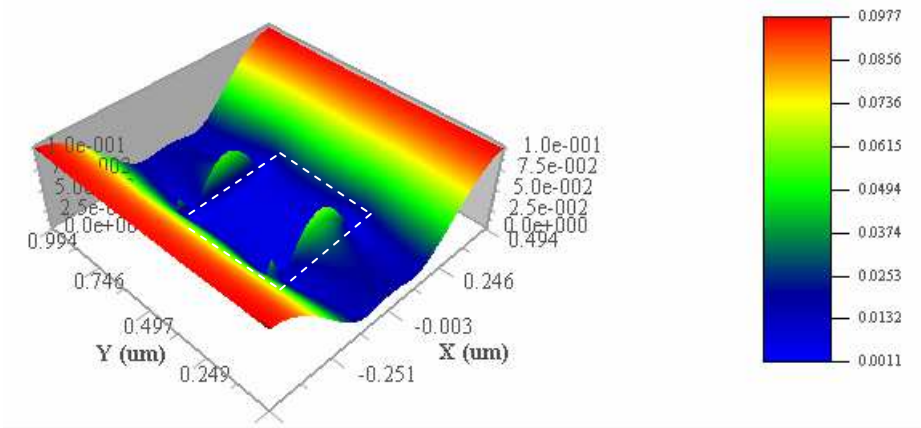

Figure 7.21. Electric field intensity distribution around one of the gold islands from Figure 7.18 at the wavelength of 1550 nm. The incident electric field is linearly polarized in the y-direction and the island is in the center of the x-y plane delineated by the white dashed lines.

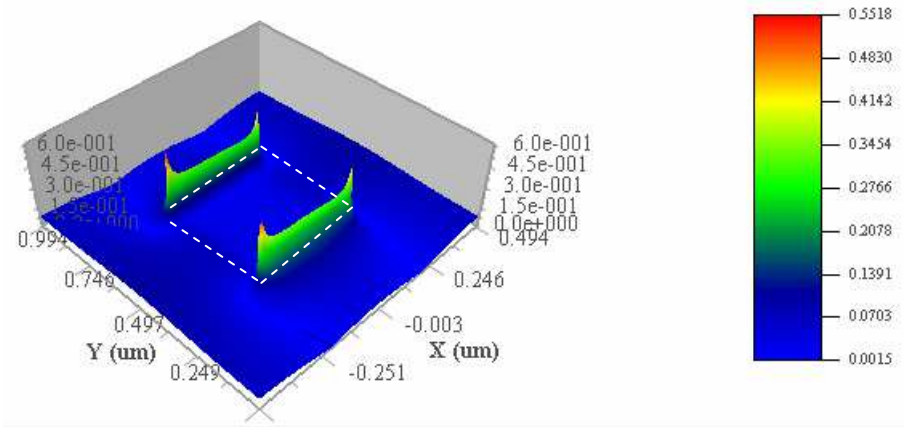

Figures 7.19 and 7.20 show that at the wavelengths of 950 nm and 1320 nm, some of the electric field is spread out in the space between the gold islands. This space is filled by the sensed dielectric medium which has negligible losses. As a result, the electromagnetic excitation can easily pass through this space so that the transmission at these wavelengths is very high. On the other hand, at the wavelength of 1550 nm, the electric field is entirely concentrated around the corners and edges of the gold islands as shown by Figure 7.21. Due to the high metallic losses, the field is rapidly attenuated in the gold layer so that the intensity of the transmitted light at this wavelength is near zero. The strong concentration of the entire electric field around the edges of the gold islands in contact with the sensed dielectric medium is however desirable for biosensing applications.

As a side note, Figure 7.18 shows completely different behavior in transmittance at 1300 nm and 1550 nm which are wavelengths of important significance in optical fiber telecommunications. The high near-unity transmission at 1300 nm and the low near-zero transmission at 1550 nm of this particular array of sub-wavelength gold islands could have potential use for other applications such as selective filtering in optical telecommunications systems.

Chapter 8

Conclusions and Perspectives

In terms of performance, the ideal biosensor should have exceedingly high sensitivity and low limits of detection as well as extremely short analysis time. As mentioned in the introduction, label-free SPR biosensors naturally offer the shortest analysis time compared to other types of biosensors. Given their extremely short analysis time, SPR biosensors are therefore excellent candidates for the ideal biosensor. On the other hand, the limits of detection of unlabeled SPR biosensors are not the most impressive. Thus to more closely approach the ideal biosensor, the inherent sensitivity of label-free SPR biosensors needs to be significantly improved so that lower limits of detection can be achieved. The objective of this work is to contribute to this quest by investigating some novel ideas for the design and optimization of SPR structure to boost the intrinsic sensitivity of label-free SPR biosensors.

In the spirit of applied research, particular emphasis is given to SPR structures in ATR Kretschmann configuration for their compatibility with most instrumental SPR setups. The enhancement of the optical sensitivity of SPR biosensors in such "traditional" configuration has been explored in Chapter 5 and briefly summarized in Table 8.1.

The use of bimetallic silver/gold SPR structure instead of simple gold or silver thin films allows one to obtain a narrower resonance linewidth while retaining the chemical stability of the resulting SPR surface. Changing the operating wavelength from the red end of the visible electromagnetic spectrum of around 680-760 nm towards the near-infrared at 1550 nm results in even narrower resonance by a factor of at least five. In the near-infrared at the wavelength of 1550 nm, the field penetration depth into the sensed medium reaches 1250 nm which is approximately five times that obtained in the visible. The maximum electric field intensity enhancement factor is also increased by at least three folds. More importantly, the figure-of-merit of SPR biosensors is approximately quadrupled when the operating the wavelength is changed from 760 nm to 1550 nm.

Table 8.1. Brief summary of optical sensitivity enhancement of SPR structures in ATR Kretschmann configuration.

	Sensitivity (°/RIU)	Linewidth (°)	Figure-of-merit (RIU^{-1})
Classical SPR (760 nm, experimental)	67.0	3.3	20
Bimetallic SPR (760 nm, experimental)	-	1.87	-
Classical SPR (1550 nm, theoretical)	64.3	0.5	130
Bimetallic SPR (1550 nm, theoretical)	64.0	0.4	160
Long-range SPR (760 nm, theoretical)	52.0	0.08	650
Long-range SPR (760 nm, experimental)	80.0	0.4	200
Long-range SPR (1550 nm, theoretical)	44.0	0.008	5500

SPR biosensors based on long-range surface plasmons mode operating at the wavelength of 760 nm have been characterized. The resonance linewidth of the long-range surface plasmons structure is theoretically predicted to be 40 times narrower compared to that of classical SPR at the same operating wavelength. However it is experimentally found to be only about eight times narrower. This discrepancy can be attributed to the formation of inhomogeneous metal-polymer interface. Therefore an improvement of the quality of this metal-polymer interface needs to be worked out in the future. Nevertheless, the obtained experimental figure-of-merit of the long-range surface plasmons structure is more significant by

an order of magnitude compared to that of classical SPR at the same operating wavelength. The electric field intensity enhancement of the long-range surface plasmons structure is seven folds stronger than that of classical SPR. The field penetration depth into the sensed medium of this long-range surface plasmons structure is around 1300 nm which is practically similar to that obtained from classical SPR structure operating at the longer wavelength of 1550 nm.

The concept of long-range surface plasmons at the wavelength of 760 nm can certainly be extended to longer operating wavelength. In particular, the long-range surface plasmons structure at the wavelength of 1550 nm yields a theoretical resonance linewidth that is 400 times narrower than that of classical SPR operating at the wavelength of 760 nm. Although similar broadening to that observed in the long-range surface plasmons structure operating at the wavelength of 760 nm is very likely to take place, the experimental resonance linewidth can still be expected to be close to two orders of magnitude narrower than that of classical SPR. The theoretical figure-of-merit of this long-range surface plasmons structure is as high as 5500 which is two orders of magnitude higher than that of classical SPR. The maximum electric field intensity enhancement factor is as high as 450 which is an order of magnitude stronger than that obtained from classical SPR. This stronger field enhancement is especially advantageous for the coupling of SPR method with fluorescence-based biosensing. Such combination is expected to be able to push the limits of detection into the attomolar range. Moreover, the field penetration depth into the sensed medium of this long-range surface plasmons structure is as large as 7500 nm which means that quite large analytes such as bacteria and certain cells can be effectively probed.

Novel graphene-based surface functionalization strategy has been investigated in Chapter 6. With such method, the biorecognition sensitivity of SPR biosensors has been experimentally shown to be enhanced compared to that obtained using conventional surface functionalization scheme. This enhancement can potentially be amplified even further by introducing a receptor matrix attached to the graphene surface and extending into the sensing medium to increase the binding capacity per unit area. Moreover, this novel graphene-based surface functionalization strategy can be applied to virtually any SPR structure. In particular, it can be immediately integrated into commercial SPR surfaces such as Biacore Au sensor chips. As a side note, a whole different set of surface chemistry based on titanium thin adlayer is also worth investigating for future work [124].

Some "non-traditional" optical designs for SPR biosensors have also been theoretically analyzed in Chapter 7. The long-period waveguide grating structures

have been predicted to offer a figure-of-merit of as high as 6000. Under the best-case scenario, the refractive index resolution of such structure is estimated to reach the 10^{-9} RIU range. Some simple arrays of micro/nanostructures have also been theoretically considered. Despite their quite modest sensitivity, such arrays have significant potential for integrated biosensor devices. Such devices can find applications where small instrument size and speed of analysis are crucial but cutting-edge accuracy and detection limits are not.

Finally, it is important to keep in mind that this work is only a brick in the attempt to construct the ideal SPR biosensor. As a whole, in addition to the aforementioned criteria for analytical performance, the ideal SPR biosensor should also be low-cost, portable, integrated, and easy to miniaturize. It is clearly a daunting task to design a single SPR biosensor that meets each and every one of these specifications. In fact, SPR biosensors research groups worldwide focus their effort to tackle different segments of these challenges. Use of white light-emitting diodes [125], [126] and polymer-based chips [127] for low-cost SPR biosensors has been proposed. The refractive index resolution is however quite modest on the order of 10^{-5} RIU. SPR biosensors based on fiber optic are excellent candidates for miniaturized systems as well as in-vivo applications. The initially poor refractive index resolution on the order of 10^{-5} RIU [126], [128] can potentially be further improved to 10^{-6} RIU by incorporating Bragg grating [129]. Recent development of the instrumentation of SPR biosensors has eventually allowed the construction of hand-held portable SPR biosensor devices [130], [131]. Although the setup used in the reported hand-held instruments is still based on Kretschmann ATR configuration with classical SPR structure, the refractive index resolution is quite promising on the order of 10^{-6} RIU. Combining such superior instrumentation in terms of size and capability with the optimized SPR sensor chips developed in this work is therefore expected to eventually bring label-free SPR biosensors even closer to the ideal biosensor.

References

[1] R. Bhadoria and H. S. Chaudhary, "Recent advances of biosensors in biomedical sciences," *Int. J. Drug Delivery*, vol. 3, pp. 571–585, 2011.

[2] S. D. Mazumdara, B. Barlena, P. Kämpfer, and M. Keusgen, "Surface plasmon resonance (SPR) as a rapid tool for serotyping of salmonella," *Biosens. Bioelectron.*, vol. 25, pp. 967–971, 2010.

[3] V. Chabot, C. M. Cuerrier, E. Escher, V. Aimez, M. Grandbois, and P. G. Charette, "Biosensing based on surface plasmon resonance and living cells," *Biosens. Bioelectron.*, vol. 24, pp. 1667–1673, 2009.

[4] L. Liu, N. Xia, and J. Wang, "Potential applications of SPR in early diagnosis and progression of alzheimer's disease," *RSC Advances*, vol. 2, no. 6, pp. 2200–2204, 2012.

[5] F. Baldini, "New trends in biosensors for health care," *Anal. Bioanal. Chem.*, vol. 381, no. 5, p. 1003, 2005.

[6] B. E. Rapp, F. J. Gruhl, and K. Lange, "Biosensors with label-free detection designed for diagnostic applications," *Anal. Bioanal. Chem.*, vol. 398, no. 6, pp. 2403–2412, 2010.

[7] S. S. Zhao, O. R. Bolduc, D. Y. Colin, J. N. Pelletier, and J.-F. Masson, "Development of LSPR and SPR sensor for the detection of an anti-cancer drug for chemotherapy," *Proc. SPIE*, vol. 8234, p. 82340L, 2012.

[8] S. Rodriguez-Mozaz, M.-P. Marco, M. J. L. de Alda, and D. Barcelo, "Biosensors for environmental applications: Future development trends," *Pure Appl. Chem.*, vol. 76, no. 4, p. 723–752, 2004.

[9] C. Tortolini, M. Frasconi, M. D. Fusco, and F. Mazzei, "Surface plasmon resonance biosensors for environmental analysis: general aspects and applications," *Int. J. Environ. Health*, vol. 4, no. 4, pp. 305–322, 2010.

[10] C. Hu, N. Gan, Y. Chen, L. Bi, X. Zhang, and L. Song, "Detection of microcystins in environmental samples using surface plasmon resonance biosensor," *Talanta*, vol. 80, no. 1, p. 407–410, 2009.

[11] S. Wang, A. Ramachandran, and S.-J. Ja, "Integrated microring resonator biosensors for monitoring cell growth and detection of toxic chemicals in water," *Biosens. Bioelectron.*, vol. 24, no. 10, p. 3061–3066, 2009.

[12] F. C. Dudak and I. H. Boyaci, “Rapid and label-free bacteria detection by surface plasmon resonance (SPR) biosensors,” *Biotechnology Journal*, vol. 4, no. 7, p. 1003–1011, 2009.

[13] I. Navratilova and A. L. Hopkins, “Emerging role of surface plasmon resonance in fragment-based drug discovery,” *Future Medicinal Chemistry*, vol. 3, no. 14, pp. 1809–1820, 2011.

[14] I. Navratilova and A. L. Hopkins, “Fragment screening by surface plasmon resonance,” *ACS Med. Chem. Lett.*, vol. 1, no. 1, pp. 44–48, 2010.

[15] K. Retra, H. Irth, and J. E. van Muijlwijk-Koezen, “Surface plasmon resonance biosensor analysis as a useful tool in FBDD,” *Drug Discovery Today: Technologies*, vol. 7, no. 3, p. e181–e187, 2010.

[16] W. Huber and F. Mueller, “Biomolecular interaction analysis in drug discovery using surface plasmon resonance technology,” *Current Pharmaceutical Design*, vol. 12, no. 31, pp. 3999–4021, 2006.

[17] M. A. Cooper, “Optical biosensors in drug discovery,” *Nature Reviews Drug Discovery*, vol. 1, pp. 515–528, 2002.

[18] Y. Li, Xia, and Z. Lin, “Recent developments and applications of surface plasmon resonance biosensors for the detection of mycotoxins in foodstuffs,” *Food Chem.*, vol. 132, no. 3, pp. 1549–1554, 2012.

[19] A. A. Bergwerff and F. V. Knapen, “Surface plasmon resonance biosensors for detection of pathogenic microorganisms: Strategies to secure food and environmental safety,” *Journal of AOAC International*, vol. 89, no. 3, pp. 826–831, 2006.

[20] R. Gambari and G. Feriotto, “Surface plasmon resonance for detection of genetically modified organisms in the food supply,” *Journal of AOAC International*, vol. 89, no. 3, pp. 893–897, 2006.

[21] A. Rasooly and K. E. Herold, “Biosensors for the analysis of food- and waterborne pathogens and their toxins,” *Journal of AOAC International*, vol. 89, no. 3, pp. 873–883, 2006.

[22] I. M. Yman, A. Eriksson, M. A. Johansson, and K.-E. Hellens, “Food allergen detection with biosensor immunoassays,” *Journal of AOAC International*, vol. 89, no. 3, pp. 856–861, 2006.

[23] R. Karlsson, “SPR for molecular interaction analysis: a review of emerging application areas,” *J. Mol. Recognit.*, vol. 17, p. 151–161, 2004.

[24] M. J. Linman, K. Sugerman, and Q. Cheng, "Detection of low levels of escherichia coli in fresh spinach by surface plasmon resonance spectroscopy with a TMB-based enzymatic signal enhancement method," *Sens. Actuators B*, vol. 145, pp. 613–619, 2010.

[25] M. Pohanka, P. Dobes, L. Drtinova, and K. Kuca, "Nerve agents assay using cholinesterase based biosensor," *Electroanalysis*, vol. 21, no. 10, p. 1177–1182, 2009.

[26] http://www.prweb.com/releases/biosensors/medical_biosensors/prweb8067456.htm

[27] J. Arlett, E. Myers, and M. Roukes, "Comparative advantages of mechanical biosensors," *Nature Nanotechnology*, vol. 6, p. 203–215, 2011.

[28] R. Rich and D. Myszka, "Advances in surface plasmon resonance biosensor analysis," *Curr. Opin. Biotechnol.*, vol. 11, no. 1, pp. 54–61, 2000.

[29] N. F. Starodub, Y. A. Ogorodniichuk, Y. A. Sitnik, and N. F. Slishik, *Biosensors for the Control of Some Toxins, Viral and Microbial Infections to Prevent Actions of Bioterrorists*. NATO Science for Peace and Security Series A: Chemistry and Biology, Springer, 2012.

[30] X. Yao, X. Li, F. Toledo, C. Zurita-Lopez, M. Gutova, J. Momand, and F. Zhou, "Sub-attomole oligonucleotide and p53 cDNA determinations via a high-resolution surface plasmon resonance combined with oligonucleotide-capped gold nanoparticle signal amplification," *Anal. Biochem.*, vol. 354, no. 2, pp. 220–228, 2006.

[31] P. Berini, "Long-range surface plasmon polaritons," *Adv. Opt. Photonics*, vol. 1, pp. 484–588, 2009.

[32] D. Sarid, "Long-range surface-plasma waves on very thin metal films," *Phys. Rev. Lett.*, vol. 47, p. 1927–1930, 1981.

[33] E. Kretschmann and H. Raether, "Radiative decay of non-radiative surface plasmons excited by light," *Z. Naturforsch., A: Astrophys., Phys. Phys. Chem.*, vol. 23A, p. 2135–2136, 1968.

[34] A. Otto, "Excitation of nonradiative surface plasma waves in silver by the method of frustrated total reflection," *Z. Phys.*, vol. 216, p. 398–410, 1968.

[35] R. Wood, "On a remarkable case of uneven distribution of light in a diffraction grating spectrum," *Philos. Mag.*, vol. 4, p. 396 – 402, 1902.

[36] R. Ritchie, E. Arakawa, J. Cowan, and R. Hamm, "Surface-plasmon resonance effect in grating diffraction," *Phys. Rev. Lett.*, vol. 21, p. 1530–1532, 1968.

[37] B. Liedberg, C. Nylander, and I. Lundstrom, "Surface plasmons resonance for gas detection and biosensing," *Sens. Actuators*, vol. 4, p. 299–304, 1983.

[38] S. J. Zalyubovskiy, M. Bogdanova, A. Deinega, Y. Lozovik, A. D. Pris, K. H. An, W. P. Hall, and R. A. Potyrailo, "Theoretical limit of localized surface plasmon resonance sensitivity to local refractive index change and its comparison to conventional surface plasmon resonance sensor," *J. Opt. Soc. Am. A*, vol. 29, no. 6, pp. 994–1002, 2012.

[39] J. Piehler, A. Brecht, and G. Gauglitz, "Affinity detection of low molecular weight analytes," *Anal. Chem.*, vol. 68, pp. 139–143, 1996.

[40] S. Chen, M. Svedendahl, M. Kall, L. Gunnarsson, and A. Dmitriev, "Ultrahigh sensitivity made simple: nanoplasmonic label-free biosensing with an extremely low limit-of-detection for bacterial and cancer diagnostics," *Nanotechnology*, vol. 20, p. 434015, 2009.

[41] S. W. Kowalczyk, M. W. Tuijtel, S. P. Donkers, and C. Dekker, "Unraveling single-stranded dna in a solid-state nanopore," *Nano Lett.*, vol. 10, no. 4, p. 1414–1420, 2010.

[42] L. Feuz, M. P. Jonsson, and F. Hook, "Material-selective surface chemistry for nanoplasmonic sensors: Optimizing sensitivity and controlling binding to local hot spots," *Nano Lett.*, vol. 12, pp. 873–879, 2012.

[43] J. N. Anker, W. P. Hall, O. Lyandres, N. C. Shah, J. Zhao, and R. P. V. Duyne, "Biosensing with plasmonic nanosensors," *Nature Materials*, vol. 7, pp. 442–453, 2008.

[44] M. Svedendahl, S. Chen, A. Dmitriev, and M. Kall, "Refractometric sensing using propagating versus localized surface plasmons: A direct comparison," *Nano Lett.*, vol. 9, no. 12, pp. 4428–4433, 2009.

[45] H. Sipova, D. Vrba, and J. Homola, "Analytical value of detecting an individual molecular binding event: The case of the surface plasmon resonance biosensor," *Anal. Chem.*, vol. 84, no. 1, pp. 30–33, 2012.

[46] H. Raether, *Surface Plasmons on Smooth and Rough Surfaces and on Gratings*. Springer, 1988.

[47] P. Lecaruyer, E. Maillart, M. Canva, and J. Rolland, “Generalization of the rouard method to an absorbing thin-film stack and application to surface plasmon resonance,” *Appl. Opt.*, vol. 45, no. 33, pp. 8419–8423, 2006.

[48] A. D. Rakic, A. B. Djurisic, J. M. Elazar, and M. L. Majewski, “Optical properties of metallic films for vertical-cavity optoelectronic devices,” *Appl. Opt.*, vol. 37, pp. 5271–5283, 1998.

[49] A. Vial, A.-S. Grimault, D. Macías, D. Barchiesi, and M. L. de la Chapelle, “Improved analytical fit of gold dispersion: Application to the modeling of extinction spectra with a finite-difference time-domain method,” *Phys. Rev. B*, vol. 71, p. 085416, 2005.

[50] P. B. Johnson and R. W. Christy, “Optical constants of the noble metals,” *Phys. Rev. B*, vol. 6, pp. 4370–4379, 1972.

[51] M. A. Ordal, L. L. Long, R. J. Bell, S. E. Bell, R. R. Bell, J. R. W. Alexander, and C. A. Ward, “Optical properties of the metals Al, Co, Cu, Au, Fe, Pb, Ni, Pd, Pt, Ag, Ti, and W in the infrared and far infrared,” *Appl. Opt.*, vol. 22, p. 1099–1119, 1983.

[52] http://www.cvimellesgriot.com/products/Documents/Catalog/Dispersion_Equations.pdf

[53] P. Schiebener, J. Straub, J. M. H. L. Sengers, and J. S. Gallagher, “Refractive index of water and steam as function of wavelength, temperature and density,” *J. Phys. Chem. Ref. Data*, vol. 19, no. 3, pp. 677–717, 1990.

[54] A. H. Harvey, J. S. Gallagher, and J. M. H. L. Sengers, “Revised formulation for the refractive index of water and steam as a function of wavelength, temperature, and density,” *J. Phys. Chem. Ref. Data*, vol. 27, pp. 761–774, 1998.

[55] J. Bertie and Z. Lan, “Infrared intensities of liquids xx: The intensity of the oh stretching band of liquid water revisited, and the best current values of the optical constants of H_2O(l) at 25°c between 15,000 and 1 cm^{-1},” *Appl. Spectrosc.*, vol. 50, no. 8, pp. 1047–1057, 1996.

[56] J. L. Person, F. Colas, C. Compere, M. Lehaitre, M.-L. Anne, C. Boussard-Pledel, B. Bureau, J.-L. Adam, S. Deputier, and M. Guilloux-Viry, “Surface plasmon resonance in chalcogenide glass-based optical system,” *Sens. Actuators B*, vol. 130, pp. 771–776, 2008.

[57] M. Piliarik and J. Homola, “Surface plasmon resonance (SPR) sensors: approaching their limits?,” *Opt. Express*, vol. 17, no. 19, pp. 16505–16517, 2009.

[58] P. Lecaruyer, M. Canva, and J. Rolland, "Metallic film optimization in a surface plasmon resonance biosensor by the extended rouard method," *Appl. Opt.*, vol. 46, no. 12, pp. 2361–2369, 2007.

[59] R. Ulrich and R. Torge, "Measurement of thin film parameters with a prism coupler," *Appl. Opt.*, vol. 12, no. 22, pp. 2901–2908, 1973.

[60] T.-N. Ding and E. Garmire, "Measuring refractive index and thickness of thin films: a new technique," *Appl. Opt.*, vol. 22, no. 20, pp. 3177–3181, 1983.

[61] A. Adams, D. Schinke, and C. Capio, "An evaluation of the prism coupler for measuring the thickness and refractive index of dielectric thin films on silicon substrates," *J. Electrochem. Soc.*, vol. 126, no. 9, pp. 1539–1543, 1979.

[62] V. Zaporojtchenko, T. Strunskus, K. Behnke, C. Bechtolsheim, A. Thran, and F. Faupel, "Formation of metal–polymer interfaces by metal evaporation: influence of deposition parameters and defects," *Microelectron. Eng.*, vol. 50, pp. 465–471, 2000.

[63] M. Frasconi, F. Mazzei, and T. Ferri, "Protein immobilization at gold–thiol surfaces and potential for biosensing," *Anal. Bioanal. Chem.*, vol. 398, p. 1545–1564, 2010.

[64] T. M. Willey, A. L. Vance, T. van Buuren, C. Bostedt, L. Terminello, and C. Fadley, "Rapid degradation of alkanethiol-based self-assembled monolayers on gold in ambient laboratory conditions," *Surf. Sci.*, vol. 576, pp. 188–196, 2005.

[65] C. Vericat, M. Vela, G. Benitez, P. Carro, and R. Salvarezza, "Self-assembled monolayers of thiols and dithiols on gold: new challenges for a well-known system," *Chem. Soc. Rev.*, vol. 39, pp. 1805–1834, 2010.

[66] N. Bhatt, P.-J. J. Huang, N. Dave, and J. Liu, "Dissociation and degradation of thiol-modified DNA on gold nanoparticles in aqueous and organic solvents," *Langmuir*, vol. 27, no. 10, p. 6132–6137, 2011.

[67] J. C. Love, L. A. Estroff, J. K. Kriebel, R. G. Nuzzo, and G. M. Whitesides, "Self-assembled monolayers of thiolates on metals as a form of nanotechnology," *Chem. Rev.*, vol. 105, pp. 1103–1169, 2005.

[68] A. K. Geim, "Graphene: Status and prospects," *Science*, vol. 324, pp. 1530–1534, 2009.

[69] A. K. Geim and K. S. Novoselov, "The rise of graphene," *Nature Materials*, vol. 6, pp. 183 – 191, 2007.

[70] X. Li, W. Cai, J. An, S. Kim, J. Nah, D. Yang, R. Piner, A. Velamakanni, I. Jung, E. Tutuc, S. K. Banerjee, L. Colombo, and R. S. Ruoff, "Large-area synthesis of high-quality and uniform graphene films on copper foils," *Science*, vol. 324, pp. 1312–1314, 2009.

[71] K. S. Kim, Y. Zhao, H. Jang, S. Y. Lee, J. M. Kim, K. S. Kim, J.-H. Ahn, P. Kim, J.-Y. Choi, and B. H. Hong, "Large-scale pattern growth of graphene films for stretchable transparent electrodes," *Nature*, vol. 457, pp. 706–710, 2009.

[72] Y. Lee, S. Bae, H. Jang, S. Jang, S.-E. Zhu, S. H. Sim, Y. I. Song, B. H. Hong, and J.-H. Ahn, "Wafer-scale synthesis and transfer of graphene films," *Nano Lett.*, vol. 10, no. 2, p. 490–493, 2010.

[73] B. Song, D. Li, W. Qi, M. Elstner, C. Fan, and H. Fang, "Graphene on Au(111): A highly conductive material with excellent adsorption properties for high-resolution bio/nanodetection and identification," *ChemPhysChem*, vol. 11, no. 3, p. 585–589, 2010.

[74] L. Song, L. Ci, W. Gao, and P. M. Ajayan, "Transfer printing of graphene using gold film," *ACS Nano*, vol. 3, no. 6, p. 1353–1356, 2009.

[75] Z. Tang, H. Wu, J. R. Cort, G. W. Buchko, Y. Zhang, Y. Shao, I. A. Aksay, J. Liu, and Y. Lin, "Constraint of dna on functionalized graphene improves its biostability and specificity," *Small*, vol. 6, no. 11, pp. 1205–1209, 2010.

[76] K. S. Novoselov, A. K. Geim, S. V. Morozov, D. Jiang, Y. Zhang, S. V. Dubonos, I. V. Grigorieva, and A. A. Firsov, "Electric field effect in atomically thin carbon films," *Science*, vol. 306, pp. 666–669, 2004.

[77] S. Park and R. S. Ruoff, "Chemical methods for the production of graphenes," *Nature Nanotechnology*, vol. 4, pp. 217 – 224, 2009.

[78] D. Yang, A. Velamakanni, G. Bozoklu, S. Park, M. Stoller, R. D. Piner, S. Stankovich, I. Jung, D. A. Field, C. A. V. Jr., and R. S. Ruoff, "Chemical analysis of graphene oxide films after heat and chemical treatments by x-ray photoelectron and micro-raman spectroscopy," *Carbon*, vol. 47, no. 1, pp. 145–152, 2009.

[79] V. C. Tung, M. J. Allen, Y. Yang, and R. B. Kaner, "High-throughput solution processing of large-scale graphene," *Nature Nanotechnology*, vol. 4, pp. 25 – 29, 2009.

[80] Z.-S. Wu, W. Ren, L. Gao, J. Zhao, Z. Chen, B. Liu, D. Tang, B. Yu, C. Jiang, and H.-M. Cheng, "Synthesis of graphene sheets with high electrical

conductivity and good thermal stability by hydrogen arc discharge exfoliation," *ACS Nano*, vol. 3, no. 2, p. 411–417, 2009.

[81] C. Gomez-Navarro, R. T. Weitz, A. M. Bittner, M. Scolari, A. Mews, M. Burghard, and K. Kern, "Electronic transport properties of individual chemically reduced graphene oxide sheets," *Nano Lett.*, vol. 7, no. 11, p. 3499–3503, 2007.

[82] P. Blake, P. D. Brimicombe, R. R. Nair, T. J. Booth, D. Jiang, F. Schedin, L. A. Ponomarenko, S. V. Morozov, H. F. Gleeson, E. W. Hill, A. K. Geim, and K. S. Novoselov, "Graphene-based liquid crystal device," *Nano Lett.*, vol. 8, no. 6, p. 1704–1708, 2008.

[83] L. Zhi and K. Mullen, "A bottom-up approach from molecular nanographenes to unconventional carbon materials," *J. Mater. Chem.*, vol. 18, pp. 1472–1484, 2008.

[84] T. Seyller, A. Bostwick, K. V. Emtsev, K. Horn, L. Ley, J. L. McChesney, T. Ohta, J. D. Riley, E. Rotenberg, and F. Speck, "Epitaxial graphene: a new material," *Phys. Status Solidi B*, vol. 245, no. 7, p. 1436–1446, 2008.

[85] Q. H. Wang and M. C. Hersam, "Room-temperature molecular-resolution characterization of self-assembled organic monolayers on epitaxial graphene," *Nat. Chem.*, vol. 1, pp. 206 – 211, 2009.

[86] C. Berger, Z. M. Song, T. B. Li, X. B. Li, A. Y. Ogbazghi, R. Feng, Z. T. Dai, A. N. Marchenkov, E. H. Conrad, P. N. First, and W. A. de Heer, "Ultrathin epitaxial graphite: 2D electron gas properties and a route toward graphene-based nanoelectronics," *J. Phys. Chem. B*, vol. 108, p. 19912–19916, 2004.

[87] A. Reina, X. Jia, J. Ho, D. Nezich, H. Son, V. Bulovic, M. S. Dresselhaus, and J. Kong, "Large area, few-layer graphene films on arbitrary substrates by chemical vapor deposition," *Nano Lett.*, vol. 9, no. 1, p. 30–35, 2009.

[88] X. Li, W. Cai, J. An, S. Kim, J. Nah, D. Yang, R. Piner, A. Velamakanni, I. Jung, E. Tutuc, S. K. Banerjee, L. Colombo, and R. S. Ruoff, "Large-area synthesis of high-quality and uniform graphene films on copper foils," *Science*, vol. 324, pp. 1312–1314, 2009.

[89] S. Garaj, W. Hubbard, and J. A. Golovchenko, "Graphene synthesis by ion implantation," *Appl. Phys. Lett.*, vol. 97, p. 183103, 2010.

[90] Y. Shao, J. Wang, H. Wu, J. Liu, I. A. Aksay, and Y. Lin, "Graphene based electrochemical sensors and biosensors: A review," *Electroanalysis*, vol. 22, no. 10, p. 1027 – 1036, 2010.

[91] L. Wang, C. Zhu, L. Han, L. Jin, M. Zhou, and S. Dong, "Label-free, regenerative and sensitive surface plasmon resonance and electrochemical aptasensors based on graphene," *Chem. Commun.*, vol. 47, pp. 7794–7796, 2011.

[92] Z. Jiang, J. Wang, L. Meng, Y. Huang, and L. Liu, "A highly efficient chemical sensor material for ethanol: Al2o3/graphene nanocomposites fabricated from graphene oxide," *Chem. Commun.*, vol. 47, pp. 6350–6352, 2011.

[93] X. Zhang, S. Li, X. Jin, and S. Zhang, "A new photoelectrochemical aptasensor for the detection of thrombin based on functionalized graphene and CdSe nanoparticles multilayers," *Chem. Commun.*, vol. 47, pp. 4929–4931, 2011.

[94] T. Oznuluer, E. Pince, E. O. Polat, O. Balci, O. Salihoglu, and C. Kocabas, "Synthesis of graphene on gold," *Appl. Phys. Lett.*, vol. 98, p. 183101, 2011.

[95] X. Li, Y. Zhu, W. Cai, M. Borysiak, B. Han, D. Chen, R. D. Piner, L. Colombo, and R. S. Ruoff, "Transfer of large-area graphene films for high-performance transparent conductive electrodes," *Nano Lett.*, vol. 9, no. 12, pp. 4359–4363, 2009.

[96] Z. Cheng, Q. Zhou, C. Wang, Q. Li, C. Wang, and Y. Fang, "Toward intrinsic graphene surfaces: A systematic study on thermal annealing and wet-chemical treatment of SiO_2-supported graphene devices," *Nano Lett.*, vol. 11, no. 2, pp. 767–771, 2011.

[97] A. Pirkle, J. Chan, A. Venugopal, D. Hinojos, C. W. Magnuson, S. McDonnell, L. Colombo, E. M. Vogel, R. S. Ruoff, and R. M. Wallace, "The effect of chemical residues on the physical and electrical properties of chemical vapor deposited graphene transferred to SiO_2," *Appl. Phys. Lett.*, vol. 99, p. 122108, 2011.

[98] W. H. Lee, J. Park, S. H. Sim, S. Lim, K. S. Kim, B. H. Hong, and K. Cho, "Surface-directed molecular assembly of pentacene on monolayer graphene for high-performance organic transistors," *J. Am. Chem. Soc.*, vol. 133, p. 4447–4454, 2011.

[99] J. D. Caldwell, T. J. Anderson, J. C. Culbertson, G. G. Jernigan, K. D. Hobart, F. J. Kub, M. J. Tadjer, J. L. Tedesco, J. K. Hite, M. A. Mastro, R. L. Myers-Ward, J. Charles R. Eddy, P. M. Campbell, and D. K. Gaskill, "Technique for the dry transfer of epitaxial graphene onto arbitrary substrates," *ACS Nano*, vol. 4, no. 2, p. 1108–1114, 2010.

[100] J. Diaz, G. Paolicelli, S. Ferrer, and F. Comin, "Separation of the sp3 and sp2 components in the C1s photoemission spectra of amorphous carbon films," *Phys. Rev. B*, vol. 54, no. 11, pp. 8064–8069, 1996.

[101] S. Yumitori, "Correlation of C1s chemical state intensities with the O1s intensity in the xps analysis of anodically oxidized glass-like carbon samples," *J. Mater. Sci.*, vol. 35, no. 1, pp. 139–146, 2000.

[102] G. Jo, M. Choe, C.-Y. Cho, J. H. Kim, W. Park, S. Lee, W.-K. Hong, T.-W. Kim, S.-J. Park, B. H. Hong, Y. H. Kahng, and T. Lee, "Large-scale patterned multi-layer graphene films as transparent conducting electrodes for GaN light-emitting diodes," *Nanotechnology*, vol. 21, p. 175201, 2010.

[103] G. Eda and M. Chhowalla, "Chemically derived graphene oxide: Towards large-area thin-film electronics and optoelectronics," *Adv. Mater.*, vol. 22, p. 2392–2415, 2010.

[104] L. Malard, M. Pimenta, G. Dresselhaus, and M. Dresselhaus, "Raman spectroscopy in graphene," *Physics Reports*, vol. 473, pp. 51–87, 2009.

[105] A. C. Ferrari, J. C. Meyer, V. Scardaci, C. Casiraghi, M. Lazzeri, F. Mauri, S. Piscanec, D. Jiang, K. S. Novoselov, S. Roth, and A. K. Geim, "Raman spectrum of graphene and graphene layers," *Phys. Rev. Lett.*, vol. 97, p. 187401, 2006.

[106] D. M. Basko, S. Piscanec, and A. C. Ferrari, "Electron-electron interactions and doping dependence of the two-phonon raman intensity in graphene," *Phys. Rev. B.*, vol. 80, p. 165413, 2009.

[107] D. Graf, F. Molitor, K. Ensslin, C. Stampfer, A. Jungen, C. Hierold, and L. Wirtz, "Spatially resolved raman spectroscopy of single- and few-layer graphene," *Nano Lett.*, vol. 7, no. 2, pp. 238–242, 2007.

[108] M. Bruna and S. Borini, "Optical constants of graphene layers in the visible range," *Appl. Phys. Lett.*, vol. 94, p. 031901, 2009.

[109] L. Wu, H. S. Chu, W. S. Koh, and E. P. Li, "Highly sensitive graphene biosensors based on surface plasmon resonance," *Opt. Express*, vol. 18, no. 14, pp. 14395–14400, 2010.

[110] M. Quintana, K. Spyrou, M. Grzelczak, W. R. Browne, P. Rudolf, and M. Prato, "Functionalization of graphene via 1,3-dipolar cycloaddition," *ACS Nano*, vol. 4, no. 6, p. 3527–3533, 2010.

[111] M. Steenackers, A. M. Gigler, N. Zhang, F. Deubel, M. Seifert, L. H. Hess, C. Haley, Y. X. Lim, K. P. Loh, J. A. Garrido, R. Jordan, M. Stutzmann, and I. D. Sharp, "Polymer brushes on graphene," *J. Am. Chem. Soc.*, vol. 133, no. 27, p. 10490–10498, 2011.

[112] W. Knoll, A. Kasry, F. Yu, Y. Wang, A. Brunsen, and J. Dostalek, "New concepts with surface plasmons and nano-biointerfaces," *J. Nonlinear Opt. Phys. Mater.*, vol. 17, p. 121–129, 2008.

[113] S. Pal and B. R. Singh, "Analysis and design of corrugated long-period gratings in silica-on-silicon planar waveguides," *J. Lightwave Technol.*, vol. 25, no. 8, pp. 2260–2267, 2007.

[114] V. Rastogi and K. S. Chiang, "Long-period gratings in planar optical waveguides," *Appl. Opt.*, vol. 41, no. 30, pp. 6351–6355, 2002.

[115] Q. Liu, K. S. Chiang, and V. Rastogi, "Analysis of corrugated long-period gratings in slab waveguides and their polarization dependence," *J. Lightwave Technol.*, vol. 21, no. 12, pp. 3399–3405, 2003.

[116] M. Piliarik, M. Vala, I. Tichy, and J. Homola, "Compact and low-cost biosensor based on novel approach to spectroscopy of surface plasmons," *Biosens. Bioelectron.*, vol. 24, pp. 3430–3435, 2009.

[117] M. Piliarik, K. Hegnerova, M. Vala, K. Chadt, I. Tichy, and J. Homola, "Compact multi-channel high-sensitivity biosensor based on spectroscopy of surface plasmons," *Proc. SPIE*, vol. 7192, p. 719212, 2009.

[118] C. Genet and T. W. Ebbesen, "Light in tiny holes," *Nature*, vol. 445, pp. 39–46, 2007.

[119] J. C. Sharpe, J. S. Mitchell, L. Lin, N. Sedoglavich, and R. J. Blaikie, "Gold nanohole array substrates as immunobiosensors," *Anal. Chem.*, vol. 80, pp. 2244–2249, 2008.

[120] A. D. Leebeeck, L. K. S. Kumar, V. de Lange, D. Sinton, R. Gordon, and A. G. Brolo, "On-chip surface-based detection with nanohole arrays," *Anal. Chem.*, vol. 79, pp. 4094–4100, 2007.

[121] K. J. K. Koerkamp, S. Enoch, F. B. Segerink, N. F. van Hulst, and L. Kuipers, "Strong influence of hole shape on extraordinary transmission through periodic arrays of subwavelength holes," *Phys. Rev. Lett.*, vol. 92, no. 18, p. 183901, 2004.

[122] C. Genet, M. van Exter, and J. Woerdman, “Fano-type interpretation of red shifts and red tails in hole array transmission spectra,” *Opt. Commun.*, vol. 225, p. 331–336, 2003.

[123] J. Ferreira, M. J. L. Santos, M. M. Rahman, A. G. Brolo, R. Gordon, D. Sinton, and E. M. Girotto, “Attomolar protein detection using in-hole surface plasmon resonance,” *J. Am. Chem. Soc.*, vol. 131, pp. 436–437, 2009.

[124] Y. Abe, K. Hiasa, I. Hirata, Y. Okazaki, K. Nogami, W. Mizumachi, Y. Yoshida, K. Suzuki, M. Okazaki, and Y. Akagawa, “Detection of synthetic RGDS(PO3H2)PA peptide adsorption using a titanium surface plasmon resonance biosensor,” *J. Mater. Sci.: Mater. Med.*, vol. 22, pp. 657–661, 2011.

[125] H. Ho, S. Wu, M. Yang, and A. Cheung, “Application of white light-emitting diode to surface plasmon resonance sensors,” *Sens. Actuators B*, vol. 80, pp. 89–94, 2001.

[126] A. Suzuki, J. Kondoh, Y. Matsui, S. Shiokawa, and K. Suzuki, “Development of novel optical waveguide surface plasmon resonance (SPR) sensor with dual light emitting diodes,” *Sens. Actuators B*, vol. 106, pp. 383–387, 2005.

[127] P. Obreja, D. Cristea, M. Kusko, and A. Dinescu, “Polymer-based chips for surface plasmon resonance sensors,” *J. Opt. A: Pure Appl. Opt.*, vol. 10, p. 064010, 2008.

[128] R. Slavik, J. Homola, and J. Ctyroky, “Miniaturization of fiber optic surface plasmon resonance sensor,” *Sens. Actuators B*, vol. 51, pp. 311–315, 1998.

[129] B. Spackova and J. Homola, “Theoretical analysis of a fiber optic surface plasmon resonance sensor utilizing a bragg grating,” *Opt. Express*, vol. 17, no. 25, pp. 23254–23264, 2009.

[130] B. Feltis, B. Sexton, F. Glenn, M. Best, M. Wilkins, and T. Davis, “A hand-held surface plasmon resonance biosensor for the detection of ricin and other biological agents,” *Biosens. Bioelectron.*, vol. 23, pp. 1131–1136, 2008.

[131] Y.-B. Shin, H. M. Kim, Y. Jung, and B. H. Chung, “A new palm-sized surface plasmon resonance (SPR) biosensor based on modulation of a light source by a rotating mirror,” *Sens. Actuators B*, vol. 150, pp. 1–6, 2010.

List of Publications and Conferences

Publications in International Journals

E. Wijaya, C. Lenaerts, S. Maricot, J. Hastanin, S. Habraken, J.-P. Vilcot, R. Boukherroub, S. Szunerits, "Surface plasmon resonance-based biosensors: From the development of different SPR structures to novel surface functionalization strategies," *Curr. Opin. Solid State Mater. Sci.* 15 (5), 208-224 (2011)

DOI: http://dx.doi.org/10.1016/j.cossms.2011.05.001

J. Hottin, **E. Wijaya**, L. Hay, S. Maricot, M. Bouazaoui and J.-P. Vilcot, "Comparison of Gold and Silver/Gold Bimetallic Surface for Highly Sensitive Near-infrared SPR Sensor at 1550 nm," *Plasmonics* (2012) (in press)

DOI: http://dx.doi.org/10.1007/s11468-012-9446-1

S. Szunerits, N. Maalouli, **E. Wijaya**, J.-P. Vilcot, R. Boukherroub, "Recent advances in the development of graphene based surface plasmon resonance (SPR) interfaces," *Anal. Bioanal. Chem.* (2012) (accepted, in press)

Conference Proceedings

E. Wijaya, N. Maalouli, R. Boukherroub, S. Szunerits, J.-P. Vilcot, "Graphene-based high-performance surface plasmon resonance biosensors," Proc. SPIE 8424: Nanophotonics IV, 84240R (2012)

DOI: http://dx.doi.org/10.1117/12.921670

C. Lenaerts, J. Hastanin, B. Pinchemel, S. Maricot, J.-P. Vilcot, S. Habraken, N. Maalouli, **E. Wijaya**, M. Bouazaoui, C. Desfours, K. Fleury-Frenette, "Integrated prism-free coupled surface plasmon resonance biochemical sensor," Proc. SPIE 8424: Nanophotonics IV, 84240P (2012)

DOI: http://dx.doi.org/10.1117/12.922579

Participation in Conferences

Europtrode XI Conference on Optical Chemical Sensors and Biosensors (1-4 April 2012, Barcelona, Spain)

E. Wijaya, N. Maalouli, R. Boukherroub, S. Szunerits, J.-P. Vilcot: Graphene-based high-performance surface plasmon resonance biosensors (oral presentation)

SPIE Photonics Europe 2012 (16-19 April 2012, Brussels, Belgium)

Conference 8424 Nanonophonics IV: Photonic Nanobiosensors

E. Wijaya, N. Maalouli, R. Boukherroub, S. Szunerits, J.-P. Vilcot: Graphene-based high-performance surface plasmon resonance biosensors (oral presentation)

META 2012, 3rd International Conference on Metamaterials, Photonic Crystals, and Plasmonics (19-22 April 2012, Paris, France)

Special session on plasmonics and biomedical applications

E. Wijaya, N. Maalouli, R. Boukherroub, S. Szunerits, J.-P. Vilcot: Graphene-based high-performance surface plasmon resonance biosensors (oral presentation)

E-MRS Spring Meeting 2012 (14-18 May 2012, Strasbourg, France)

Symposium Q on novel materials and fabrication methods for new emerging devices

E. Wijaya, N. Maalouli, R. Boukherroub, S. Szunerits, J.-P. Vilcot: Graphene-based high-performance surface plasmon resonance biosensors (oral presentation)

Appendices

A.1. Field Enhancement due to Surface Plasmons

The word “transmission” mentioned in Sections 4.1.2 and 4.1.3 is used freely to treat the general case whether or not there is an actual transmitted wave.

When the angle of incidence is smaller than the critical angle of total internal reflection, there is an actual transmitted wave that carries optical energy away from the metal-dielectric interface. The optical energy (proportional to the field intensity) contained in the transmitted wave is always less than or equal to that of the incident wave. As a result of this conservation of energy, the transmission coefficient in this case is always less than unity.

In the case of surface plasmons, the use of the word “transmission” is rather abusive for lack of appropriate terminology. In this case, the angle of incidence is always larger than the critical angle of total internal reflection. As a result, the “transmitted” wave is in fact evanescent. Around the SPR angle, the field enhancement due to surface plasmons makes the “transmission” coefficient as defined in Equations (4.28) and (4.32) larger than unity. This is in no way a violation of the principle of conservation of energy since there is no actual transmitted wave that carries optical energy away from the metal-dielectric interface. Indeed, the optical energy of the incident wave is transformed into surface plasmons and later dissipated in the metal.

A useful analogy concerning the phase velocity and the group velocity in a waveguide (e.g., a hollow waveguide as the simplest example) can be used to illustrate this point. While the group velocity of a guided wave in such a waveguide is always less than c (i.e., the speed of light in vacuum), its phase velocity can be larger than c. It even approaches infinity near the cut-off frequency of the waveguide. However, this does not contradict the theory of special relativity which places c as an upper limit of velocity of “material” bodies. The reason is that the speed with which energy or information (i.e., the “material” bodies in a wave) travels is associated with the group velocity and not the phase velocity.

A.2. Example of Matlab Implementation

The Fresnel equations as well as the materials models elaborated in Chapter 4 are implemented in Matlab to generate the theoretical results presented in Chapters 4 and 5. As an example, Matlab codes for the calculation of SPR curve of water from bimetallic silver/gold structure on BK7 glass substrate at the wavelength of 760 nm are shown below.

```
---------------------------------------------------------------------------------------------

clear

lbd0 = 760;
% free-space wavelength expressed in nm

theta = linspace(60,75,100000);
% angle of incidence ranging from 60° to 75° with 100000 points

e1 = sqrt(Sellmeier(lbd0,'BK7'));
% relative electric permittivity of the prism
e2 = LD_model(lbd0,'Ag');
% relative electric permittivity of the first metallic layer
e3 = LD_model(lbd0,'Au');
% relative electric permittivity of the second metallic layer
nd = nwater(lbd0);
% refractive index of the sensed medium
e4 = nd.^2;
% relative electric permittivity of the sensed medium

d2 = 30;
% thickness of the first metallic layer (nm)
d3 = 5;
% thickness of the second metallic layer (nm)

k0 = 2*pi./lbd0;
kx = k0.*np.*sind(theta);
kz1 = sqrt(k0.^2.*e1 - kx.^2);
kz2 = sqrt(k0.^2.*e2 - kx.^2);
kz3 = sqrt(k0.^2.*e3 - kx.^2);
kz4 = sqrt(k0.^2.*e4 - kx.^2);

r12 = (e2.*kz1 - e1.*kz2)./(e2.*kz1 + e1.*kz2);
r23 = (e3.*kz2 - e2.*kz3)./(e3.*kz2 + e2.*kz3);
r34 = (e4.*kz3 - e3.*kz4)./(e4.*kz3 + e3.*kz4);

r24=(r23+r34.*exp(1i*2*d3.*kz3))./(1+r23.*r34.*exp(1i*2*d3.*kz3));
r14=(r12+r24.*exp(1i*2*d2.*kz2))./(1+r12.*r24.*exp(1i*2*d2.*kz2));

t12 = 1 + r12;
t23 = 1 + r23;
t34 = 1 + r34;

t24 = t23.*t34.*exp(1i*d3.*kz3)./(1 + 23.*r34.*exp(1i*2*d3.*kz3));
t14 = t12.*t24.*exp(1i*d2.*kz2)./(1 + 12.*r24.*exp(1i*2*d2.*kz2));
```

```
% plot of SPR curve
R4 = (abs(r14)).^2;
plot(theta,R4)
xlabel('Angle of incidence (deg)')
ylabel('Reflectance')

% magnetic field enhancement factor
T4 = (abs(t14)).^2;

% electric field enhancement factor
figure
plot(theta,e1.*T4./e4)
xlabel('Angle of incidence (deg)')
ylabel('Electric field intensity enhancement factor')

[Y,I] = min(R4);
tmin = theta(I);
% angle of resonance
fpdepth = 1./abs(kz4(I))
% field penetration depth (nm) into the sensed dielectric
```

The subroutine for the evaluation of the relative electric permittivity of dielectric media based on Sellmeier equation is shown below

---

```
function [ eg ] = Sellmeier( lbd0, glass )
%Sellmeier series equation describing glass dispersion
%   This function calculates the dispersion of
%   selected glasses based on Sellmeier equation.
%
%   Input parameters are:
%       lbd0 : the wavelength of interest in nm
%       glass: the glass of interest (data type: string)
%           'BK7' = BK7 glass
%           'FS'  = Fused silica glass
%           'CaF2' = Calcium fluoride
%           'MgF2o' = Magnesium fluoride, ordinary ray
%           'MgF2e' = Magnesium fluoride, extraordinary ray
%
%   Output eg is the dielectric constant = n^2
%
lbdu = lbd0/1000;

switch glass
    case('BK7')
        A = 1;
        B = [1.03961212 2.31792344e-1 1.01046945];
        C = [6.00069867e-3 2.00179144e-2 1.03560653e2];
    case('FS')
        A = 1;
        B = [0.6961663 0.4079426 0.8974794];
```

```
        C = [0.0046791 0.0135121 97.9340025];
    case('CaF2')
        A = 1;
        B = [5.675888e-1 4.710914e-1 3.8484723];
        C = [2.52642999e-3 1.00783328e-2 1.20055597e3];
    case('MgF2o')
        A = 1;
        B = [4.8755108e-1 3.9875031e-1 2.3120353];
        C = [1.882178e-3 8.95188847e-3 5.66135591e2];
    case('MgF2e')
        A = 1;
        B = [4.1344023e-1 5.0497499e-1 2.4904862];
        C = [1.35737865e-3 8.23767167e-3 5.65107755e2];
end

s_term = 0;
      for m = 1:3
      s_term = s_term + B(m)*lbdu.^2./(lbdu.^2 - C(m));
      end
eg = A + s_term;

end
```

The subroutine for the evaluation of the relative electric permittivity of metals based on the Lorentz-Drude model is shown below

---

```
function [ er ] = LD_model( lbd0, metal )
%Lorentz-Drude model fit of relative dielectric permittivity
%
%   Input parameters are:
%      lbd0 : the wavelength in nm
%      metal: the chemical symbol of the metal (data type: string)

c = 2.99792458e8;
w = 2*pi*c./(1e-9*lbd0);

switch metal
    case('Au')
        wp = 0.137188E+17;
        Gm = [0.76 0.024 0.01 0.071 0.601 4.384];
        wm = [0 0.630488E+15 0.126098E+16 0.451065E+16
0.653885E+16 0.202364E+17];
        Dm = [0.805202E+14 0.366139E+15 0.524141E+15 0.132175E+16
0.378901E+16 0.336362E+16];
    case('Ag')
        wp = 0.136884E+17;
        Gm = [0.8450 0.0650 0.1240 0.0110 0.8400 5.6460];
        wm = [0 0.123971E+16 0.680775E+16 0.124351E+17
0.137993E+17 0.308256E+17];
        Dm = [0.729239E+14 0.590380E+16 0.686701E+15 0.987512E+14
0.139163E+16 0.367506E+16];
```

```
    case('Cu')
        wp = 0.164535E+17;
        Gm = [0.5750 0.0610 0.1040 0.7230 0.6380 0];
        wm = [0 0.442101E+15 0.449242E+16 0.805202E+16
0.169852E+17 0];
        Dm = [0.455775E+14 0.574276E+15 0.160433E+16 0.488135E+16
0.654037E+16 0];
    case('Al')
        wp = 0.227583E+17;
        Gm = [0.5230 0.2270 0.0500 0.1660 0.0300 0];
        wm = [0 0.246118E+15 0.234572E+16 0.274680E+16
0.527635E+16 0];
        Dm = [0.714047E+14 0.505910E+15 0.474006E+15 0.205251E+16
0.513810E+16 0];
    case('Be')
        wp = 0.281213E+17;
        Gm = [0.0840 0.0310 0.1400 0.5300 0.1300 0];
        wm = [0 0.151925E+15 0.156786E+16 0.483577E+16
0.699462E+16 0];
        Dm = [0.531737E+14 0.100878E+16 0.515785E+16 0.676673E+16
0.273769E+16 0];
    case('Cr')
        wp = 0.163319E+17;
        Gm = [0.1680 0.1510 0.1500 1.1490 0.8250 0];
        wm = [0 0.183829E+15 0.824952E+15 0.299292E+16
0.133314E+17 0];
        Dm = [0.714047E+14 0.482362E+16 0.198262E+16 0.406551E+16
0.202820E+16 0];
    case('Ni')
        wp = 0.241864E+17;
        Gm = [0.0960 0.1000 0.1350 0.1060 0.7290 0];
        wm = [0 0.264349E+15 0.884203E+15 0.242624E+16
0.925071E+16 0];
        Dm = [0.729239E+14 0.685333E+16 0.202668E+16 0.330892E+16
0.955911E+16 0];
    case('Pd')
        wp = 0.147671E+17;
        Gm = [0.3300 0.6490 0.1210 0.6380 0.4530 0];
        wm = [0 0.510468E+15 0.761144E+15 0.252043E+16
0.868251E+16 0];
        Dm = [0.121540E+14 0.448178E+16 0.843183E+15 0.702045E+16
0.491629E+16 0];
    case('Pt')
        wp = 0.145696E+17;
        Gm = [0.3300 0.1910 0.6590 0.5470 3.5760 0];
        wm = [0 0.118501E+16 0.199629E+16 0.477196E+16
0.140515E+17 0];
        Dm = [0.121540E+15 0.785452E+15 0.279238E+16 0.557261E+16
0.129394E+17 0];
    case('Ti')
        wp = 0.110753E+17;
        Gm = [0.1480 0.8990 0.3930 0.1870 0.0010 0];
        wm = [0 0.118046E+16 0.234724E+16 0.381180E+16
0.295190E+17 0];
        Dm = [0.124578E+15 0.345781E+16 0.382547E+16 0.252651E+16
0.267692E+16 0];
    case('W')
        wp = 0.200845E+17;
```

```
        Gm = [0.2060 0.0540 0.1660 0.7060 2.5900 0];
        wm = [0 0.152533E+16 0.291240E+16 0.543891E+16
0.113913E+17 0];
        Dm = [0.972319E+14 0.805202E+15 0.194616E+16 0.506214E+16
0.886634E+16 0];
end

ld_term = 0;
      for m = 1:6
    ld_term = ld_term + Gm(m)./(wm(m)^2 - w.^2 + 1j*w*Dm(m));
      end
er = real(1 + wp^2*ld_term) - 1j*imag(1 + wp^2*ld_term);

end
```

The subroutine for the evaluation of the refractive index of water at room temperature (298 K) is shown below

---

```
function [ n ] = nwater( lbd0 )
% temperature is 298 K
p = 0.997;
T = 298/273.15;

w = lbd0./589;

a0 = 0.244257733;
a1 = 9.74634476e-3;
a2 = -3.73234996e-3;
a3 = 2.68678472e-4;
uv = 0.229202;
a4 = 1.58920570e-3;
a5 = 2.45934259e-3;
a6 = 0.900704920;
a7 = -1.66626219e-2;
ir = 5.432937;

tmp = a0+a1*p+a2*T+a3*T.*w.^2+a4./w.^2+a5./(w.^2-uv^2)+a6./(w.^2-
ir^2)+a7*p^2;
n = sqrt((1+2*p*tmp)./(1-p*tmp));

end
```

A.3. Simulation Details (Lumerical MODE and OptiFDTD)

In the presence of very thin metallic layers (15-20 nm), non-uniform meshing is used for the numerical simulations. Around the thin metallic layer, the mesh size is set to 1 nm (minimum mesh size) which is smoothly expanded to 10 nm (maximum mesh size) in the dielectric layers. The maximum mesh increase rate corresponding to this metal/dielectric transition is set at 0.08 which means that the mesh size grows progressively at the rate of at most 8 percent.

In most simulations, the device substrate and other surrounding materials extend far beyond the edge of the simulation region. Therefore, the most obvious choice of boundary conditions is the perfectly matched layer (PML), which will absorb fields at the simulation boundary. However, the more numerically efficient metallic (perfect electrical conductor, PEC) boundary conditions can frequently be used even though the real device is not surrounded by a metal box. As a matter of fact, if the modal fields are negligible at the edge of the simulation region, then the choice of boundary conditions is basically irrelevant. In such cases, the most numerically efficient rather than the most physically correct boundary conditions can be used for faster simulation. Based on this reasoning, metal boundary conditions are chosen for the simulations of waveguide structures using Lumerical MODE Solutions.

For the simulations of the periodic arrays of sub-wavelength structures with OptiFDTD, the most judicious choice of the appropriate boundary conditions is dictated by the symmetry of the problem. In these simulations, periodic boundary conditions (PBC) are used in the x-y plane so that only one unit cell needs to be considered. In the direction of propagation (z axis), anisotropic PML boundary conditions are called for as the field intensity is generally non-negligible.